

University of Alberta

Three Dimensional Deformation of Orthodontic Brackets

By

Garrett William Melenka

A thesis submitted to the Faculty of Graduate Studies and Research
in partial fulfillment of the requirements for the degree of

Masters of Science

Department of Mechanical Engineering

©Garrett William Melenka
Fall 2012
Edmonton, Alberta

Permission is hereby granted to the University of Alberta Libraries to reproduce single copies of this thesis and to lend or sell such copies for private, scholarly or scientific research purposes only. Where the thesis is converted to, or otherwise made available in digital form, the University of Alberta will advise potential users of the thesis of these terms.

The author reserves all other publication and other rights in association with the copyright in the thesis and, except as herein before provided, neither the thesis nor any substantial portion thereof may be printed or otherwise reproduced in any material form whatsoever without the author's prior written permission.

Abstract

Braces are commonly used to correct misalignments or malocclusions in the mouth. One particular orthodontic treatment utilizes archwire rotation to control the anterior inclination of a tooth and motion is achieved through the interaction of a rectangular archwire within the rectangular bracket slot. The mechanical interaction between the wire and bracket slot can result in both elastic and plastic bracket deformation. To investigate bracket deformation due to archwire rotation the Orthodontic Torsion Simulator (OTS) was developed at the University of Alberta. A three dimensional (3D) DIC measurement method will be employed to determine the 3D deformation of the orthodontic brackets. The 3D DIC method will utilize two CCD cameras coupled with a stereo microscope and deformation of self-ligating orthodontic brackets of varying geometry will be compared using the 3D DIC method to demonstrate the 3D behavior of orthodontic brackets due to archwire rotation.

Table of Contents

Chapter 1 Introduction	1
1.1 Motivation.....	1
1.2 Thesis Objectives	2
1.3 Thesis Scope	2
1.4 Thesis Outline	3
1.5 References.....	4
Chapter 2 Background	6
2.1 Orthodontic Brackets	6
2.1.1 Orthodontic Bracket Designs	9
2.1.2 Malocclusions and Orthodontic Brackets	11
2.1.3 Bracket and Archwire Interaction	14
2.2 Optical Measurement Techniques.....	16
2.2.1 Full-Field Measurement Techniques	16
2.2.2 Two-Dimensional Digital Image Correlation	18
2.2.3 Three-Dimensional Digital Image Correlation	19
2.2.4 Stereo Microscope and Digital Image Correlation.....	20
2.3 Deformation of Orthodontic Brackets.....	21
2.4 Conclusions.....	23
2.5 References.....	24

Chapter 3 Design of an Orthodontic Torque Simulator for Measurement of Bracket	29
3.1 Introduction.....	29
3.2 Design Details of the Orthodontic Torque Simulator	30
3.2.1 Force and torque measurement	31
3.2.2 Archwire rotation control.....	32
3.2.3 Bracket position control	32
3.2.4 Bracket Imaging.....	33
3.2.5 Bracket/Load Cell Force Torque Conversion	33
3.3 Orthodontic Torque Simulator Experiment	35
3.3.1 Overhead Images	36
3.3.2 Measured Bracket Force/Moment.....	38
3.4 Digital Image Correlation of Bracket Images	43
3.4.1 DIC Method Source of Error	49
3.5 Orthodontic Bracket Comparison	54
3.6 Discussion.....	56
3.7 Conclusions.....	57
3.8 References.....	58
Chapter 4 Three-Dimensional Deformation of Orthodontic Brackets	60
4.1 Introduction.....	60
4.2 Methods	61
4.2.1 Description of the Orthodontic Torque Simulator	61

4.2.2 Stereo Microscope and CCD Cameras.....	62
4.2.3 Mounting Orthodontic Brackets.....	63
4.2.4 Digital Image Correlation	63
4.2.5 Sample Preparation	66
4.2.6 Stereo Camera Calibration	69
4.2.7 Image Post Processing	70
4.2.8 Accuracy of Bracket Deformation	70
4.2.9 Measurement of Bracket Deformation.....	73
4.2.10 Repeatability of 3D Bracket Measurements	81
4.2.11 Deformation Characteristics of Two Orthodontic Brackets.....	82
4.3 Results and Discussion	84
4.3.1 Repeatability of 3D Bracket Measurements	84
4.3.2 Deformation Characteristics of Two Orthodontic Brackets.....	87
4.4 Conclusions.....	95
4.5 References.....	97
Chapter 5 Three-Dimensional Comparison of Self-Ligating Brackets.....	100
5.1 Introduction.....	100
5.2 Methods and Materials.....	101
5.3 Results.....	113
5.4 Discussion.....	124
5.5 Conclusions.....	131

5.6 References.....	132
Chapter 6 Conclusions, Recommendations and Future Work	135
6.1 Conclusions.....	135
6.2 Recommendations.....	137
6.3 Future Work.....	138

List of Tables

Table 3.1: Specifications of the 6-axis load cell	32
Table 3.2: Bracket offset from load cell measurements and uncertainty.	40
Table 3.3: Maximum bracket force and torque measurement uncertainty.....	40
Table 3.4: Digital image correlation image displacement vector resolution.	50
Table 3.5: Measured bracket offset from load cell	54
Table 3.6: Comparison of orthodontic bracket deformation results	55
Table 4.1: Displacement vector precision [15].	70
Table 4.2: Maximum TW motion.	85
Table 4.3: Maximum ARC motion in three directions.	86
Table 4.4: Maximum and plastic deformation due to archwire rotation for Damon 3MX and In-Ovation R brackets. Bolded values show significant differences.....	89
Table 4.5: Comparison of orthodontic bracket TW motion. Bolded values show significant differences.....	90
Table 4.6: Comparison of orthodontic bracket ARC motion. Bolded values show significant differences.....	93
Table 5.1: Maximum and plastic deformation due to archwire rotation for Damon Q and In-Ovation R brackets. Bolded values show significant differences.	129
Table 5.2: Maximum ARC motion.	130

List of Figures

Figure 2.1: Example of Braces (a) braces bonded to teeth (b) solid model of Ormco Orthos conventional orthodontic bracket (Solid model provided courtesy of Ormco Corporation).....	7
Figure 2.2: Self-ligating orthodontic bracket components (a) Top view of bracket showing tie-wings, archwire and bracket base (b) Side view of bracket showing the angle of the bracket slot (prescription). Archwire rotation occurs about the x^* axis of the bracket coordinate system. (c) Archwire rotation ϕ relative to the neutral position of the wire in the bracket slot. Wire is in the neutral position when the base of the bracket slot is parallel to the minor axis of the archwire.	9
Figure 2.3: Top and Side views of orthodontic brackets (a) Damon Q (b) Speed (c) Innovation R	11
Figure 2.4: Buccolingual Inclination (a) Teeth with a Malocclusion (b) Teeth with correct alignment (c) Example of an archwire rotating in a bracket slot to control tooth angulation.....	12
Figure 2.5: Comparison of Controlled and Uncontrolled Tipping (a) Uncontrolled Tipping where tooth root position is changed due to applied force (b) Controlled Tipping where tooth root position is maintained due to combination of applied force and archwire rotation	13
Figure 2.6: Tooth Alignment Examples (a) Translation (b) Root Movement	14
Figure 2.7: Flow diagram of the 2D DIC method showing an object with a random speckle pattern at time t_n and t_{n+1} . The cross-correlation peak between the original and deformed images is also shown.	19
Figure 2.8: Stereo DIC processing method.....	20

Figure 3.1: Device used to measure loads applied to orthodontic brackets and bracket deformation (a) Rendered image of Orthodontic Torque Simulator (b) Close-up of the Orthodontic Torque Simulator.	31
Figure 3.2: Load cell and bracket coordinate systems. (a) Offset of orthodontic bracket from load cell (b) Coordinate system transformation showing displacement, rotation about the z axis and the angle ϕ indicating the direction of archwire rotation.	34
Figure 3.3: Flowchart of Orthodontic Torque Simulator operation.	36
Figure 3.4: Deformation of a Damon Q (Ormco Corporation) orthodontic bracket due to archwire rotation. Archwire rotation (ϕ) is shown in 9° increments to a maximum angle of 78°	37
Figure 3.5: Profile image of an orthodontic bracket showing the original bracket and the outline of a deformed bracket.	38
Figure 3.6: Load cell transformation showing transformed and measured m_y , (a) transformed and measured force ($f_x f_y f_z$). (b) transformed and measured moments (m_x, m_y, m_z).	41
Figure 3.7: Load cell transformation showing transformed and measured m_x as well as effect of increasing and decreasing archwire rotation. Error bars are shown to demonstrate the uncertainty in the $m_{xbracket}$ measurement.	41
Figure 3.8: Engagement of archwire in retentive component of the orthodontic bracket resulting in a change in the measured moment $m_{ybracket}$. (a) archwire rotation of 45° (b) archwire rotation of 54° showing the opening of the archwire retentive component and a displacement in the y^* direction due to archwire rotation.	43
Figure 3.9: Bracket images showing image subsets (a) 64x64 pixel subsets (b) 128x128 pixel subsets.	44

Figure 3.10: Preparation of orthodontic brackets (a) Bracket without micro-etching (b) Bracket with micro-etching. (c) Correlation peak for bracket without micro- etching (d) Correlation peak for bracket with micro- etching.	46
Figure 3.11: Tracking of bracket TWs. (a) Bracket in original position shown by solid lines, square boxes showing maximum TW displacement and diamonds showing final TW position after applied torque has been removed. (b) Plot of bracket TW deformation measured using digital image correlation showing initial and final deformation of the left hand and right hand side of the bracket TWs.....	48
Figure 3.12: Effect of window size on overhead images with artificial displacement (a) Single pass processing (b) Multi pass processing.	52
Figure 3.13: Orthodontic bracket displacement results (a) Bracket displacement plots for all 30 brackets (b) Average of multiple bracket displacement results showing standard deviation for the 30 brackets. (c) Single bracket displacement showing error bars resulting from DIC accuracy	53
Figure 3.14: Comparison of Damon Q (a) and Speed (b) self- ligating orthodontic brackets	54
Figure 3.15: Comparison of Damon Q and Speed orthodontic brackets (a) Deformation results (b) Measured applied moment.....	56
Figure 4.1: Orthodontic Torque Simulator used to replicate the effect of archwire rotation on orthodontic brackets (a) single camera version (b) stereo camera version	62
Figure 4.2: Load cell and bracket coordinate systems. (a) Offset of orthodontic bracket from load cell (b) Close-up of bracket load cell system	63
Figure 4.3: Stereo DIC processing method.....	66
Figure 4.4: Orthodontic bracket sample preparation (a) bracket without speckle pattern (b) bracket with speckle pattern (c) Correlation peak for bracket without speckling (d) correlation peak for bracket with speckling.....	68

Figure 4.5: 3D DIC bulk motion validation (a) in-plane motion (b) out-of-plane motion	72
Figure 4.6: Orthodontic bracket box regions used to track TW motion	75
Figure 4.7: Stereo images of a Damon 3MX bracket showing the different camera perspectives (a) Left Camera (b) Right Camera	76
Figure 4.8: Damon 3MX orthodontic bracket deformation due to archwire rotation (ϕ) (a) Increasing 0° (b) Increasing 21° (c) Increasing 45° (d) Decreasing 21° (e) Decreasing 0° 3D DIC Bracket Deformation	77
Figure 4.9: Profile image of a Speed orthodontic bracket showing deformation due to archwire rotation.	78
Figure 4.10: 3D bracket surface visualized from stereo image pair 3D DIC data (a) Damon 3MX and (b) In-Ovation R; and (c) Damon 3MX bracket image (d) In-Ovation R bracket image.	79
Figure 4.11: 3D bracket surface and 3D displacement vectors for Damon 3MX and In-Ovation R brackets (a) Damon 0° rotation (b) In-Ovation 0° rotation (c) Damon 12° (d) In-Ovation 12° (e) Damon 24° (f) In-Ovation 24° (g) Damon 36° (h) In-Ovation 36° (i) Damon 45° (j) In-Ovation 45°	81
Figure 4.12: Comparison of self-ligating brackets (a) passive ligation Damon Q (solid model provided courtesy ofOrmco) (b) In-Ovation R (solid model provided courtesy of GAC) active ligation applies a preload to the wire. (c) Schematic of passive and active ligation brackets retention system.....	83
Figure 4.13: Repeatability of Damon 3MX bracket TW motion. Average and standard deviation displacements for (a) TW#1-3 x^* (b) TW#2-4 x^* (c) TW#1-3 y^* (d) TW#2-4 y^* (e) TW#1-3 z^* (f) TW#2-4 z^* . Solid line indicates increasing archwire rotation. Dashed line indicates decreasing archwire rotation.	84

Figure 4.14: Repeatability of Damon 3MX bracket ARC. Average and standard deviation of archwire retentive displacements (a) component x^* (b) ARC y^* (c) ARC z^* . Solid line indicates increasing archwire rotation. Dashed line indicates decreasing archwire rotation.	86
Figure 4.15: Damon 3MX and In-Ovation R bracket TW average motion and standard deviation as a function of wire rotation angle. (a) TW#1-3 x^* (b) TW#2-4 x^* (c) TW#1-3 y^* (d) TW#2-4 y^* (e) TW#1-3 z^* (f) TW#2-4 z^* . Solid line indicates In-Ovation R bracket Dashed line indicates Damon 3MX bracket.	88
Figure 4.16: Bracket ARC motion (a) ARC x^* (b) ARC y^* (c) ARC z^* . Solid line indicates In-Ovation R bracket Dashed line indicates Damon 3MX bracket.	91
Figure 5.1: Self-ligating orthodontic bracket components (a) Top view of bracket showing TWs, archwire and bracket base (b) Side view of bracket showing the angle of the bracket slot (prescription). Archwire rotation occurs about the x^* axis of the bracket coordinate system. (c) Control of tooth angulations using archwire rotation (d) Archwire rotation, ϕ	102
Figure 5.2: Top and side views of self-ligating orthodontic brackets (a) Damon Q (b) Speed (c) Innovation R	104
Figure 5.3: Comparison of self-ligating brackets (a) passive ligation Damon Q (solid model provided by Ormco) (b) In-Ovation R (solid model provided by GAC) active ligation applies a preload to the wire. (c) schematic of passive and active ligation brackets	105
Figure 5.4: Orthodontic Torque Simulator	106
Figure 5.5: Orthodontic bracket box regions used to track TW motion (a) Damon Q (b) In-Ovation R (c) Speed	109

Figure 5.6: Damon Q orthodontic bracket deformation due to archwire rotation (ϕ) (a) increasing 0° (b) increasing 21° (c) increasing 45° (d) decreasing 21° (e) decreasing 0°.	111
Figure 5.7: Orthodontic bracket 3D surfaces (a) Damon Q (b) In-Ovation R (c) Speed (d) Damon Q 3D Surface (e) In-Ovation R 3D surface (f) Speed 3D surface.	112
Figure 5.8: In-Ovation R bracket image and 3D surface comparison (a) original bracket image (b) 3D surface.	113
Figure 5.9: Damon Q image sequence demonstrating increasing and decreasing archwire rotation for selected archwire angles (a) 0° (b) 9° (c) 21° (d) 33° (e) 45° (f) -33° (g) -21° (h) -9° (i) -0°.	114
Figure 5.10: Damon Q 3D image sequence x^* displacement (a) 0° (b) 9° (c) 21° (d) 33° (e) 45° (f) -33° (g) -21° (h) -9° (i) -0°. Displacement measured in micrometers (μm). Minimal motion occurred in the x^* direction for the Damon Q TWs or ARC as indicated by no change in the 3D bracket contour plot sequence.	115
Figure 5.11: Damon Q 3D image sequence y^* displacement (a) 0° (b) 9° (c) 21° (d) 33° (e) 45° (f) -33° (g) -21° (h) -9° (i) -0°. Displacement measured in micrometers (μm). The dominant motion occurs for tie-wings #1 and #2 in this image sequence.	115
Figure 5.12: Damon Q 3D image sequence x^* displacement (a) 0° (b) 9° (c) 21° (d) 33° (e) 45° (f) -33° (g) -21° (h) -9° (i) -0°. Displacement measured in micrometers (μm). Maximum motion for the ARC can be seen at 45° of archwire rotation.	116
Figure 5.13: In-Ovation R image sequence demonstrating increasing and decreasing archwire rotation for selected archwire angles (a) 0° (b) 9° (c) 21° (d) 33° (e) 45° (f) -33° (g) -21° (h) -9° (j) -0°.	117
Figure 5.14: In-Ovation R 3D image sequence x^* displacement (a) 0° (b) 9° (c) 21° (d) 33° (e) 45° (f) -33° (g) -21° (h) -9° (i) -0°. Displacement measured in micrometers (μm).	

Minimal motion occurred in the x^* direction for the In-Ovation R TWs or ARC as indicated by no change in the 3D bracket contour plot sequence.	118
Figure 5.15: In-Ovation R 3D image sequence y^* displacement (a) 0° (b) 9° (c) 21° (d) 33° (e) 45° (f) -33° (g) -21° (h) -9° (j) -0° . Displacement measured in micrometers (μm). The dominant motion occurs for tie-wings #1 and #2 in this image sequence.	118
Figure 5.16: In-Ovation R 3D image sequence z^* displacement (a) 0° (b) 9° (c) 21° (d) 33° (e) 45° (f) -33° (g) -21° (h) -9° (j) -0° . Maximum motion for the ARC can be seen at 45° of archwire rotation. The final position of the ARC is lower than the start position as shown for the final bracket image indicating that the ARC has intruded into the bracket slot.....	119
Figure 5.17: Speed image sequence (a) 0° (b) 9° (c) 21° (d) 33° (e) 45° (f) -33° (g) -21° (h) -9° (j) -0° . The ARC of the Speed bracket opened during testing and at 33° of wire rotation and remains open through the image sequence.	120
Figure 5.18: Speed 3D image sequence x^* displacement (a) 0° (b) 9° (c) 21° (d) 33° (e) 45° (f) -33° (g) -21° (h) -9° (j) -0° . Displacement measured in micrometers (μm). Motion of the ARC in the x^* direction can be see for decreasing wire rotation indicating that the ARC has opened during testing.....	121
Figure 5.19: Speed 3D image sequence y^* displacement (a) 0° (b) 9° (c) 21° (d) 33° (e) 45° (f) -33° (g) -21° (h) -9° (j) -0° . Displacement measured in micrometers (μm). Maximum motion occurred at 45° of archwire rotation. The ARC opened during testing as indicated by the color of the ARC after 33° of archwire rotation.....	121
Figure 5.20: Speed 3D image sequence z^* displacement (a) 0° (b) 9° (c) 21° (d) 33° (e) 45° (f) -33° (g) -21° (h) -9° (j) -0° . Displacement measured in micrometers (μm). Maximum motion for the ARC can be seen for 45° of AW rotation. The contour plot indicates that the ARC opened during testing and that the ARC did not return to the original postion after the AW was returned to the origin.	122

Figure 5.21: Comparison on Damon Q and In-Ovation R bracket TW motion. Average and standard deviation displacements for (a) TW#1-3 x^* (b) TW#2-4 x^* (c) TW#1-3 y^* (d) TW#2-4 y^* (e) TW#1-3 z^* (f) TW#2-4 z^* . Solid line indicates In-Ovation R bracket. Dashed line indicates Damon Q bracket. 123

Figure 5.22: Damon Q and In-Ovation R ARC motion. Average and standard deviation of archwire retentive displacements (a) ARC x^* (b) ARC y^* (c) ARC z^* 124

List of Abbreviations

2D	Two Dimensional
3D	Three Dimensional
3D DIC	Three Dimensional Digital Image Correlation
AW	Archwire
ARC	Archwire retentive Component
CAD	Computer Aided Design
CC	Cross-Correlation correlation criterion
CCD	Charge-Couple Device
CMO	Common Main Objective
DAQ	Data Acquisition System
DIC	Digital Image Correlation
ESPI	Electronic Speckle Pattern Interferometry
FEA	Finite Element Analysis
OTS	Orthodontic Torque Simulator
PDL	Periodontal Ligament
SL	Self-Ligating
SSD	Sum-squared difference correlation criterion
TW	Tie-Wing
UofA	University of Alberta
UR1	Upper Right Incisor

List of Symbols

x^*	Defined as parallel to the archwire
y^*	The direction of lateral motion of the bracket tie wings due to archwire rotation
z^*	The direction from the base of the orthodontic bracket to the top of the bracket tie wings
ϕ	Archwire rotation occurs about the x^* axis and the angle of archwire rotation
μ	Micro
Δx	Offset of Bracket in x direction
Δy	Offset of Bracket in y direction
Δz	Offset of Bracket in z direction
θ	Bracket angular rotation about the z -axis
$f_{xbracket}$	Bracket force in x^* -direction
$f_{ybracket}$	Bracket force in y^* -direction
$f_{zbracket}$	Bracket force in z^* -direction
$m_{xbracket}$	Bracket moment about the bracket x^* -axis
$m_{ybracket}$	Bracket moment about the bracket y^* -axis
$m_{zbracket}$	Bracket moment about the bracket z^* -axis
f_{xLC}	The load cell force in the x -direction
f_{yLC}	The load cell force in the y -direction
f_{zLC}	The load cell force in the z -direction
m_{xLC}	Load cell moment about the x -axis
m_{yLC}	Load cell moment about the y -axis
m_{zLC}	Load cell moment about the z -axis
u	Displacement in x -direction
v	Displacement in y -direction
w	Displacement in z -direction
$\overline{D_{TieWing}}$	Average displacement of the defined regions for Tie-Wings
LHS_D	Displacement between tie-wings 1 and 3
RHS_D	Displacement between tie-wings 2 and 4
$RelativeRC$	Relative retentive component motion

Chapter 1 Introduction

1.1 Motivation

Orthodontics is now an integral part of proper oral care. Based on the Third National Health and Nutrition Examination Survey, Phase 1 1988-91, approximately 20% of all adults 18-50 and 18% of children have required orthodontic treatment [1]. However, orthodontic treatment is a lengthy, iterative, and inefficient process [2]. Treatment biomechanics is complex and requires an understanding of the behaviour of the basic treatment tools.

Braces and archwires are commonly used by orthodontists to correct teeth misalignment (malocclusions) within the dental arch. Braces are typically worn for over two years and patients require regular checkups to monitor and adjust the realignment progress [3]. An understanding of the deformation that occurs to orthodontic brackets is necessary to ensure that the desired amount of torque is applied to a tooth. Multiple variables affect the deformation of orthodontic brackets, namely, magnitude of archwire rotation, bracket geometries, archwire size, and ligation method [4-8].

To investigate the deformation of a bracket as an archwire is rotated within the bracket slot the Orthodontic Torsion Simulator (OTS) was developed, designed, and constructed at the University of Alberta through collaboration between the Department of Mechanical Engineering and Department of Dentistry. Initially, the OTS was developed by Badawi et al. [9] to measure the torque applied to brackets as a function of wire rotation but did not attempt to assess bracket deformation. Due to the small size, complicated geometries, and complex loading conditions of orthodontic brackets, conventional deformation measurement methods such as strain gauges are impractical. OTS measurement

capabilities were expanded to include bracket surface deformation during torque application by Lacoursiere et al. [10] using an overhead camera. A CCD camera and a full-field digital image correlation (DIC) measurement based system were added to OTS to measure the displacement of bracket tie-wings (TW) as a load is applied [10]. Since, the OTS has been used to demonstrate the deformation of self-ligating brackets and to compare geometrically similar titanium and stainless steel brackets [11, 12]. The OTS has shown that material properties affect the deformation of orthodontic brackets with response to the same amount of archwire rotation [12]. As well, the design of self-ligating brackets has been shown to affect the amount of bracket deformation due to archwire rotation [11, 13].

Using the OTS system, many groundbreaking findings were made, but the system is still limited to measuring in-plane motion of orthodontic brackets. Three-dimensional (3D) measurements are required to properly quantify the deformation behaviour of brackets as a function of varying archwire angulations, applied torque, bracket geometries, archwire size and ligation method.

1.2 Thesis Objectives

For this thesis, a new two camera, digital image correlation-based 3D measurement system will be developed for the OTS to describe the 3D motion of orthodontic brackets due to archwire rotation. A full assessment of both the 2D and 3D optical measurement systems and OTS will be performed. Finally, a comparative study of the deformation behaviour of three orthodontic brackets to applied archwire rotation will be undertaken.

1.3 Thesis Scope

This thesis focuses on developing a tool for measuring bracket deformation and its show clinical and research relevance. This work could encompass vast numbers of tests due to

the number of brackets and wires available on the market, many adapted for different human teeth. As such upper right incisor brackets (UR1) were selected for the evaluation of the 3D OTS and all bracket tests will be performed using the same size 0.483 x 0.635mm (0.019 x 0.025") archwire. Furthermore, it has been shown that the ligation method used to secure the archwire within the bracket slot can affect the bracket-archwire interaction[14]; therefore, self-ligating brackets were selected to evaluate the accuracy of this measurement technique to reduce the variability caused by other bracket ligation methods such as elastic or steel ligatures. Once the 3D OTS measurement system has been evaluated and validated it will be possible to measure brackets of varying ligation, archwire size and brackets of different prescription.

1.4 Thesis Outline

The thesis is organized into six chapters. Critical background for this work is discussed in Chapter 2; this will focus on bracket deformation and tooth movement, optical measurement techniques and methods that have been previously used to measure orthodontic bracket deformation. Chapter 3 consists of a description of the orthodontic torque simulator as well as the 2D DIC method to measure orthodontic bracket deformation. A detailed error analysis for the load cell and 2D deformation measurements is performed. Chapter 4 describes the addition of a second camera to the OTS and describes the method for measuring the three dimensional deformation of orthodontic brackets. Additionally, a detailed error analysis of the 3D deformation method is performed. Three self-ligating orthodontic brackets are compared using the 3D deformation method in Chapter 5 to demonstrate the variability between brackets used for similar treatment; this will provide valuable information to clinicians on the 3D motion of self-ligating brackets. A summary of the results and future work are described in Chapter 6.

Detailed calculations and description of the methods used to quantify bracket deformation are described in the Appendix of this thesis. Appendix A details the calculation used to transform data acquire at the load cell to bracket forces and torques. Appendix B provides a detailed description of the digital image correlation method. Appendix C describes the experimental procedure used to prepare and test the orthodontic brackets to measure 3D deformation. Appendix D describes the method used to visualize the 3D bracket deformation and Appendix E provides detailed CAD drawings of the OTS to describe the size and construction of the measurement device.

1.5 References

- [1] J. A. Brunelle, M. Bhat and J. A. Lipton, "Prevalence and distribution of selected occlusal characteristics in the US population, 1988-1991," *J. Dent. Res.*, vol. 75, pp. 706-713, 1996.
- [2] J. H. Marangalou, F. Ghalichi and B. Mirzakouchaki, "Numerical simulation of orthodontic bone remodeling," *Orthodontic Waves*, vol. 68, pp. 64-71, 2009.
- [3] F. R. Beckwith, R. J. Ackerman Jr., C. M. Cobb and D. E. Tira, "An evaluation of factors affecting duration of orthodontic treatment." *Am. J. Orthod. Dentofacial Orthop.*, vol. 115, pp. 439-447, 1999.
- [4] D. A. Flores, L. K. Choi, J. M. Caruso, J. L. Tomlinson, G. E. Scott and M. T. Jeiroudi, "Deformation of metal brackets: a comparative study." *Angle Orthod.*, vol. 64, pp. 283-290, 1994.
- [5] J. Odegaard, T. Meling and E. Meling, "An evaluation of the torsional moments developed in orthodontic applications. An in vitro study." *Am. J. Orthod. Dentofacial Orthop.*, vol. 105, pp. 392-400, 1994.
- [6] H. Fischer-Brandies, W. Orthuber, M. Es-Souni and S. Meyer, "Torque Transmission between Square Wire and Bracket as a Function of Measurement, Form and Hardness Parameters," *Journal of Orofacial Orthopedics*, vol. 61, pp. 258-265, 2000.
- [7] H. Gmyrek, C. Bourauel, G. Richter and W. Harzer, "Torque capacity of metal and plastic brackets with reference to materials, application, technology and biomechanics," *Journal of Orofacial Orthopedics*, vol. 63, pp. 113-128, 2002.

- [8] C. Gioka and T. Eliades, "Materials-induced variation in the torque expression of preadjusted appliances," *American Journal of Orthodontics and Dentofacial Orthopedics*, vol. 125, pp. 323-328, 2004.
- [9] H. M. Badawi, R. W. Toogood, J. P. R. Carey, G. Heo and P. W. Major, "Torque expression of self-ligating brackets," *American Journal of Orthodontics and Dentofacial Orthopedics*, vol. 133, pp. 721-728, 2008.
- [10] R. Lacoursiere, D. Nobes, D. Homeniuk, J. P. Carey, H. Badawi and P. W. Major. Measurement of orthodontic bracket TW elastic and plastic deformation by arch wire torque expression utilizing an optical image correlation technique. *Journal of Dental Biomechanics* vol. 2010(Article ID 397037), 2010.
- [11] T. W. Major, J. P. Carey, D. S. Nobes, G. Heo, G. W. Melenka and P. W. Major, "An investigation into the mechanical characteristics of select self-ligated brackets at a series of clinically relevant maximum torquing angles: loading and unloading curves and bracket deformation," *Eur. J. Orthod.*, Jul 12, 2011.
- [12] G. W. Melenka, R. A. Lacoursiere, J. P. Carey, D. S. Nobes, G. Heo and P. W. Major, "Comparison of deformation and torque expression of the orthos and orthos Ti bracket systems," *Eur. J. Orthod.*, Oct 19, 2011.
- [13] T. W. Major, J. P. Carey, D. S. Nobes, G. Heo and P. W. Major, "Mechanical effects of third-order movement in self-ligated brackets by the measurement of torque expression," *American Journal of Orthodontics and Dentofacial Orthopedics*, vol. 139, pp. e31-e44, 2011.
- [14] N. W. Harradine, "Self-ligating brackets: where are we now?" *J. Orthod.*, vol. 30, pp. 262-273, 2003.

Chapter 2 Background

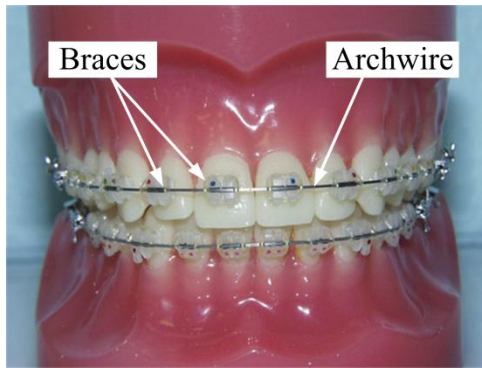
Brackets and wires have long been used in orthodontic practice to produce tooth movement. Until recently it was assumed that the brackets and wires did not deform and thus all of the elastic energy of the twisted wire was transmitted to the tooth through a bracket that behaved as a rigid body [1, 2]; however, it has been shown that brackets deform [3-6] and thus some of the wire elastic energy is dissipated in gross deformation or local (notching) strain energy.

In this chapter, the effect of orthodontic bracket deformation will be put into clinical context by presenting a basic overview of the method by which braces and archwires achieve tooth movement. Current methods to measure bracket deformations will then be discussed. Optical methods used to measure deformation and strain will be presented and discussed in the context of bracket deformation. Finally, current bracket deformation measurement results using the OTS developed at the University of Alberta will be described.

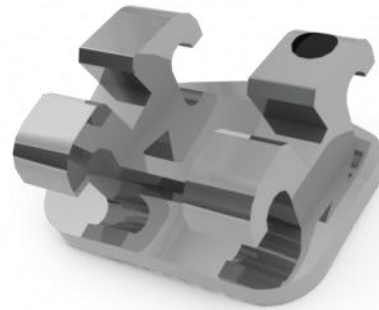
2.1 Orthodontic Brackets

Brackets and archwires, generally known as braces, are commonly used by orthodontists to correct misalignment of teeth (malocclusions) within the dental arch. Braces are typically worn for over two years and patients require regular checkups to monitor and adjust the realignment progress [7]. Braces consist of a series of brackets that are bonded to the crown of individual teeth and an archwire that passes between each bracket and is ligated to the brackets. An example of braces bonded to teeth can be seen in Figure 2.1 (a) while an individual bracket is shown in Figure 2.1 (b). Short term tooth movement results from the deformation of the periodontal ligament (PDL), the connective tissue which attaches the tooth to the alveolar bone [8, 9]. Forces applied through the tooth's

crown apply pressure and deform the PDL [10, 11]. Pressures applied to the PDL are alleviated initially by creep-like internal fluid flow, which is then followed by the resorption and apposition of alveolar bone to support the tooth in its post-loading position [8-10]. Tooth movement is therefore the result of the loading created by the mechanical interaction of the archwire with the bracket.



(a)



(b)

Figure 2.1: Example of Braces (a) braces bonded to teeth (b) solid model of Ormco Orthos conventional orthodontic bracket (Solid model provided courtesy of Ormco Corporation)

Pictorial schematics of an in-situ orthodontic bracket are shown in Figure 2.2. The self-ligating bracket, shown in Figure 2.2 (a), consists of a base, tie wings and an archwire slot and is presented in reference to a central incisor tooth. The base is bonded to the tooth using a dental adhesive. The tie-wings (TW) provide a retentive means to hold an archwire within the bracket slot. The archwire is retained in the bracket slot using either elastic ligation or stainless steel ligation wires, alternatively self-ligating brackets include a movable component used to secure the archwire without the need for additional ligation [12, 13]. A self ligating bracket is shown in Figure 2.2 whereas a conventional ligation bracket is shown in Figure 2.1 (b). It can be seen in Figure 2.2 that for a coordinate system attached to the bracket (x^*, y^*, z^*) the x^* axis is defined as parallel to the archwire, the y^* axis is defined as the direction of lateral motion of the bracket tie wings due to

archwire rotation, and the z^* axis defines the direction from the base of the orthodontic bracket to the top of the bracket tie wings. The coordinate system shown in Figure 2.2 will be used to describe orthodontic bracket deformation. Archwire rotation occurs about the x^* axis and the angle of archwire rotation is defined as ϕ with respect to the neutral position of the archwire. The neutral position of the archwire is defined as the position when the archwire is parallel to the base of the bracket slot as shown in Figure 2.2 (c). The figure also shows the relative size of the bracket/archwire system compared to the tooth and the complex geometry of the bracket. The size of orthodontic brackets will vary between manufacturers. Figure 2.2 shows the typical size of a Damon Q bracket that has a bracket base with dimensions of approximately 3.25x3.20mm and a height of 2.20mm.

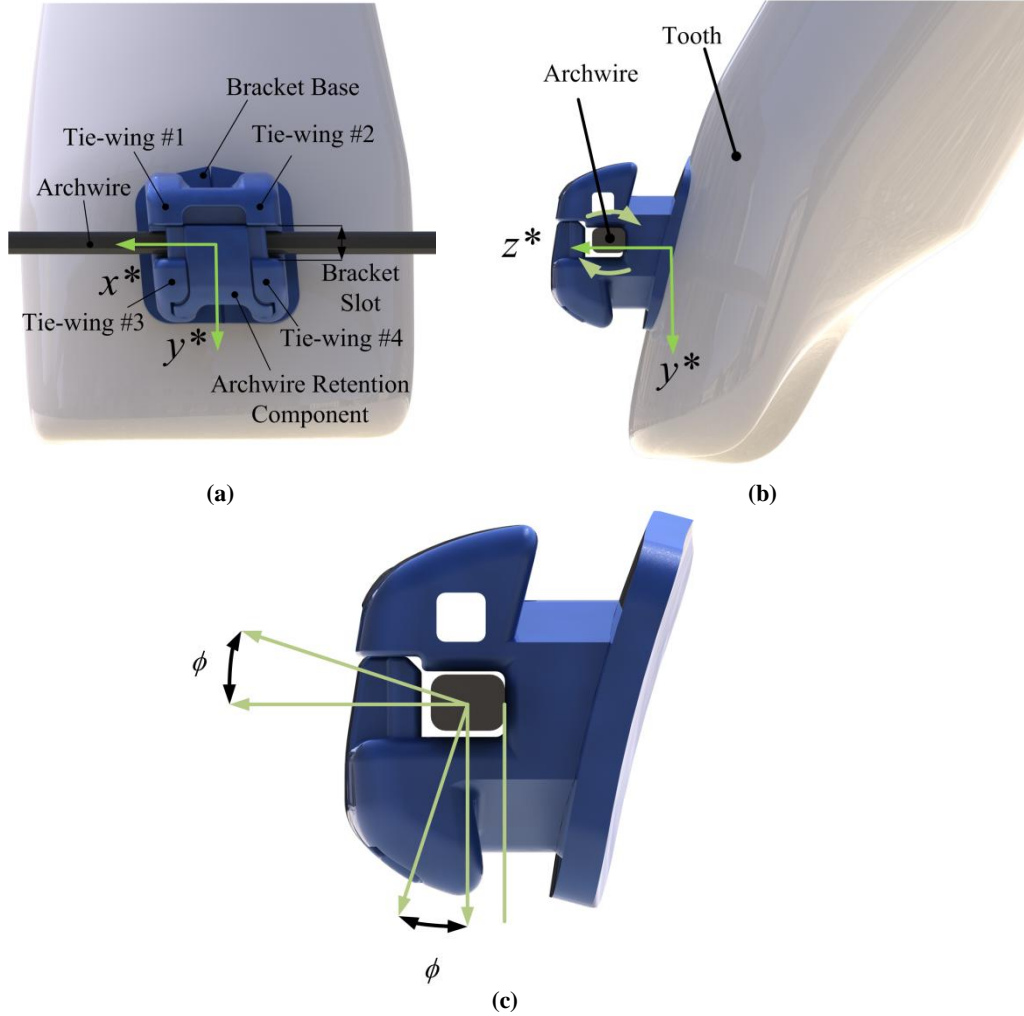


Figure 2.2: Self-ligating orthodontic bracket components (a) Top view of bracket showing tie-wings, archwire and bracket base (b) Side view of bracket showing the angle of the bracket slot (prescription). Archwire rotation occurs about the x^* axis of the bracket coordinate system. (c) Archwire rotation ϕ relative to the neutral position of the wire in the bracket slot. Wire is in the neutral position when the base of the bracket slot is parallel to the minor axis of the archwire.

2.1.1 Orthodontic Bracket Designs

Archwires are maintained in the bracket slot using two main methods: elastomeric or steel ligatures or self-ligating brackets. Self-ligating brackets are advantageous as the archwire can be ligated in the bracket slot more quickly than conventional elastic or steel ligation [14, 15]. As well, the archwire retentive component (ARC) will not degrade as would elastic ligatures due to the temperature and chemical environment within the mouth [14].

Top and side images of three orthodontic brackets are shown in Figure 2.3. This figure shows both active and passive ligation brackets. The top and side bracket images exhibit the irregular geometries of these particular self-ligating brackets. The brackets shown are Damon Q (Ormco Corporation, Orange, California, USA), Speed (Strite Industries, Cambridge, Ontario, Canada), and In-Ovation R (GAC, Bohemia, NY, USA) self-ligating brackets. The In-Ovation R and Speed brackets are active ligation brackets while the Damon Q is a passive ligation bracket. Active ligation brackets are designed with a curved leaf spring type ARC which applies force to the archwire [16]. The ARC for active ligation brackets encroaches in the bracket slot to maintain contact with the archwire [16]. This contact will help to maintain the alignment of the wire in the brackets slot. A disadvantage of the active ligation brackets is the possibility of reduced torque transmitted to the tooth due to reduced gingival slot wall depth to allow for the elastic ARC to secure the archwire in the bracket slot [15]. The curved leaf spring ARC is shown in the side images of the In-Ovation R and Speed brackets. Passive ligation brackets have a more rigid ARC that does not maintain contact with the archwire [16].

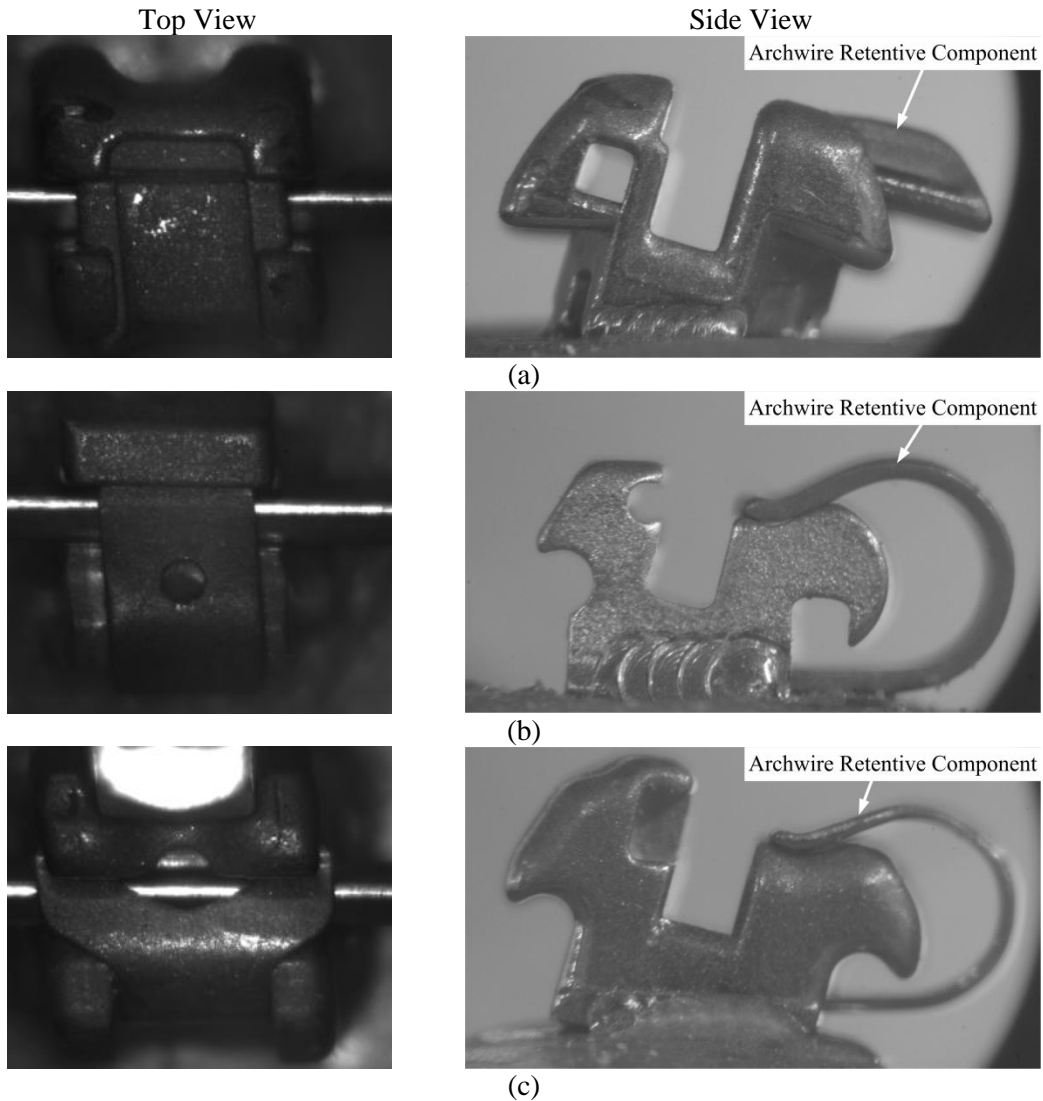


Figure 2.3: Top and Side views of orthodontic brackets (a) Damon Q (b) Speed (c) Innovation R

2.1.2 Malocclusions and Orthodontic Brackets

Correct buccolingual inclination of posterior and anterior teeth is required to provide post treatment stability [8, 17-20]. The diagrams of Figure 2.4 illustrate situations where archwire rotation is used in orthodontics to control the inclination of a tooth in the mouth. An example of a tooth before and after alignment is demonstrated in Figure 2.4 (a) and (b). Proper buccolingual alignment is maintained by rotating a rectangular archwire within a bracket slot as seen in Figure 2.4 (c).

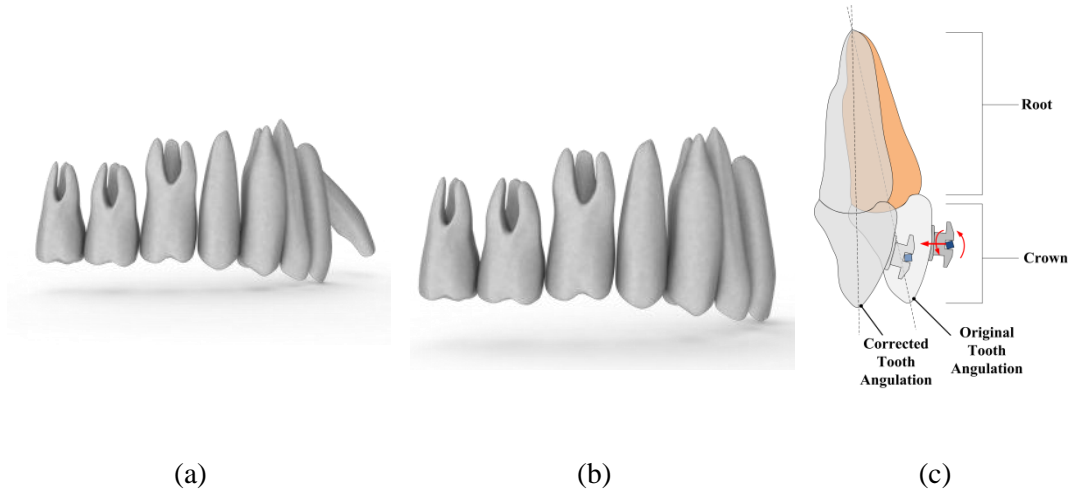


Figure 2.4: Buccolingual Inclination (a) Teeth with a Malocclusion (b) Teeth with correct alignment (c) Example of an archwire rotating in a bracket slot to control tooth angulation.

There are several cases in orthodontics where archwire rotation is necessary: controlled tipping, translation and root movement [9]. Controlled tipping is used when a force is applied to a tooth in order to adjust the position of the tooth crown. Controlled tipping is desirable as the position of the root of the tooth is maintained. The difference between controlled tipping and uncontrolled tipping are illustrated in Figure 2.5. This figure shows that uncontrolled tipping occurs when the root of the tooth is moved due to an applied force (Figure 2.5 (a)). Conversely controlled tipping, which requires a force and a torque applied at the bracket, results in movement of the tooth crown while maintaining root position (Figure 2.5 (b)).

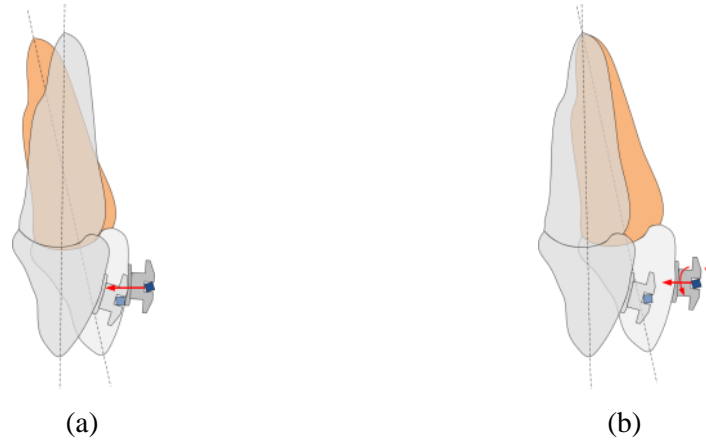


Figure 2.5: Comparison of Controlled and Uncontrolled Tipping (a) Uncontrolled Tipping where tooth root position is changed due to applied force (b) Controlled Tipping where tooth root position is maintained due to combination of applied force and archwire rotation

Similarly, archwire rotation is used in cases where an incisor is to be retracted. In this case it is desired that the tooth translates but does not rotate. In this situation the archwire is rotated in order to counter-act the tendency of a tooth to tip when a translational force is applied to the crown of the tooth (Figure 2.6a). Archwire rotation is also used when it is required to adjust the position of the root of a tooth while preserving the crown orientation (Figure 2.6b). The ratio of moment caused by archwire rotation with respect to the applied force to the tooth will affect the ultimate tooth movement i.e. whether root movement or pure translation of a tooth will occur. This relationship is defined as the *moment-to-force* ratio [9].



Figure 2.6: Tooth Alignment Examples (a) Translation (b) Root Movement

2.1.3 Bracket and Archwire Interaction

There exists a disparity between science and orthodontic definitions for torque. The traditional definition of torque is the tendency of a system of forces to rotate an object and create internal torsional shear stresses [21]. In the orthodontic context, twisted wires experience torsion, or torque, along their long axis. The orthodontic definition of torque refers to the angle of rotation of an archwire within a bracket. “Torque” is also defined as the buccal-lingual root inclination of a tooth and the magnitude of torque that achieves tooth root tipping [3, 22]. “Torque” is used by orthodontists to correct the faciolingual inclination of a tooth within the dental arch. For this thesis, torque will refer to the engineering definition. Archwire rotation will refer to the angle that the wire has been rotated in the bracket slot. The angle of archwire rotation with respect to the neutral position will be defined as ϕ as shown in Figure 2.2 (c).

Tooth movement is achieved through loads applied to the tooth through the archwire. Specific to the torque focus of this thesis, the resulting tooth movement depends highly on the magnitude of torsion applied through archwire rotation; the material properties of the archwire and bracket; bracket and archwire geometry; and the location of the bracket on the tooth [1, 18, 23-26]. Not only does tooth movement depend on the mechanical bracket-archwire interaction but also on biological factors. Biological factors affecting

tooth movement include: patient health and compliance of the PDL [10, 11]. The aforementioned factors will greatly affect the speed and efficacy of treatment. In addition, the magnitude of torsion applied to an archwire can have implications on the bracket-archwire complex. Significant archwire rotation and associated loads can result in permanent deformation to the bracket tie wings [1]. If permanent deformation occurs the orthodontic brackets will cease to function as expected and consequently treatment time will be affected. Depending on the bracket and archwire material properties and bracket slot dimensions the magnitude of torque will affect the bracket- archwire complex differently. Therefore, it is desirable to quantify the motion of bracket TWs due to archwire rotation and torque.

2.2 Optical Measurement Techniques

Optical measurement techniques are desirable for the measurement of bracket deformation due to their inherent size and complex geometry. The irregular geometries illustrated previously in Figure 2.3 demonstrate the need for an optical technique in order to measure TW motion. The following section briefly describes the method of digital image correlation. More specific information will be provided in the following chapters as they relate to individual studies.

2.2.1 Full-Field Measurement Techniques

Full-field optical techniques are commonly used for strain or displacement measurement. Non full-field techniques, such as strain gauges are limited to specific locations and require direct contact with samples. Examples of full-field optical techniques include: photo elasticity, Moiré interferometry, electronic speckle pattern interferometry (ESPI), holographic interferometry, and digital image correlation (DIC) [27-30]. Photoelasticity relies on the birefringence properties of specific transparent materials since birefringent materials have two refractive indices' [27]. A fringe pattern is generated when polarized light passes through a photoelastic material since the refractive indices result in a relative phase retardation between wave components. The interference between the two waves are brought together using a polariscope and a fringe pattern results on the object surface. Moiré interferometry uses the mechanical interference of light by superimposed networks of lines [27]. Strain is measured by deforming a grid which has been applied to the test object surface with respect to a reference grid and then measuring the resulting moiré pattern. Electronic speckle pattern interferometry (ESPI) uses a laser to create a speckle pattern on the test object surface. Deformation is measured by recording the interference between two light fields. The interference between the reference and the illumination light field create a speckle pattern. The speckle pattern will change when the object is

deformed [27]. Most interferometric methods require that measurements be conducted in a vibration free environment and require a coherent light source such as a laser [30] to produce a fringe pattern which represents the deformation of the test object surface. Data processing of the fringe pattern is time consuming in order to quantify the measured strain on the test object surface. Digital image correlation (DIC) is an alternative method for optical strain measurement that uses a random contrast pattern to measure deformation. DIC is a relatively simple experimental setup which consists of a CCD (charge-couple device) camera, a computer to record the digital images and a test sample with a random speckle pattern applied to the object surface. The DIC method does not have the rigorous stability requirements of interferometric methods. As well, the DIC method does not require a laser to produce a speckle pattern like ESPI, rather test samples can be illuminated using white light or natural light. DIC can be used for macroscopic and microscopic measurements since a variety of imaging devices can be used to collect digital images. Digital image correlation can be performed in either single camera or dual camera configurations. The single camera configuration allows for in-plane displacement/ strain measurements. By contrast the dual camera configuration allows for in-plane and out-of-plane displacement/ strain measurements.

The DIC method is advantageous as it does not require contact with the specimen contrary to devices like strain gauges for example. Deformation is measured by tracking contrast features on the specimen surface between subsequent images [30]. Each digital image is segmented into evenly spaced subsets and an image correlation algorithm is performed for each image subset. The average displacement in each subset is then determined as the displacement vector from the center of the region to the maximum of the correlation function. DIC can be used in 2D or 3D configurations. The 2D configuration (single camera) allows for in-plane motion (x^*, y^*) to be measured whereas

the 3D configuration (2 or more cameras) allows for both in-plane and out of plane motion (x^*, y^*, z^*) [29]. DIC displacement measurement is comprised of four consecutive steps (1) specimen preparation, (2) image calibration (3) collection of specimen deformation before and after loading (4) post processing of images to determine displacement or strain [28]. DIC can be performed on a sample which has a natural high contrast surface pattern or by speckling the surface with a material such as paint to achieve a random contrast surface pattern. Images are calibrated to convert from pixels to physical space (mm, inches) by acquiring an image of a target with a grid of known spacing.

2.2.2 Two-Dimensional Digital Image Correlation

Two dimensional (2D) DIC is a full field optical measurement technique that uses a random speckle pattern on a specimen surface to measure deformations and strains [31]. DIC technique was first proposed for strain measurement of a planar surface by Peters et al [32]. This work was expanded on by Sutton et al., Chu et al., and Bruck et al. to validate the accuracy of the DIC method and to improve the speed of the DIC algorithm [30, 33, 34]. DIC has since become a widely used method for contact free strain measurements [35, 36].

Once digital images of the test object have been collected the DIC method can be used to measure displacement/ strain. Each digital image is segmented into evenly spaced subsets and an image correlation algorithm is performed for each subset to produce a displacement vector. The image subsets are of the size $(N=2M+1) \times (N=2M+1)$ pixels where N is the size of the image subset and M is the distance from the subset center. The basic principle of digital image correlation is shown in Figure 2.7. This image shows the reference image at time t_n and the deformed image at t_{n+1} with an applied speckle pattern. Also shown is the reference and deformed image discretized into image subsets. The

reference and deformed image subsets are compared using either a cross-correlation (CC) or sum-squared difference (SSD) correlation criterion. An example of the peak correlation coefficient is shown in Figure 2.7. The correlation methods compute either a peak maximum or minimum between the reference and deformed subset. After the peak correlation coefficient has been detected the position of the deformed subset can be found. The difference between the position of the reference and deformed subset produce the in-plane displacement vector (u,v) indicating the motion of the surface over time.

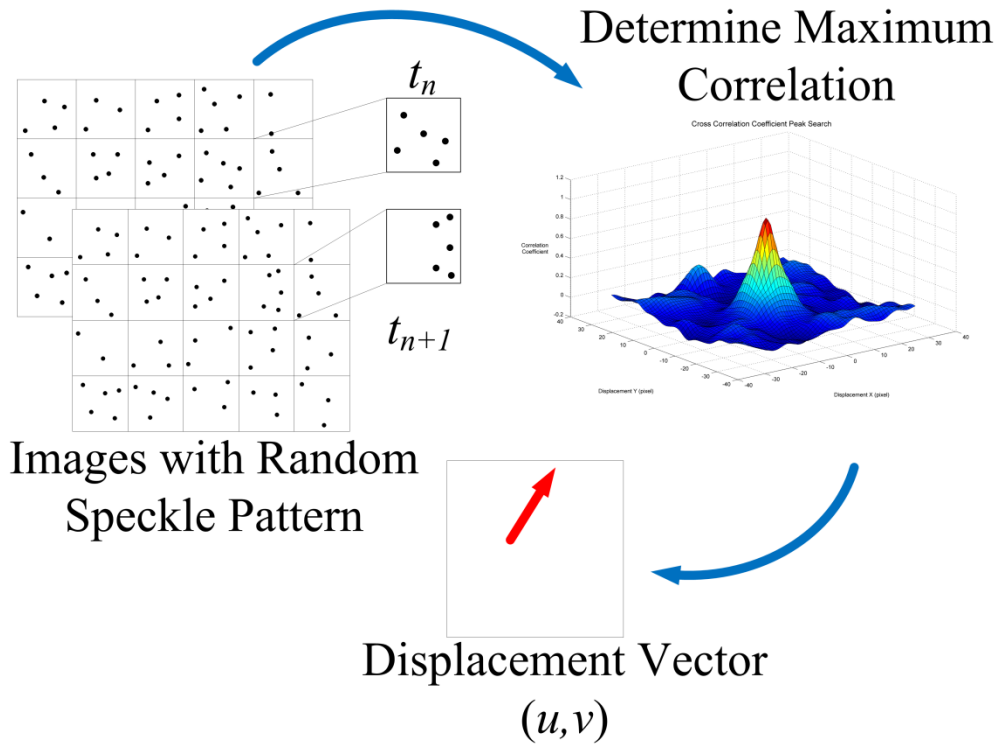


Figure 2.7: Flow diagram of the 2D DIC method showing an object with a random speckle pattern at time t_n and t_{n+1} . The cross-correlation peak between the original and deformed images is also shown.

2.2.3 Three-Dimensional Digital Image Correlation

Three dimensional (3D) DIC is an extension of 2D DIC. By adding a second camera it is possible to measure the both the in-plane and out-of-plane motion of an object. The method of measuring 3D deformation of an object was first outlined by Luo et al. [37] and has been successfully used to measure 3D deformation of objects by many authors

[29, 38-40]. In addition, 3D DIC has been used in conjunction with stereo microscope to measure the 3D deformation of small scale objects [41, 42].

A schematic of the 3D DIC processing method is shown in Figure 2.8. This figure shows that the same cross correlation described in Section 2.2.2 is performed between images 1 and 2 for cameras A and B to determine the 2D displacement vectors (u_1, v_1) and (u_2, v_2) . The 3D Displacement vectors (u, v, w) are determined using the 2D displacement vectors for each camera and the determined surface height from the stereo cross correlation of the test object [29, 40, 43].

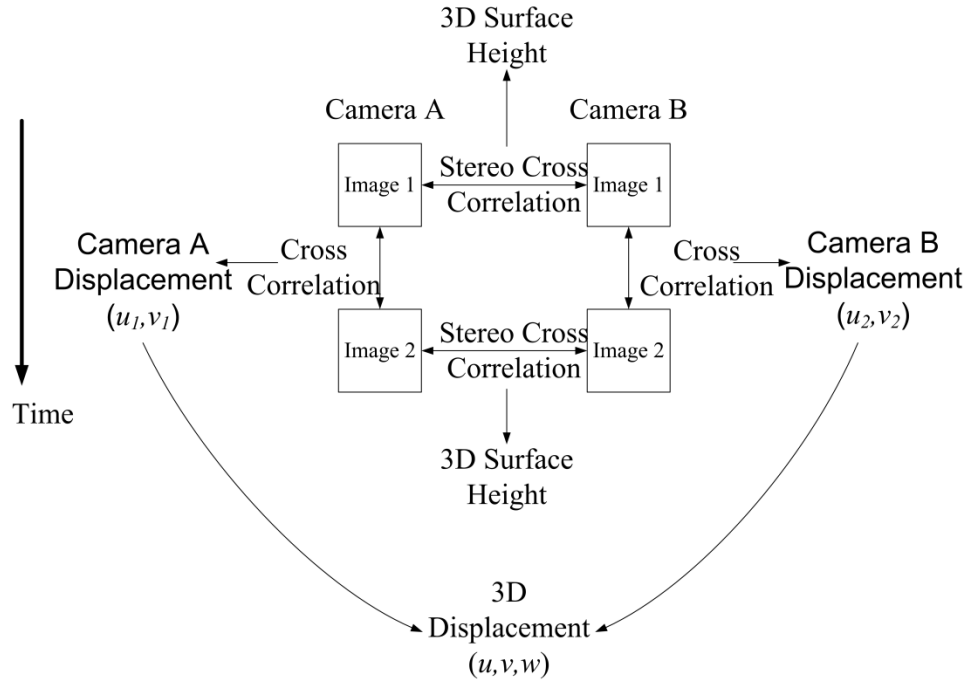


Figure 2.8: Stereo DIC processing method

2.2.4 Stereo Microscope and Digital Image Correlation

DIC can be extended to the measurement of micro scale three dimensional (3D) deformations. The 3D deformation of microscopic objects can be measured by using a pair of CCD cameras with a stereo microscope. Stereo microscopes are manufactured in two configurations: Greenough or Common Main Object (CMO) [44]. The Greenough

stereo microscope consists of two compound microscopes offset by an angle to provide stereo perception. The CMO stereo microscope operates by acquiring images from different sides of the common objective lens [44, 45]. The CMO stereo microscopes are typically more compact than Greenough stereo microscopes. Several authors have performed 3D DIC in conjunction with a stereo microscope [42, 45, 46]. The method of measuring microscopic deformations using a stereo microscope has been described by Schreier et al. [47]. A particular example where a stereo microscope and digital image correlation is the measurement of mouse carotid arteries [42].

2.3 Deformation of Orthodontic Brackets

Several studies examined archwire rotation in a bracket to investigate recoverable and permanent bracket deformation [1, 2, 26, 48, 49] by measuring brackets before and after an applied archwire rotation. The shape of the test brackets before and after archwire rotation was used to determine if permanent deformation of the bracket occurred. Several of these studies have made reference to bracket deformation without quantification [1, 26, 48]. Kapur et al [2] measured the permanent change in titanium and stainless steel bracket slot profile before and after archwire rotation using a stereomicroscope to quantify bracket deformation. This study only measured permanent change to the bracket slot and an assessment of the measurement resolution was not given. Their findings indicate that plastic deformation occurs to orthodontic brackets as a result of a 45° archwire rotation. Similarly, a study by Feldner et al [49] measured bracket deformation at a variety of archwire rotation angles. Bracket deformation was measured optically using a stereomicroscope and a protractor with a reported resolution of 0.2°. Neither study is able to determine the wire torque at which the onset of permanent deformation occurs.

The effect of incremental archwire twist on the loads experienced by orthodontic brackets has also been examined [19, 23, 24] by measuring the bulk forces and moments applied to the bracket by an archwire using load cells connected to the bracket. These approaches do not assess whether the bracket undergoes elastic and plastic deformation or what the interaction mechanism is between the archwire and the bracket; nor does it indicate what properties of the mechanical bracket/wire coupling are important. These unresolved questions complicate the development of a model of the archwire-bracket interaction which would be used to optimize the bracket-archwire mechanical system.

The development of an optical method of measuring bracket deformation by Lacoursiere et al. [3] demonstrated that the loads applied to an orthodontic bracket through archwire rotation can result in both plastic and elastic deformation. This method allows for bracket deformation to be measured as a function of archwire rotation. The optical bracket deformation method utilizes digital image correlation in order to determine the motion of the bracket TWs. The bracket deformation study indicates that deformation can affect clinical treatment as a plastically deformed bracket will not transfer the equivalent force as an undeformed bracket. DIC has further been used in the field of orthodontics to measure the shrinkage of resin based dental composites [50].

The optical bracket deformation measurement method developed by Lacoursiere et al. [3] has since been used to measure the deformation of conventional and self-ligating brackets [4-6]. Melenka et al. [6] demonstrated that the deformation of orthodontic brackets is affected by material properties. Geometrically similar titanium and stainless steel conventional ligation brackets were compared. It was demonstrated that stainless steel brackets plastically deformation 2.8 times more than the titanium brackets for a maximum archwire rotation of 51° . Major et al. [5] compared self-ligating brackets and demonstrated that In-Ovation R brackets exhibit less total deformation at 51° and plastic

deformation than Damon Q or Speed brackets. In another study, Major et al. [4] showed that plastic deformation for the Damon Q brackets first occurs approximately between 24 and 28° of archwire rotation, while the Speed brackets began to plastically deform approximately between 20 and 24° of archwire rotation. These optical bracket deformation measurement studies have conclusively demonstrated that permanent deformation occurs to orthodontic brackets due to archwire rotation.

2.4 Conclusions

The objective of this chapter was to introduce the problem of orthodontic bracket deformation as a rationale for the thesis work undertaken and how this deformation can affect orthodontic treatment. Bracket deformation was put in context by describing the bracket-archwire interaction necessary to achieve tooth movement. The current approaches to measure bracket deformation have been described and the OTS developed at the University of Alberta has been presented. This device was developed to address the need for a systematic method of quantifying the torque expressed by orthodontic brackets and to measure bracket deformation. The OTS utilizes the method of DIC to measure bracket deformation. This method is used to measure bracket deformation since the size and complicated geometry prohibits the use of conventional deformation measurement methods. The optical measurement method of DIC has been successfully used to measure the 2D deformation of orthodontic brackets. The current OTS is limited to measuring the in-plane motion of orthodontic brackets and cannot detect the full deformations occurring during treatment. The addition of a second camera to the OTS will allow for both in-plane and out-of-plane bracket deformation to be measured. The method of 3D DIC was described and evidence of the use of a stereo microscope and 3D DIC to measure the deformation of small scale objects was presented.

Chapter 3 will describe in detail the measurement of 2D bracket deformation using the OTS and will describe the errors associated with the 2D bracket deformation. Chapter 4 will extend the measurement of orthodontic brackets to 3D deformations using a pair of CCD cameras and a stereo microscope. Finally, three self-ligating bracket designs will be compared in Chapter 5 to demonstrate the 3D motion of orthodontic brackets due to archwire rotation. Active and passive self-ligating brackets will be compared using the 3D OTS to show the 3D motion of the bracket TWs. As well, the motion of ARC of the self-ligating brackets will be compared using this method.

2.5 References

- [1] D. A. Flores, L. K. Choi, J. M. Caruso, J. L. Tomlinson, G. E. Scott and M. T. Jeiroudi, "Deformation of metal brackets: a comparative study." *Angle Orthod.*, vol. 64, pp. 283-290, 1994.
- [2] R. Kapur, P. K. Sinha and R. S. Nanda, "Comparison of load transmission and bracket deformation between titanium and stainless steel brackets." *Am. J. Orthod. Dentofacial Orthop.*, vol. 116, pp. 275-278, 1999.
- [3] R. Lacoursiere, D. Nobes, D. Homeniuk, J. P. Carey, H. Badawi and P. W. Major. Measurement of orthodontic bracket tie wing elastic and plastic deformation by arch wire torque expression utilizing an optical image correlation technique. *Journal of Dental Biomechanics* vol. 2010(Article ID 397037), 2010.
- [4] T. W. Major, J. P. Carey, D. S. Nobes, G. Heo, G. W. Melenka and P. W. Major, "An investigation into the mechanical characteristics of select self-ligated brackets at a series of clinically relevant maximum torquing angles: loading and unloading curves and bracket deformation," *Eur. J. Orthod.*, Jul 12, 2011.
- [5] T. W. Major, J. P. Carey, D. S. Nobes, G. Heo and P. W. Major, "Measurement of plastic and elastic deformation due to third-order torque in self-ligated orthodontic brackets," *Am. J. Orthod. Dentofacial Orthop.*, vol. 140, pp. 326-339, Sep, 2011.
- [6] G. W. Melenka, R. A. Lacoursiere, J. P. Carey, D. S. Nobes, G. Heo and P. W. Major, "Comparison of deformation and torque expression of the orthos and orthos Ti bracket systems," *Eur. J. Orthod.*, Oct 19, 2011.

- [7] F. R. Beckwith, R. J. Ackerman Jr., C. M. Cobb and D. E. Tira, "An evaluation of factors affecting duration of orthodontic treatment." *Am. J. Orthod. Dentofacial Orthop.*, vol. 115, pp. 439-447, 1999.
- [8] W. R. Proffit, H. W. Fields and D. M. Sarver, *Contemporary Orthodontics*. St. Louis, Mo.: Mosby Elsevier, 2007.
- [9] R. Nanda and A. Kuhlberg, "Principles of biomechanics," in *Biomechanics in Clinical Orthodontics*, R. Nanda, Ed. Philadelphia, PA: Saunders, 1997, pp. 1-20.
- [10] T. S. Fill, J. P. Carey, R. W. Toogood and P. W. Major, "Experimentally determined mechanical properties of, and models for, the periodontal ligament: critical review of current literature," *J. Dent. Biomech.*, vol. 2011, pp. 312980, 2011.
- [11] T. S. Fill, R. W. Toogood, P. W. Major and J. P. Carey, "Analytically determined mechanical properties of, and models for the periodontal ligament: Critical review of literature," *J. Biomech.*, vol. 45, pp. 9-16, 2012.
- [12] W. A. Brantley and T. Eliades, "Orthodontic brackets," in *Orthodontic Materials: Scientific and Clinical Aspects*, W. A. Brantley and T. Eliades, Eds. New York: Thieme, 2001, pp. 144-147, 165.
- [13] N. Harradine, "Self-ligating brackets: Theory, practice, and evidence," in *Orthodontics : Current Principles and Techniques*, 5th ed., L. W. Graber, Ed. Philadelphia, PA: Elsevier/Mosby, 2012, pp. 581.
- [14] N. W. Harradine, "Historical aspects and evolution of ligation and appliances," in *Self-Ligation in Orthodontics: An Evidence-Based Approach to Biomechanics and Treatment*, T. Eliades and N. Pandis, Eds. Chichester, U.K. ; Ames, Iowa: Wiley-Blackwell, 2009, pp. 1.
- [15] N. W. Harradine, "Self-ligating brackets: where are we now?" *J. Orthod.*, vol. 30, pp. 262-273, 2003.
- [16] N. Pandis, T. Eliades and C. Bourauel, "Biomechanics of self-ligation: Analysis of forces and moments exerted by self-ligating brackets," in *Self-Ligation in Orthodontics: An Evidence-Based Approach to Biomechanics and Treatment*, T. Eliades and N. Pandis, Eds. Chichester, U.K. ; Ames, Iowa: Wiley-Blackwell, 2009, pp. 33-44.
- [17] E. A. O'Higgins, R. H. Kirschen and R. T. Lee, "The influence of maxillary incisor inclination on arch length." *Br. J. Orthod.*, vol. 26, pp. 97-102, 1999.
- [18] C. Gioka and T. Eliades, "Materials-induced variation in the torque expression of preadjusted appliances," *American Journal of Orthodontics and Dentofacial Orthopedics*, vol. 125, pp. 323-328, 2004.
- [19] H. M. Badawi, R. W. Toogood, J. P. R. Carey, G. Heo and P. W. Major, "Torque expression of self-ligating brackets," *American Journal of Orthodontics and Dentofacial Orthopedics*, vol. 133, pp. 721-728, 2008.

- [20] J. A. Wagner and R. J. Nikolai, "Stiffness of incisor segments of edgewise arches in torsion and bending." *Angle Orthod.*, vol. 55, pp. 37-50, 1985.
- [21] R. C. Hibbler, "Stress," in *Mechanics of Materials*, 6th ed., R. C. Hibbler, Ed. New York: Prentice Hall, 2004, pp. 8.
- [22] A. Archambault, R. Lacoursiere, H. Badawi, P. W. Major, J. Carey and C. Flores-Mir, "Torque expression in stainless steel orthodontic brackets," *Angle Orthod.*, vol. 80, pp. 201-210, 2010.
- [23] J. Odegaard, T. Meling and E. Meling, "An evaluation of the torsional moments developed in orthodontic applications. An in vitro study." *Am. J. Orthod. Dentofacial Orthop.*, vol. 105, pp. 392-400, 1994.
- [24] T. R. Meling, J. Odegaard and E. O. Meling, "On mechanical properties of square and rectangular stainless steel wires tested in torsion." *Am. J. Orthod. Dentofacial Orthop.*, vol. 111, pp. 310-320, 1997.
- [25] H. Fischer-Brandies, W. Orthuber, M. Es-Souni and S. Meyer, "Torque Transmission between Square Wire and Bracket as a Function of Measurement, Form and Hardness Parameters," *Journal of Orofacial Orthopedics*, vol. 61, pp. 258-265, 2000.
- [26] H. Gmyrek, C. Bourauel, G. Richter and W. Harzer, "Torque capacity of metal and plastic brackets with reference to materials, application, technology and biomechanics," *Journal of Orofacial Orthopedics*, vol. 63, pp. 113-128, 2002.
- [27] G. L. Cloud, *Optical Methods of Engineering Analysis*. Cambridge ; New York: Cambridge University Press, 1995.
- [28] B. Pan, K. Qian, H. Xie and A. Asundi, "Two-dimensional digital image correlation for in-plane displacement and strain measurement: A review," *Meas Sci Technol*, vol. 20, 2009.
- [29] J. -. Orteu, "3-D computer vision in experimental mechanics," *Opt Lasers Eng*, vol. 47, pp. 282-291, 2009.
- [30] T. C. Chu, W. F. Ranson and M. A. Sutton, "Applications of digital-image-correlation techniques to experimental mechanics," *Exp. Mech.*, vol. 25, pp. 232-244, 1985.
- [31] M. A. Sutton, J. J. Orteu and H. W. Schreier, *Image Correlation for Shape, Motion and Deformation Measurements : Basic Concepts, Theory and Applications*. New York, N.Y: Springer, 2009.
- [32] W. H. Peters and W. F. Ranson, "Digital Imaging Techniques in Experimental Stress Analysis," *Optical Engineering*, vol. 21, pp. 427-431, 1982.

- [33] M. Sutton, C. Mingqi, W. Peters, Y. Chao and S. McNeill, "Application of an optimized digital correlation method to planar deformation analysis," *Image Vision Comput.*, vol. 4, pp. 143-150, 1986.
- [34] H. A. Bruck, S. R. McNeill, M. A. Sutton and W. H. Peters III, "Digital image correlation using Newton-Raphson method of partial differential correction," *Exp. Mech.*, vol. 29, pp. 261-267, 1989.
- [35] F. Hild and S. Roux, "Digital image correlation: From displacement measurement to identification of elastic properties - A review," *Strain*, vol. 42, pp. 69-80, 2006.
- [36] B. Pan, K. Qian, H. Xie and A. Asundi, "Two-dimensional digital image correlation for in-plane displacement and strain measurement: A review," *Measurement Science and Technology*, vol. 20, 2009.
- [37] P. F. Luo, Y. J. Chao, M. A. Sutton and W. H. Peters III, "Accurate measurement of three-dimensional deformations in deformable and rigid bodies using computer vision," *Exp. Mech.*, vol. 33, pp. 123-132, 1993.
- [38] P. Synnergren, "Measurement of three-dimensional displacement fields and shape using electronic speckle photography," *Optical Engineering*, vol. 36, pp. 2302-2310, 1997.
- [39] P. Synnergren and M. Sjö Dahl, "A stereoscopic digital speckle photography system for 3-D displacement field measurements," *Optics and Lasers in Engineering*, vol. 31, pp. 425-443, 1999.
- [40] D. Garcia, J. J. Orteu and L. Penazzi, "A combined temporal tracking and stereo-correlation technique for accurate measurement of 3D displacements: Application to sheet metal forming," *J. Mater. Process. Technol.*, vol. 125-126, pp. 736-742, 2002.
- [41] N. J. Lawson and J. Wu, "Three-dimensional particle image velocimetry: Experimental error analysis of a digital angular stereoscopic system," *Measurement Science and Technology*, vol. 8, pp. 1455-1464, 1997.
- [42] M. A. Sutton, X. Ke, S. M. Lessner, M. Goldbach, M. Yost, F. Zhao and H. W. Schreier, "Strain field measurements on mouse carotid arteries using microscopic three-dimensional digital image correlation," *Journal of Biomedical Materials Research - Part A*, vol. 84, pp. 178-190, 2008.
- [43] LaVision GmbH, "Product-Manual for DaVis 7.2 StrainMaster Software Item-Number(s): 1105022," 2006.
- [44] H. - Schnitzler and K. - Zimmer, "- Advances in stereomicroscopy," - *Proceedings of SPIE*, pp. - 71000P, .
- [45] H. W. Schreier, D. Garcia and M. A. Sutton, "Advances in light microscope stereo vision," *Exp. Mech.*, vol. 44, pp. 278-288, 2004.

- [46] L. Larsson, M. Sjö Dahl and F. Thuvander, "Microscopic 3-D displacement field measurements using digital speckle photography," *Optics and Lasers in Engineering*, vol. 41, pp. 767-777, 2004.
- [47] H. Schreier, D. Garcia and M. Sutton, "Advances in light microscope stereo vision," *Experimental Mechanics*, vol. 44, pp. 278-288, 2004.
- [48] R. Sadat-Khonsari, A. Moshtaghy, V. Schlegel, B. Kahl-Nieke, M. Möller and O. Bauss, "Torque deformation characteristics of plastic brackets: A comparative study," *Journal of Orofacial Orthopedics*, vol. 65, pp. 26-33, 2004.
- [49] J. C. Feldner, N. K. Sarkar, J. J. Sheridan and D. M. Lancaster, "In vitro torque-deformation characteristics of orthodontic polycarbonate brackets," *American Journal of Orthodontics and Dentofacial Orthopedics*, vol. 106, pp. 265-272, 9, 1994.
- [50] J. Li, A. S. L. Fok, J. Satterthwaite and D. C. Watts, "Measurement of the full-field polymerization shrinkage and depth of cure of dental composites using digital image correlation," *Dental Materials*, vol. 25, pp. 582-588, 2009.

Chapter 3 Design of an Orthodontic Torque Simulator for

Measurement of Bracket

A version of this chapter has been submitted as:

Melenka G.W., Nobes, D.S., Major, P.W., Carey, J.P., Design of an Orthodontic Torque Simulator for Measurement of Orthodontic Bracket Deformation, Experimental Mechanics, EXME-D-12-01693 (2012).

3.1 Introduction

As previously discussed braces and archwires are used by orthodontists to correct teeth misalignment (malocclusions) within the dental arch [1]. Braces consist of a series of brackets that are bonded to the crown of individual teeth and an archwire which passes between each and is ligated to the brackets. Tooth movement is the result of the mechanical interaction of the archwire with the bracket. As a preliminary focus, bracket behaviour needs to be assessed; however, their small size, complicated geometries, and complex loading conditions make conventional measurement methods are impractical.

The objectives of this chapter is to detail the design and development of this novel DIC-based measurement technique used with a modified torque measurement device and assess the level of systematic error associates with the instrumentation within the context of a practical and clinical case-study application. A comparison will be made between the systematic measurement errors to the variability in orthodontic brackets to investigate sources of variability in results. An example test set comparing two styles of bracket will also be discussed to highlight system capability.

3.2 Design Details of the Orthodontic Torque Simulator

To investigate the interaction of the archwire and bracket a physical simulation of archwire rotation within a bracket slot was developed. The Orthodontic Torque Simulator (OTS) presented in Figure 3.1 shows a rendered version of the device in Figure 3.1(a) and a close up digital image of the archwire rotation assembly in Figure 3.1(b). This custom testing device was required to simulate the clinical situation of archwire rotation and measure the loads applied to the bracket. Additionally, an overhead imaging system was added that collects images of the brackets allowing for digital image correlation (DIC) to be performed on the brackets to identify TW movement. Figure 3.1(a) shows the camera system used to collect images of the orthodontic brackets. Archwire rotation is achieved using a computer controlled stepper motor and gear box. Two dies shown in Figure 3.1(b) are used to clamp the archwire are mechanically locked together by a yoke to provide support to the archwire and even rotation from both sides. Also shown in this figure is the 6-axis load cell which is used to collect force and moment data applied to an orthodontic bracket due to archwire rotation.

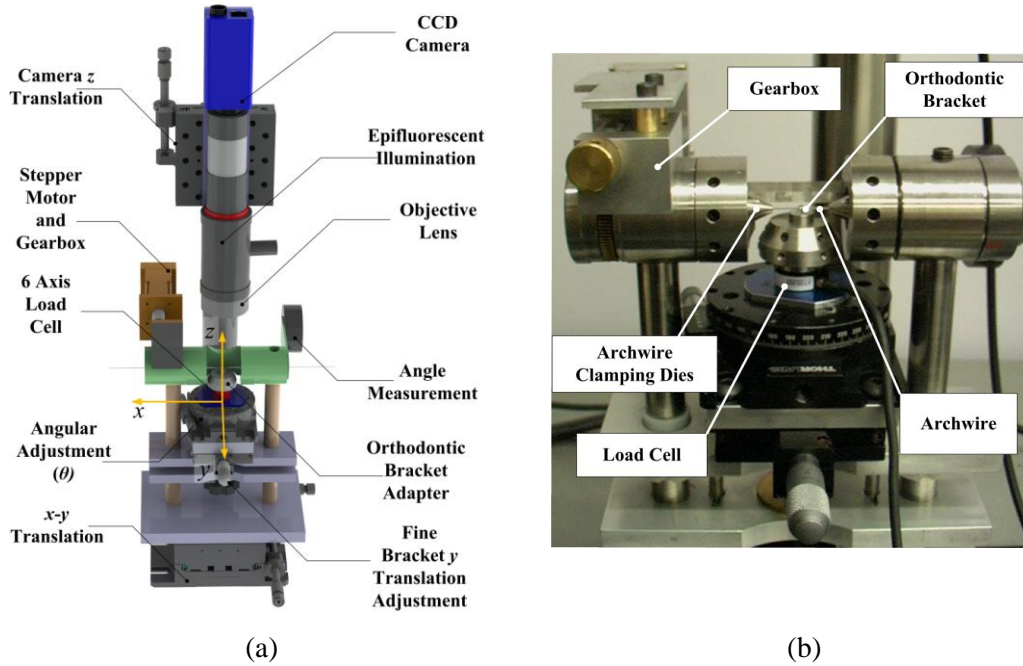


Figure 3.1: Device used to measure loads applied to orthodontic brackets and bracket deformation (a) Rendered image of Orthodontic Torque Simulator (b) Close-up of the Orthodontic Torque Simulator.

3.2.1 Force and torque measurement

The loads applied to the orthodontic brackets were measured using a 6-axis load cell (Nano17 SI-25-0.25, ATI Industrial Automation, Apex, NC, USA) located immediately under the bracket. As shown in Figure 3.1(b), each bracket for testing was bonded to a standard support cylinder (9mm diameter stainless steel \times 9mm long) which was held in a support adaptor. The adaptor allowed connection of the bracket/support cylinder to the load cell while allowing adjustment of angular position of the bracket to align with the archwire. The use of this support cylinder and adaptor offsets the measured loads from the applied loads. The specifications and uncertainties for the load cell are shown in Table 3.1. Data from the load cell was collected using a data acquisition system (DAQ 16-Bit E series NI PCI-6033E; National Instruments, Austin, TX) that had 16 bit input resolution and a maximum sampling rate of 100kS/s. Load cell data was collected at 1000 Hz and 1000 samples per channel were recorded for each load cell reading.

Table 3.1: Specifications of the 6-axis load cell

	F_x	F_y	F_z	T_x	T_y	T_z
Rated Full Scale Loads	25 N	25 N	35 N	250 Nmm	250 Nmm	250 Nmm
Resolution	1/80 N	1/80 N	1/80 N	1/16 Nmm	1/16 Nmm	1/16 Nmm
Measurement Uncertainty (Percent of full scale load)	1.00%	1.00%	1.00%	1.75%	1.5%	1.75%

3.2.2 Archwire rotation control

Archwire rotation is achieved with a stepper motor (Cool Muscle CM1-C-11L30, Myostat Motion Control Inc., Newmarket, ON, Canada) coupled to a custom design worm and wheel gear box that rotates a yoke that holds the two archwire clamping dies. The clamping dies, gearbox, and archwire are shown in Figure 3.1(b). The gear system is designed with a 1:96 gear ratio and a 3.75° rotation (1000 stepper motor counts) represents one revolution of the worm gear. The backlash in the gear system is less than the 0.05° resolution of a inclinometer (model T2-7200-1N; US Digital, Vancouver, Wa.) which was used for monitoring only. Archwire rotation was defined by the input to the stepper motor which was achieved via serial communication from the control PC and custom software.

3.2.3 Bracket position control

Two translation stages were used to adjust the x - y position of the entire torque assembly underneath the imaging system (LT01 Translation Stage, Thor Labs, Newton NJ, USA) as shown in Figure 3.1(a) allowing for the bracket to be centered in the camera field of view. A translation stage was also used to control the height (z) of the camera above the orthodontic bracket. Additionally, a translation stage with a micrometer shown in Figure 3.1(b) was used to control the position of the bracket (MT01 Translation Stage, Thor

Labs, Newton NJ, USA). This precision translation stage allows for control over the bracket y -position and ensures the archwire can be placed within the bracket slot while minimizing any initial forces or moments. A rotation stage controlling rotation about the z^* -axis was used to ensure the bracket slot is also parallel to the archwire (PR01 Rotation Stage, Thor Labs, Newton NJ, USA).

3.2.4 Bracket Imaging

An imaging system composing of a CCD camera (piA2400 12gm, Basler Vision Technologies, Exton, PA, USA) connected to a long working distance microscope (55-908 MMS R4, Edmund Optics, Barrington, NJ, USA) collected images at 2448×2050 pixels and 8-bit resolution. The objective lens viewed the top of the bracket, normal to the archwire rotation axis at its nominal working distance of 67mm. Test specimens are illuminated using epi-illumination (MVO® MMS® In-Line Attachment 56-244, Edmund Optics, Barrington, NJ, USA) to provide even illumination across the field of view.

3.2.5 Bracket/Load Cell Force Torque Conversion

The load cell measures forces and moments at the origin of its coordinate system (x,y,z) as defined in Figure 3.2. This figure shows a close up rendered image of the relationship of the load cell to the bracket with the bracket cylinder and mounting adapter. To determine forces and moments applied directly to the bracket by the archwire, a force/moment coordinate transformation is required. The offset of the bracket from the origin of the load cell is measured using a commercial coordinate measurement machine (FaroArm, FARO USA, Lake Mary, FL, USA). The relationship of the two coordinate systems requiring the transformation from the load cell (x,y,z) to the bracket (x^*,y^*,z^*) is illustrated in Figure 3.2. The offset of the orthodontic bracket from the load cell comprises of a displacement in the x , y and z -directions as well as a rotation about the z -

axis, θ as shown in Figure 3.2(b). The details of the bracket-load cell offset calculation and error analysis can be seen in Appendix A.

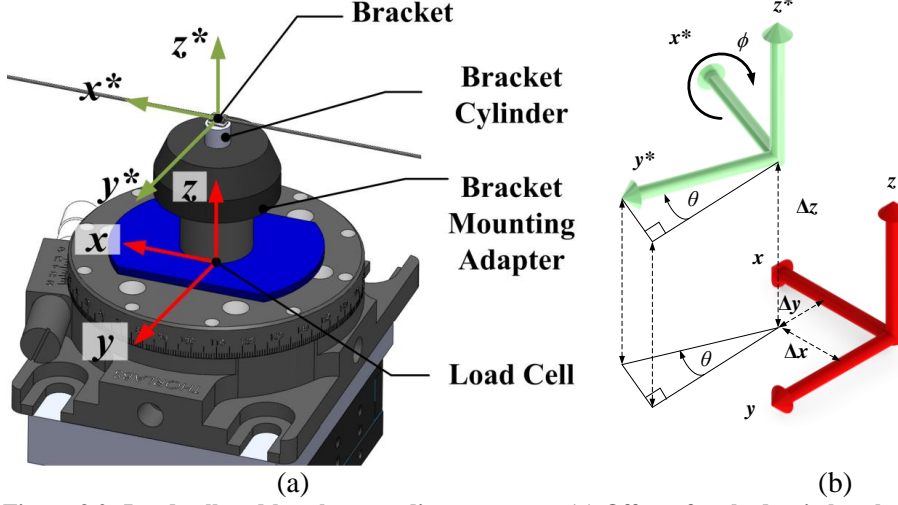


Figure 3.2: Load cell and bracket coordinate systems. (a) Offset of orthodontic bracket from load cell (b) Coordinate system transformation showing displacement, rotation about the z axis and the angle ϕ indicating the direction of archwire rotation.

The transformation of measured forces and torques to bracket forces and torques can be defined as:

$$F_{\text{bracket}} = \begin{pmatrix} m_{x\text{bracket}} \\ m_{y\text{bracket}} \\ m_{z\text{bracket}} \\ f_{x\text{bracket}} \\ f_{y\text{bracket}} \\ f_{z\text{bracket}} \end{pmatrix}$$

where,

$$\begin{aligned} m_{x\text{bracket}} &= m_{xLC} \cos \theta - f_{zLC} (\Delta y \cos \theta - \Delta x \sin \theta) + m_{yLC} \Delta x \sin \theta + \Delta z (f_{yLC} \cos \theta - f_{xLC} \sin \theta) \\ m_{y\text{bracket}} &= f_{zLC} (\Delta x \cos \theta + \Delta y \sin \theta) + m_{xLC} \cos \theta - m_{yLC} \sin \theta - \Delta z (f_{xLC} \cos \theta + f_{yLC} \sin \theta) \\ m_{z\text{bracket}} &= m_{zLC} - \Delta x f_{yLC} + \Delta y f_{xLC} \\ f_{x\text{bracket}} &= f_{xLC} \cos \theta + f_{yLC} \sin \theta \\ f_{y\text{bracket}} &= f_{yLC} \cos \theta - f_{xLC} \sin \theta \\ f_{z\text{bracket}} &= f_{zLC} \end{aligned} \quad (3.1)$$

This relationship converts forces and moments measured at the load cell (i.e. f_{xLC} , the load cell force in the x -direction, m_{xLC} the load cell moment about the x -axis) to forces and moments at the bracket (i.e. $f_{x\text{bracket}}$, bracket force in x^* -direction, $m_{x\text{bracket}}$, bracket

moment about the bracket x^* -axis). The load cell to bracket transformation equation was determined using a transformation between coordinate frames utilized for robot manipulators [1]. This equation shows that the forces and moments experienced by the bracket depend on the offset of the bracket from the center of the load cell and the rotation of the bracket relative to the load cell.

3.3 Orthodontic Torque Simulator Experiment

The OTS was controlled using custom designed software (LabWindows/ CVI, National Instruments, Austin TX). This program automates the control of the stepper motor, acquisition of data from the load cell and image acquisition. Data recorded from the load cell and current bracket image are displayed on screen to monitor the status of the experiment in real time. Parameters such as the maximum angle of archwire rotation; angle increment; and time between archwire rotations can be controlled using this software. The recording sequence for the OTS is shown in Figure 3.3 and highlights the flexibility to run different experiment configurations as well as repeat experiments. The software was designed to allow the system to be used by a variety of researchers with non-specific backgrounds including orthodontic students using the system as part of their graduate research program.

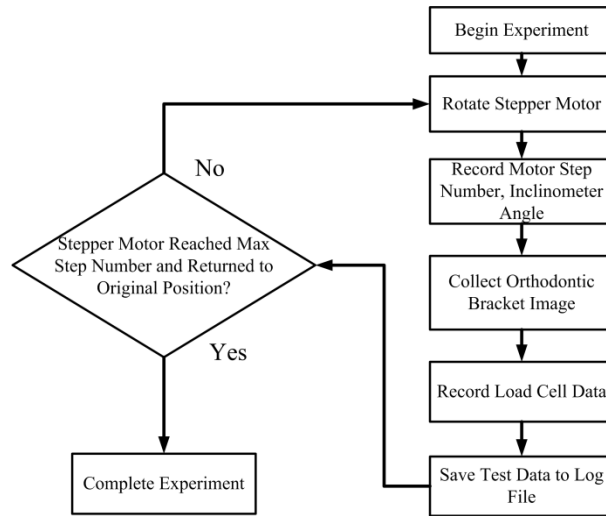


Figure 3.3: Flowchart of Orthodontic Torque Simulator operation.

3.3.1 Overhead Images

An example of an image sequence collected from the OTS of a Damon Q (Ormco Corporation) orthodontic bracket is shown in Figure 3.4. The figure shows images collected for every nine degrees of archwire rotation (ϕ) to a maximum angle of 78° . This style of bracket is self-ligating with an archwire retentive component (ARC) that is closed over the bracket slot to hold the archwire in place. The brackets have been marked using a micro-etcher to provide contrast features on the surface of the bracket. These are needed as part of the DIC analysis which tracks regions of similar contrast to determine displacement. The change in archwire angulations can be seen in each of the successive images. The image sequence also shows the bracket slot opening as a result of archwire rotation.

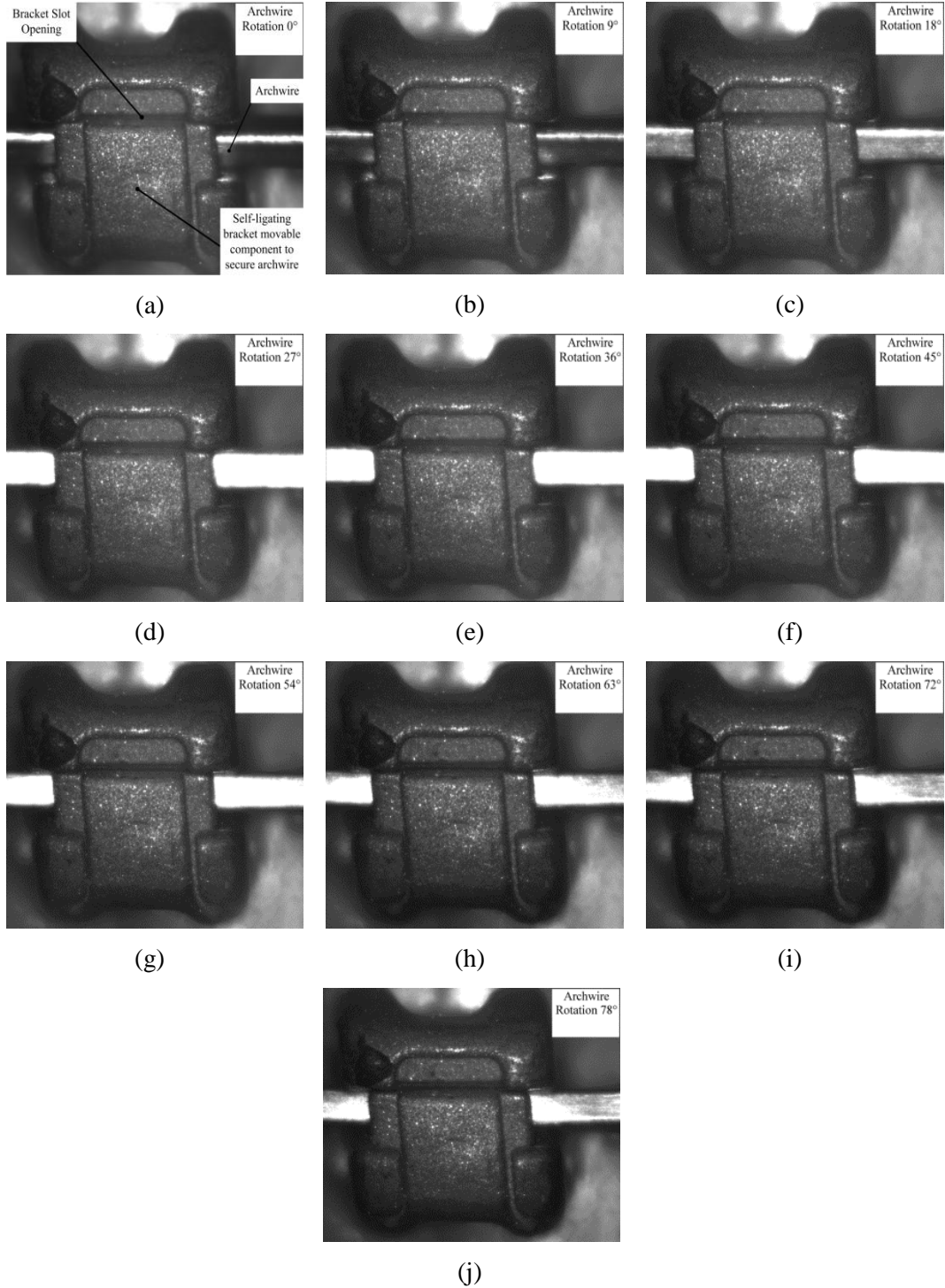


Figure 3.4: Deformation of a Damon Q (Ormco Corporation) orthodontic bracket due to archwire rotation. Archwire rotation (ϕ) is shown in 9° increments to a maximum angle of 78°.

A profile image of an orthodontic bracket is shown in Figure 3.5. Profile images of orthodontic brackets were examined to show the variability in bracket slot sizes [2]. The main image in the figure shows a bracket before an archwire has been rotated in the

bracket slot using the OTS. Overlaid on this image is the outline of the same bracket after archwire rotation showing bracket deformation in the x^* and z^* directions defined in Figure 3.5. Figure 3.5 shows that there is localized deformation (notching) where the archwire contacts the bracket slot. Archwire rotation and the torque caused by its rotation can result in both elastic and plastic deformation to the orthodontic bracket TWs [3]. Deformation of the orthodontic brackets can alter how the bracket behaves due to archwire rotation. An understanding of bracket deformation is necessary to ensure that the desired amount of force is applied to a tooth [4].

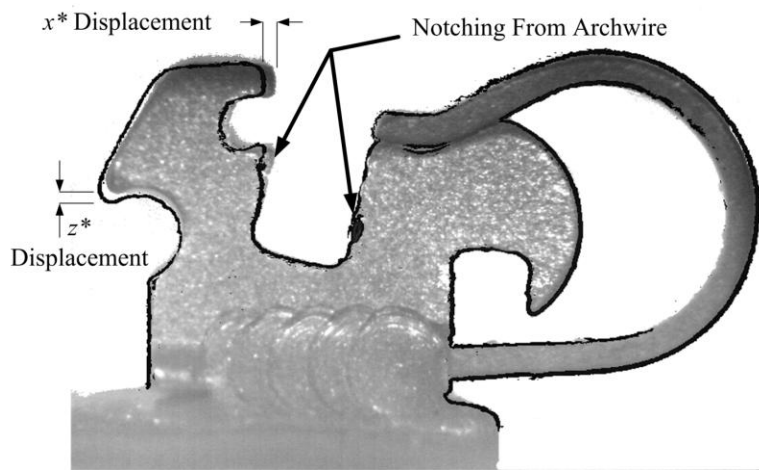


Figure 3.5: Profile image of an orthodontic bracket showing the original bracket and the outline of a deformed bracket.

3.3.2 Measured Bracket Force/Moment

In addition to collecting images of orthodontic brackets for successive archwire wire rotation, load cell data is also collected. Load cell data was synchronized with the acquired bracket images allowing for bracket deformation and applied moment to be compared. The measurement that is of most interest to practitioners is the amount of torque applied to the orthodontic bracket caused by pure archwire rotation ($m_{xbracket}$). Load cell data for a typical $0.019 \times 0.025''$ stainless steel wire (Ormco Corporation)

archwire and a self-ligating Damon Q (Ormco Corporation, Orange, California, USA) bracket-archwire combination is shown in Figure 3.6 for the determined forces and moments respectively. The need for the bracket / load cell transformation as illustrated in Figure 3.2 is required to determine the forces and moments that occur at the bracket instead of at the load cell. The computed transformed forces and moments are also plotted in Figure 3.6 for comparison with raw data.

Measurement of a test bracket has been performed to illustrate the force/torque conversion and the propagation of errors that result from this transformation [5]. Measurements of the test bracket offset from the load cell are show in Table 3.2. Several sources of uncertainty have been identified which will contribute to the errors associated with the load cell/ bracket transformation, including the load cell force $f_{xLC}, f_{yLC}, f_{zLC}$; load cell moment $m_{xLC}, m_{yLC}, m_{zLC}$; bracket offset $\Delta x, \Delta y, \Delta z$ and bracket angular offset θ . The uncertainty for the load cell measurements are show in Table 3.1 which were used to calculate measurement uncertainty for the bracket/ load cell offset listed in Table 3.2. Error propagation analysis was carried out in order to account for the uncertainty in the load cell / bracket transformation. Equation (3.2 shows that the load cell / bracket transformation is a function of $\Delta x, \Delta y, \Delta z, \theta, f_{xLC}, f_{yLC}, f_{zLC}, m_{xLC}, m_{yLC},$ and m_{zLC} . Equation (3.3 also shows that the uncertainty in the load cell / bracket transformation is a function of the uncertainty of the offset of the bracket from the load cell ($\Delta x, \Delta y, \Delta z, \theta$) and the uncertainty in the load cell measurement ($f_{xLC}, f_{yLC}, f_{zLC}, m_{xLC}, m_{yLC}, m_{zLC}$). The individual uncertainties were used to find the total uncertainty in the load cell / bracket transformation.

$$F_{bracket} = f(\Delta x, \Delta y, \Delta z, \theta, f_{xLC}, f_{yLC}, f_{zLC}, m_{xLC}, m_{yLC}, m_{zLC}) \quad (3.2)$$

$$u_{F_{bracket}} = f(u_{\Delta x}, u_{\Delta y}, u_{\Delta z}, u_{\theta}, u_{f_{xLC}}, u_{f_{yLC}}, u_{f_{zLC}}, u_{m_{xLC}}, u_{m_{yLC}}, u_{m_{zLC}}) \quad (3.3)$$

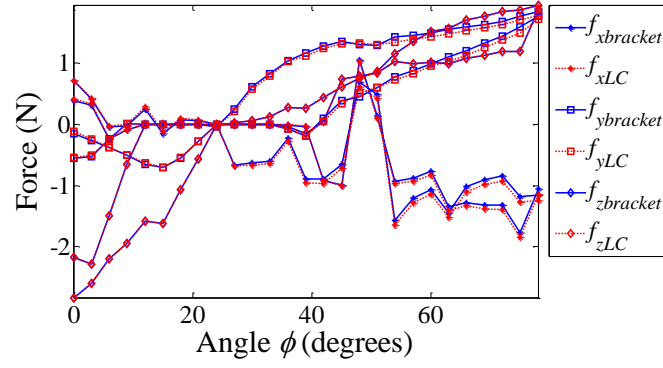
Table 3.2: Bracket offset from load cell measurements and uncertainty.

Measurement	Measured Offset	Uncertainty
Δx	-0.4047mm	$\pm 0.018\text{mm}$
Δy	0.7673mm	$\pm 0.018\text{mm}$
Δz	17.650mm	$\pm 0.018\text{mm}$
θ	3°	$\pm 0.5^\circ$

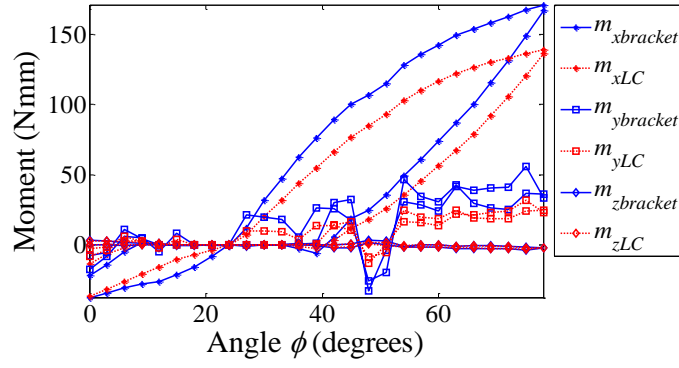
The maximum measurement uncertainty for the measured bracket forces and moments are summarized in Table 3.3. The uncertainty for the bracket forces and moments was determined by performing an error propagation analysis based on the ASME Power Test Codes (PTC) 19.1 Test Uncertainty test standard discussed in [5]. The uncertainty in the bracket moment $m_{x\text{bracket}}$ is indicated by error bars in Figure 3.7. The value of $m_{x\text{bracket}}$ is the main focus of the OTS measurement system. This value represents the measured moment that has been applied to the bracket due to archwire rotation. The OTS is designed to apply a pure rotation to the orthodontic bracket. In orthodontic pure archwire rotation is known as torque expression [6]. The measured load cell data shows that the magnitude of torque is largest about the x^* -axis this can be seen in Figure 3.6(a). Figure 3.7 also shows that the magnitude of torque changes for increasing and decreasing torque which indicates that a change in the bracket TWs occurs due to an applied load.

Table 3.3: Maximum bracket force and torque measurement uncertainty

Max $m_{x\text{bracket}}$	Max $m_{y\text{bracket}}$	Max $m_{z\text{bracket}}$	Max $f_{x\text{bracket}}$	Max $f_{y\text{bracket}}$	Max $f_{z\text{bracket}}$
Uncertainty	Uncertainty	Uncertainty	Uncertainty	Uncertainty	Uncertainty
(%)	(%)	(%)	(%)	(%)	(%)
1.44	2.79	2.33	2.18	1.17	1.45



(a)



(b)

Figure 3.6: Load cell transformation showing transformed and measured m_y , (a) transformed and measured force (f_x, f_y, f_z). (b) transformed and measured moments (m_x, m_y, m_z).

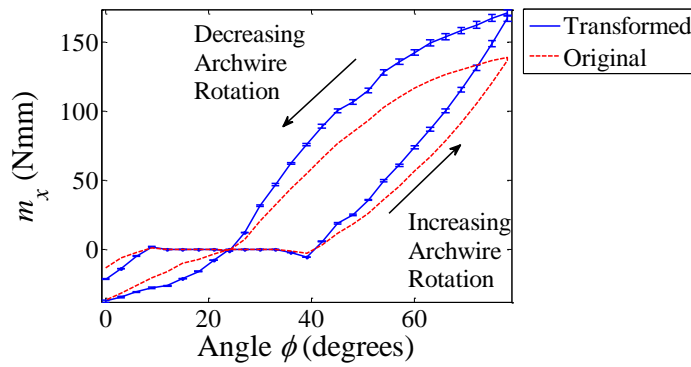


Figure 3.7: Load cell transformation showing transformed and measured m_x as well as effect of increasing and decreasing archwire rotation. Error bars are shown to demonstrate the uncertainty in the $m_{xbracket}$ measurement.

The magnitude of force applied to the bracket as well as $m_{ybracket}$ and $m_{zbracket}$ are small compared to $m_{xbracket}$ as shown in Figure 3.6. While $m_{xbracket}$ is the dominate and intentional moment introduced into the system, measured values for the other moments, $m_{ybracket}$ and $m_{zbracket}$ are due to variations in the bracket slot dimensions and the ability to visually align the bracket slot with the archwire. The measured moment $m_{ybracket}$ shows a distinct change at angles ϕ of 48° and 51° . This change can also be seen in Figure 3.8, a detailed set of images about the angle where there is a shift in the position of the bracket. At these angles the corner of the archwire begins to engage the archwire retention component and apply a load to in the z^* -direction of the bracket thus causing a sharp change in the measured moment $m_{ybracket}$ and a sharp change also occurs to the measured force $f_{xbracket}$. This relaxes with increased rotation of the archwire and is believed to be a result of the archwire repositioning within the slot. Additionally, all forces measured by the load cell are small with respect to the applied moment ($m_{xbracket}$). Figure 3.6 (b) shows that typical forces measured by the load cell range between -2.5 and 1.5N. The measured moment $m_{xbracket}$ will be used to along with the digital image processing method described in Section 3.4 to better describe the bracket/archwire interaction.

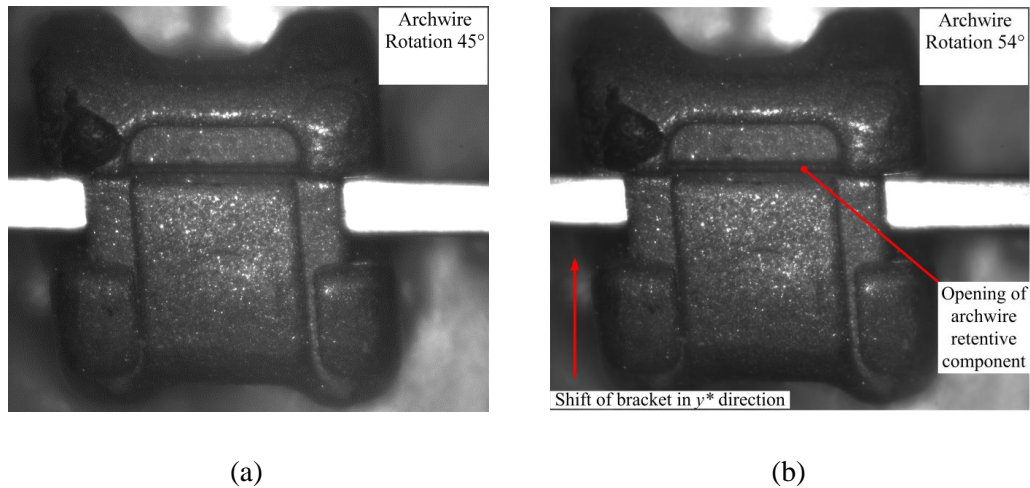


Figure 3.8: Engagement of archwire in retentive component of the orthodontic bracket resulting in a change in the measured moment $m_{y\text{bracket}}$. (a) archwire rotation of 45° (b) archwire rotation of 54° showing the opening of the archwire retentive component and a displacement in the y^* direction due to archwire rotation.

3.4 Digital Image Correlation of Bracket Images

Images collected using the OTS were processed using a DIC technique in order to ascertain the movement and deformation that occurs to bracket TWs as an archwire is rotated within a bracket slot. A commercial software package (LaVision GmbH, DaVis 7.2, Göttingen, Germany, 2007) was used to determine the displacement vectors from the set of bracket images that characterize the movement of the bracket. DIC is a full-field measurement technique that measures deformation by comparing the gray intensity levels between successive images [7, 8]. Each digital image is segmented into evenly spaced subsets and an image correlation algorithm is performed for each image subset. The average displacement in each subset is then determined as the displacement vector from the center of the region to the maximum of the correlation function.

Image subsets used in this study ranged in size from 64 x 64 pixels to 256 x 256 pixels. Examples of the subsets used for the DIC algorithm are illustrated in Figure 3.9 in comparison to the size and position of the bracket. The field of view for the overhead images is 2448 x 2050 pixels or 3.76 x 3.15 mm. Figure 3.9 also shows the four TW box regions that will be used to measure the deformation of the orthodontic brackets. From

this figure it can be seen that more pixel subsets are within the TW box regions for Figure 3.9 (a) than Figure 3.9 (b). The number of subsets will affect the ability to resolve the deformation of the TWs.

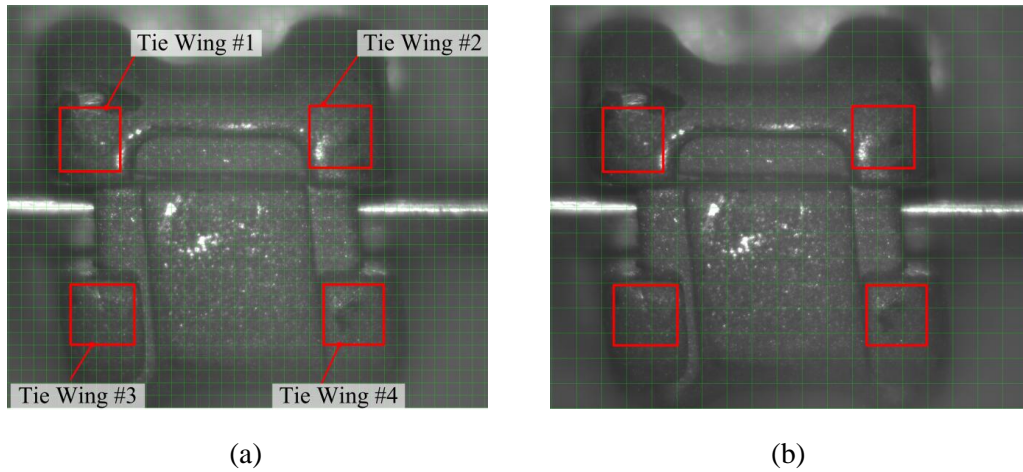


Figure 3.9: Bracket images showing image subsets (a) 64x64 pixel subsets (b) 128x128 pixel subsets.

A random speckle pattern was applied to the surface of the orthodontic brackets using a micro-etcher (The Arum Group, Spokane, WA, USA). Micro-etching improved the contrast of the bracket images which has an important effect of the strength and shape of the resultant correlation peak used to determine movement in successive images. A comparison between a bracket with and without speckling is shown in Figure 3.10. This figure also shows the corresponding correlation peak for the brackets with and without speckling. From this figure it is evident that a pronounced correlation peak exists for the micro-etched bracket whereas the correlation peak for the bracket without micro-etching is not as distinct.

The DIC algorithm will calculate a peak maximum which represents the average displacement within the image subset. A peak detection algorithm is used to locate that maximum within the cross-correlation function and its location within the 2-D function is the magnitude and direction of movement. Examples of the correlation peak generated from the cross correlation algorithm are shown in Figure 3.10 (c) and (d). The

pronounced correlation peak in Figure 3.10(d) shows that a strong correlation can be found between bracket image frame (i) and ($i + 1$) which can be easily be detected by the peak detection section of the DIC system. Conversely, a strong correlation peak does not exist for the bracket image shown in Figure 3.10(a) [9] where similar high intensity light values measured by the CCD over a majority of the bracket due to its high reflection broaden the correlation peak. Image data of this type can skew the position of the maximum correlation resulting in a false peak detection that does not represent average movement within the subset. Therefore, all brackets which were examined using the OTS were micro-etched prior to testing. Several processing schemes [7, 8] are available that can be used to improve the accuracy of the DIC algorithm. These algorithms allow for subset window off-set as well as single / multiple pass approaches. The effect of subset window offset and single/ multiple pass approaches are discussed in Section 3.4.1

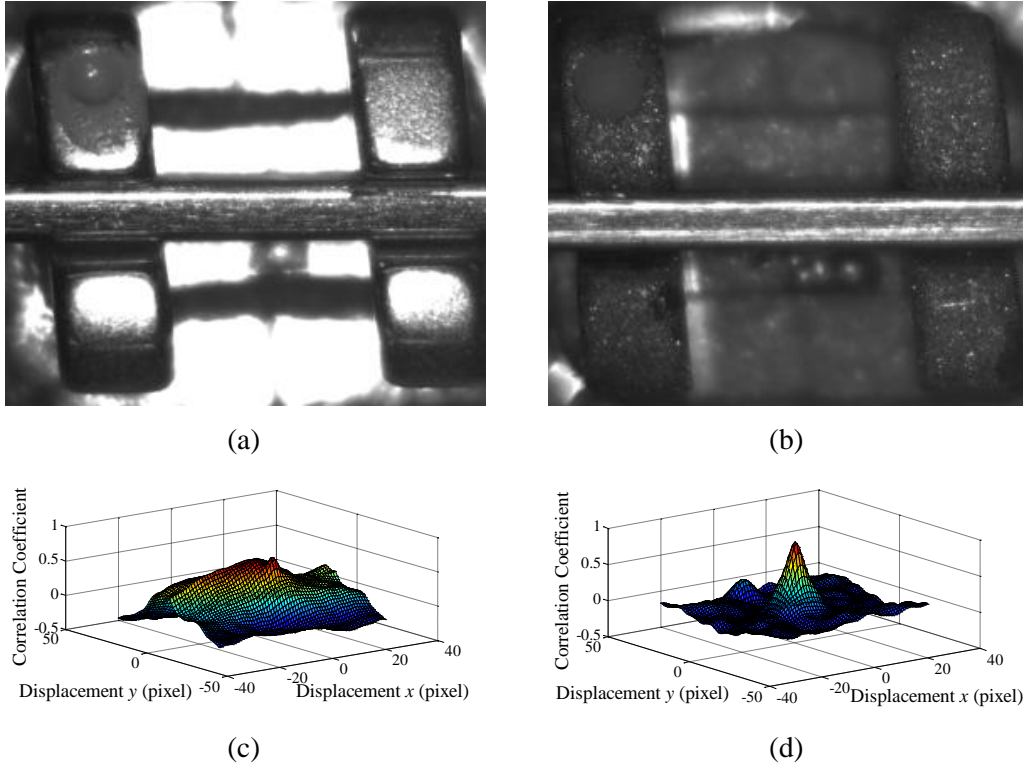


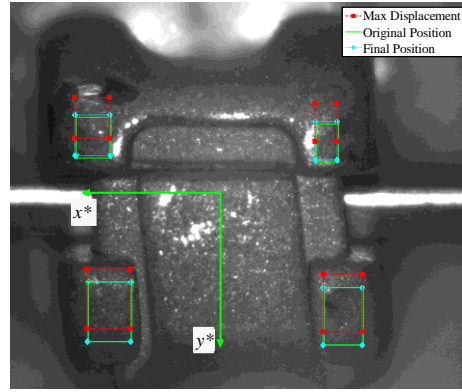
Figure 3.10: Preparation of orthodontic brackets (a) Bracket without micro-etching (b) Bracket with micro-etching. (c) Correlation peak for bracket without micro- etching (d) Correlation peak for bracket with micro- etching.

Bracket TW separation was investigated by tracking a defined region for each TW as shown in Figure 3.11(a). The initial region for each TW is shown in the figure as a green box. The measured displacement in the y^* -direction was determined by averaging the displacement results for the smaller subsets within the defined regions shown in the figure. As the archwire is rotated within the bracket slot relative motion exists between TWs. Additionally, bulk motion is observed as the entire bracket moves due to the applied loads from archwire rotation and relaxation of the support cylinder within the support adaptor. The maximum movement of the bracket TWs is shown in Figure 3.11(a) by the position of the boxes with solid squares. Once the archwire reaches the prescribed maximum angle the archwire rotates back to the start position. The final position of the bracket TWs is shown by the boxes with closed diamonds where it can be

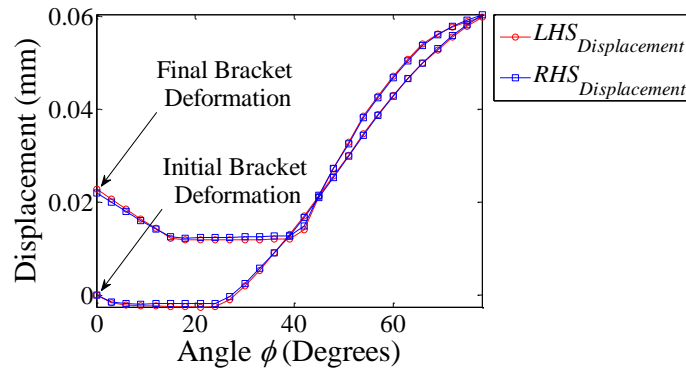
seen that the final position of the TWs is slightly offset from the original position indicating permanent bracket deformation has occurred.

The change in average displacement in the y^* direction between the top left and bottom left boxes for TW #1 and TW #3 as well as the top right and bottom right brackets of TW #2 and TW #4 was used to determine the deformation of the orthodontic brackets this can be seen in Figure 3.11(b). This figure shows the difference between the average displacement of TW #1 and TW #3 that occurred between these two TWs in the y^* -direction and is denoted as LHS_D . Similarly the average displacement of TW#2 and TW #4 is denoted as RHS_D . Figure 3.11(b) shows that there is both hysteresis and permanent deformation occurred to the bracket due to archwire rotation. Figure 3.11(b) also shows the result for the displacement of the left and hand right hand TW displacement are similar therefore only the LHS_D will be used for the remainder of this discussion to compare the deformation of brackets of varying geometry. Equation (3.4 details the calculation of the bracket TW displacement in the y^* direction. In this equation $\overline{D_{TieWing}}$ denotes the average displacement of the defined regions for TWs 1,2,3, and 4 for the $i=x^*$ and y^* directions.

$$\begin{aligned} LHS_{Displacement} &= \left[\overline{D_{TieWing1}} - \overline{D_{TieWing3}} \right]_i \\ RHS_{Displacement} &= \left[\overline{D_{TieWing2}} - \overline{D_{TieWing4}} \right]_i \end{aligned} \tag{3.4}$$



(a)



(b)

Figure 3.11: Tracking of bracket TWs. (a) Bracket in original position shown by solid lines, square boxes showing maximum TW displacement and diamonds showing final TW position after applied torque has been removed. (b) Plot of bracket TW deformation measured using digital image correlation showing initial and final deformation of the left hand and right hand side of the bracket TWs.

3.4.1 DIC Method Source of Error

There are a number of potential sources of error that exist when using a DIC technique. Errors can result from either the measurement devices or due to factors associated with the DIC processing technique [10]. Examples of measurement device errors are the lighting quality, optical lens distortion and test specimen out-of-plane motion. Errors related to the correlation technique are speckle pattern quality, subset size and correlation algorithm used.

The errors associated with the DIC technique were quantified by collecting an image of a bracket from the OTC and then applying artificial displacements to the digital image with a custom program (The MathWorks, Inc., Matlab, Natick, MA, USA). The images were artificially displaced in increments of 1 pixel (1.538 μm) to a maximum displacement of 20 pixels (30.76 μm). This method is commonly used to quantify errors associated with the digital image correlation process [10-12]. A Damon Q (Ormco Corporation, Orange, California, USA) bracket was used to assess the accuracy of the digital image correlation process.

The artificial displacement technique allows for the assessment of the digital image correlation algorithm, image subset size and quality of the speckle pattern. The overhead images collected were processed using a commercial code (LaVision GmbH DaVis 7.4. Gottingen, Germany; 2007). The resolution of the DIC process depends on the size of interrogation window used as shown in Figure 3.9, magnification of the image, speckle pattern and lighting. The measurement resolutions for the case investigated are shown in Table 3.4 [13].

Table 3.4: Digital image correlation image displacement vector resolution.

Interrogation Window Size (pixels x pixels)	Vector Resolution (pixels)		Orthodontic Torque Simulator Resolution (μm)	
	Min	Max	Min	Max
128x128	0.01	0.03	0.01538	0.04614
64x64	0.02	0.05	0.03076	0.0769
32x32	0.05	0.2	0.0769	0.3076
16x16	0.1	0.3	0.1538	0.4614

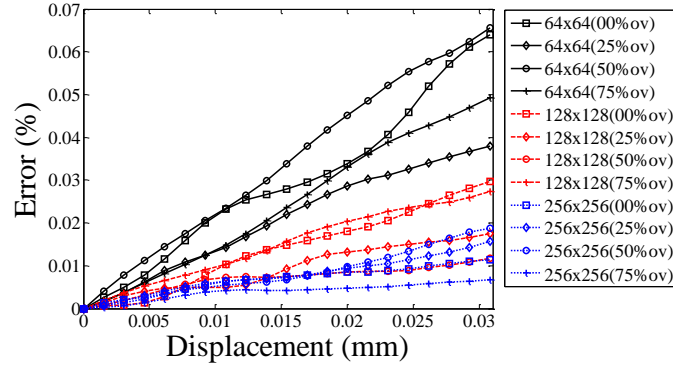
3.4.1.1 Measurement Errors from Digital Image Correlation

Errors associated with the overhead images were found by calculating the displacement between the TWs of the orthodontic bracket as shown in Figure 3.9. For rigid body translation tests, the displacement between the bracket TWs should remain constant since deformation has not occurred to the bracket TWs. A variety of settings were examined for the processing of the overhead images of the orthodontic brackets. The method for determining the optimal processing method was outlined by Crump et al [14]. The bracket images were processed by varying the subset window size as well as subset windows percent overlap. In addition, the bracket images were also processed using both a single pass and multi-pass DIC approach.

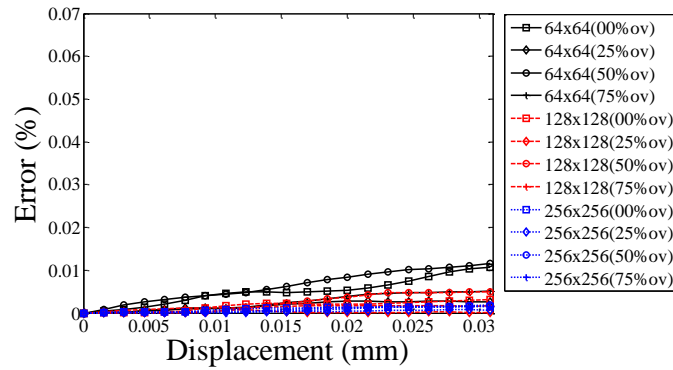
The error associated with each processing method for artificial image displacement is shown in Figure 3.12. This figure shows the errors associated with single pass and multi-pass processing as well as the effect of varying subset window size and percent overlap. It is observed that the multi-pass processing approach resulted in lower errors for all

window sizes and percent overlap than the single pass approach. It is further shown that the increase in subset window sizes results in improved accuracy of the correlation process. Window cell size is a compromise between spatial and displacement resolution where larger subsets means more data to perform the averaging process.

From Figure 3.12 it was found that a good compromise between spatial and displacement resolution for the bracket images is a multi-pass approach with a 64x64 window size and a 25% overlap. As shown in Figure 3.9 the bracket TWs comprise of approximately only 4 sub-windows when using a 128x128 pixel window whereas approximately 25 sub-windows are used for the 64x64 pixel windows. Therefore, to increase the averaging number used to define average displacement for the TW all bracket images collected from the OTS will be processed using a multi-pass approach and a 64x64 window size with 25% overlap. For the current setup of the OTS the measurement resolution is $0.0769\mu\text{m}$ (Table 3.4) since an interrogation window of 64x64 was used for the processing of the overhead bracket images. The maximum error found for the multi-pass approach for a window size of 64x64 with a 25% overlap was 0.0924% whereas the maximum error for the single pass approach was 0.2292%.



(a)

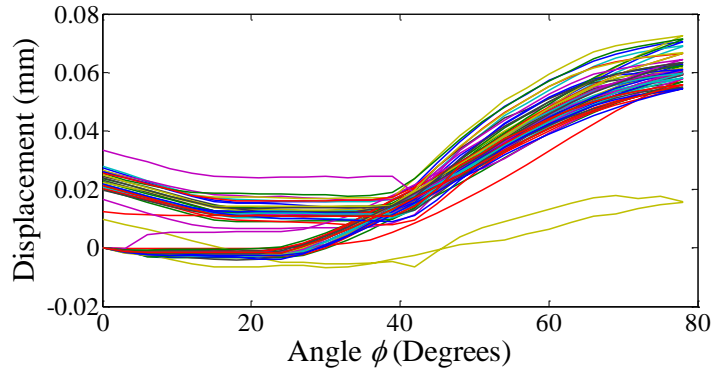


(b)

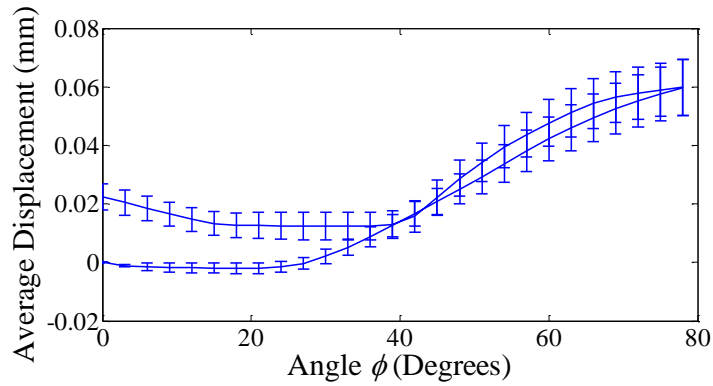
Figure 3.12: Effect of window size on overhead images with artificial displacement (a) Single pass processing (b) Multi pass processing.

Using the defined regions shown in Figure 3.11, the bracket TW displacement results for 30 Damon Q brackets measured using the OTS is shown in Figure 3.13 (a). Shown in Figure 3.13 (b) is the average deformation and computed standard deviations for the same 30 Damon Q brackets tested with the OTS. This figure shows the large variation that exists between brackets. The orthodontic bracket TW displacement as the archwire is rotated in the bracket slot is shown in Figure 3.13(c). This figure shows the displacement of the bracket TWs for a single Damon Q bracket as well as error bars indicating the uncertainty in the DIC technique. It can be seen that permanent deformation occurred to all the orthodontic brackets since the initial and final TW displacement are not the same. The important observation from these figures is that the uncertainty from the optical

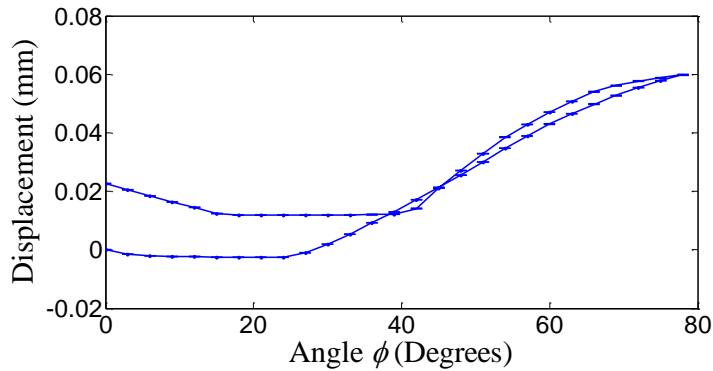
measurement method is significantly less than the variability found between individual brackets.



(a)



(b)



(c)

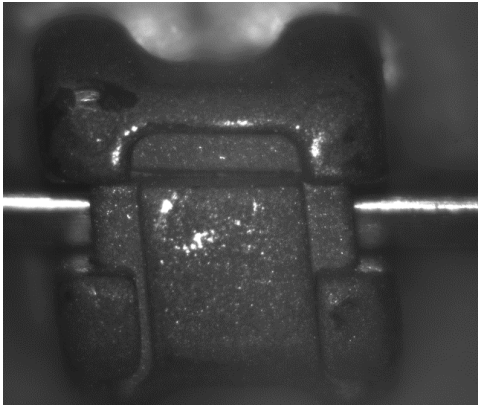
Figure 3.13: Orthodontic bracket displacement results (a) Bracket displacement plots for all 30 brackets (b) Average of multiple bracket displacement results showing standard deviation for the 30 brackets. (c) Single bracket displacement showing error bars resulting from DIC accuracy

3.5 Orthodontic Bracket Comparison

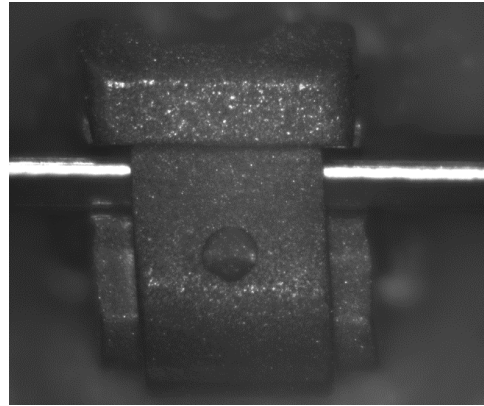
Two orthodontic brackets were compared to exhibit the difference seen for bracket deformation and moment applied due to archwire rotation using the OTS. Shown in Figure 3.14 are the Damon Q and Speed brackets used for this comparison. From this figure the difference in bracket geometry can be readily seen. Both brackets are self-ligating meaning that no elastic ligature or steel ties are required to hold the archwire in the bracket slot. The two brackets were examined to demonstrate the results produced by the OTS and to show how brackets of different design can be compared using this device. The measured offsets of the brackets from the load cell are summarized in Table 3.5.

Table 3.5: Measured bracket offset from load cell

Bracket	Δx (mm)	Δy (mm)	Δz (mm)	θ (degrees)
Damon	-0.6203	0.7399	17.69	3
Speed	-0.4189	0.798	17.65	2



(a)



(b)

Figure 3.14: Comparison of Damon Q (a) and Speed (b) self-ligating orthodontic brackets

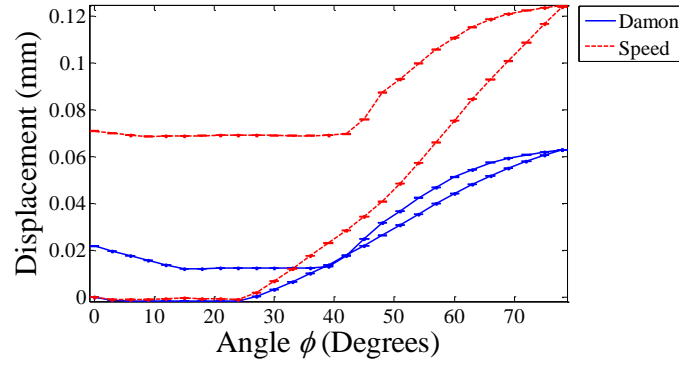
The results from the OTS to compare the Damon Q (Ormco Corporation, Glendora, California, USA) and Speed (Strite Industries, Cambridge, Ontario, Canada) brackets are shown in Figure 3.15 for two individual brackets of this type. Figure 3.15(a) compares the deformation of the bracket TWs 1 and 3 of the two brackets while Figure 3.15(b)

shows the measured moment, $m_{x\text{bracket}}$ applied to the brackets. From this figure it can be seen that a similar applied moment results in different deformation for the two brackets. Both brackets begin to displace and transmit load at a similar archwire angular position of $\phi \sim 25^\circ$.

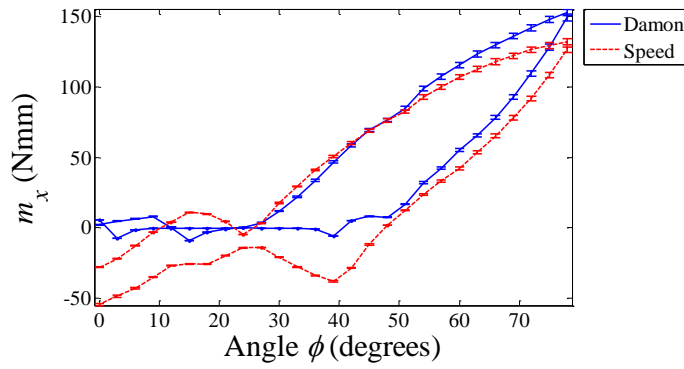
Torque loading and relative TW displacement are non-linear up to maximum archwire rotation. The relative TW displacement of the Speed bracket is approximately double that of the Damon Q but transmits $\sim 10\%$ less torque at maximum archwire rotation. Hysteresis is present for both relative TW displacement and transmitted torque for both brackets. Summarized in Table 3.6 is the maximum measured moment for the two brackets as well as the maximum and final bracket deformation. The final position of the TWs of the two brackets also shows that the Speed bracket exhibited greater plastic deformation than the Damon Q bracket. Figure 3.15 and Table 3.6 demonstrate that the maximum deformation of the Damon Q bracket is 3.2 times less than the Speed bracket. Additionally, the error bars associated with the optical measurement and error from the load cell transformation are shown with the results in Figure 3.15. These two figures show that the measurement uncertainty from the OTS is small compared to the difference seen in the deformation and measured moment of the two brackets.

Table 3.6: Comparison of orthodontic bracket deformation results

Bracket	Maximum Measured Moment m_x (Nmm)	Maximum Deformation (mm)	Final Deformation (mm)
Damon Q	152.7	0.0628	0.0217
Speed	132.0	0.1246	0.0709



(a)



(b)

Figure 3.15: Comparison of Damon Q and Speed orthodontic brackets (a) Deformation results (b) Measured applied moment

3.6 Discussion

Several studies have examined the effect of archwire rotation on orthodontic brackets [3, 4, 15-19]. The major focus has been on measurement of the moment applied to the orthodontic bracket by the rotating archwire. Several of these studies have made reference to bracket deformation but the deformation was not quantified [4, 15, 16].

The OTS presented here is capable of measuring the final deformation of orthodontic brackets due to archwire rotation. In addition, this device allows for measurement of the deformation that occurs due to successive increases in archwire angle. Force and moment data is also recorded for each archwire rotation. As a result, the presented OTS is capable of measuring both the elastic and plastic bracket deformation. Both the elastic

and plastic deformation of the orthodontic brackets should be understood since both deformations result in energy lost to the deformation of the orthodontic bracket rather than causing tooth movement. Additionally, the OTS is capable of measuring the forces and moments applied to the orthodontic bracket using a 6-axis load cell. Since load cell measurement and images of the bracket are taken simultaneously The OTS data can be used to match these two measurements.

Two orthodontic brackets were compared to demonstrate how results from the OTS can be used to compare brackets of varying make and geometry. This comparison shows that the maximum and final deformation of the Damon Q brackets is less than the Speed bracket for the same amount of archwire rotation. As well, 30 brackets of the design Damon Q were analyzed to show that the variability in the orthodontic brackets is much greater than the measurement uncertainty of this device.

3.7 Conclusions

It was demonstrated that the OTS was been designed to measure the forces and moments applied to orthodontic brackets. The maximum bracket force and moment measurement uncertainty are significantly less than both the range of movement and torques expected and the observed variability within the bracket design. This device is also capable of measuring the displacement of the orthodontic bracket TWs due to archwire rotation within 0.09% error. Two sample orthodontic brackets were compared to demonstrate how this device can be used to compare brackets of varying geometry. From this comparison presented it was found that maximum deformation of the Damon Q bracket is 3.2 times less than the Speed bracket for similar magnitudes of applied moment. An understanding of the elastic and plastic deformation that occurs to brackets is critical to clinicians since brackets are selected for treatment based on the advertised prescription the particular bracket provides to apply torques to tooth crown. Bracket deformations can

alter the geometry of the bracket slot which can affect the efficiency of the treatment. Knowledge of bracket deformation will allow clinicians to select brackets based on the expected deformation that will occur or to adjust the treatment regime to compensate for bracket deformation.

3.8 References

- [1] R. P. Paul, *Robot Manipulators: Mathematics, Programming, and Control: The Computer Control of Robot Manipulators*. Cambridge, Mass: MIT Press, 1981.
- [2] T. W. Major, J. P. Carey, D. S. Nobes and P. W. Major, "Orthodontic Bracket Manufacturing Tolerances and Dimensional Differences between Select Self-Ligating Brackets," *J. Dent. Biomech.*, vol. 2010, pp. 781321, Jun 27, 2010.
- [3] R. Kapur, P. K. Sinha and R. S. Nanda, "Comparison of load transmission and bracket deformation between titanium and stainless steel brackets." *Am. J. Orthod. Dentofacial Orthop.*, vol. 116, pp. 275-278, 1999.
- [4] D. A. Flores, L. K. Choi, J. M. Caruso, J. L. Tomlinson, G. E. Scott and M. T. Jeiroudi, "Deformation of metal brackets: a comparative study." *Angle Orthod.*, vol. 64, pp. 283-290, 1994.
- [5] R. S. Figliola, "Uncertainty analysis," in *Theory and Design for Mechanical Measurements*, 5th ed. Anonymous Hoboken, NJ: John Wiley & Sons, 2011, pp. 161.
- [6] J. A. Wagner and R. J. Nikolai, "Stiffness of incisor segments of edgewise arches in torsion and bending." *Angle Orthod.*, vol. 55, pp. 37-50, 1985.
- [7] M. A. Sutton, J. J. Orteu and H. W. Schreier, *Image Correlation for Shape, Motion and Deformation Measurements : Basic Concepts, Theory and Applications*. New York, N.Y: Springer, 2009.
- [8] B. Pan, K. Qian, H. Xie and A. Asundi, "Two-dimensional digital image correlation for in-plane displacement and strain measurement: A review," *Meas Sci Technol*, vol. 20, 2009.
- [9] M. Raffel, C. Willert, S. Wereley and J. Kompenhans, "Mathematical background of statistical PIV evaluation," in *Particle Image Velocimetry : A Practical Guide*, 2nd ed. Anonymous New York: Springer, 2007, pp. 79.

- [10] H. Haddadi and S. Belhabib, "Use of rigid-body motion for the investigation and estimation of the measurement errors related to digital image correlation technique," *Optics and Lasers in Engineering*, vol. 46, pp. 185-196, 2008.
- [11] T. C. Chu, W. F. Ranson and M. A. Sutton, "Applications of digital-image-correlation techniques to experimental mechanics," *Exp. Mech.*, vol. 25, pp. 232-244, 1985.
- [12] F. Hild and S. Roux, "Digital image correlation: From displacement measurement to identification of elastic properties - A review," *Strain*, vol. 42, pp. 69-80, 2006.
- [13] LaVision GmbH, "Product-Manual for DaVis 7.2 StrainMaster 2D Item-Number(s): 1105021," .
- [14] D. A. Crump, J. M. Dulieu-Barton and J. Savage, "Design and commission of an experimental test rig to apply a full-scale pressure load on composite sandwich panels representative of an aircraft secondary structure," *Measurement Science and Technology*, vol. 21, 2010.
- [15] H. Gmyrek, C. Bourauel, G. Richter and W. Harzer, "Torque capacity of metal and plastic brackets with reference to materials, application, technology and biomechanics," *Journal of Orofacial Orthopedics*, vol. 63, pp. 113-128, 2002.
- [16] R. Sadat-Khonsari, A. Moshtaghy, V. Schlegel, B. Kahl-Nieke, M. Möller and O. Bauss, "Torque deformation characteristics of plastic brackets: A comparative study," *Journal of Orofacial Orthopedics*, vol. 65, pp. 26-33, 2004.
- [17] T. R. Meling, J. Odegaard and E. O. Meling, "On mechanical properties of square and rectangular stainless steel wires tested in torsion." *Am. J. Orthod. Dentofacial Orthop.*, vol. 111, pp. 310-320, 1997.
- [18] J. Odegaard, T. Meling and E. Meling, "An evaluation of the torsional moments developed in orthodontic applications. An in vitro study." *Am. J. Orthod. Dentofacial Orthop.*, vol. 105, pp. 392-400, 1994.
- [19] H. M. Badawi, R. W. Toogood, J. P. R. Carey, G. Heo and P. W. Major, "Torque expression of self-ligating brackets," *American Journal of Orthodontics and Dentofacial Orthopedics*, vol. 133, pp. 721-728, 2008.

Chapter 4 Three-Dimensional Deformation of Orthodontic

Brackets

A version of this chapter has been submitted as:

Melenka G.W., Nobes, D.S., Major, P.W., Carey, J.P., Three Dimensional Deformation of Orthodontic Brackets, Journal of Dental Biomechanics, JDB-12-0010 (2012).

4.1 Introduction

Prior to the development of the OTS several studies examined the effect of archwire on bracket deformation [1-5]. These studies were limited to measuring permanent deformation since the brackets were only evaluated pre and post archwire rotation. For example Kapur et al. [3] measured the permanent change in titanium and stainless steel bracket slot profile before and after archwire rotation using a stereo microscope to quantify bracket deformation. This study only measured permanent change to the bracket slot and an assessment of the measurement resolution was not given. Similarly, Feldner et al. [5] measured bracket deformation at a variety of archwire rotation angles. Bracket deformation was measured visually using a stereo microscope and a protractor. The studies by Feldner and Kapur [3, 5] are unable to determine the wire torque at which the onset of permanent deformation occurs and were unable to specifically show the specific ranges of elastic and plastic deformations; thus failing to provide the clinically critical limit at which onset of plastic deformation occurs. Understanding the relationship between the applied loads and resulting deformations to orthodontic brackets is important to improve treatment efficiency and to generate accurate bracket-archwire-tooth interaction models for treatment optimization.

Deformation measurements using a single camera [6-9] can only measure surface in-plane motion of the bracket; out-of-plane motion and deformation measurements require

a minimum of two cameras [10]. The ability to measure 3D deformation of the orthodontic bracket will enable the interaction of the archwire-bracket to be fully described using three dimensional digital image correlation (3D DIC). This chapter will resolve the level of 3D deformation of orthodontic brackets and will illustrate the additional level of detail that can be acquired using the 3D DIC approach for completely understanding orthodontic bracket deformation.

4.2 Methods

4.2.1 Description of the Orthodontic Torque Simulator

The OTS, initially developed for 2D measurements, was expanded from a single to a stereo camera configuration as shown in Figure 4.1 (a) and (b), respectively. As described in [6-8, 11], the OTS was designed to simulate clinical archwire rotation and measures bracket forces and moments. Figure 4.1 (a) shows the single camera system used to collect images of the orthodontic brackets. The overhead imaging system collects images of the brackets allowing for two dimensional (2D) DIC to measure bracket TW movement. The addition of a second camera and stereo microscope, shown in Figure 4.1 (b), allows for 3D DIC bracket TWs deformation measurements. The OTS is positioned in the camera and microscope field-of-view using three translation stages (LT01 Translation Stage, Thor Labs, Newton NJ, USA). The height (z) of the microscope above the OTS is adjusted to focus on the top surface of the bracket. The OTS in-plane positions (x,y) are also adjusted using these translations stages to center the bracket in the microscope field-of-view. Drawings of the stereo camera version of the OTS can be seen in Appendix E.

Archwire rotation is achieved using a computer controlled stepper motor and gear box. Two dies, used to clamp the archwire, are mechanically locked together by a yoke to

provide support to the archwire and even rotation from both sides. A 6-axis load cell (Nano17 SI-25-0.25, ATI Industrial Automation, Apex, NC, USA) is used to collect applied force and moment data. The complete details of the OTS design are described by [6-8, 11].

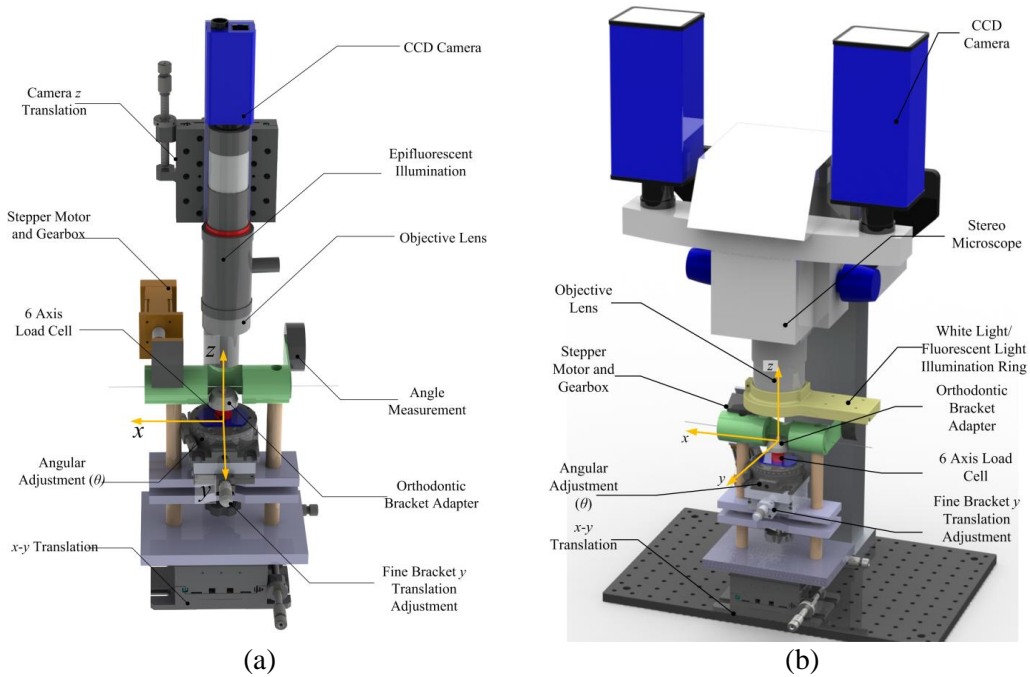


Figure 4.1: Orthodontic Torque Simulator used to replicate the effect of archwire rotation on orthodontic brackets (a) single camera version (b) stereo camera version

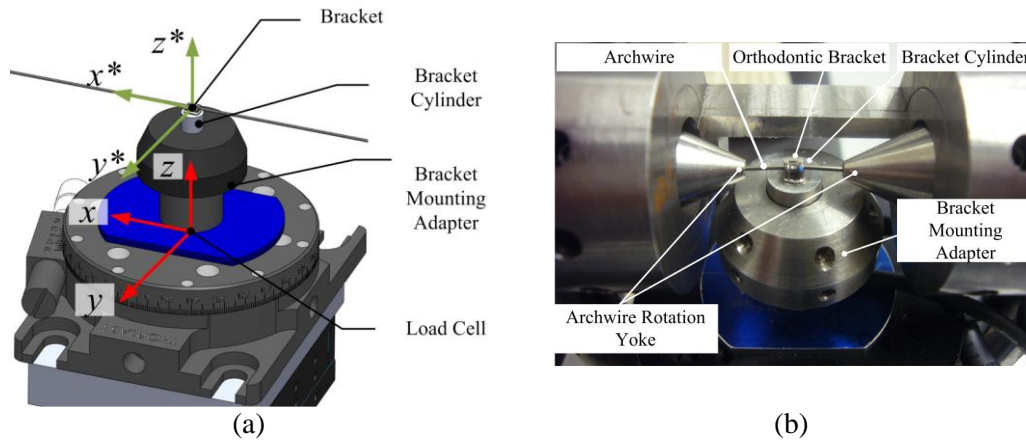
4.2.2 Stereo Microscope and CCD Cameras

The addition of a stereo microscope allows for the in- and out-of-plane (x^*, y^*, z^*) motions of the orthodontic bracket to be measured. This OTS configuration shown in Figure 4.1 (b) is comprised of a stereo microscope (Zeiss SteREO Discovery v8 microscope Carl Zeiss Micro Imaging GmbH Göttingen, Germany) with a 60mm working distance objective lens (1.0X Zeiss V8 Plan Apo Objective Lens, Zeiss MicroImaging GmbH Göttingen, Germany). Images were collected using two CCD cameras (Imager Intense, LaVision GmbH, Göttingen, Germany) having a 1376×1040 pixel array and 12-bit resolution. The cameras were connected to the stereo microscope using an intermediate phototube (Intermediate Phototube S 50:50 ports, Zeiss

MicroImaging GmbH Göttingen, Germany). The brackets were imaged at 2.0x magnification to maximize the bracket in the camera field-of-view. Test specimens were illuminated using a ring light (2.64" Ring Light, Variable Frequency, Edmund Optics, Barrington, NJ, USA) and a 365nm black-light (Black (365nm Peak) Replacement Bulb, Edmund Optics, Barrington, NJ, USA) to provide even illumination across the field-of-view.

4.2.3 Mounting Orthodontic Brackets

The bracket, bracket cylinder and load cell are shown in Figure 4.2. A stainless steel bracket cylinder with a 9.0mm nominal diameter was used as an analog for a tooth as described by Badawi et al. [11]. Brackets were mounted to the cylinder using an epoxy (Loctite E-20HP; Hysol, Henkel, Rocky Hill, Conn.). Cylinders were used to transmit the loads applied to the orthodontic bracket by the archwire to a 6-axis load cell and to allow for free rotation of the archwire in the bracket slot.



**Figure 4.2: Load cell and bracket coordinate systems. (a) Offset of orthodontic bracket from load cell
(b) Close-up of bracket load cell system**

4.2.4 Digital Image Correlation

DIC is a full field optical measurement technique that uses a random speckle pattern on a specimen surface to measure deformations and strains [10, 12]. This method is advantageous as it does not require contact with the specimen. Deformation is measured

by tracking contrast features on the specimen surface between subsequent images. A detailed description of the DIC process is described in Appendix B DIC displacement measurement comprises of four consecutive steps (1) specimen preparation (2) calibration of the imaging system for a defined field-of-view (3) collection of specimen deformation before and after loading, and (4) post processing of images to determine displacement or strain [13]. A detailed description of the bracket sample preparation, testing and post-processing is described in Appendix C. A specimen is prepared by applying a random pattern to the object surface using natural surface features or paints. Images are calibrated to convert from pixels to physical space (e.g. mm, inches) by acquiring an image of a target with a grid of known spacing. Each digital image is segmented into evenly spaced subsets of size $(2M + 1) \times (2M + 1)$ and an image correlation algorithm is performed for each image subset. The displacement of a subset is determined by maximizing a typical cross-correlation coefficient equation, S , shown in Equation (4.1) for the image before and after deformation [13, 14].

$$S(x, y, u, v, \frac{\partial u}{\partial x}, \frac{\partial u}{\partial y}, \frac{\partial v}{\partial x}, \frac{\partial v}{\partial y}) = 1 - \frac{\sum_{i=-M}^M \sum_{i=-M}^M [f(x_i, y_i) g(x_i', y_i')]}{\left[\sum_{i=-M}^M \sum_{i=-M}^M [f(x_i, y_i)]^2 * \sum_{i=-M}^M \sum_{i=-M}^M [g(x_i', y_i')]^2 \right]^{1/2}} \quad (4.1)$$

In this equation $f(x_i, y_j)$ represents the gray scale intensity at positions (x_i, y_i) for the reference image and $g(x_i', y_j')$ represents the gray scale intensity at positions (x_i', y_i') of the deformed image. Displacement between the reference and deformed image is calculated using the displacement mapping function:

$$\begin{aligned}
x'_i &= x_i + u + \frac{\partial u}{\partial x} \Delta x + \frac{\partial u}{\partial y} \Delta y \\
y'_i &= y_i + v + \frac{\partial v}{\partial x} \Delta x + \frac{\partial v}{\partial y} \Delta y \\
(i, j &= -M : M)
\end{aligned} \tag{4.2}$$

Where, u and v are the displacements for the subset centers in the x and y directions and

$\frac{\partial u}{\partial x}, \frac{\partial u}{\partial y}, \frac{\partial v}{\partial x}, \frac{\partial v}{\partial y}$ are the first-order displacement gradients for the reference subset [13,

14]. Also, $\Delta x = x_i - x_o$ and $\Delta y = y_i - y_o$ where x_o, y_o represents the undeformed coordinates and x_i, y_i is the deformed coordinate for each image subset.

A flowchart of the 3D DIC processing method is shown in Figure 2.8. This figure shows that cross correlation is performed between images 1 and 2 for cameras A and B to determine the 2D displacement vectors (u_1, v_1) and (u_2, v_2) . The surface height of the test object is determined through stereo cross correlation between camera A and B for each image pair. The 3D displacement vectors (u, v, w) are determined using the 2D displacement vectors for each camera and the determined surface height from the stereo cross correlation of the test object [15-17].

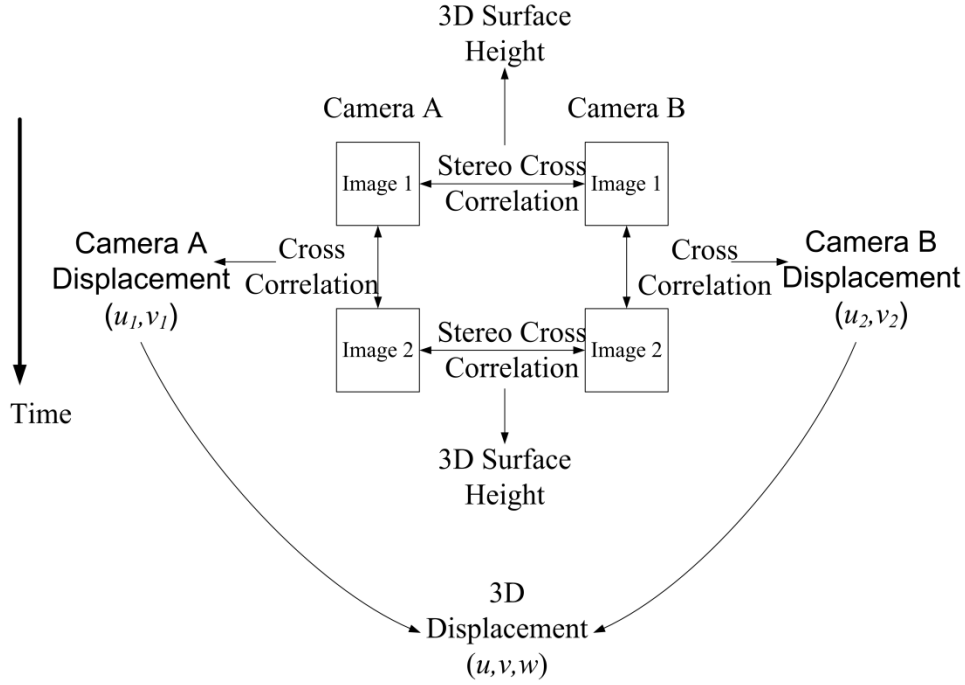


Figure 4.3: Stereo DIC processing method.

4.2.5 Sample Preparation

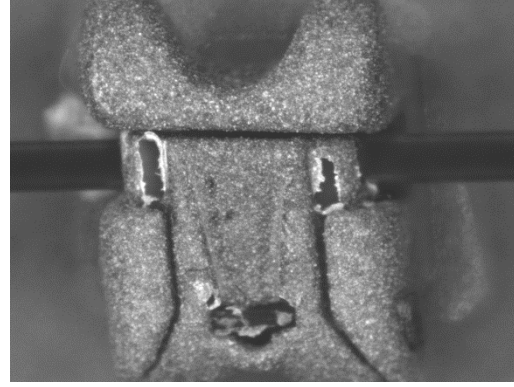
Orthodontic brackets were prepared prior to testing by coating the surface of the bracket with green fluorescent airbrush paint (5404 Fluorescent Green Createx Airbrush Colors, Createx Colors, East Granby CT). The paint was reduced at a ratio of approximately 2:1 to improve the flow of the paint through an airbrush (Wicked W100 Reducer Createx Airbrush Colors, Createx Colors, East Granby CT). Fluorescent paint was chosen for the speckle pattern to reduce specular reflection from the metallic bracket surfaces. The fluorescent paint is excited using a 365nm black light and the fluorescent paint particles emit light in the visible spectrum at approximately 510nm. The CCD cameras have a peak quantum efficiency for light collected at approximately 500nm [18] and the paint upon excitation appears white when viewed through the camera. The fluorescent paint produces a distinct pattern on the test object surface and the intensity of the speckle pattern remains constant as the test object deforms. Fluorescent paint is advantageous for this particular application since the fluorescent particles act as a light source rather than

reflecting light. The speckle pattern was applied using a high quality airbrush (Custom Micron B, Iwata Medea Inc. Portland OR). The use of an airbrush and fluorescent particles for digital image correlation was outlined by [19].

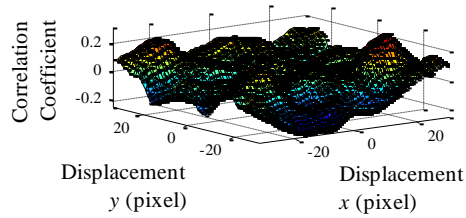
An example of an orthodontic bracket with and without the fluorescent speckle pattern is shown in Figure 4.4. The reflectivity of the bracket surface can be seen in Figure 4.4 (a) as locations of high image intensity. Since the orthodontic brackets have irregular geometry the reflection of the bracket surface will vary with bracket deformation; this will affect the accuracy of the 3D DIC measurements. A bracket with the fluorescent speckle pattern is shown in Figure 4.4 (b) and shows minimal reflection from the bracket surface. The effect of the contrast pattern on example correlation peaks for the two brackets is compared in Figure 4.4 (c) and (d). There is minimal contrast at a small scale for the bracket without an applied speckle pattern with reflective light as shown in Figure 4.4 (a) resulting in the correlation map shown in Figure 4.4 (c). The use of the fluorescent speckle pattern as shown in Figure 4.4 (b) with a small contrast feature results in a correlation map that a single distinctive correlation peak that can easily be distinguished from the background. The prominence of this peak has a strong effect on accuracy and repeatability of the measurement.



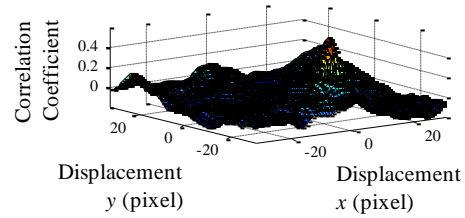
(a)



(b)



(c)



(d)

Figure 4.4: Orthodontic bracket sample preparation (a) bracket without speckle pattern (b) bracket with speckle pattern (c) Correlation peak for bracket without speckling (d) correlation peak for bracket with speckling

Prior bracket deformation measurements have used a micro-etcher to produce a random speckle pattern on the bracket surface; however, this method may alter the surface material properties of the brackets [7-9]. The fluorescent paint allows for a speckle pattern to be produced on the surface of the brackets without changing the material properties of the bracket. As well, use of a black light with the fluorescent paint reduces the specular reflection from the metallic bracket surfaces as the wavelength of the black light is outside the range of the CCD cameras. The fluorescent paint acts as a light source since the paint is excited using a black-light. Prior bracket measurements required light to be reflected off the surface of the brackets, which is a potential source for error.

A similar method for speckling samples on a micro-scale was outlined by [19]. The author demonstrated that an airbrush can be used to produce an adequate speckle pattern for images resolutions that range between 3 to 10 μm /pixel using a stereo microscope.

4.2.6 Stereo Camera Calibration

Calibration of the stereo cameras is performed to orient the cameras in 3D space. The stereo calibration process is essential to acquiring accurate 3D measurements [16, 17, 20, 21]. The calibration procedure determines the 3D position of each camera relative to the world coordinate system. The stereo camera calibration procedure consists of two steps; (1) camera calibration and (2) stereo image matching. The camera calibration is used to determine the intrinsic and extrinsic camera parameters described by Luo et al. [22].

Calibration for the stereo microscope camera setup was carried out using a glass calibration target (Microscope Calibration Plate 0.25mm to 1mm dot spacing, LaVision GmbH, Gottingen, Germany) that has a known regular grid on the surface. The 0.50mm grid with 0.12mm diameter marks was used for the calibration of the stereo microscope. The calibration plate was displaced in known increments of 25.4 μm in the z^* direction using a micrometer driven stage (MT01 Translation Stage, Thor Labs, Newton NJ, USA) and stereo images of the calibration target were acquired at three locations in the z^* direction. The calibration of a stereo camera setup is typically performed using a pin-hole camera model but it has been shown [23] that the pin-hole calibration model is not valid for the calibration of a stereo microscope due to distortions caused by the internal microscope optics. Therefore a 3rd order polynomial calibration [24] was implemented for the current stereo microscope setup.

4.2.7 Image Post Processing

Images collected using the OTS were acquired and post processed using a commercial software package (LaVision GmbH DaVis 8.06. Gottingen, Germany, 2009). Image subsets, or window size, used to determine the 3D displacement of the brackets were 64x64 pixels as a compromise between vector precision and maximization of the number of interrogation windows for each TW. A geometric mask was applied to each bracket image to eliminate the out-of-focus regions such as the bracket base and the dowel. A sliding average and max-min normalization filters were used to improve the contrast of the bracket images. As well the 64x64 image subset was used with a multi-pass approach with a box offset of 87%. The precision of displacement vectors as a function of interrogation window size are summarized in Table 4.1 [15]. The field of view for the brackets was 1376x1040 pixels or 4.25x3.2 mm.

Table 4.1: Displacement vector precision [15].

Interrogation Window Size	Precision of 2D Vectors (pixels)	Precision of 3D Vectors (pixels)
16x16	0.05	0.1
32x32	0.025	0.05
64x64	0.01	0.025
128x128	0.005	0.01

4.2.8 Accuracy of Bracket Deformation

The accuracy of the 3D DIC measurement system was assessed by analyzing the known motion of a rigid body [25]. A flat test sample was chosen to simplify the rigid body analysis by eliminating complications due to irregular geometries by using a sample with a regular known shape. The sample was cut out of clear acrylic, painted black (OPTIX acrylic sheet 2.0mm thickness Plaskolite Inc. Columbus, OH) and speckled using the airbrush technique described earlier. The sample was displaced using two micrometer driven translation stages (MT01 Translation Stage, Thor Labs, Newton NJ, USA). The

translation stages have a range of 12.7mm and a minimum resolution of 12.7 μ m. The sample was moved in increments of 25.4 μ m using the micrometers to a maximum distance of 254 μ m in two directions, x^* and z^* . The x^* and z^* displacements were used to assess the accuracy of the in-plane and out-of-plane 3D DIC measurements respectively. Rigid body displacements in the x^* and z^* directions were each performed ten times to reduce the effect of human error on the movement of the micrometers. Images were collected for each position of the sample.

Comparison of the correlated displacements with the actual displacement is shown in Figure 4.5. The in-plane bulk displacement comparison is shown in Figure 4.5 (a) while the out-of-plane displacement comparison is shown in Figure 4.5 (b). The maximum standard deviation for the in-plane motion and out-of-plane was found to be 2.93 μ m and 5.82 μ m, respectively. Range bars highlight that the in-plane variation is relatively consistent over the range of measurement while there is a steady increase in out-of-plane variation with increasing measured distance. This can be linked to the larger out-of-plane error compared to in-plane for stereo imaging which is a function of viewing angle. As the angle between the views reduces below 10°, the out-plane variance is estimated to be greater than 4 times the in-plane variance [26, 27].

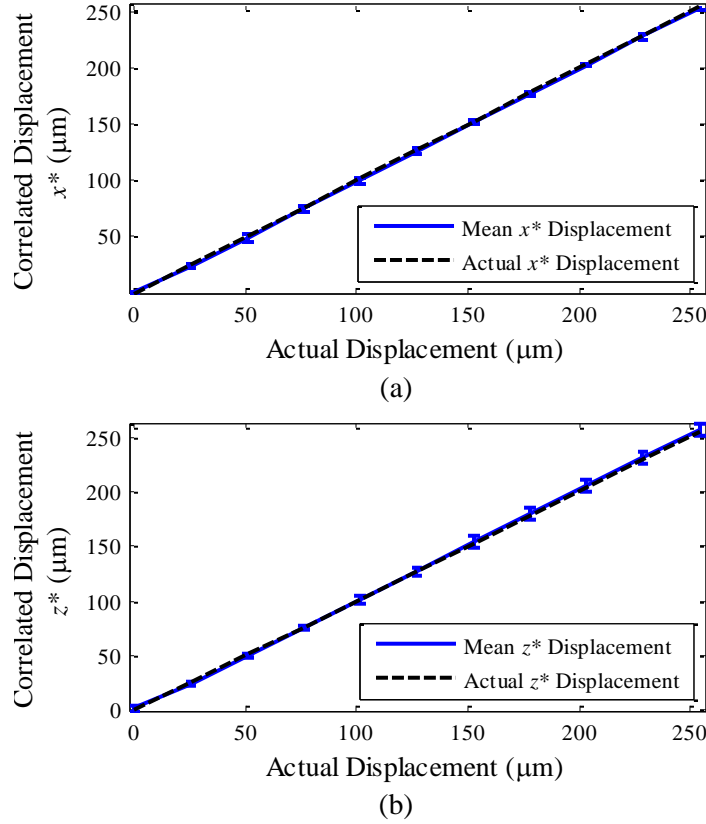


Figure 4.5: 3D DIC bulk motion validation (a) in-plane motion (b) out-of-plane motion

The accuracy of the 3D DIC measurement method has been assessed using a sample with a regular geometry. A similar method to assess the overall error of the 3D DIC method was outlined by [25]. From Figure 4.5 it can be seen that there is agreement between the measured 3D DIC displacement in the x^* and z^* directions and the physical displacements. The 3D DIC measurement using a 64x64 subset size will have a resolution of 0.025 pixels as shown in Table 4.1 [15]. The field of view for the brackets was 1376x1040 pixels or 4.25x3.2 mm therefore the optimum resolution for this camera setup with a 64x64 subset size will be 0.07μm. This optimum resolution is much less than the maximum deviation of 2.93μm and 5.82μm found for the x^* and z^* directions. Rigid body motion tests were also performed by Berfield et al. [19] for samples speckled using an airbrush. A computer controlled servo motor with sub-micron precision was

used for the motion of the test samples and the author was able to achieve a measurement of $1\mu\text{m}$ using a camera with a 640×480 pixel field of view. The micrometer minimum resolution used in this study is $12.7\mu\text{m}$; therefore, the deviation from the expected displacement seen in Figure 4.5 can be attributed to human error in the movement of the test sample using the micrometers.

The in-plane and out-of-plane accuracy for 3D DIC are typically 1-2% and 3-4%, respectively [26]. In addition, for stereo DIC the in-plane to out-of-plane error ratio is affected by the included angle between the two cameras [27]. This indicates that the out-of-plane error should be greater than the in-plane error and that the in-plane to out-of-plane error ratio is a function of the angle between the stereo cameras. The in-plane and out-of-plane plots in Figure 4.5 (a) and (b) show that the standard deviation for the out-of-plane motion is greater than the standard deviation for the in-plane motion which indicates the precision of the in-plane motion is greater than the out-of-plane motion. The maximum standard deviation for the in-plane motion was found to be $2.93\mu\text{m}$ and the out of plane maximum standard deviation was found to be $5.82\mu\text{m}$. This indicates that the out of plane error was approximately 2 times greater than the in-plane motion, which agrees with expected measurement in-plane and out-of-plane resolutions [26, 27].

4.2.9 Measurement of Bracket Deformation

To demonstrate the 3D displacement of orthodontic brackets a Damon 3MX (Ormco Corporation, Orange, California, USA) bracket was tested. The Damon 3MX bracket was selected as it is a typical self-ligating bracket. The design of the Damon 3MX bracket is such that a significant difference in the height of the four bracket TWs does not exist; therefore, the four bracket TWs should not move out of the stereo microscope's depth of focus. Other self-ligating bracket designs demonstrate a substantial difference in the height of the bracket TWs which may affect the ability to maintain focus on all four

bracket TWs. The OTS is controlled using custom software (LabWindows/ CVI, National Instruments, Austin TX). This program automates the control of the stepper motor, acquisition of data from the load cell and image acquisition. The automated process is described in [6-9] for the 2D measurement of bracket deformation and is identical to the approach reported here.

Deformation of the bracket was assessed by determining the relative motion between the four bracket TWs described in Figure 4.6. This figure also shows the 64x64 pixel subset used for the measurement of the 3D displacement of the bracket. Equation (4.3) details the calculation of the bracket displacement in the x^* , y^* and z^* directions. In this equation $\overline{D_{TieWin*i*}}$ denotes the average displacement of the defined regions for TWs #1,2,3, and 4 for the $i = x^*, y^*, z^*$ directions. LHS_D is the displacement between TWs #1 and #3 while RHS_D is the displacement between TWs #2 and #4.

$$\begin{aligned}
 LHS_{D_i} &= \left[\overline{D_{TieWin1}} - \overline{D_{TieWin3}} \right] \\
 RHS_{D_i} &= \left[\overline{D_{TieWin2}} - \overline{D_{TieWin4}} \right]
 \end{aligned}
 \tag{4.3}$$

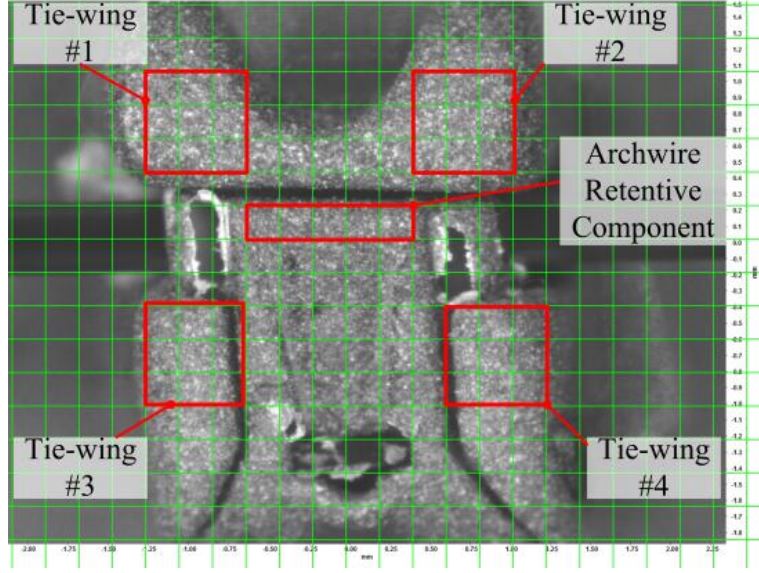


Figure 4.6: Orthodontic bracket box regions used to track TW motion

In addition, the motion of the bracket ARC in the $i = x^*, y^*, z^*$ directions was measured. Bulk motion of the entire bracket was eliminated to find the relative motion of the bracket retentive component by subtracting the average displacement of the TWs from the motion of the bracket retentive component. The relative retentive component motion is denoted as $RelativeRC_i$ and the retentive component motion is denoted as RC_i as shown in Equation (4.4).

$$RelativeRC_i = RC_i - \left[\frac{1}{4} \sum_{j=1}^4 \overline{D_{TieWing_j}} \right]_i \quad (4.4)$$

An example of a pair of stereo images collected using the OTS and stereo microscope are shown in Figure 4.7 (a) and (b) showing the left and right camera views of the bracket. The different perspective views of the stereo images of a Damon 3MX bracket allows for the 3D surface to be generated and subsequently the 3D displacement vectors.

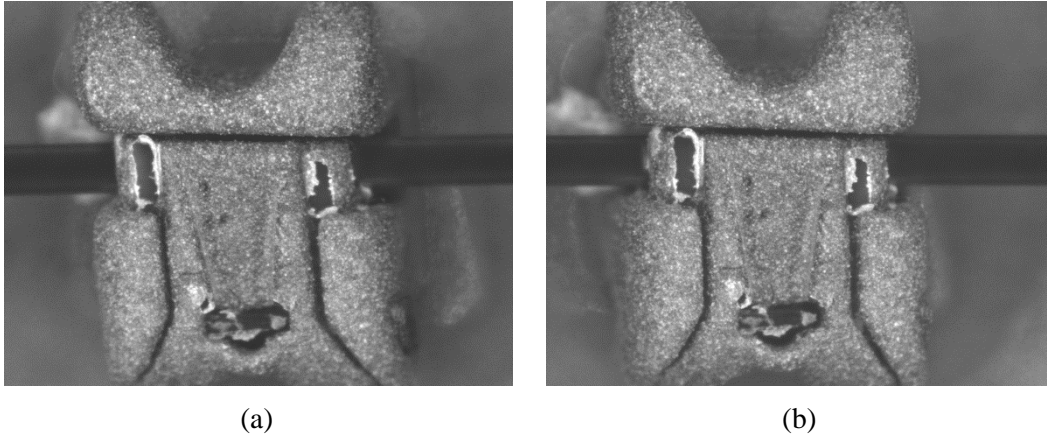
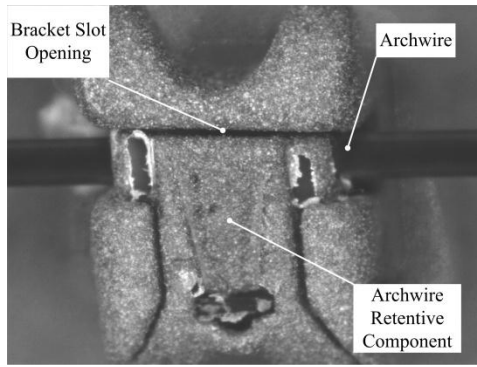
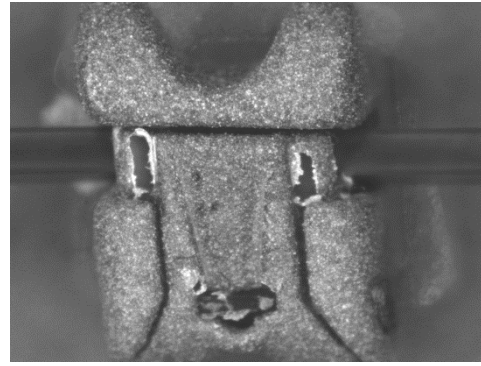


Figure 4.7: Stereo images of a Damon 3MX bracket showing the different camera perspectives (a) Left Camera (b) Right Camera

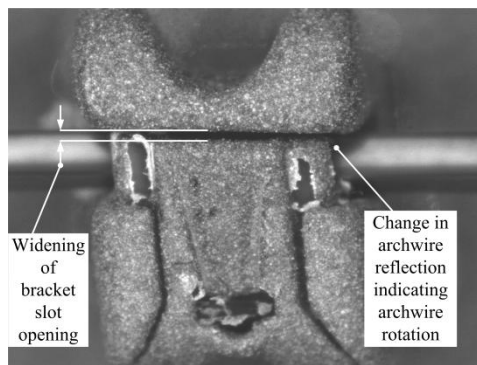
A sequence of images at increasing archwire rotations (ϕ) of 0° , 21° , and 45° as well as decreasing archwire rotation of 21° and 0° is shown in Figure 4.8. The image sequence shows the motion of the Damon 3MX bracket due to archwire rotation. A number of features that present in the system are also defined here. This includes the changing aspect of the archwire as it is rotated and the widening of the gap between the ARC and the top TWs (as shown in the image) which is a result of the widening of the bracket slot due to applied torque.



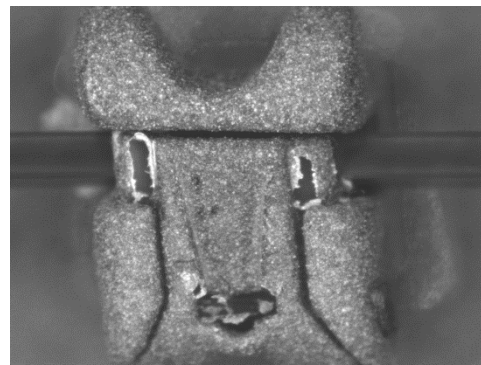
(a)



(b)



(c)



(d)



(e)

Figure 4.8: Damon 3MX orthodontic bracket deformation due to archwire rotation (ϕ) (a) Increasing 0° (b) Increasing 21° (c) Increasing 45° (d) Decreasing 21° (e) Decreasing 0° 3D DIC Bracket Deformation

A profile image of a Speed (Strite Industries, Cambridge, Ontario, Canada) self-ligating orthodontic bracket is shown in Figure 4.9. This figure shows a main image of the bracket prior to deformation as well as the outline of the bracket after archwire rotation. The Speed bracket was selected to demonstrate the deformation in the y^* and z^* directions as this bracket has been shown to plastically deform more than other self-ligating orthodontic brackets [7]. This image illustrates that the bracket TWs displace in both the y^* and z^* directions. It can also be seen that localized deformation (notching) occurs due to engagement of the archwire in the sides of the bracket slot.

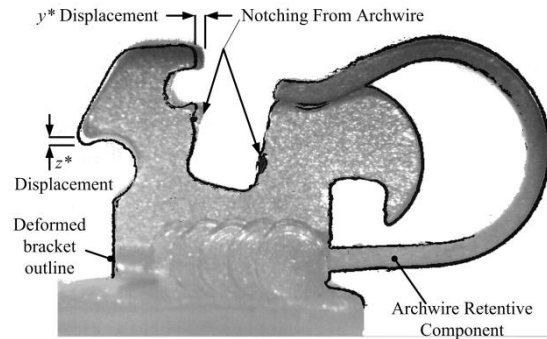


Figure 4.9: Profile image of a Speed orthodontic bracket showing deformation due to archwire rotation.

Example 3D bracket surfaces created from the 3D DIC displacement vector coordinates are shown in Figure 4.10 (a) and (b), for the Damon 3MX and In-Ovation R brackets, respectively. This figure shows that the stereo image pairs can be used to generate a three dimensional surface that can be visualized using a 3D rendering software (ParaView, Kitware, Inc. Clifton Park, New York). The process to create the 3D bracket surface from the 3D DIC data is described in Appendix D. The original bracket images for the Damon 3MX and In-Ovation R brackets are also shown in Figure 4.10 (c) and (d) for comparison. Figure 4.10 shows that the general 3D surface features of the orthodontic brackets can be recreated from the stereo image pairs collected using the OTS.

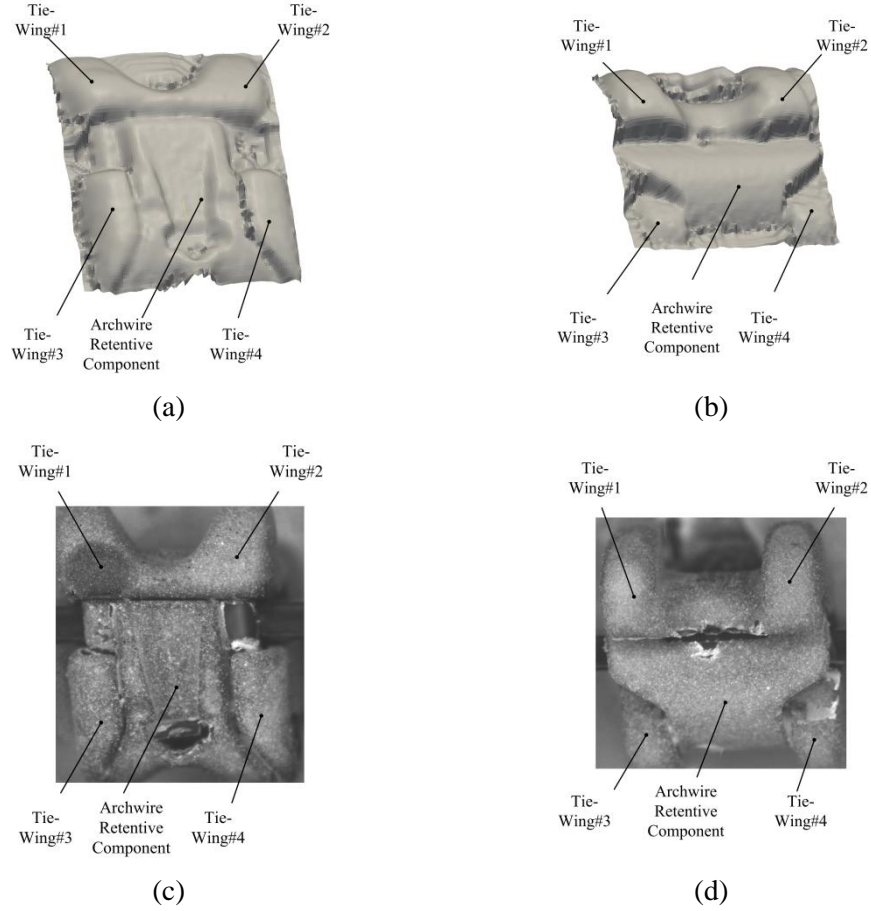


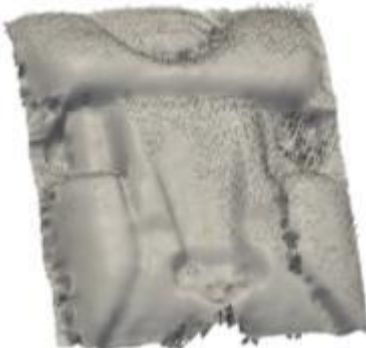

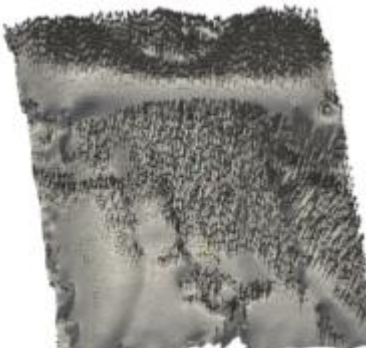



Figure 4.10: 3D bracket surface visualized from stereo image pair 3D DIC data (a) Damon 3MX and (b) In-Ovation R; and (c) Damon 3MX bracket image (d) In-Ovation R bracket image.

A sequence of bracket surfaces and displacement vectors are shown in Figure 4.10; all left images are Damon 3MX brackets, while all right images are In-Ovation R brackets. The motion of the bracket in the x^* , y^* and z^* directions is represented by 3D displacement vectors. This figure shows the displacement vectors increasing with increasing archwire rotation up to 45° of the two brackets side by side. The majority of the relative motion is localized to the archwire retention component and the TWs that the archwire loads at the top of the image.

Rotation Angle (ϕ)	Damon 3MX	In-Ovation R
0°	 (a)	 (b)
12°	 (c)	 (d)
24°	 (e)	 (f)

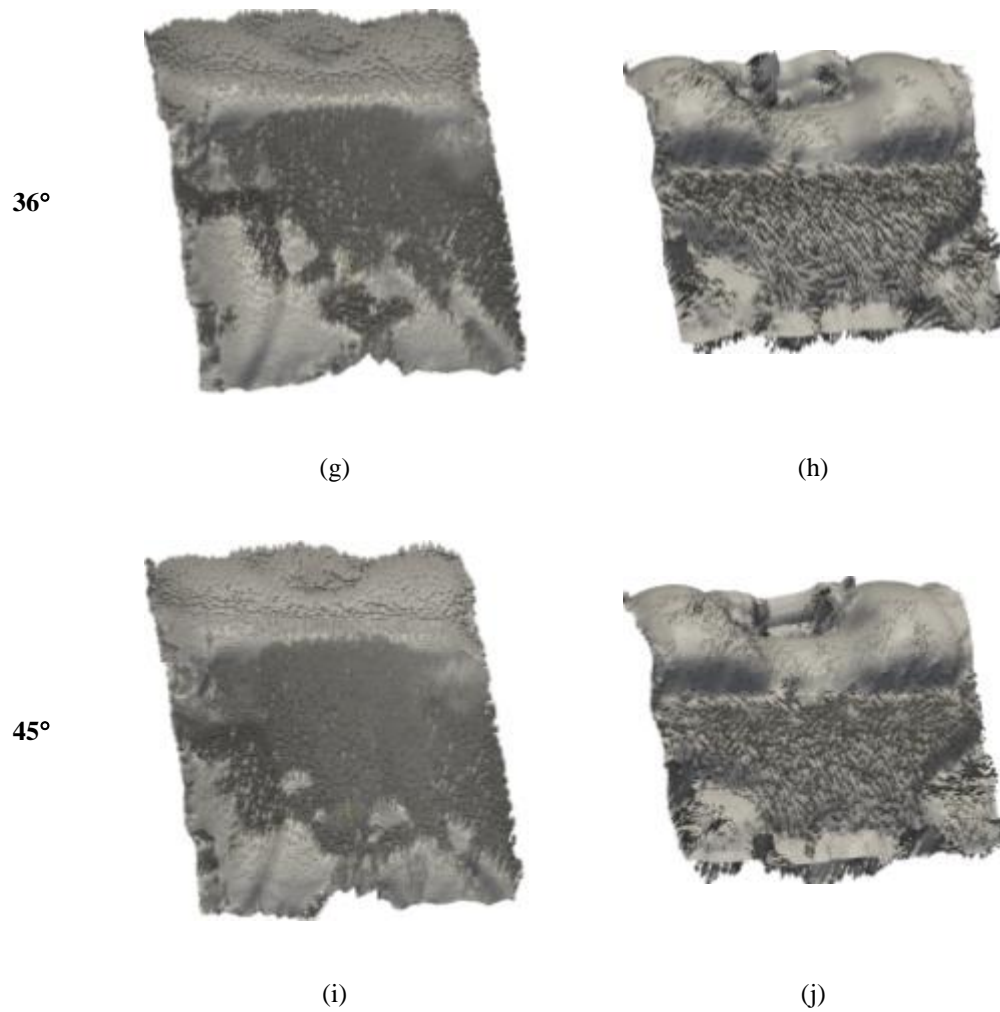


Figure 4.11: 3D bracket surface and 3D displacement vectors for Damon 3MX and In-Ovation R brackets (a) Damon 0° rotation (b) In-Ovation 0° rotation (c) Damon 12° (d) In-Ovation 12° (e) Damon 24° (f) In-Ovation 24° (g) Damon 36° (h) In-Ovation 36° (i) Damon 45° (j) In-Ovation 45°

4.2.10 Repeatability of 3D Bracket Measurements

The repeatability of the 3D bracket deformation measurement method and OTS will be assessed by performing multiple archwire rotation tests using the same bracket and archwire. A Damon 3MX (Ormco Corporation, Orange, California, USA) bracket with a common prescription of 12° Torque, 5° angulation and, 0° rotation for the upper right incisor [28] was used to test OTS repeatability. A 0.483 x 0.635mm (0.019x0.025”) archwire was used for this study. Using the automated OTS software the angle of the

archwire, ϕ , was rotated in 2° increments to a maximum angle of 20° . The maximum archwire rotation of 20° was used to ensure plastic deformation does not occur to the bracket TWs. Once the maximum angle was reached the archwire was returned to the original position in 2° increments. At each increment a pair of stereo images of the orthodontic bracket was collected resulting in twenty-two (22) image pairs collected. A one second delay was used between each archwire rotation increment.

4.2.11 Deformation Characteristics of Two Orthodontic Brackets

Two orthodontic brackets were compared to assess the difference in three dimensional deformation caused by archwire rotation. A 0.483 x 0.635mm cross section stainless steel archwire was used. A total of 10 brackets were tested; five Damon 3MX (Ormco Corporation, Orange, California, USA) and five In-Ovation R (GAC, Bohemia, NY) brackets. Two upper right incisor (UIR) brackets with a nominal slot width of 0.5588mm and the same prescription were selected. The In-Ovation R brackets have active ligation whereas the Damon 3MX brackets are passive ligation brackets. The archwire retentive component for the active ligation brackets maintains contact between the archwire and ARC and applies a force in the z^* direction to the archwire. Conversely, the passive ligation brackets only apply a force to the archwire when the archwire contacts the ARC. An illustration of the difference between active and passive bracket ligation is shown in Figure 4.12.

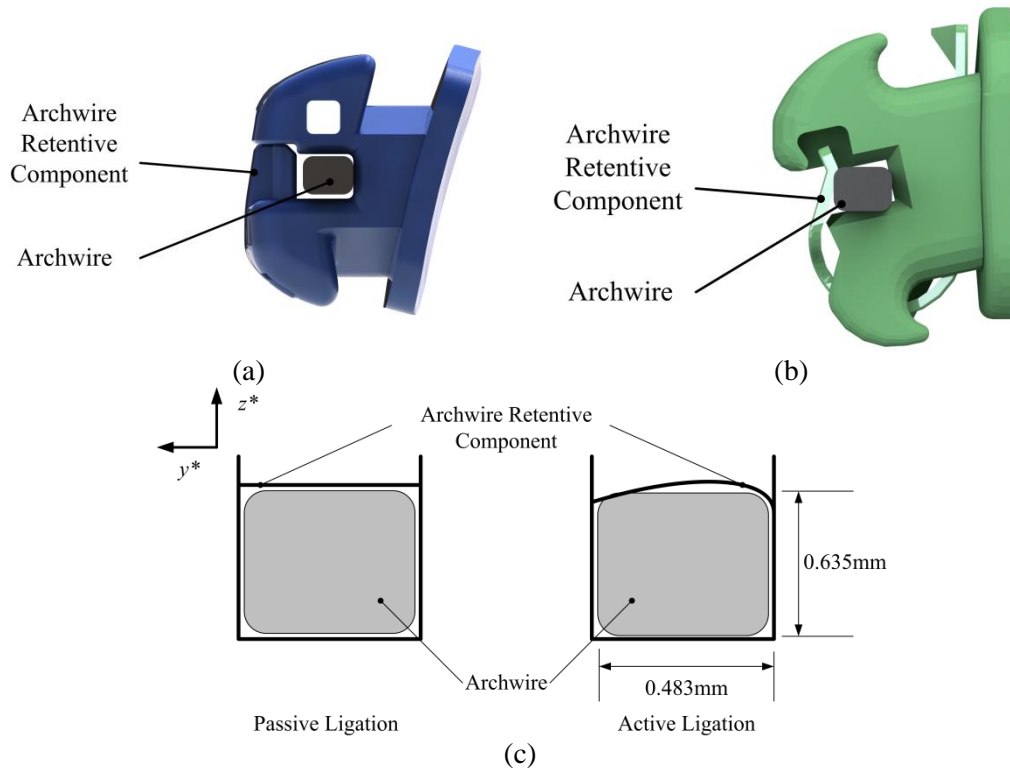


Figure 4.12: Comparison of self-ligating brackets (a) passive ligation Damon Q (solid model provided courtesy of Ormco) (b) In-Ovation R (solid model provided courtesy of GAC) active ligation applies a preload to the wire. (c) Schematic of passive and active ligation brackets retention system

Using the automated OTS software the angle of the archwire, ϕ , was rotated in 3° increments to a maximum angle of 45° . Once the maximum angle was reached, the archwire was returned to the original position in 3° increments. At each increment a pair of stereo images of the orthodontic bracket was collected resulting in thirty-two (32) image pairs collected. The stereo image sequence was used to measure the 3D deformation of the bracket due to archwire rotation by post processing the images using the previously described method.

A Mann-Whitney U nonparametric test (ranksum function, Statistics Toolbox, MATLAB, 2009a, The MathWorks, Natick, MA, U.S.A.) was used to determine if a statistically significant difference can be found between the Damon 3MX and In-Ovation R brackets. The test was selected due to the small sample size for each bracket.

A P -value of less than 0.05 indicates that a statistical difference exists between the two brackets.

4.3 Results and Discussion

4.3.1 Repeatability of 3D Bracket Measurements

The repeatability of the 3D bracket deformation measurement method and OTS was assessed by performing multiple archwire rotation tests on the same bracket. A total of 30 archwire rotation tests were performed using the same Damon 3MX orthodontic bracket and archwire. The average and standard deviation TW motion for the x^* , y^* and z^* directions at every rotation angle determined using Equation (4.3) are summarized in Figure 4.13.

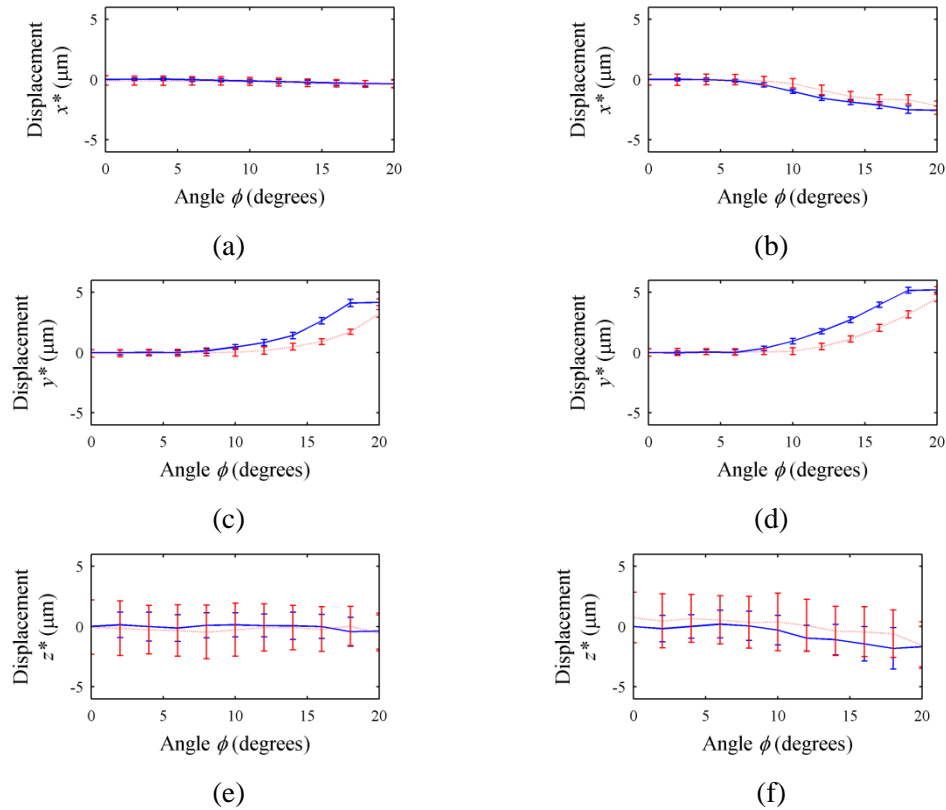


Figure 4.13: Repeatability of Damon 3MX bracket TW motion. Average and standard deviation displacements for (a) TW#1-3 x^* (b) TW#2-4 x^* (c) TW#1-3 y^* (d) TW#2-4 y^* (e) TW#1-3 z^* (f) TW#2-4 z^* . Solid line indicates increasing archwire rotation. Dashed line indicates decreasing archwire rotation.

The maximum TW displacement and standard deviations are summarized in Table 4.2. The maximum displacement in the y^* direction is 4.2 ± 0.29 and $5.2 \pm 0.26\mu\text{m}$ for TWs#1-3 and #2-4, respectively. In addition the final deformation, as seen in Figure 4.13 (c) and (d), in the y^* direction is -0.07 ± 0.31 and $-0.008 \pm 0.30\mu\text{m}$ for TWs #1-3 and #2-4, respectively, indicating that the bracket TWs did not plastically deform in the y^* direction due to repeated archwire rotation. Plastic deformation was not seen in the y^* direction since the archwire was rotated to a maximum angle of 20° and wire rotations below this angle typically do not result in bracket deformation. Figure 4.13 shows that the greatest motion for the bracket TWs occurred in the y^* direction. The maximum magnitude of motion in the y^* direction was 10.7 and 3.0 times greater than the maximum z^* motion for TWs#1-3 and #2-4 respectively. Similarly, the maximum magnitude of motion in the y^* direction was 12.0 and 2.0 times greater than the x^* motion for TWs #1-3 and #2-4 respectively. This indicates that the dominant motion of the Damon 3MX bracket TWs is the y^* direction. The range bars in Figure 4.13 show the variation of the test bracket for 30 archwire rotation tests. This figure shows that the largest range bars occur in the z^* direction while the x^* and y^* directions exhibit similar range bars. The large range bars in the z^* direction may indicate motion of the entire bracket in this direction rather than TW deformation.

Table 4.2: Maximum TW motion.

TW motion (stdev) [μm]					
x^*		y^*		z^*	
#1-3	#2-4	#1-3	#2-4	#1-3	#2-4
-0.35(0.3)	-2.5(0.36)	4.2(0.29)	5.2(0.26)	-0.39(1.5)	-1.7(1.7)

The average motion and standard deviation of the bracket retentive component at each angle as determined using Equation (4.4) is shown in Figure 4.14. The maximum archwire retentive component motion is summarized in Table 4.3. This table shows that

the greatest motion for the ARC was observed in the z^* direction since maximum magnitude of motion in the z^* direction was 1.5 and 6.2 times greater than the x^* and y^* motion.

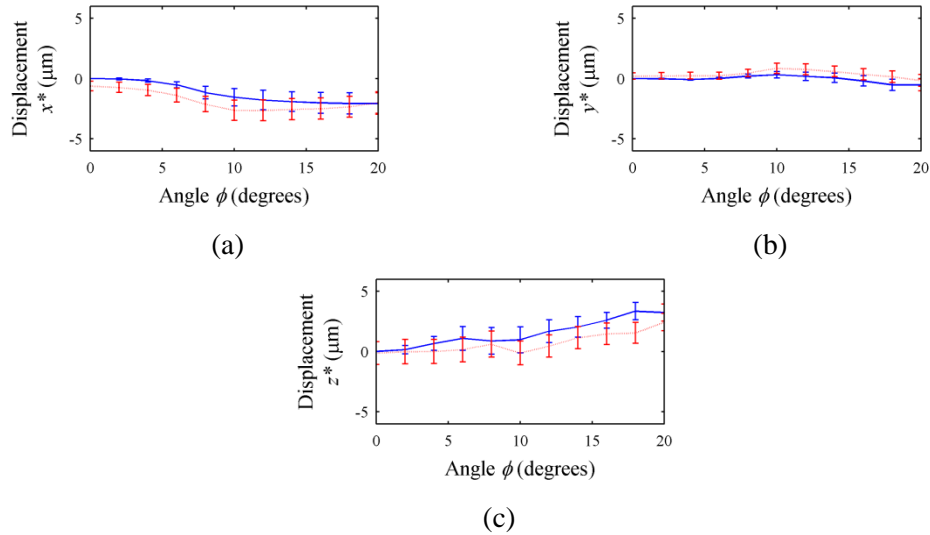


Figure 4.14: Repeatability of Damon 3MX bracket ARC. Average and standard deviation of archwire retentive displacements (a) component x^* (b) ARC y^* (c) ARC z^* . Solid line indicates increasing archwire rotation. Dashed line indicates decreasing archwire rotation.

Table 4.3: Maximum ARC motion in three directions.

x^* (stdev) [μm]	y^* (stdev) [μm]	z^* (stdev) [μm]
-2.1(0.89)	-0.52(0.49)	3.2(0.71)

Figure 4.13 shows that the dominant motion for the bracket TWs is in the y^* direction while Figure 4.14 shows that the dominant ARC motion is in the z^* direction. The maximum variation for the TWs and ARC displacement is summarized in Table 4.2 and Table 4.3. From these tables it can be seen that the variation between each bracket test is much greater than the $0.07\mu\text{m}$ resolution of the 3D DIC method. As a result the variation seen in the bracket TW and ARC motion can be attributed to variation due to the wire-bracket interaction. Table 4.2 shows that the variation in the x^* and y^* motion was in the region of $0.3\mu\text{m}$ while the variation in the z^* direction was $1.5\mu\text{m}$. As well, Table 4.3 shows that the variation of the ARC was in the region of $0.7\mu\text{m}$.

4.3.2 Deformation Characteristics of Two Orthodontic Brackets

Deformation characteristics of two orthodontic brackets were compared to assess differences and observe first hand 3D general behavior due to archwire rotation. The geometric differences between the self-ligating Damon 3MX (passive) and In-Ovation R (active) brackets can be seen in Figure 4.12. The two brackets were examined to demonstrate the results produced by the OTS and to show how brackets of different design can be compared using this device.

Comparison of the resulting TW motion of the Damon 3MX and In-Ovation R brackets is shown in Figure 4.15 and the motion of the ARC of the two brackets is compared in Figure 4.16. The maximum TW motion for the Damon 3MX and In-Ovation R brackets and final plastic deformation are shown in Table 4.4. Both the Damon 3MX and In-Ovation R brackets exhibited similar deformation in the y^* direction for a maximum archwire rotation of 45° . Table 4.4 shows that a significant difference can be seen in the x^* direction for the TWs #1-3 and 2-4.

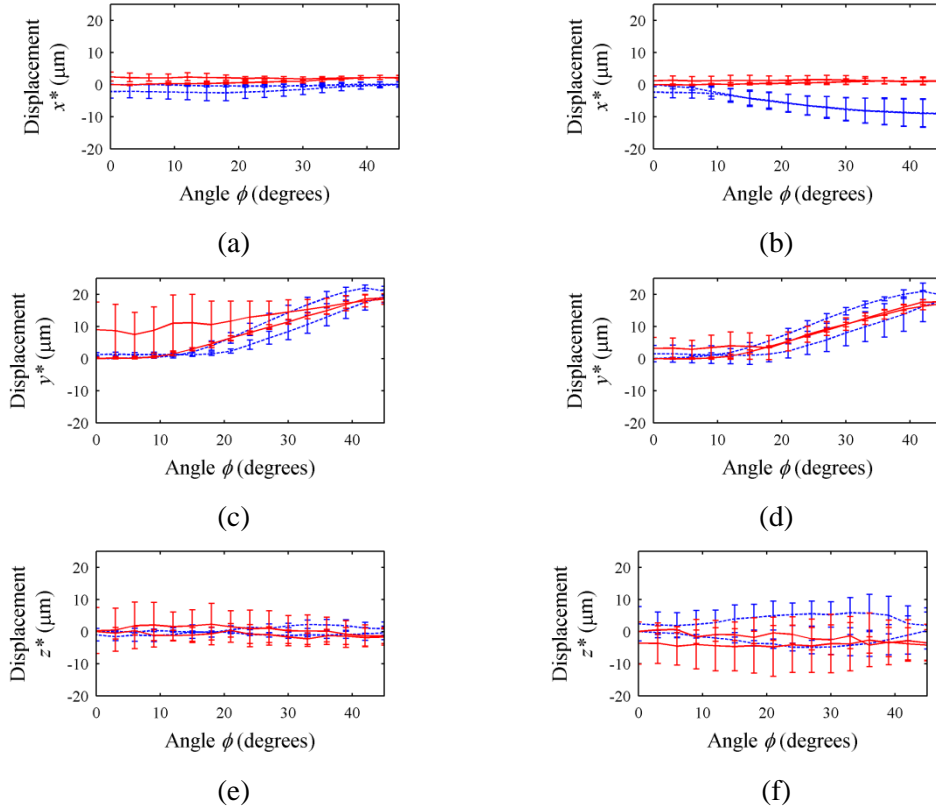


Figure 4.15: Damon 3MX and In-Ovation R bracket TW average motion and standard deviation as a function of wire rotation angle. (a) TW#1-3 x^* (b) TW#2-4 x^* (c) TW#1-3 y^* (d) TW#2-4 y^* (e) TW#1-3 z^* (f) TW#2-4 z^* . Solid line indicates In-Ovation R bracket Dashed line indicates Damon 3MX bracket.

Table 4.4: Maximum and plastic deformation due to archwire rotation for Damon 3MX and In-Ovation R brackets. Bolded values show significant differences.

Bracket TW	Maximum Average Displacement (μm)			Plastic Deformation (μm)		
	Damon	In-Ovation	<i>P</i> -Value	Damon	In-Ovation	<i>P</i> -Value
TW#1-3 x^* (stdev)	0.10(0.79)	2.13(0.65)	0.008	-2.11(2.14)	2.42(1.39)	0.008
TW#2-4 x^* (stdev)	-9.07(4.32)	1.15(0.99)	0.008	-2.34(1.69)	1.23(1.39)	0.008
TW#1-3 y^* (stdev)	21.03(1.39)	18.87(1.30)	0.095	1.32(0.52)	9.04(8.54)	0.032
TW#2-4 y^* (stdev)	19.80(3.52)	17.64(1.00)	0.548	1.50(2.55)	3.23(3.35)	1.000
TW#1-3 z^* (stdev)	-0.42(2.09)	-1.69(2.57)	0.841	-0.99(1.97)	0.33(7.14)	0.310
TW#2-4 z^* (stdev)	0.27(5.76)	-4.20(4.76)	0.690	2.42(5.34)	-3.58(6.52)	0.310

The calculated *P*-Values using the Mann-Whitney U nonparametric test for comparing the TW motion of the two brackets at every angle are summarized in Table 4.5. From Table 4.5 it can be seen that a statistically significant difference exists between the two brackets in the x^* direction for an archwire rotation greater than 9° . A statistically significant difference was detected for increasing archwire rotation between 33 - 39° in the y^* motion for both the left and right TWs. No differences were detected between the z^* motion of the two brackets.

Bracket design may affect the bracket response to archwire rotation. This is demonstrated by the x^* motion of the two brackets shown in Figure 4.15 (a) and (b). The greater motion in the x^* direction shown by the Damon 3MX bracket could be the result of a taper in the bracket slot due to manufacturing resulting in uneven load transfer from the archwire. As well, the In-Ovation R bracket demonstrated positive motion in the x^* direction while the Damon 3MX bracket moved in the negative x^* direction. The difference in the taper of the two bracket slots will affect the tendency of the bracket to rotate due to archwire rotation. The difference between the brackets could also be due to

the ligation method. The active-ligation In-Ovation R brackets could ensure that the archwire remains aligned in the bracket slot whereas the archwire is free to move in the bracket slot of the passive-ligation Damon 3MX bracket.

Table 4.5: Comparison of orthodontic bracket TW motion. Bolded values show significant differences

Angle [°]	TW#1-3 x^* <i>P</i> -Value	TW#2-4 x^* <i>P</i> -Value	TW#1-3 y^* <i>P</i> -Value	TW#2-4 y^* <i>P</i> -Value	TW#1-3 z^* <i>P</i> -Value	TW#2-4 z^* <i>P</i> -Value
0	1.000	1.000	1.000	1.000	1.000	1.000
3	1.000	0.310	0.690	0.310	1.000	0.421
6	0.056	0.222	0.841	0.032	0.841	0.310
9	0.095	0.016	0.690	0.056	0.151	1.000
12	0.008	0.016	0.310	0.310	0.151	0.421
15	0.008	0.008	0.421	0.222	0.222	0.310
18	0.016	0.008	0.841	0.151	0.548	0.056
21	0.016	0.008	1.000	0.016	0.310	0.056
24	0.008	0.008	0.841	0.008	0.690	0.056
27	0.008	0.008	0.310	0.008	1.000	0.310
30	0.008	0.008	0.095	0.008	1.000	0.548
33	0.008	0.008	0.032	0.008	0.222	0.421
36	0.008	0.008	0.016	0.008	1.000	1.000
39	0.008	0.008	0.008	0.008	1.000	1.000
42	0.008	0.008	0.008	0.056	0.841	0.690
45	0.008	0.008	0.095	0.548	0.841	0.310
45	0.008	0.008	0.548	0.841	0.222	0.310
42	0.008	0.008	0.548	0.690	0.421	0.421
39	0.008	0.008	0.310	0.690	0.310	0.151
36	0.008	0.008	0.095	0.690	0.841	0.151
33	0.008	0.008	0.095	0.421	1.000	0.095

30	0.008	0.008	0.095	0.421	0.690	0.151
27	0.008	0.008	0.032	0.310	0.841	0.032
24	0.008	0.008	0.016	0.095	1.000	0.095
21	0.008	0.008	0.008	0.222	0.421	0.151
18	0.008	0.008	0.095	0.548	0.310	0.151
15	0.008	0.008	0.151	1.000	0.421	0.222
12	0.008	0.008	0.095	0.548	0.310	0.222
9	0.008	0.008	0.056	0.841	0.222	0.222
6	0.008	0.008	0.056	0.841	0.222	0.151
3	0.008	0.008	0.056	0.841	0.421	0.310
0	0.008	0.008	0.032	1.000	0.310	0.310

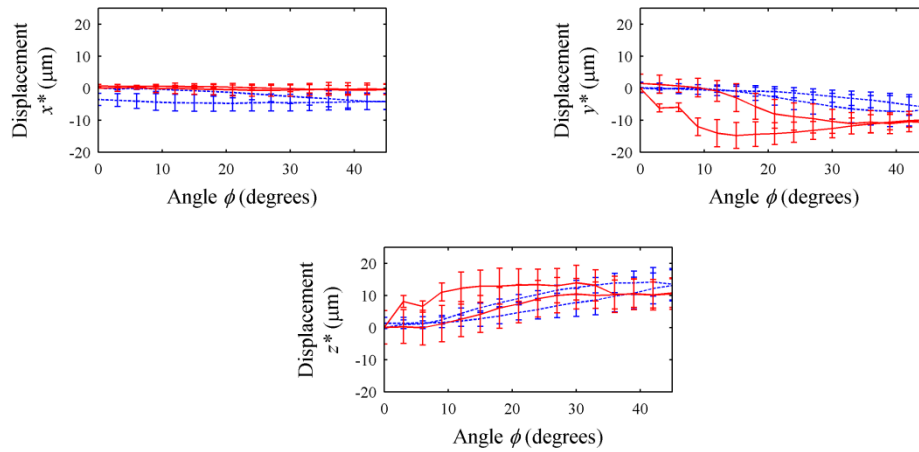


Figure 4.16: Bracket ARC motion (a) ARC x^* (b) ARC y^* (c) ARC z^* . Solid line indicates In-Ovation R bracket Dashed line indicates Damon 3MX bracket.

The calculated P -Values for the ARC of the two brackets are summarized Table 4.6. The In-Ovation R brackets demonstrated a sharp change in the y^* and z^* displacement of the ARC at 6° of archwire rotation as shown in Figure 4.16 (b) and (c). The change in the ARC is due to the interaction between the archwire and the retentive component. By contrast a distinct change in the retentive component was not observed for the Damon 3MX bracket. The difference in the ARC behavior is related to the design of the brackets

as shown in Figure 4.12. Damon 3MX is a passive-ligation bracket while the In-Ovation R is an active-ligation bracket. The sharp change in the In-Ovation R brackets occurs when the bevel of the archwire is no longer in contact with the ARC causing a sudden change in the y^* and z^* motion of the retentive component [29]. Table 4.6 shows that a significant difference exists for the motion of the ARC in the y^* and z^* directions for archwire rotation between 3 and 15° indicating that the initial ARC motion is affected by the design of the test bracket. The difference in the behavior of the two brackets is due to the compliance of the ARC as discussed by Pandis et al [30]. The In-Ovation R brackets have a more elastic retentive component while the Damon 3MX retentive component is more rigid.

Table 4.6: Comparison of orthodontic bracket ARC motion. Bolded values show significant differences.

Angle [°]	ARC x^* P -Value	ARC y^* P -Value	ARC z^* P -Value
0	1.000	1.000	1.000
3	1.000	0.008	0.008
6	0.421	0.008	0.008
9	1.000	0.008	0.008
12	0.548	0.008	0.008
15	0.421	0.008	0.008
18	0.548	0.008	0.095
21	0.421	0.008	0.310
24	0.310	0.016	0.421
27	0.310	0.016	1.000
30	0.222	0.032	0.690
33	0.151	0.151	1.000
36	0.151	0.310	0.421
39	0.056	0.222	0.222
42	0.056	0.222	0.222
45	0.032	0.310	0.421
45	0.032	0.056	0.222
42	0.032	0.095	0.222
39	0.032	0.032	1.000
36	0.032	0.016	1.000
33	0.016	0.016	0.690
30	0.016	0.016	0.421
27	0.016	0.016	0.310
24	0.008	0.032	0.421
21	0.008	0.016	0.548

18	0.008	0.151	0.690
15	0.008	0.690	1.000
12	0.008	1.000	1.000
9	0.008	1.000	0.421
6	0.008	1.000	0.421
3	0.008	1.000	0.310
0	0.008	1.000	0.222

Prior measurements of TW displacement have been limited to measuring bracket deformation in the x^* and y^* directions [6-9]. The addition of a second camera to the OTS allows for the measurement of the z^* displacement. Deformation of the orthodontic bracket was measured by post processing a sequence of stereo images collected using the OTS. Post processing of the image sequence was performed using the aforementioned 3D DIC method.

The image sequence in Figure 4.8 shows the archwire rotation between subsequent images. The change in light reflected by the archwire indicates archwire rotation in this image sequence. The motion of the ARC and widening of the bracket TWs can also be seen between Figure 4.8 (b) and (d). This motion is indicated by a widening in the bracket slot opening. The permanent deformation of the bracket slot could affect clinical treatment by increasing the amount of “play” or “slop” that exists between the archwire and the bracket slot [31]. Increased “play” between the bracket slot and archwire can affect treatment time since the desired force is not transmitted to the tooth [4].

The images shown in Figure 4.9 demonstrate that not only does the archwire engage the bracket slot sides but also engages the ARC. The lateral motion of the bracket TWs in the y^* direction and motion of the ARC in the z^* direction are the dominant displacement

vector directions. The image sequence in Figure 4.11 shows the difference in displacement vectors between the Damon 3MX and In-Ovation R brackets. It can be seen that the In-Ovation R bracket ARC exhibits greater displacement than the TWs. The In-Ovation R bracket ARC indicates motion at 12° archwire rotation, while the Damon bracket does not exhibit such motion at this wire angle. The difference in motion of the ARC is due to the difference in bracket design as shown in Figure 4.12. The difference between the design of the In-Ovation R and Damon 3MX brackets has been noted by Pandis et al. [30] and the author notes that the In-Ovation R bracket has an ARC that is more compliant than the Damon 3MX bracket design therefore it is expected that greater motion of the In-Ovation R retentive component should occur.

4.4 Conclusions

A novel method for measuring the three dimensional deformation of orthodontic brackets has been developed using a contact-free 3D DIC technique. Using this method it is possible to measure the bracket deformation in the x^*, y^* and z^* directions. This technique also shows the interaction between the archwire and the ARC. The repeatability of the OTS was evaluated and compared to the resolution of the 3D DIC method. As well, two self-ligating brackets were compared using the 3D DIC method; the method highlighted clear differences in the behavior of active and passive ligation brackets.

Orthodontic brackets that have been plastically deformed can affect treatment times since brackets are used for multiple archwire rotations and a bracket with altered TW geometry will not exert the anticipated force to a tooth. Understanding the 3D deformation of orthodontic brackets will help to reduce treatment times by better describing the relation between archwire deformation (x^*, y^*, z^*) and clinically applied archwire rotation (ϕ). The bracket images and 3D displacement vectors indicate that not only does the archwire

engage the two sides of the bracket slot, but also engages the ARC. This is indicated by the displacement vectors acting in the z^* direction. Engagement of the archwire in the bracket retentive component could affect treatment effectiveness since the archwire rotation applies a force to the retentive component instead of the expected force to the TWs leading to inefficient force couple transfer.

The bracket repeatability tests performed on a Damon 3MX bracket show that the dominant TW motion is in the y^* direction. The dominant motion for the ARC for this bracket was found to be in the z^* direction. The results from the 3D DIC method indicates substantial motion cannot be detected in the z^* direction for the bracket TWs showing that the additional displacement component gained by using a stereo microscope is not necessary for characterizing the TW motion. The additional displacement component gained using the 3D DIC method does show that motion of the ARC exists in the z^* direction. Therefore, characterization of the motion of the bracket TWs only requires a 2D DIC measurement system but a 3D DIC method is necessary to describe the motion of the ARC.

The ability to measure and visualize 3D deformation of orthodontic bracket will enable for the archwire-bracket interaction to be fully described. Understanding the 3D deformation of orthodontic brackets will also allow for the validation of a finite element model for the archwire-bracket interaction. Validation of a finite element model of the bracket-archwire interaction will lead to the investigation of loading conditions other than pure archwire rotation and other wire-bracket combinations that cannot be achieved using the OTS. .

Accurate measurement of the deformation of orthodontic brackets may reduce patient treatment times and improve the overall success of an orthodontic operation by providing

a helpful guide for orthodontists to select an appropriate amount of archwire adjustment for each treatment and lead to improved designs.

4.5 References

- [1] H. Gmyrek, C. Bourauel, G. Richter and W. Harzer, "Torque capacity of metal and plastic brackets with reference to materials, application, technology and biomechanics," *Journal of Orofacial Orthopedics*, vol. 63, pp. 113-128, 2002.
- [2] R. Sadat-Khonsari, A. Moshtaghy, V. Schlegel, B. Kahl-Nieke, M. Möller and O. Bauss, "Torque deformation characteristics of plastic brackets: A comparative study," *Journal of Orofacial Orthopedics*, vol. 65, pp. 26-33, 2004.
- [3] R. Kapur, P. K. Sinha and R. S. Nanda, "Comparison of load transmission and bracket deformation between titanium and stainless steel brackets." *Am. J. Orthod. Dentofacial Orthop.*, vol. 116, pp. 275-278, 1999.
- [4] D. A. Flores, L. K. Choi, J. M. Caruso, J. L. Tomlinson, G. E. Scott and M. T. Jeiroudi, "Deformation of metal brackets: a comparative study." *Angle Orthod.*, vol. 64, pp. 283-290, 1994.
- [5] J. C. Feldner, N. K. Sarkar, J. J. Sheridan and D. M. Lancaster, "In vitro torque-deformation characteristics of orthodontic polycarbonate brackets," *American Journal of Orthodontics and Dentofacial Orthopedics*, vol. 106, pp. 265-272, 9, 1994.
- [6] R. Lacoursiere, D. Nobes, D. Homeniuk, J. P. Carey, H. Badawi and P. W. Major. Measurement of orthodontic bracket TW elastic and plastic deformation by arch wire torque expression utilizing an optical image correlation technique. *Journal of Dental Biomechanics* vol. 2010(Article ID 397037), 2010.
- [7] T. W. Major, J. P. Carey, D. S. Nobes, G. Heo and P. W. Major, "Measurement of plastic and elastic deformation due to third-order torque in self-ligated orthodontic brackets," *Am. J. Orthod. Dentofacial Orthop.*, vol. 140, pp. 326-339, Sep, 2011.
- [8] T. W. Major, J. P. Carey, D. S. Nobes, G. Heo, G. W. Melenka and P. W. Major, "An investigation into the mechanical characteristics of select self-ligated brackets at a series of clinically relevant maximum torquing angles: loading and unloading curves and bracket deformation," *Eur. J. Orthod.*, Jul 12, 2011.
- [9] G. W. Melenka, R. A. Lacoursiere, J. P. Carey, D. S. Nobes, G. Heo and P. W. Major, "Comparison of deformation and torque expression of the orthos and orthos Ti bracket systems," *Eur. J. Orthod.*, Oct 19, 2011.

- [10] M. A. Sutton, J. J. Orteu and H. W. Schreier, *Image Correlation for Shape, Motion and Deformation Measurements : Basic Concepts, Theory and Applications*. New York, N.Y: Springer, 2009.
- [11] H. M. Badawi, R. W. Toogood, J. P. R. Carey, G. Heo and P. W. Major, "Torque expression of self-ligating brackets," *American Journal of Orthodontics and Dentofacial Orthopedics*, vol. 133, pp. 721-728, 2008.
- [12] T. C. Chu, W. F. Ranson and M. A. Sutton, "Applications of digital-image-correlation techniques to experimental mechanics," *Exp. Mech.*, vol. 25, pp. 232-244, 1985.
- [13] B. Pan, K. Qian, H. Xie and A. Asundi, "Two-dimensional digital image correlation for in-plane displacement and strain measurement: A review," *Meas Sci Technol*, vol. 20, 2009.
- [14] H. A. Bruck, S. R. McNeill, M. A. Sutton and W. H. Peters III, "Digital image correlation using Newton-Raphson method of partial differential correction," *Exp. Mech.*, vol. 29, pp. 261-267, 1989.
- [15] LaVision GmbH, "Product-Manual for DaVis 7.2 StrainMaster Software Item-Number(s): 1105022," 2006.
- [16] D. Garcia, J. J. Orteu and L. Penazzi, "A combined temporal tracking and stereo-correlation technique for accurate measurement of 3D displacements: Application to sheet metal forming," *J. Mater. Process. Technol.*, vol. 125-126, pp. 736-742, 2002.
- [17] J. -. Orteu, "3-D computer vision in experimental mechanics," *Opt Lasers Eng*, vol. 47, pp. 282-291, 2009.
- [18] LaVision GmbH, "Imager Intense & FlowMaster3 Item-Number(s) 1101024, 1101030," 2007.
- [19] T. A. Berfield, J. K. Patel, R. G. Shimmin, P. V. Braun, J. Lambros and N. R. Sottos, "Micro-and nanoscale deformation measurement of surface and internal planes via digital image correlation," *Exp. Mech.*, vol. 47, pp. 51-62, 2007.
- [20] P. F. Luo, Y. J. Chao, M. A. Sutton and W. H. Peters III, "Accurate measurement of three-dimensional deformations in deformable and rigid bodies using computer vision," *Exp. Mech.*, vol. 33, pp. 123-132, 1993.
- [21] B. Pan, H. Xie, L. Yang and Z. Wang, "Accurate measurement of satellite antenna surface using 3D digital image correlation technique," *Strain*, vol. 45, pp. 194-200, 2009.
- [22] P. F. Luo, Y. J. Chao, M. A. Sutton and W. H. Peters III, "Accurate measurement of three-dimensional deformations in deformable and rigid bodies using computer vision," *Exp. Mech.*, vol. 33, pp. 123-132, 1993.

- [23] H. Schreier, D. Garcia and M. Sutton, "Advances in light microscope stereo vision," *Experimental Mechanics*, vol. 44, pp. 278-288, 2004.
- [24] S. M. Soloff, R. J. Adrian and Z. - Liu, "Distortion compensation for generalized stereoscopic particle image velocimetry," *Measurement Science and Technology*, vol. 8, pp. 1441-1454, 1997.
- [25] H. Haddadi and S. Belhabib, "Use of rigid-body motion for the investigation and estimation of the measurement errors related to digital image correlation technique," *Optics and Lasers in Engineering*, vol. 46, pp. 185-196, 2008.
- [26] N. J. Lawson and J. Wu, "Three-dimensional particle image velocimetry: Experimental error analysis of a digital angular stereoscopic system," *Measurement Science and Technology*, vol. 8, pp. 1455-1464, 1997.
- [27] N. J. Lawson and J. Wu, "Three-dimensional particle image velocimetry: Error analysis of stereoscopic techniques," *Measurement Science and Technology*, vol. 8, pp. 894-900, 1997.
- [28] T. D. Creekmore and R. L. Kunik, "Straight wire: the next generation." *Am. J. Orthod. Dentofacial Orthop.*, vol. 104, pp. 8-20, 1993.
- [29] N. W. Harradine, "Self-ligating brackets: where are we now?" *J. Orthod.*, vol. 30, pp. 262-273, 2003.
- [30] N. Pandis, T. Eliades, S. Partowi and C. Bourauel, "Moments generated during simulated rotational correction with self-ligating and conventional brackets," *Angle Orthod.*, vol. 78, pp. 1030-1034, 2008.
- [31] M. M. McKnight, S. P. Jones and E. H. Davies, "A study to compare the effects of simulated torquing forces on pre-adjusted orthodontic brackets." *Br. J. Orthod.*, vol. 21, pp. 359-365, 1994.

Chapter 5 Three-Dimensional Comparison of Self-Ligating

Brackets

A version of this chapter will be submitted as:

Melenka G.W., Nobes, D.S., Carey, J.P., Major, P.W., Three Dimensional Comparison of Self-Ligating Brackets, American Journal of Orthodontics and Dentofacial Orthopedics

5.1 Introduction

The measurement of bracket TW deformation using a single camera is limited to only measuring two-dimensional (2D) of the brackets. Major et al. [1] compared the 2D deformation of three self-ligating brackets and determined that In-Ovation R plastically deform less than Speed and Damon Q brackets for a maximum torquing angle of 63°. Orthodontic brackets and archwires move and interact in three dimensions (3D) therefore it is necessary to determine if significant deformation of the orthodontic brackets occurs in all three-dimensions. The addition of a second camera will allow for the 3D deformation of the orthodontic brackets to be measured using a 3D DIC technique [2-5] to demonstrate if significant deformation in all 3 directions exists. The ability to measure 3D deformation of orthodontic bracket will enable for the archwire-bracket interaction to be fully described.

The addition of a second camera to the OTS measurement system will also allow for the motion of the movable component used to secure the archwire of self-ligating brackets to be measured [6, 7]. The movable component used to secure the archwire is often referred to as a spring clip or slide depending on the bracket design [8, 9] but for the remainder of this discussion the movable component will be referred to as the archwire retentive component (ARC). Measurement of the ARC motion will allow for comparison of active and passive ligation brackets designs. Currently the motion of the ARC has not been

evaluated to determine if compliance of active and passive ligation ARC designs can affect treatment [9-11]. The goal of this study is to examine the deformation of self-ligating brackets in three dimensions using the 3D DIC version of the OTS and the motion of the ARC. Active and passive self-ligating bracket will be compared to address the wide range of claims on the advantages and disadvantages of active and passive self-ligating bracket design [9, 12]. A repeatable and standardized method of evaluating bracket designs will be described and will be used to illustrate the differences in active and passive ligation brackets.

5.2 Methods and Materials

A schematic of a tooth, self-ligating bracket and archwire is shown in Figure 5.1. Figure 5.1 (a) and (b) shows the coordinate system assigned to the bracket (x^* , y^* , z^*) where the x^* axis is defined as parallel to the archwire, the y^* axis is defined as the direction of lateral motion of the bracket TWs due to archwire rotation and the z^* axis defines the direction from the base of the orthodontic bracket to the top of the bracket TWs. This coordinate system will be used to quantify the deformation that occurs to the bracket due to archwire rotation. Archwire rotation occurs about the x^* axis and the angle of archwire rotation is defined as ϕ . The angle of archwire rotation, ϕ , is shown in Figure 5.1 (c). The neutral position of the archwire is defined as when the archwire is parallel to the base of the bracket slot in Figure 5.1 (c). Orthodontic brackets will be tested with archwire rotation occurring in the clockwise direction as shown in Figure 5.1 (b). This motion is commonly used in orthodontics to control the labial (towards the lip of the mouth) root angle of the maxillary incisors.

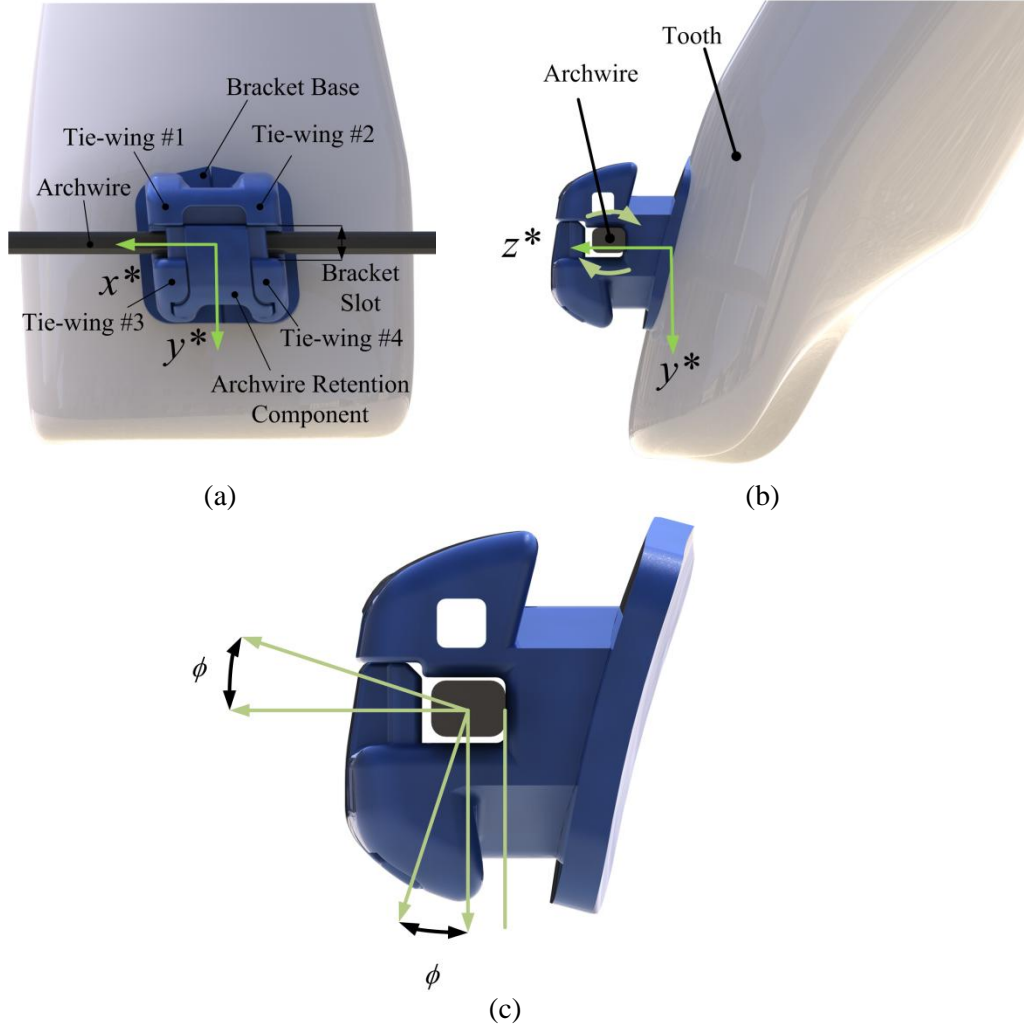


Figure 5.1: Self-ligating orthodontic bracket components (a) Top view of bracket showing TWs, archwire and bracket base (b) Side view of bracket showing the angle of the bracket slot (prescription). Archwire rotation occurs about the x^* axis of the bracket coordinate system. (c) Control of tooth angulations using archwire rotation (d) Archwire rotation, ϕ .

Archwires are maintained in the bracket slot using two main methods: elastomeric or steel ligatures, or self-ligating brackets. Self-ligating brackets are advantageous as the archwire can be ligated in the bracket slot more quickly than conventional elastic or steel ligation [9, 10]. As well, the ARC is not prone to degradation like elastic ligatures due to the temperature and chemical environment within the mouth [10]. Active and passive self-ligating brackets will be compared using the 3D OTS to show the 3D motion of the bracket TWs and the motion of the ARC.

Top and side images of three orthodontic brackets are shown in Figure 5.2 to demonstrate the difference between active and passive ligation bracket designs. These images show the irregular geometries of these particular self-ligating brackets. The brackets shown are Damon Q (Ormco Corporation, Orange, California, USA), Speed (Strite Industries, Cambridge, Ontario, Canada), and In-Ovation R (GAC, Bohemia, NY, USA) self-ligating brackets. The In-Ovation R and Speed brackets are active ligation brackets while the Damon Q is a passive ligation bracket. Active ligation brackets are designed with a curved leaf spring type ARC which applies force to the archwire [13]. The ARC for active ligation brackets encroaches in the bracket slot to maintain contact with the archwire [13]. The material properties of the ARC will vary depending on bracket design and manufacturer. The Damon Q and the In-Ovation R brackets are manufactured with a stainless steel ARC while the Speed bracket ARC is nickel-titanium [13]. Interaction between the ARC and archwire may be affected by the ARC material properties. Contact between the archwire and ARC will help to maintain the alignment of the wire in the brackets slot. A disadvantage of the active ligation brackets is the possibility of reduced torque transmitted to the tooth due to reduced gingival slot wall depth to allow for the elastic ARC to secure the archwire in the bracket slot [9]. The curved leaf spring ARC is shown in the side images of the In-Ovation R and Speed brackets. Passive ligation brackets have a more rigid ARC that does not maintain contact with the archwire [13].

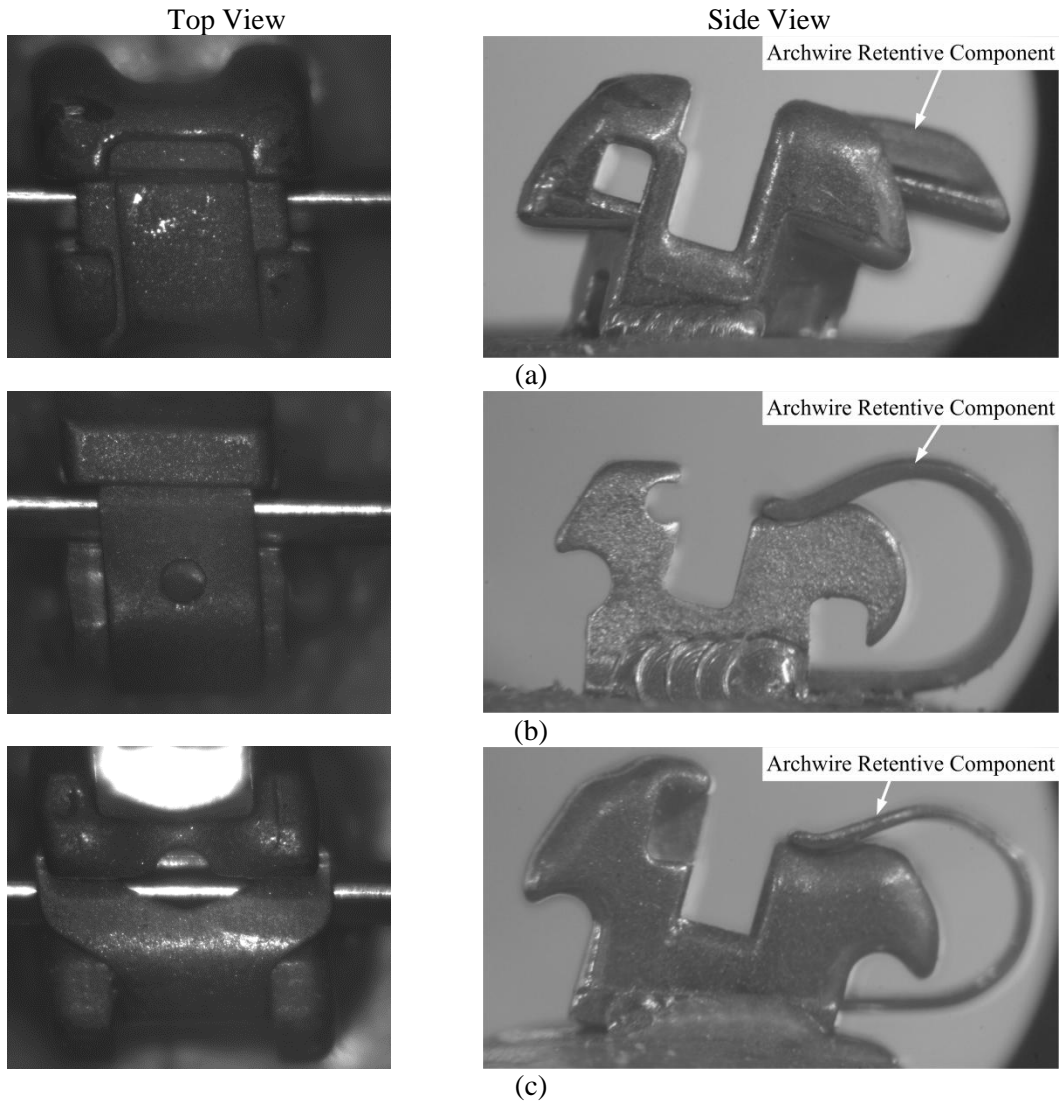


Figure 5.2: Top and side views of self-ligating orthodontic brackets (a) Damon Q (b) Speed (c) Innovation R

A comparison of active and passive ligation brackets is shown in Figure 5.3. Figure 5.3 (a) shows that there is clearance between the archwire and the ARC for the Damon Q bracket while in Figure 5.3 (b) the ARC is in contact with the archwire.

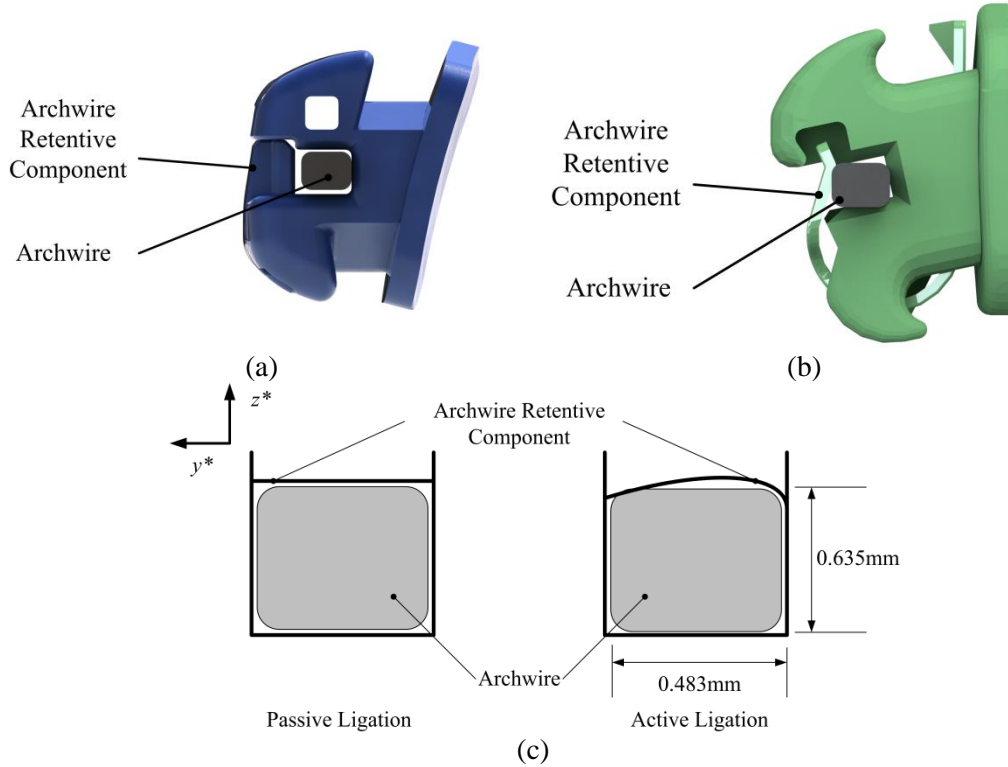


Figure 5.3: Comparison of self-ligating brackets (a) passive ligation Damon Q (solid model provided byOrmco) (b) In-Ovation R (solid model provided by GAC) active ligation applies a preload to the wire. (c) schematic of passive and active ligation brackets

The 3D deformation of orthodontic brackets was measured using a modified version of the OTS [14, 15]. The 3D DIC measurement version of the OTS is shown in Figure 5.4. A computer controlled stepper motion (Cool Muscle CM1-C-11L30, Myostat Motion Control Inc., Newmarket, ON, Canada) and gear box rotates the archwire in the bracket. Two dies, that clamp the archwire, are mechanically locked together by a yoke provide support to the archwire and even rotation from both sides. Also shown in this figure is the 6-axis load cell (Nano17 SI-25-0.25, ATI Industrial Automation, Apex, NC, USA) used to collect force and moment data applied to an orthodontic bracket due to archwire rotation. Control of the OTS stepper motor, acquisition of data from the load cell and image acquisition is automated using custom designed software (LabWindows/ CVI, National Instruments, Austin TX). The complete details of the OTS design and description of the archwire rotation mechanism is described by [1, 14-17].

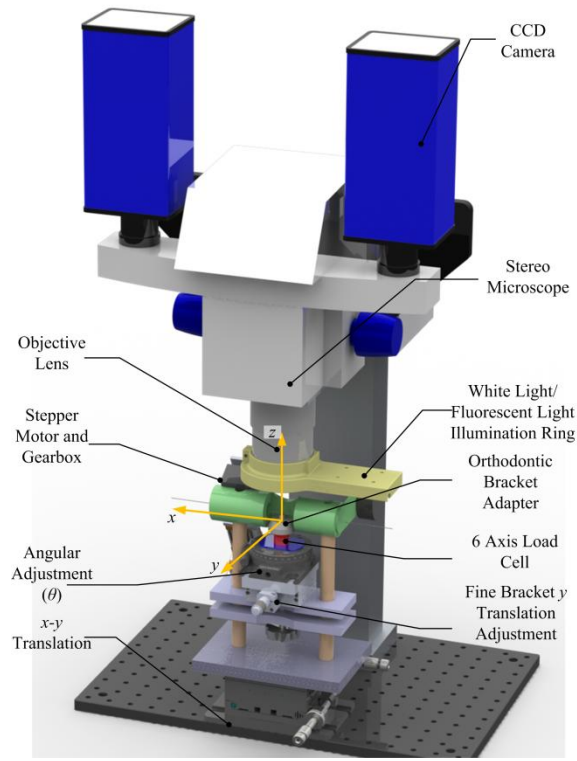


Figure 5.4: Orthodontic Torque Simulator

The image acquisition system shown in Figure 5.4 collects images of orthodontic brackets using a stereo microscope (Zeiss SteREO Discovery v8 microscope Carl Zeiss Micro Imaging GmbH Göttingen, Germany) with a 60mm working distance objective lens (1.0X Zeiss V8 Plan Apo Objective Lens, Zeiss MicroImaging GmbH Göttingen, Germany). Images were collected using two CCD cameras (Imager Intense, LaVision GmbH, Göttingen, Germany) at 1376×1040 pixels and 12-bit resolution. The cameras were connected to the stereo microscope using an intermediate phototube (Intermediate Phototube S 50:50 ports, Zeiss MicroImaging GmbH Göttingen, Germany). The brackets were imaged at 2.0x magnification to maximize the bracket in the camera field of view. Test specimens were illuminated using a ring light (2.64" Ring Light, Variable Frequency, Edmund Optics, Barrington, NJ, USA) and a 365nm black-light (Black

(365nm Peak) Replacement Bulb, Edmund Optics, Barrington, NJ, USA) to provide even illumination across the field of view.

A stainless steel bracket cylinder with a 9.0mm nominal diameter was used as an analog for a tooth as described by Badawi et al. [14] and the brackets were mounted to the cylinder using an epoxy (Loctite E-20HP; Hysol, Henkel, Rocky Hill, Conn.). Cylinders were used to transmit the loads applied to the orthodontic bracket by the archwire to a 6-axis load cell and to allow for free rotation of the archwire in the bracket slot.

Images collected using the OTS were acquired and post processed using a commercial software package (StrainMaster 3D, LaVision GmbH DaVis 8.06. Gottingen, Germany, 2009). Image subsets, or window size, used to determine the 3D displacement of the brackets were 64x64 pixels as a compromise between vector precision and maximization of the number of interrogation windows for each TW [18]. The field of view for the brackets was 1376 x 1040 pixels or 4.25 x 3.2 mm therefore the resolution for this camera setup with a 64x64 subset size will be 0.07 μ m [18].

DIC displacement measurement comprises of four consecutive steps (1) specimen preparation (2) calibration of the imaging system for a defined field-of-view (3) collection of specimen deformation before and after loading, and (4) post processing of images to determine displacement or strain [19]. The complete experimental procedure for testing and post-processing the orthodontic brackets is described in detail in Appendix C. A specimen is prepared by applying a random pattern to the object surface. Images are calibrated to convert from pixels to physical space (e.g. mm, inches) by acquiring an image of a target with a grid of known spacing. Each digital image is segmented into evenly spaced subsets and an image correlation algorithm is performed for each image subset. Deformation is measured by tracking contrast features on the specimen surface

between subsequent images. The displacement of a subset is determined by maximizing a cross-correlation equation for the images collected before and after deformation [19, 20].

Orthodontic brackets were prepared prior to testing by coating the surface of the bracket with fluorescent airbrush paint (5404 Fluorescent Green Createx Airbrush Colors, Createx Colors, East Granby CT). The speckle pattern was applied using an airbrush (Custom Micron B, Iwata Medea Inc. Portland OR). The paint was reduced at a ratio of approximately 2:1 to improve the flow of the paint through an airbrush (Wicked W100 Reducer Createx Airbrush Colors, Createx Colors, East Granby CT). Fluorescent paint was chosen for the speckle pattern to reduce reflection from the metallic bracket surfaces which can introduce errors in the DIC image processing. The use of an airbrush and fluorescent particles for DIC was described by Berfield et al. [21]. Previously, bracket deformation measurements have used a micro-etcher to produce a random speckle pattern on the bracket surface [7-9] but the fluorescent paint allows for a speckle pattern to be produced on the surface of the brackets without affecting the material properties of the bracket.

Deformation of the bracket will be assessed by determining the relative motion between the four bracket TWs shown in Figure 4.6. Figure 4.6 shows the bracket TW and ARC regions for the Damon Q, In-Ovation R and Speed brackets. The displacement vector fields generated using the 3D DIC software were further processed using a custom code to determine the motion of the bracket TWs and ARC (MATLAB, 2009a, The MathWorks Inc., Natick, MA, U.S.A.). Figure 4.6 also shows the 64x64 pixel subset which was used for the measurement of the 3D displacement of the bracket. Equation (4.3 details the calculation of the bracket displacement in the x^* , y^* and z^* directions. In this equation $\overline{D_{TWing}}$ denotes the average displacement of the defined regions for TWs

1,2,3, and 4 for the $i=x^*,y^*,z^*$ directions. LHS_D is the displacement between TWs 1 and 3 while RHS_D is the displacement between TWs 2 and 4.

$$\begin{aligned} LHS_{D_i} &= \left[\overline{D_{TieWIng1}} - \overline{D_{TieWIng3}} \right]_i \\ RHS_{D_i} &= \left[\overline{D_{TieWIng2}} - \overline{D_{TieWIng4}} \right]_i \end{aligned} \quad (5.1)$$

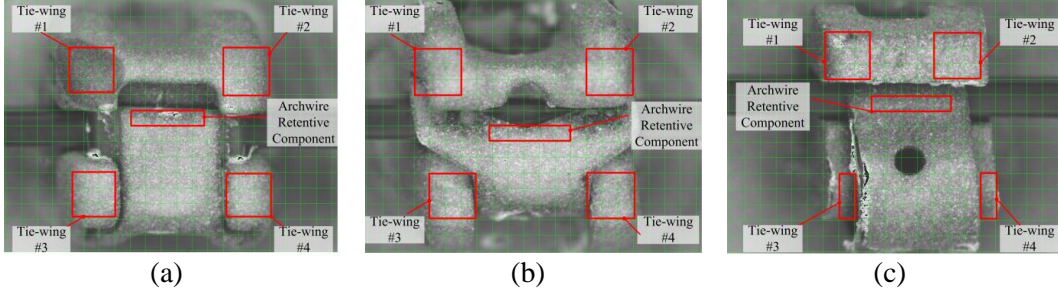


Figure 5.5: Orthodontic bracket box regions used to track TW motion (a) Damon Q (b) In-Ovation R (c) Speed

In addition, the motion of the bracket ARC in the $i=x^*,y^*,z^*$ directions was measured. Bulk motion of the entire bracket was eliminated to find the relative motion of the ARC by subtracting the average displacement of the TWs from the motion of the bracket retentive component. The relative ARC motion is denoted as $RelativeARC_i$ and the retentive component motion is denoted as ARC_i as shown in Equation (5.2).

$$RelativeARC_i = ARC_i - \left[\frac{1}{4} \sum_{j=1}^4 \overline{D_{TieWIng_j}} \right]_i \quad (5.2)$$

Three self-ligating orthodontic brackets were used in this study. A total of 30 brackets were tested, ten Damon Q (Ormco Corporation, Orange, California, USA) and 10 In-Ovation R (GAC, Bohemia, NY, USA) brackets and 10 Speed (Strite Industries, Cambridge, Ontario, Canada). All brackets are maxillary right incisor (U1R) with a nominal slot width of 0.5588mm(0.022"). All brackets were selected to have comparable medium torque prescriptions. The Damon Q brackets have a prescription of 15° torque, 5° angle and 0° rotation while the Speed and In-Ovation brackets have a prescription of

17° torque, 5° angle and 0° rotation. The archwire (Ormco, Orange, California, USA) used for this investigation had a 0.483 x 0.635mm (0.019 x 0.025”) cross section.

Using the automated OTS software the angle of the archwire, ϕ , was rotated in 3° increments to a maximum angle of 45°. Once the maximum angle was reached the archwire was returned to the original position in 3° increments. At each increment a pair of stereo images of the orthodontic bracket was collected resulting in thirty-two (32) image pairs collected. The stereo image sequence was used to measure the 3D deformation of the bracket due to archwire rotation by post processing the images using the previously described 3D DIC method. Deformation of the orthodontic bracket and the 3D displacement vectors were visualized using a scientific visualization software package (ParaView, Kitware, Inc. Clifton Park, New York). The visualization software package was used to view the result of the bracket-archwire interaction in three dimensions. The process for creating 3D surface images using ParaView is described in Appendix D.

Example images collected of a Damon Q bracket are shown in

. The sequence shows increasing archwire rotations (ϕ) of 0°, 21°, and 45° as well as decreasing archwire rotation of 21° and 0°. The image sequence shows a number of features that materialize for archwire rotation in the bracket slot. These features include the changing aspect of the archwire due to rotation and the widening of the gap between the ARC and the top TWs (as shown in the image) which is a result of the widening of the bracket slot due to applied torque. Image sequences, like the one shown in , will be post-processed using the LaVision 3D DIC software in order to determine the 3D motion of the bracket TWs and ARC.

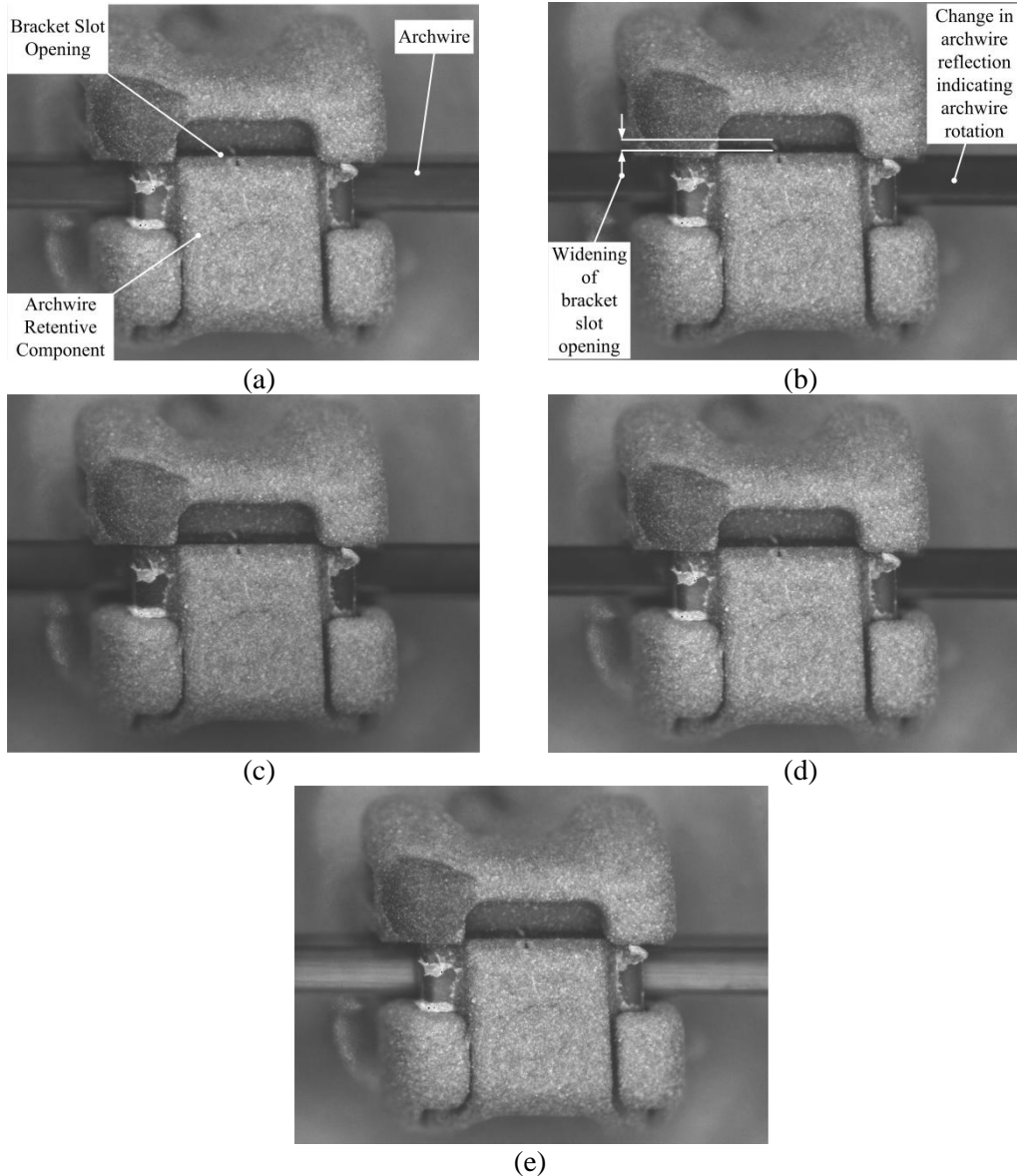


Figure 5.6: Damon Q orthodontic bracket deformation due to archwire rotation (ϕ) (a) increasing 0° (b) increasing 21° (c) increasing 45° (d) decreasing 21° (e) decreasing 0° .

Images of self-ligating brackets collected using the stereo-microscope version of the OTS are shown in Figure 5.7. Also shown are the 3D surfaces generated from the 3D DIC measurement method for comparison. The ParaView surfaces will be used to visualize the motion of the brackets. Figure 5.7 shows that the 3D bracket geometry can be reconstructed from stereo images pairs collected using the 3D OTS.

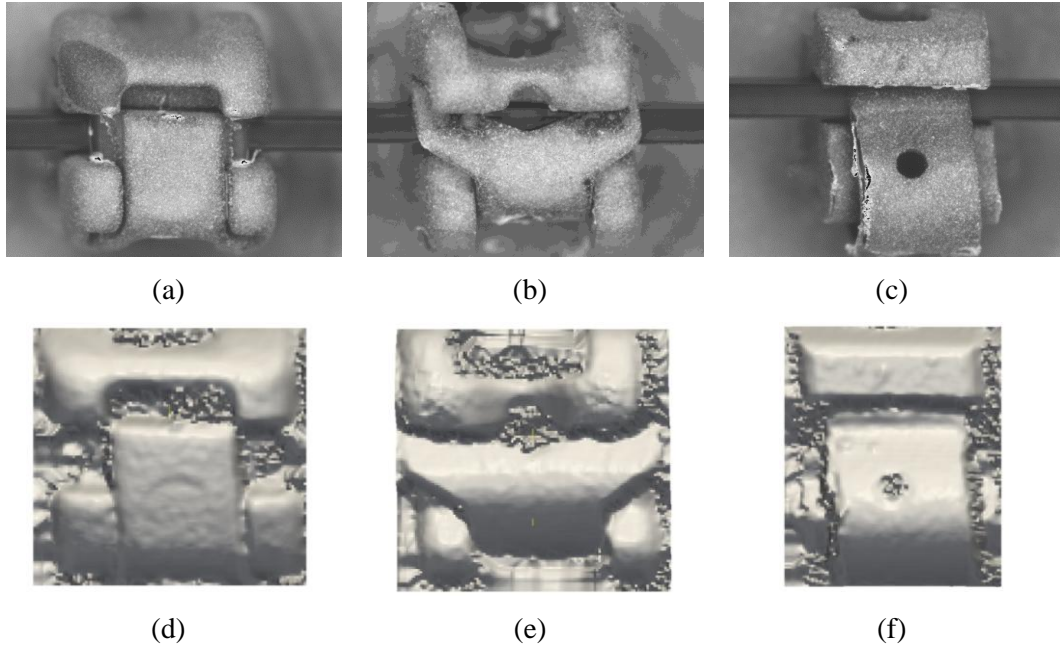


Figure 5.7: Orthodontic bracket 3D surfaces (a) Damon Q (b) In-Ovation R (c) Speed (d) Damon Q 3D Surface (e) In-Ovation R 3D surface (f) Speed 3D surface.

The original image and 3D surface of an In-Ovation R bracket are compared in Figure 5.8. Three regions are highlighted (a,b,c) in this figure. The highlighted regions indicate where the bracket image is out-of-focus. The out-of-focus regions from the original bracket image result in uneven surfaces in the 3D images shown in Figure 5.8 (b). Regions a and c correspond to the out-of-focus bracket base and region b corresponds to the archwire. The uneven surface in region b occurs since a speckle pattern was not applied to the archwire; therefore no DIC displacement or surface data can be obtained from this region. The regions a,b,c in Figure 5.8 will not be evaluated to determine bracket deformation.

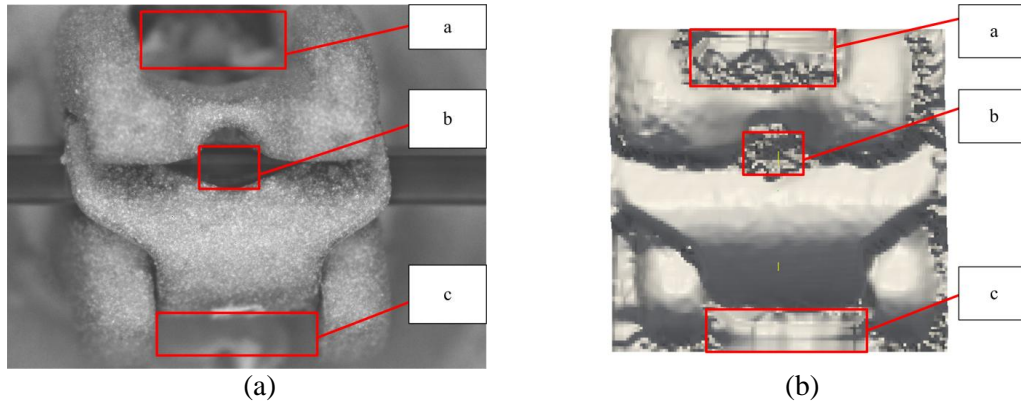


Figure 5.8: In-Ovation R bracket image and 3D surface comparison (a) original bracket image (b) 3D surface

The bracket deformation results collected using the 3D OTS will be compared using a Mann-Whitney U nonparametric test (ranksum function, Statistics Toolbox, MATLAB, 2009a, The MathWorks, Natick, MA, U.S.A.) to determine if a statistically significant difference can be found between the brackets. The test was selected due to the small sample size for each bracket. A *P*-value of less than 0.05 is the criteria that will indicate if a statistical difference exists between the two brackets.

5.3 Results

Representative image sequences of the Damon Q, In-Ovation R and Speed brackets will be compared to visualize 3D bracket deformation due to archwire rotation. A sequence of images of a Damon Q bracket is shown in Figure 5.9 for selected angles as the archwire was progressively rotated from 0 to 45° in 3° increments. The change in wire angle can be seen in each successive image.

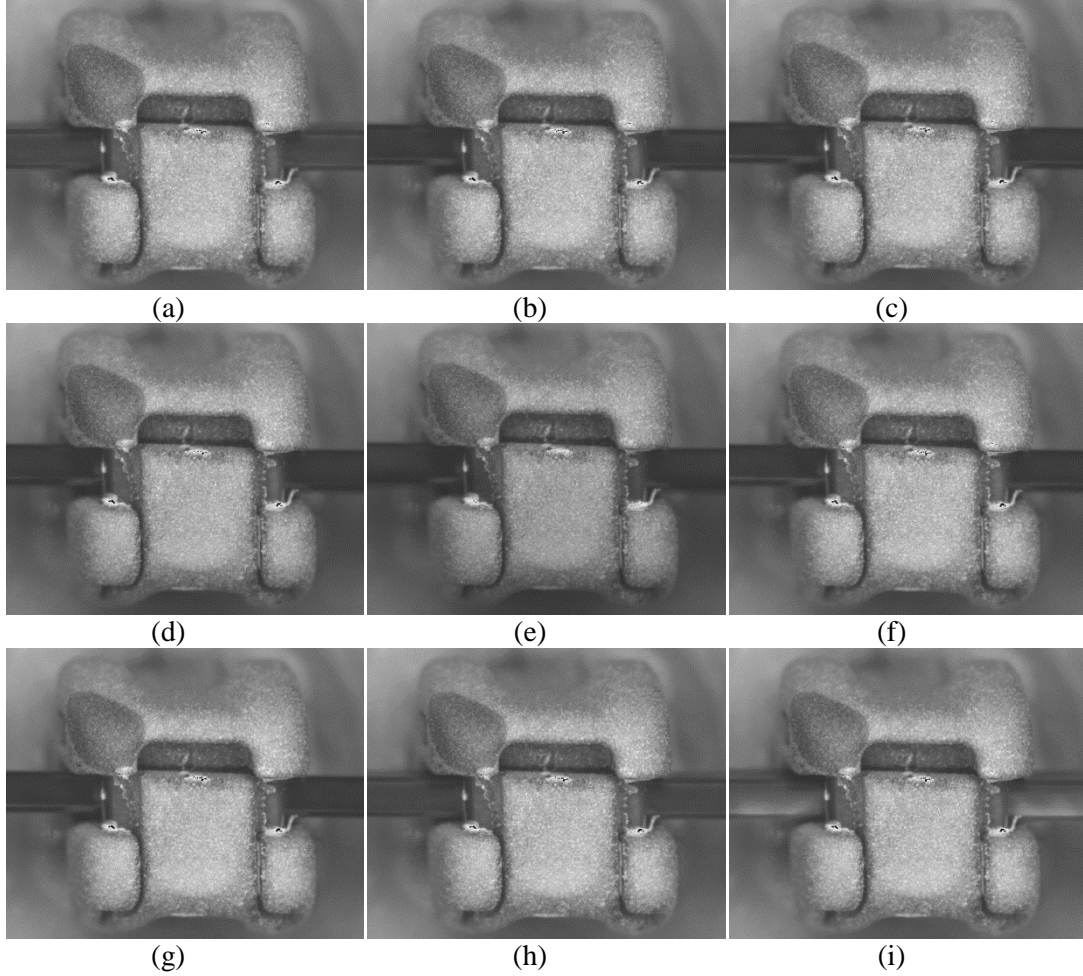


Figure 5.9: Damon Q image sequence demonstrating increasing and decreasing archwire rotation for selected archwire angles (a) 0° (b) 9° (c) 21° (d) 33° (e) 45° (f) -33° (g) -21° (h) -9° (i) -0°.

The same image sequence shown in Figure 5.9 was processed using the 3D DIC method and then visualized using 3D. The image sequences in Figure 5.10, Figure 5.11 and Figure 5.12 show the displacement field in the x^* , y^* and z^* directions. In these sequences red indicates maximum deformation while green indicates zero deformation. These figures show that the maximum displacement of occurred at a wire rotation of 45°. The image sequence also shows the increase and decrease in TW motion as the wire is rotated to a maximum angle of 45° and then returned to the origin. The original image sequences in Figure 5.9 and 3D surfaces in Figure 5.10, Figure 5.11 and Figure 5.12 show that images collected using the 3D OTS can be collected and processed to visualize bracket deformation due to archwire rotation.

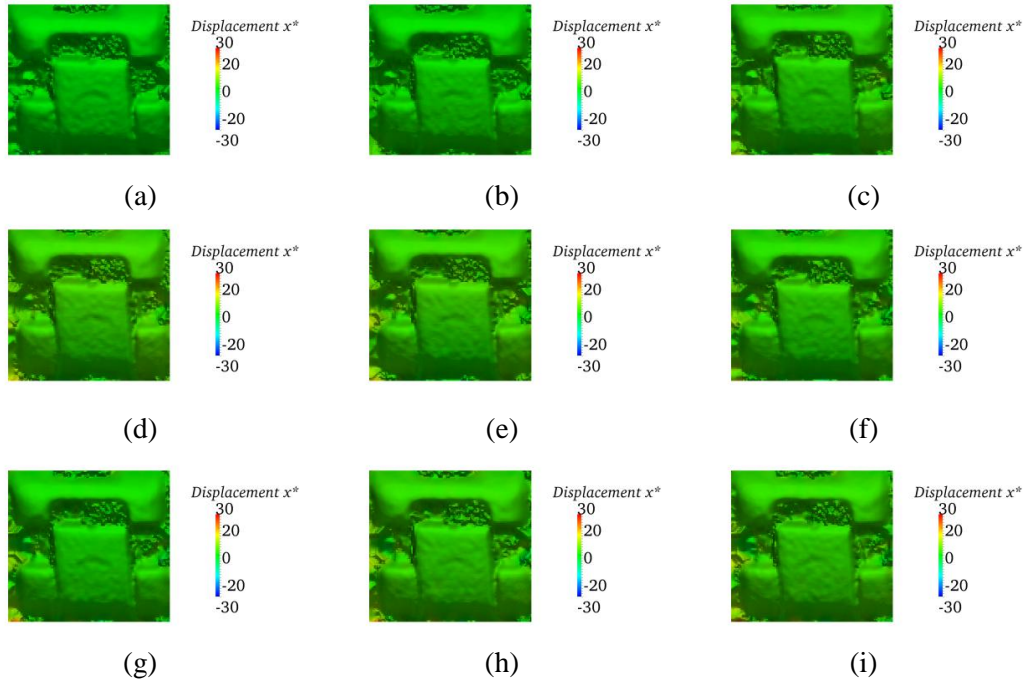


Figure 5.10: Damon Q 3D image sequence x^* displacement (a) 0° (b) 9° (c) 21° (d) 33° (e) 45° (f) -33° (g) -21° (h) -9° (i) -0° . Displacement measured in micrometers (μm). Minimal motion occurred in the x^* direction for the Damon Q TWs or ARC as indicated by no change in the 3D bracket contour plot sequence.

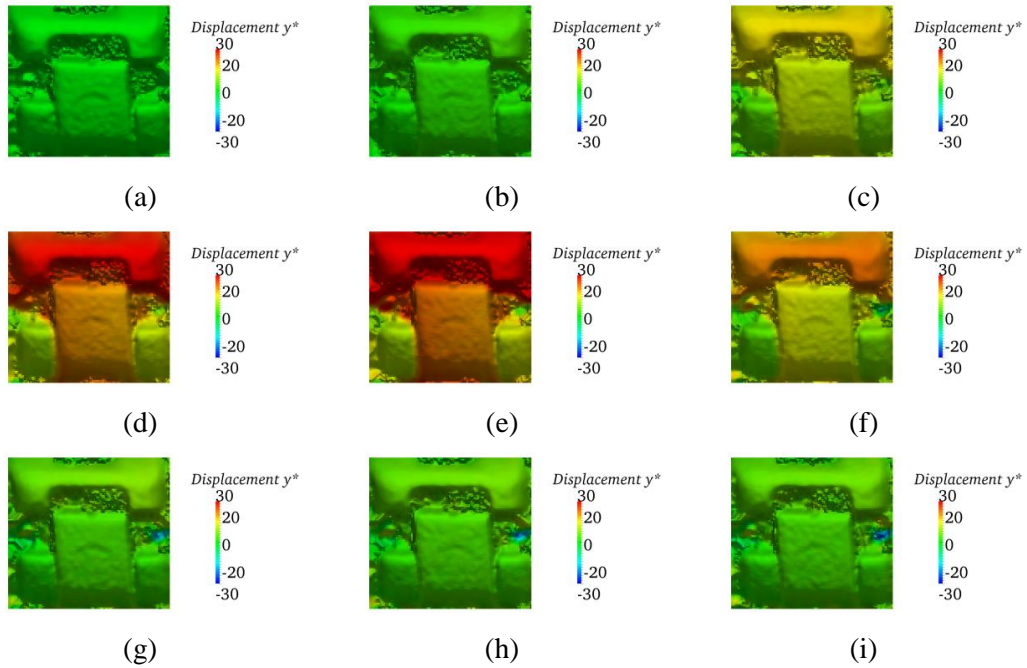


Figure 5.11: Damon Q 3D image sequence y^* displacement (a) 0° (b) 9° (c) 21° (d) 33° (e) 45° (f) -33° (g) -21° (h) -9° (i) -0° . Displacement measured in micrometers (μm). The dominant motion occurs for tie-wings #1 and #2 in this image sequence.

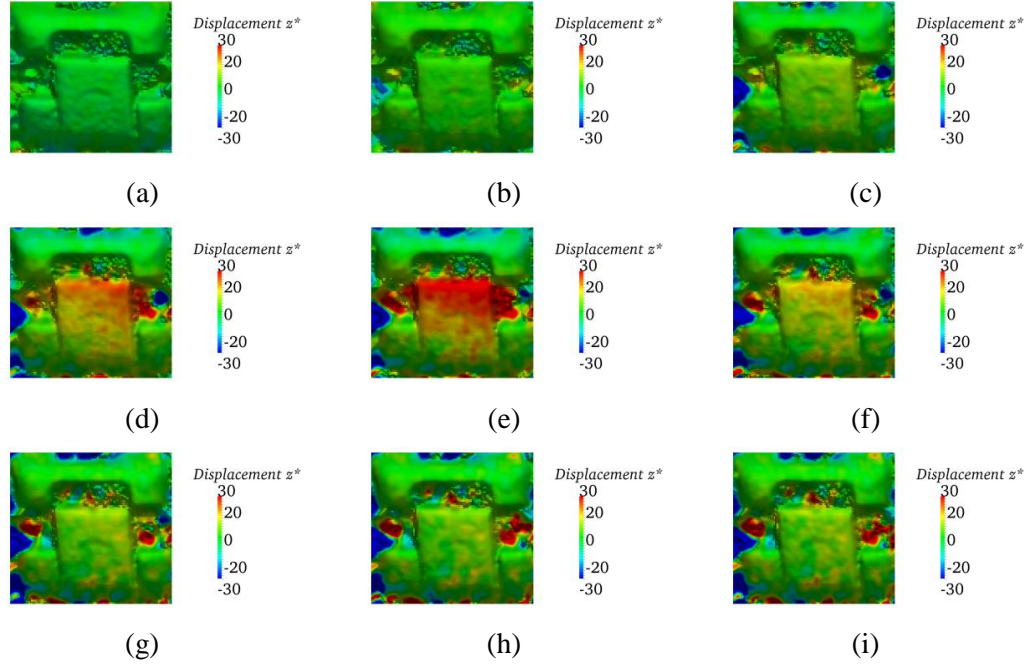


Figure 5.12: Damon Q 3D image sequence z^* displacement (a) 0° (b) 9° (c) 21° (d) 33° (e) 45° (f) -33° (g) -21° (h) -9° (i) -0° . Displacement measured in micrometers (μm). Maximum motion for the ARC can be seen at 45° of archwire rotation.

Similarly, an image sequence of a typical In-Ovation R bracket is shown in Figure 5.13.

The corresponding 3D surface and deformation of the In-Ovation R bracket is shown in Figure 5.14, Figure 5.15, and Figure 5.16. The image sequences again indicate that the maximum displacement occurred for a wire rotation of 45° .

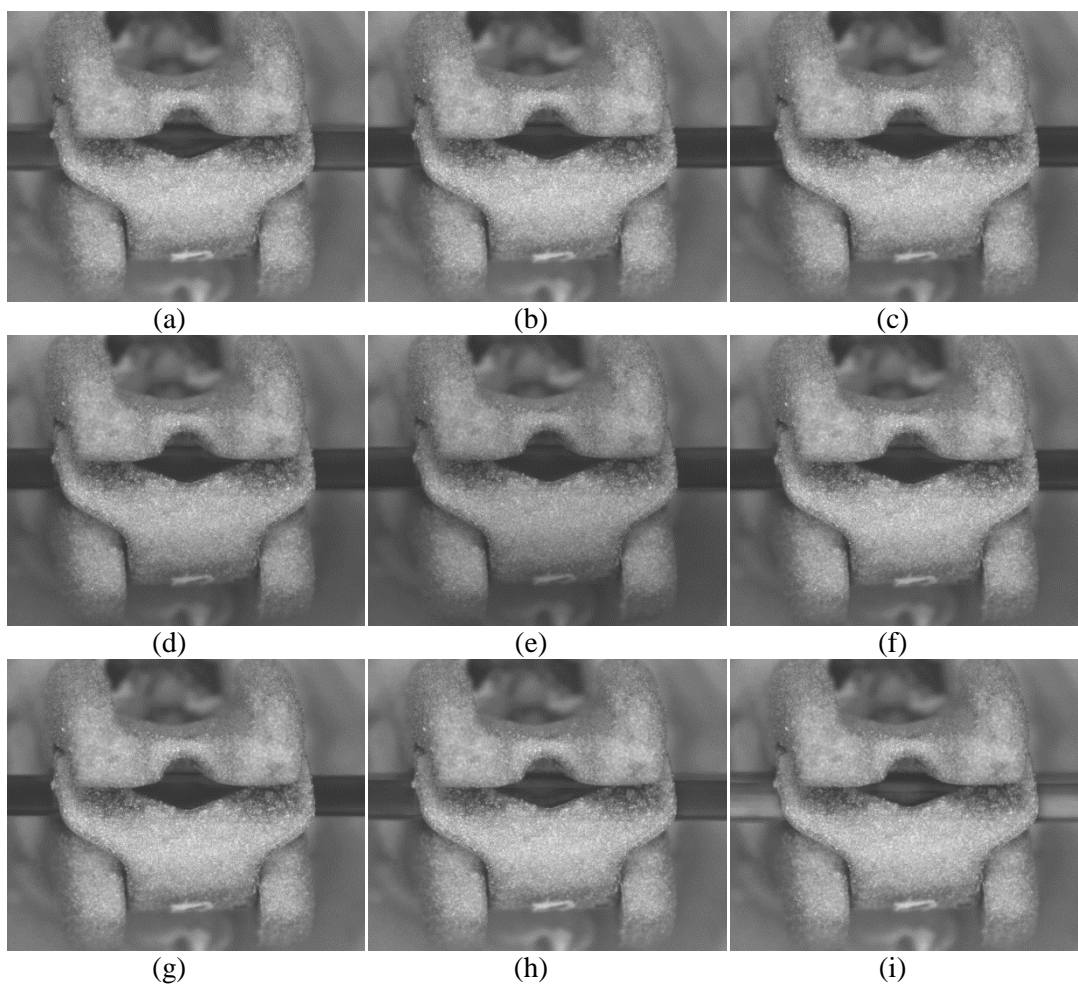


Figure 5.13: In-Ovation R image sequence demonstrating increasing and decreasing archwire rotation for selected archwire angles (a) 0° (b) 9° (c) 21° (d) 33° (e) 45° (f) -33° (g) -21° (h) -9° (i) -0°

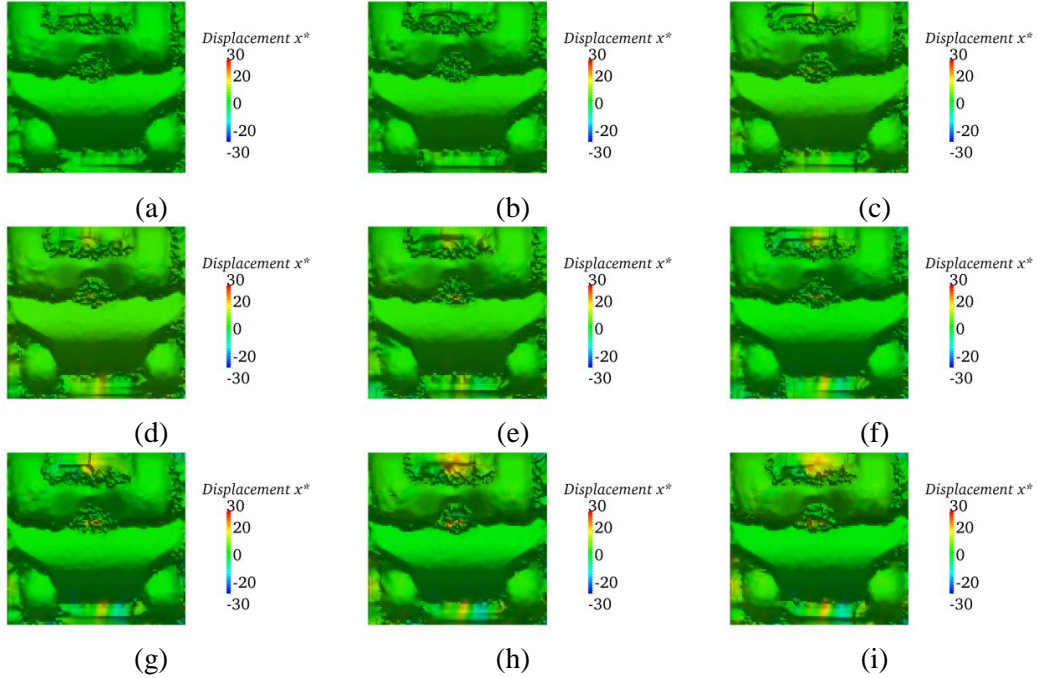


Figure 5.14: In-Ovation R 3D image sequence x^* displacement (a) 0° (b) 9° (c) 21° (d) 33° (e) 45° (f) -33° (g) -21° (h) -9° (i) -0° . Displacement measured in micrometers (μm). Minimal motion occurred in the x^* direction for the In-Ovation R TWs or ARC as indicated by no change in the 3D bracket contour plot sequence.

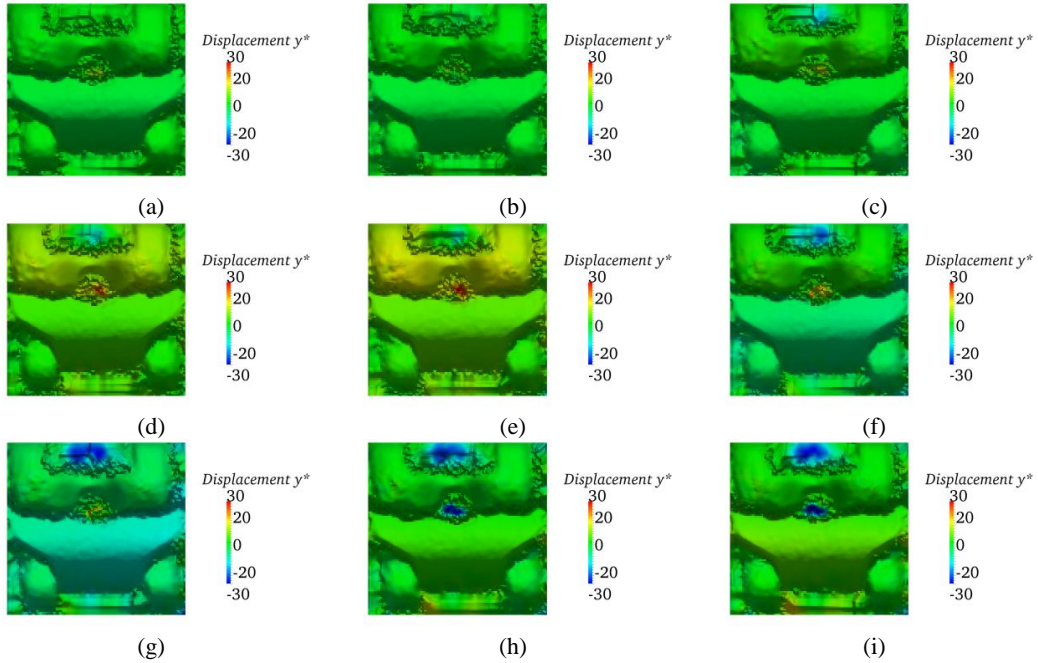


Figure 5.15: In-Ovation R 3D image sequence y^* displacement (a) 0° (b) 9° (c) 21° (d) 33° (e) 45° (f) -33° (g) -21° (h) -9° (i) -0° . Displacement measured in micrometers (μm). The dominant motion occurs for tie-wings #1 and #2 in this image sequence.

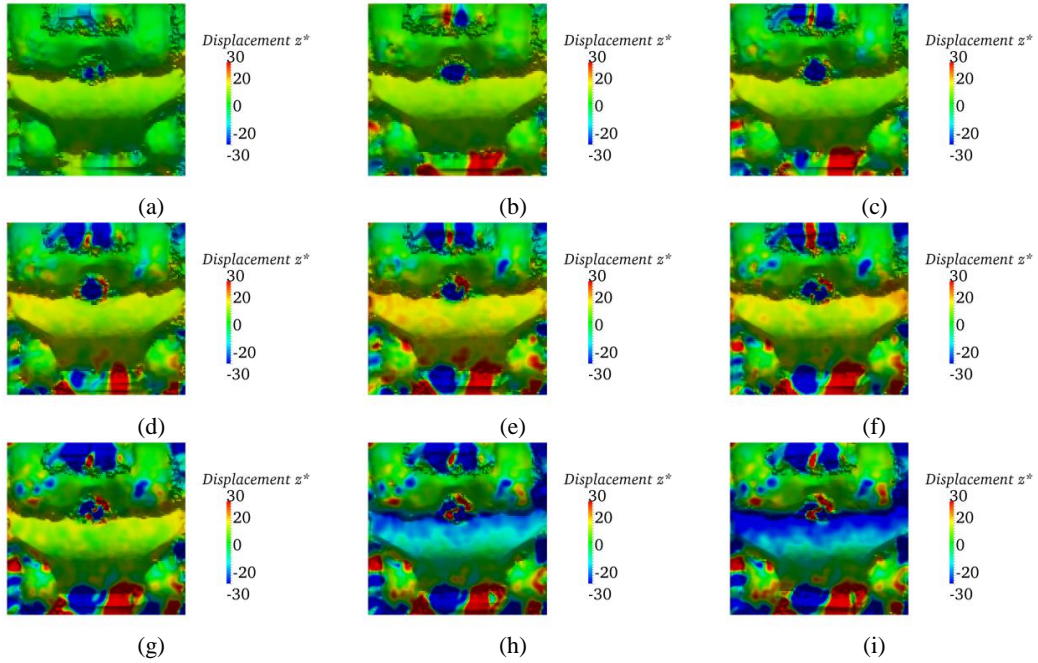


Figure 5.16: In-Ovation R 3D image sequence z^* displacement (a) 0° (b) 9° (c) 21° (d) 33° (e) 45° (f) -33° (g) -21° (h) -9° (j) -0° . Maximum motion for the ARC can be seen at 45° of archwire rotation. The final position of the ARC is lower than the start position as shown for the final bracket image indicating that the ARC has intruded into the bracket slot.

An image sequence of a Speed bracket was also processed and visualized for comparison with the Damon Q and In-Ovation R brackets. The original image sequence of the Speed bracket is shown in Figure 5.17 and the resultant 3D surface and displacement is shown in Figure 5.18, Figure 5.19 and Figure 5.20. The image sequence of the Speed bracket in Figure 5.17 shows a bracket where the ARC opened during testing. The opening of the ARC during testing is also shown in the resulting contour plots in Figure 5.18, Figure 5.19 and Figure 5.20.

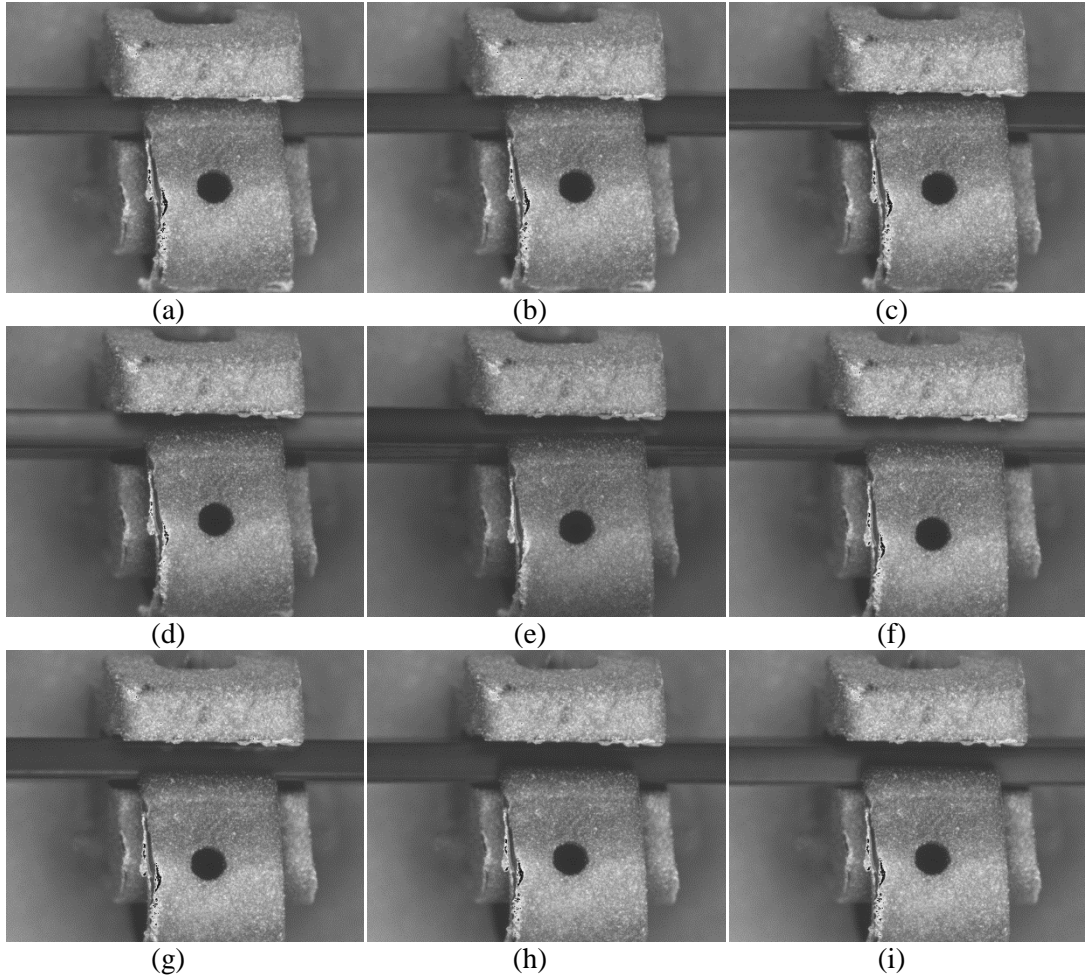


Figure 5.17: Speed image sequence (a) 0 ° (b) 9 ° (c) 21 ° (d) 33 ° (e) 45 ° (f) -33 ° (g) -21 ° (h) -9 ° (i) -0 °. The ARC of the Speed bracket opened during testing and at 33° of wire rotation and remains open through the image sequence.

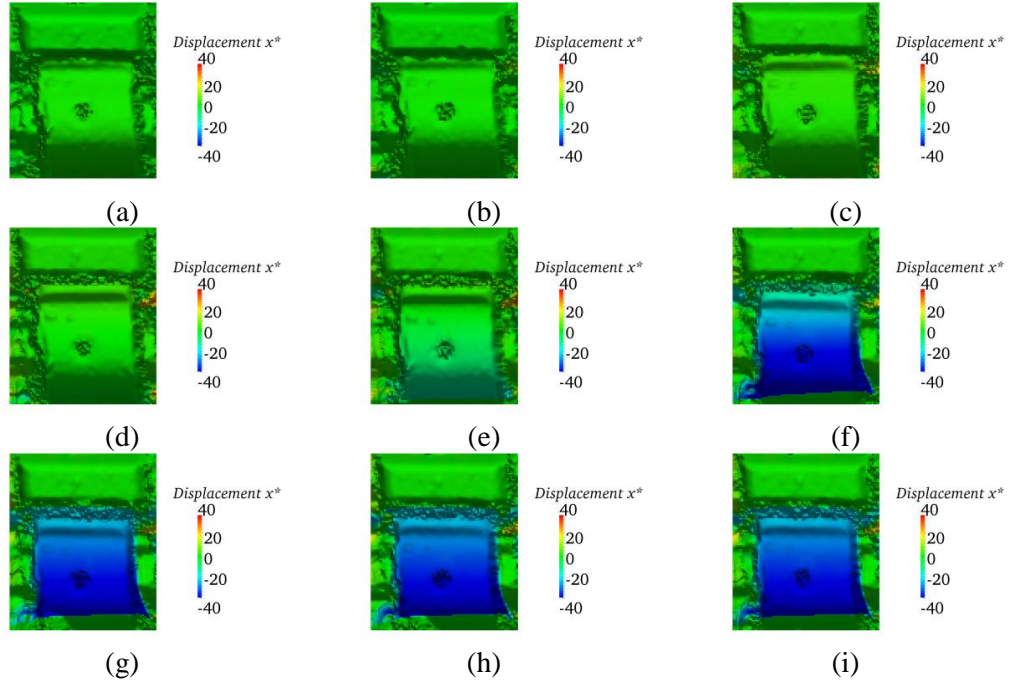


Figure 5.18: Speed 3D image sequence x^* displacement (a) 0° (b) 9° (c) 21° (d) 33° (e) 45° (f) -33° (g) -21° (h) -9° (j) -0° . Displacement measured in micrometers (μm). Motion of the ARC in the x^* direction can be seen for decreasing wire rotation indicating that the ARC has opened during testing.

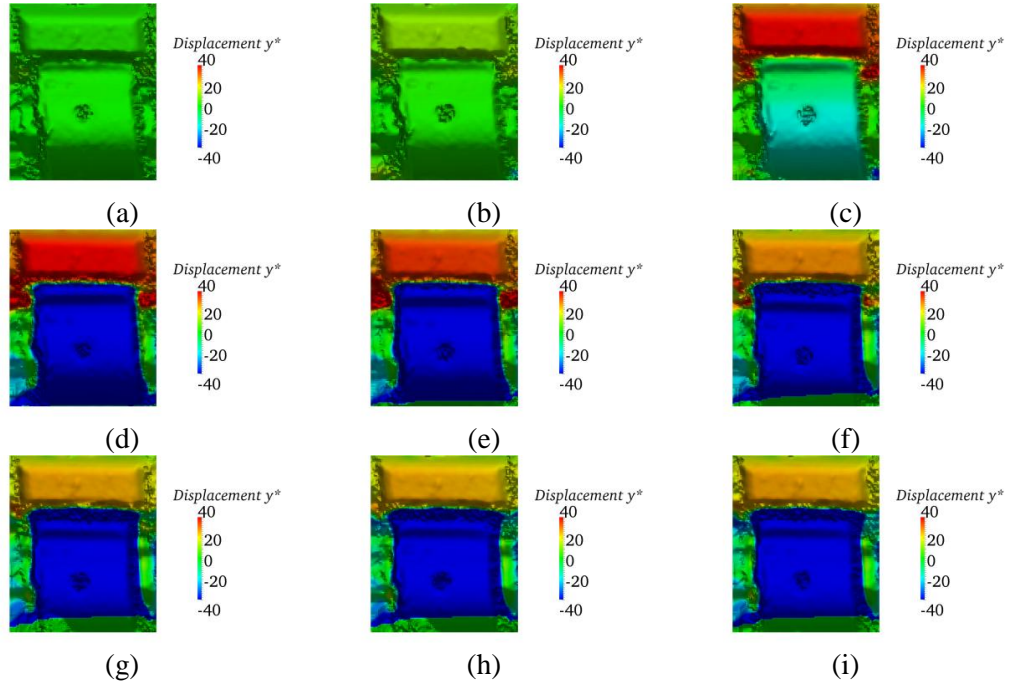


Figure 5.19: Speed 3D image sequence y^* displacement (a) 0° (b) 9° (c) 21° (d) 33° (e) 45° (f) -33° (g) -21° (h) -9° (j) -0° . Displacement measured in micrometers (μm). Maximum motion occurred at 45° of archwire rotation. The ARC opened during testing as indicated by the color of the ARC after 33° of archwire rotation.

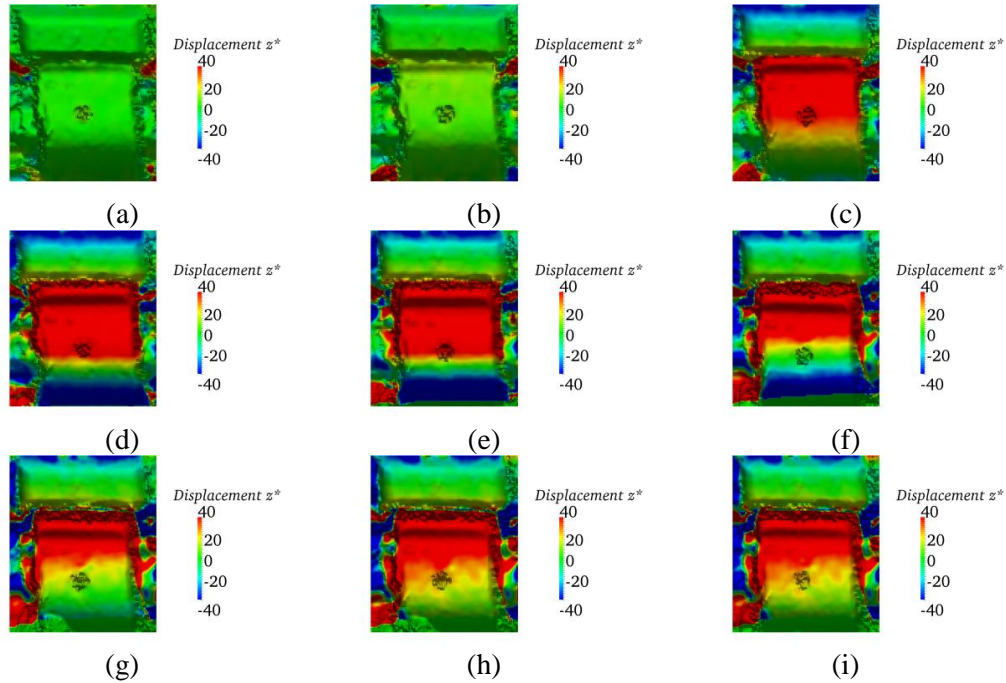


Figure 5.20: Speed 3D image sequence z^* displacement (a) 0° (b) 9° (c) 21° (d) 33° (e) 45° (f) -33° (g) -21° (h) -9° (j) -0° . Displacement measured in micrometers (μm). Maximum motion for the ARC can be seen for 45° of AW rotation. The contour plot indicates that the ARC opened during testing and that the ARC did not return to the original position after the AW was returned to the origin.

The images and contour plots of the three brackets shown in Figure 5.11 to Figure 5.20 demonstrate the 3D motion of the three brackets due to archwire rotation. The motion of the bracket TWs quantified using (5.1). Comparison of the average motion of the Damon Q and In-Ovation R bracket TWs in the x^*, y^*, z^* directions are shown in Figure 5.21. Range bars in Figure 5.21 indicate the variation for the 8 Damon Q and 10 In-Ovation R brackets. The Speed brackets were not used for comparison with the Damon Q and In-Ovation R brackets. Several of the brackets debonded during testing and the ARC opened during testing. The opening of the ARC will result in a loss in the torque that is applied to the bracket due to wire rotation. Major et al. [1] demonstrated that Speed brackets where the ARC opened during testing exhibited a loss in the torque applied to the bracket as well as substantial plastic deformation which would affect the behaviour of these brackets.

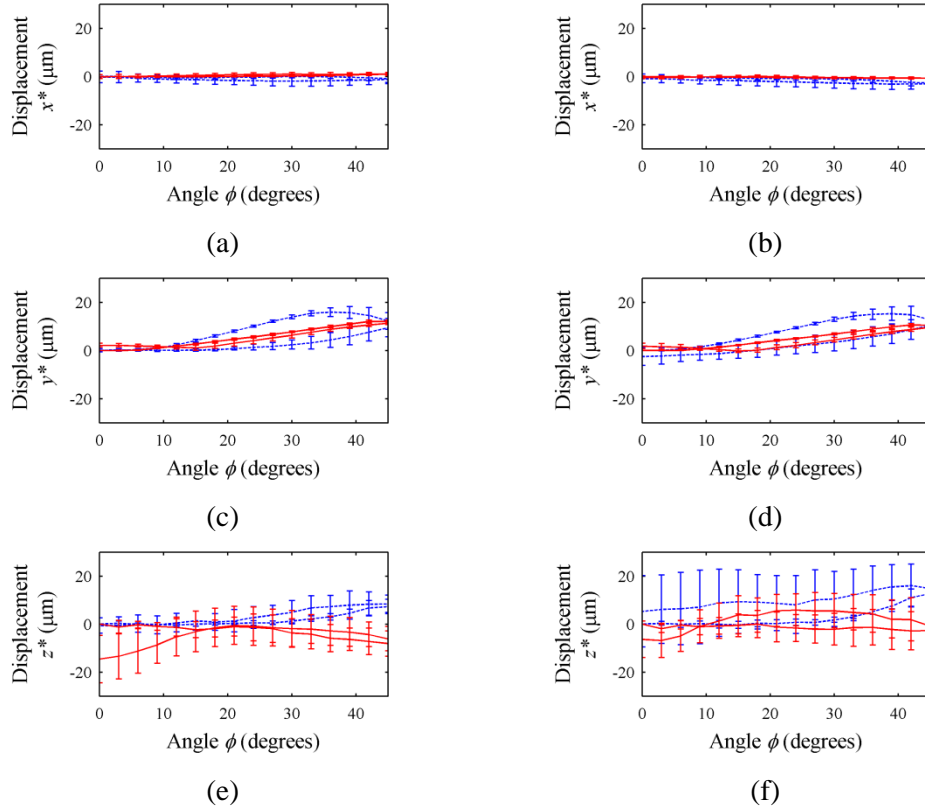


Figure 5.21: Comparison on Damon Q and In-Ovation R bracket TW motion. Average and standard deviation displacements for (a) TW#1-3 x^* (b) TW#2-4 x^* (c) TW#1-3 y^* (d) TW#2-4 y^* (e) TW#1-3 z^* (f) TW#2-4 z^* . Solid line indicates In-Ovation R bracket. Dashed line indicates Damon Q bracket.

The average motion of the ARC of the Damon Q and In-Ovation R brackets are compared in Figure 5.22. The ARC motion was quantified using Equation (5.2). Range bars indicate the variation between each bracket tests. Figure 5.22 shows that the major motion for the two brackets occurs in the z^* direction.

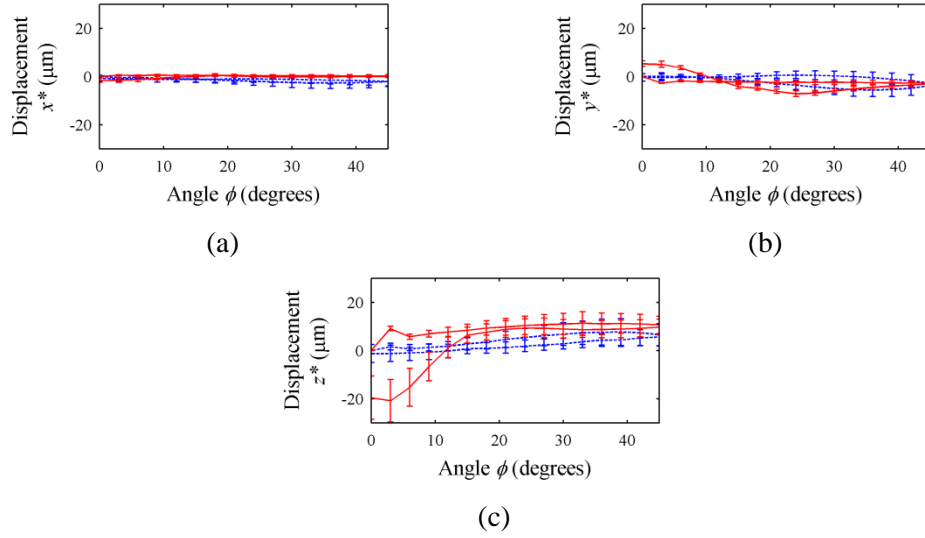


Figure 5.22: Damon Q and In-Ovation R ARC motion. Average and standard deviation of archwire retentive displacements (a) ARC x^* (b) ARC y^* (c) ARC z^*

5.4 Discussion

A total of 30 brackets were selected for the testing with the 3D OTS. For the ten (10) Damon Q brackets tested two (2) of the bracket debonded from the metal cylinder, therefore the Damon Q brackets were tested eight (8) times successfully. For the In-Ovation R brackets ten (10) tests were completed successfully. The Speed brackets were problematic. Of the ten (10) Speed bracket five (5) could not be used as the epoxy used to secure the bracket to the metal dowel adhered to the ARC as a result only five (5) brackets were available for testing. Results from the Speed brackets were not used to compare self-ligating brackets. The same bonding method was used for the Damon Q and In-Ovation R brackets as the Speed brackets and the epoxy was not found to interfere with the ARC. Figure 5.2 (b) and (c) shows the ARC for a Speed and In-Ovation R brackets. In this figure it can be seen that there is less clearance between the base of the bracket and the ARC for the Speed bracket than the In-Ovation R brackets. The clearance between the ARC and bracket base allows for sufficient epoxy to be applied to the bracket to ensure that the bracket does not debond during testing. In addition, the ARC of the Speed brackets opened during 4 of the wire rotation tests. Therefore only

one successful test was completed for the Speed brackets. A similar problem was noted by Major et al [1] for Speed brackets where the ARC opened for 16 of 30 brackets. As a result the Damon Q and In-Ovation R brackets were compared to demonstrate the difference between passive and active ligation brackets.

The images and contour plots of the three brackets shown in Figure 5.11 to Figure 5.20 demonstrate the 3D motion of the three brackets due to archwire rotation. The original bracket image sequences were processed using the 3D DIC method and then visualized using ParaView to display the deformation that occurs to the bracket due to archwire rotation. The three sets of contour plots show the different behavior of the three self-ligating brackets for the same amount of archwire rotation and highlight regions where bracket deformation occurs for the x^* , y^* and z^* directions. Also shown is the difference in magnitude of deformation across the three self-ligating brackets.

The image sequence for the Speed bracket shown in Figure 5.18 shows that motion of the ARC occurred in the x^* direction since the ARC opened during testing. This can be seen by comparing Figure 5.18 with the original image sequence in Figure 5.17. By contrast Figure 5.10 and Figure 5.14 show that little motion occurred in the x^* direction for the Damon Q and In-Ovation R brackets. The x^* motion for the bracket TWs and ARC was determined using (5.1 and (5.2). The x^* TW motion is shown in Figure 5.21 (a) and (b) and the motion in the x^* motion for the Damon and In-Ovation R brackets is less than $5\mu\text{m}$. Similarly, the x^* ARC motion is shown in Figure 5.22 (a) and the measured ARC motion was found to be less than $5\mu\text{m}$.

Substantial motion can be seen for TWs #1 and #2 in Figure 5.19 for the Speed bracket and also shows that since the bracket ARC opened during testing the TWs did not return to the original position. The predominant motion for the bracket TWs is in the y^* direction for the Damon Q and In-Ovation R self-ligating brackets in Figure 5.21. By

comparing the image sequences in Figure 5.11 and Figure 5.15 it can be seen that less deformation occurred to the In-Ovation R bracket in the y^* direction as indicated by the color gradient than the Damon Q bracket.

The z^* displacement for the Speed bracket is displayed in Figure 5.20 showing that the ARC displaced in the z^* direction and did not return to the original position as the archwire was returned to the starting position. The image sequence also shows that the predominant motion in the z^* direction is the ARC rather than the bracket TWs. The z^* motion of the Damon Q bracket was also visualized using ParaView and the resulting image sequence is shown in Figure 5.12. This figure shows that the greatest z^* motion occurs for the ARC of the Damon Q bracket at 45° archwire rotation. The images in Figure 5.12 also show that there is minimal motion in the z^* direction for the four TWs of the Damon Q bracket. The z^* displacement of the In-Ovation R brackets is also shown in Figure 5.16 where the greatest motion in the z^* direction occurs for the ARC. This contour image sequence for the In-Ovation R bracket also shows that the ARC is lower for the final bracket image compared to the initial image. The In-Ovation R brackets exhibited large variation in the z^* direction as shown in Figure 5.21 (e) and (f). The large z^* TW variation for the In-Ovation R brackets is due to the bracket geometry. With the current stereo microscope setup the four TWs of the In-Ovation R brackets are difficult to keep in focus due to the shallow depth-of-focus of the stereo microscope. Major et al. [1] also described the difficulty in maintaining focus on all of the In-Ovation R bracket features. Figure 5.2 (c) shows the difference in height between TWs 1-2 and 3-4 for the In-Ovation R bracket. The variation in height between TWs 1-2 and 3-4 is less for the Damon Q and Speed brackets than the In-Ovation R bracket seen in Figure 5.2 (a) and (b). The height of the TWs affects the ability to focus on all four TWs with the stereo-

microscope. Figure 5.21 also shows that the variation between bracket tests is much less in the x^* and y^* directions than in the z^* direction.

The calculated P -Values using the Mann-Whitney U nonparametric test for comparing the TW motion of the two brackets are summarized in Table 5.1. This table compares the brackets for 45° archwire rotation and for the final deformation after the archwire has returned to the origin. From Table 5.1 it can be seen that a statistically significant difference exists between the two brackets in the x^* and z^* directions for 45° of wire rotation. A statistically significant difference was also detected for the final displacement in the y^* motion for both the left and right TWs. The average plastic deformation in the y^* direction was found to be greater for the In-Ovation R than the Damon Q bracket.

Table 5.1 also shows that the predominant motion for the bracket TWs occurs in the y^* direction. For the Damon Q bracket the magnitude of y^* motion was 13.7 and 4.8 times greater than the x^* motion for TWs#1-3 and #2-4. As well the magnitude of y^* motion was 1.67 and 0.96 times greater than the z^* motion for TWs#1-3 and #2-4. Similarly, the In-Ovation y^* motion was 13.2 and 14.4 times greater than the x^* motion for TWs#1-3 and #2-4. Also, the y^* motion was 1.5 and 3.8 times greater than the z^* motion for the In-Ovation R bracket for TWs#1-3 and #2-4. Table 5.1 and Figure 5.21 show that the most displacement occurs in the y^* direction for the bracket TWs due to archwire rotation. Therefore, the y^* motion should be used to assess variations between bracket TW designs.

A total of 10 In-Ovation R and 8 Damon Q brackets were used in this study. The standard deviations in Table 5.1 to determine the sample size required detect a difference between the brackets of $5\mu\text{m}$ with $\alpha = 0.05$ and $\beta = 0.1$. For a standard deviation of $3.50\mu\text{m}$ a sample size of 10 is required to detect a difference of $5\mu\text{m}$.

The bracket TWs behaved differently in the z^* direction for the Damon Q and In-Ovation R brackets as shown in Table 5.1. From this table it can be seen that the Damon Q bracket maximum TW deformation was found to be positive in the z^* direction while the In-Ovation R maximum TW deformation in the z^* direction was negative. The difference in behaviour of the two brackets is due to the bracket design and the interaction between the bracket ARC, AW and TWs. For the In-Ovation R bracket AW rotation causes the ARC to displace in the positive z^* direction. Motion of the ARC in the z^* direction will cause TW #3 and 4 of the In-Ovation R bracket to move in the positive z^* direction due to the interaction between the ARC and TW #3 and 4 therefore there will be a relative decrease in the difference in height between TWs #1-3 and #2-4. The final z^* position of the In-Ovation R bracket TWs indicates that TWs #3 and #4 are higher than TWs #1 and #2. This indicates that the In-Ovation R brackets rotated due to AW rotation which results in the final position of TWs #3 and #4 above TWs #1 and #2. As well, there is a large difference in the height between TWs #1-2 and #3-4 due to geometry of the In-Ovation R brackets. The large difference in bracket TWs height may result in the bracket TWs going out of focus during testing due to the shallow depth of field of the stereo microscope. The limitations of the optics could explain the large standard deviations for the z^* motion of the In-Ovation R bracket TWs.

Table 5.1: Maximum and plastic deformation due to archwire rotation for Damon Q and In-Ovation R brackets. Bolded values show significant differences.

Bracket TW		Maximum Deformation (μm)			Plastic Deformation (μm)		
		Damon Q	In-Ovation R	<i>P</i> - Value	Damon Q	In-Ovation R	<i>P</i> - Value
TW#1-3 (stdev)	<i>x</i> *	-0.89(1.55)	0.91(0.52)	0.014	-0.20(2.37)	-0.05(0.82)	0.3822
TW#2-4 (stdev)	<i>x</i> *	-2.71(1.83)	-0.73(0.38)	0.010	-0.81(1.81)	-0.36(0.54)	0.6453
TW#1-3 (stdev)	<i>y</i> *	12.21(3.50)	12.00(0.57)	0.959	0.09(0.63)	2.20(0.82)	0.0001
TW#2-4 (stdev)	<i>y</i> *	12.67(3.86)	10.48(0.71)	0.050	-2.46(3.74)	1.82(1.14)	0.0206
TW#1-3 (stdev)	<i>z</i> *	7.31(2.98)	-8.08(5.26)	0.0001	-0.61(3.21)	-14.60(9.88)	0.0018
TW#2-4 (stdev)	<i>z</i> *	12.71(5.46)	-2.70(7.85)	0.0003	5.37(14.86)	-6.32(7.65)	0.1303

Table 5.1 also compares the maximum and plastic deformation for the In-Ovation R and Damon Q brackets. From this table it can be seen that a significant difference was found for the maximum deformation in the x^* and z^* directions. Also, a significant difference was found between the final plastic deformation of the two brackets in the y^* direction. Table 5.1 shows that the In-Ovation R bracket had a final plastic deformation of approximately 2.0 μm while the Damon Q bracket exhibited less plastic deformation for the same amount of archwire rotation.

The z^* motion of the ARC for the In-Ovation R bracket, shown in Figure 5.22 (c), shows a sharp increase at 3° archwire rotation. This increase is due to the initial contact of the archwire with the ARC. The ARC z^* displacement continues to increase after 3° of archwire rotation. As the archwire reached 20-25° wire rotation the z^* motion of the ARC began to plateau. The plateau seen for the In-Ovation R z^* motion is most likely due to the ARC contacting the “slot blocker” or small slots where the ARC is retained by the TWs shown in Figure 5.2 (c) and Figure 4.12 (b) which prevents the ARC from becoming separated from the bracket TWs. By contrast a sharp increase is not seen in the ARC of the Damon Q brackets.

The calculated *P*-Values for comparing the ARC motion of the two brackets are summarized in Table 5.2. This table compares the brackets for 45° archwire rotation and for the final deformation after the archwire has returned to the original position. From Table 5.2 it can be seen that a statistically significant difference exists between the two brackets in the x^* and z^* directions for 45° of wire rotation. A statistically significant difference was also detected for the final displacement in the y^* and z^* ARC motion. The magnitude of motion in the z^* direction is 2.2 and 2.9 times greater than the x^* and y^* direction for the Damon Q ARC. As well, motion in the z^* direction for the In-Ovation R bracket is 81.4 and 3.18 times greater than the x^* and y^* directions. Therefore, the z^* motion should be used to assess variations between bracket ARC designs. The final position of the ARC for the In-Ovation R bracket is much less than the Damon Q bracket. This is indicated by the significant difference in final z^* position in Table 5.2. Comparison of the final position of the ARC of the Damon Q and In-Ovation R is also shown in Figure 5.22. The final position of the ARC of the In-Ovation R bracket is due to the compliance of the ARC which causes the ARC to encroach the bracket slot [9]. The large final displacement of the ARC is also shown in the contour plot of the In-Ovation R bracket in Figure 5.16.

Table 5.2: Maximum ARC motion.

ARC Displacement	Maximum Displacement (μm)			Final Deformation (μm)		
	Damon Q	In-Ovation R	<i>P</i> -Value	Damon Q	In-Ovation R	<i>P</i> -Value
x^* (stdev) [μm]	-1.95(1.93)	0.12(0.55)	0.0046	-0.77(1.18)	-1.56(0.91)	0.3822
y^* (stdev) [μm]	-2.63(2.63)	-3.07(1.05)	0.8784	-0.39(1.55)	5.29(1.15)	0.0002
z^* (stdev) [μm]	5.70(3.91)	9.77(3.28)	0.0379	-1.23(3.75)	-19.62(8.99)	0.0002

There has been limited investigation into the behavior of the ARC [10]. Pandis et al. [11] examined the deformation and change in stiffness of the ARC of two active ligation brackets by measuring the force applied by the ARC. An archwire was displaced labially

(towards the inside of the cheek) in the bracket slot in 0.02mm (20 μ m) increments to a maximum displacement of 1.5mm and the force applied by the ARC was measured at each increment. This motion is well beyond the displacement that was seen for a typical bracket due to archwire rotation using the OTS. Therefore, no comparable study has been performed that examines the effect of archwire rotation of the deformation of the ARC. Figure 5.22 shows that for a maximum archwire rotation of 45° the ARC displaced 9.77 μ m for the In-Ovation R bracket and 5.70 μ m for the Damon Q bracket. The displacement of the ARC measured using the 3D OTS was found to be 2.0 and 3.5 times less for the In-Ovation and Damon Q brackets than the initial displacement used by Pandis et al. [11].

The OTS has been used with a 3D DIC technique to quantify bracket deformation in three dimensions. Using this method brackets of varying design were compared for the same amount of archwire rotation. This measurement method has shown that the bracket TWs deform in three dimensions due to archwire rotation and that the most substantial motion for the bracket TWs occurs in the y^* direction. The 3D DIC technique has demonstrated the interaction between the ARC and archwire in three dimensions. Engagement of the archwire and ARC could affect treatment effectiveness since the archwire rotation applies a force to the ARC instead of the expected force to the TWs leading to inefficient force couple transfer. Using the 3D OTS it will be possible to evaluate effects such as cyclic loading on the ARC to determine if loading over time affects the mechanical properties of the ARC and if deformation of the ARC results in a loss in the force that can be applied to a tooth.

5.5 Conclusions

A non-contact measurement method has been developed to evaluate the 3D motion of orthodontic brackets. This method has been used to measure the displacement of two

self-ligating brackets to measure TW and ARC motion. The motion of the ARC has not been extensively evaluated for self-ligating brackets nor has the 3D motion of bracket TWs. The 3D OTS allows for the 3D motion of the ARC to be measure in response to archwire rotation and can be used to determine how the compliance of the ARC. Contour plots of three self-ligating brackets have been created using data acquired using a 3D DIC method. The contour plots show the displacement that occurs to the orthodontic brackets due to progressive archwire rotation and can be used to visualize regions where large deformation occurs. The displacement of the ARC measured using the 3D OTS was found to be 2.0 and 3.5 times less for the In-Ovation and Damon Q brackets than previous studies used to examine the compliance of the ARC.

Investigation the motion of the bracket TWs for the Damon Q and In-Ovation R bracket has shown the magnitude of y^* motion was greater than the x^* and z^* TW motion due to archwire rotation. Therefore, the y^* motion should be used for comparison of bracket designs and there 3D DIC measurement method is not necessary to compare bracket TW motion since the single camera 2D DIC method is capable of measuring the y^* TW motion. Conversely, the z^* motion of the ARC was found to be greater than the x^* and y^* motion for both the Damon Q and In-Ovation R brackets. As a result there stereo microscope version of the OTS should be used to compare the compliance of the ARC of self-ligating brackets.

5.6 References

[1] T. W. Major, J. P. Carey, D. S. Nobes, G. Heo and P. W. Major, "Measurement of plastic and elastic deformation due to third-order torque in self-ligated orthodontic brackets," *Am. J. Orthod. Dentofacial Orthop.*, vol. 140, pp. 326-339, Sep, 2011.

- [2] P. F. Luo, Y. J. Chao, M. A. Sutton and W. H. Peters III, "Accurate measurement of three-dimensional deformations in deformable and rigid bodies using computer vision," *Exp. Mech.*, vol. 33, pp. 123-132, 1993.
- [3] D. Garcia, J. J. Orteu and L. Penazzi, "A combined temporal tracking and stereo-correlation technique for accurate measurement of 3D displacements: Application to sheet metal forming," *J. Mater. Process. Technol.*, vol. 125-126, pp. 736-742, 2002.
- [4] J. -. Orteu, "3-D computer vision in experimental mechanics," *Opt Lasers Eng*, vol. 47, pp. 282-291, 2009.
- [5] M. A. Sutton, J. J. Orteu and H. W. Schreier, *Image Correlation for Shape, Motion and Deformation Measurements : Basic Concepts, Theory and Applications*. New York, N.Y: Springer, 2009.
- [6] W. A. Brantley and T. Eliades, "Orthodontic brackets," in *Orthodontic Materials: Scientific and Clinical Aspects*, W. A. Brantley and T. Eliades, Eds. New York: Thieme, 2001, pp. 144-147,165.
- [7] N. Harradine, "Self-ligating brackets: Theory, practice, and evidence," in *Orthodontics : Current Principles and Techniques*, 5th ed., L. W. Graber, Ed. Philadelphia, PA: Elsevier/Mosby, 2012, pp. 581.
- [8] G. A. Thorstenson and R. P. Kusy, "Effect of archwire size and material on the resistance to sliding of self-ligating brackets with second-order angulation in the dry state," *American Journal of Orthodontics and Dentofacial Orthopedics*, vol. 122, pp. 295-305, 2002.
- [9] N. W. Harradine, "Self-ligating brackets: where are we now?" *J. Orthod.*, vol. 30, pp. 262-273, 2003.
- [10] N. W. Harradine, "Historical aspects and evolution of ligation and appliances," in *Self-Ligation in Orthodontics: An Evidence-Based Approach to Biomechanics and Treatment*, T. Eliades and N. Pandis, Eds. Chichester, U.K. ; Ames, Iowa: Wiley-Blackwell, 2009, pp. 1.
- [11] N. Pandis, C. Bourauel and T. Eliades, "Changes in the stiffness of the ligating mechanism in retrieved active self-ligating brackets," *American Journal of Orthodontics and Dentofacial Orthopedics*, vol. 132, pp. 834-837, 2007.
- [12] D. J. Rinchuse and P. G. Miles, "Self-ligating brackets: Present and future," *American Journal of Orthodontics and Dentofacial Orthopedics*, vol. 132, pp. 216-222, 2007.
- [13] N. Pandis, T. Eliades and C. Bourauel, "Biomechanics of self-ligation: Analysis of forces and moments exerted by self-ligating brackets," in *Self-Ligation in Orthodontics: An Evidence-Based Approach to Biomechanics and Treatment*, T. Eliades and N. Pandis, Eds. Chichester, U.K. ; Ames, Iowa: Wiley-Blackwell, 2009, pp. 33-44.

- [14] H. M. Badawi, R. W. Toogood, J. P. R. Carey, G. Heo and P. W. Major, "Torque expression of self-ligating brackets," *American Journal of Orthodontics and Dentofacial Orthopedics*, vol. 133, pp. 721-728, 2008.
- [15] R. Lacoursiere, D. Nobes, D. Homeniuk, J. P. Carey, H. Badawi and P. W. Major. Measurement of orthodontic bracket TW elastic and plastic deformation by arch wire torque expression utilizing an optical image correlation technique. *Journal of Dental Biomechanics* vol. 2010(Article ID 397037), 2010.
- [16] T. W. Major, J. P. Carey, D. S. Nobes, G. Heo, G. W. Melenka and P. W. Major, "An investigation into the mechanical characteristics of select self-ligated brackets at a series of clinically relevant maximum torquing angles: loading and unloading curves and bracket deformation," *Eur. J. Orthod.*, Jul 12, 2011.
- [17] G. W. Melenka, R. A. Lacoursiere, J. P. Carey, D. S. Nobes, G. Heo and P. W. Major, "Comparison of deformation and torque expression of the orthos and orthos Ti bracket systems," *Eur. J. Orthod.*, Oct 19, 2011.
- [18] LaVision GmbH, "Product-Manual for DaVis 7.2 StrainMaster Software Item-Number(s): 1105022," 2006.
- [19] B. Pan, K. Qian, H. Xie and A. Asundi, "Two-dimensional digital image correlation for in-plane displacement and strain measurement: A review," *Meas Sci Technol*, vol. 20, 2009.
- [20] H. A. Bruck, S. R. McNeill, M. A. Sutton and W. H. Peters III, "Digital image correlation using Newton-Raphson method of partial differential correction," *Exp. Mech.*, vol. 29, pp. 261-267, 1989.
- [21] T. A. Berfield, J. K. Patel, R. G. Shimmin, P. V. Braun, J. Lambros and N. R. Sottos, "Micro-and nanoscale deformation measurement of surface and internal planes via digital image correlation," *Exp. Mech.*, vol. 47, pp. 51-62, 2007.

Chapter 6 Conclusions, Recommendations and Future Work

6.1 Conclusions

The OTS is a novel and unique device capable of simulating the clinical situation of archwire rotation on orthodontic brackets. The OTS consists of a stepper motor and worm gear which rotate a pair of dies. The dies, which hold the archwire, are connected by a yoke that provides even archwire rotation. Deformation is measured by collecting images of the orthodontic bracket as the wire is rotated in the bracket slot. The collected bracket images are post-processed using a DIC technique to measure deformation. The OTS has been used in two configurations to measure bracket deformation: (1) single camera (2) stereo camera. The single camera configuration of the OTS is capable of measuring the 2D deformation of orthodontic brackets. The out-of-plane motion of the orthodontic bracket cannot be detected using the single camera version of the OTS. The addition of a stereo microscope and camera pair allows for the in-plane and out-of-plane motion of the orthodontic bracket to be measured. The stereo camera version of the OTS was used to determine if substantial out-of-plane motion of the orthodontic bracket can be detected. The 3D version of the OTS is also capable of detecting the motion of the ARC.

The 2D version of the OTS was evaluated to quantify the errors associated with the measurement of forces and moments using a 6-axis load cell. The accuracy of the 2D DIC method to quantify bracket deformation was also evaluated. The evaluation of the 2D version of the OTS demonstrated that the errors associated with the 2D DIC measurement method are less than the variability in bracket deformation. Therefore, the single camera version of the OTS is capable of quantifying the deformation that occurs to orthodontic brackets due to archwire rotation.

The 3D version of the OTS was evaluated to quantify the errors associated with the 3D DIC method used to quantify bracket deformation. The bracket repeatability tests performed on an orthodontic bracket show that the dominant TW motion is in the y^* direction. The dominant motion for the ARC for this bracket was found to be in the z^* direction. The results from the 3D DIC method indicates substantial motion cannot be detected in the z^* direction for the bracket TWs showing that the additional displacement component gained by using a stereo microscope is not necessary for characterizing the TW motion. The additional displacement component gained using the 3D DIC method does show that motion of the ARC exists in the z^* direction. The 3D DIC technique has demonstrated the interaction between the ARC and archwire in three dimensions. Engagement of the archwire and ARC could affect treatment effectiveness since the archwire rotation applies a force to the ARC instead of the expected force to the TWs leading to inefficient force couple transfer. Therefore, characterization of the motion of the bracket TWs only requires a 2D DIC measurement system but a 3D DIC method is necessary to describe the motion of the ARC.

The 3D version of the OTS was used to visualize the deformation that occurs to three self-ligating brackets due to archwire rotation. Using this method it is possible to determine locations where large deformation has occurred. In addition to measuring 3D bracket deformation a visualization method has been developed which is used to display the 3D DIC data generated from post processing stereo bracket images. The visualization method allows for the 3D shape of the test bracket to be displayed and contour plot or vector displacement plots showing the x^* , y^* and z^* motion. This visualization method is useful to demonstrate the full 3D bracket behaviour and will be readily comparable to finite element models of the bracket-archwire interaction.

6.2 Recommendations

Further developments to the OTS will help to improve the accuracy and repeatability of the bracket deformation measurements. The following recommendations will ensure that the OTS is a highly repeatable and user friendly measurement device.

The Zeiss Stereo Discovery v8 stereo microscope used to measure 3D bracket deformation has a shallow stereo angle. The exact stereo angle between the left and right views of the stereo microscope is also not reported in the microscope documentation. The shallow stereo angle is a limitation of using a CMO style stereo microscope. A steeper stereo angle will allow for out-of-plane motion to be more accurately detected. In addition, the stereo microscope has a shallow depth-of-focus. As a result it is difficult to focus on all bracket features for brackets which have a significant difference in TW height. During testing, the orthodontic bracket may move outside the depth-of-focus of the stereo microscope therefore optics should be selected so that the bracket remains in focus over the entire range of archwire rotation.

Calibration and validation of the accuracy of the 3D DIC method can be improved by using higher precision translation stages. Currently the translation stage that was used to calibrate the stereo camera has a resolution of $25.4\mu\text{m}$ and the current translation stage utilizes a hand operated micrometer. Human error in the movement of the translation stage can be eliminated by using a computer controlled translation stage. The 3D DIC method with the stereo microscope is capable of resolving displacements that are less than $1\mu\text{m}$. Therefore, to improve the accuracy of the 3D DIC calibration a translation stage with at least $1\mu\text{m}$ would ensure that an accurate calibration has been performed. A computer controlled translation stage with sub-micron precision will allow for much more accurate bulk translations as well and could be used to validate the 3D DIC results with physical displacements performed with the computer controlled translation stage.

The procedure used to bond the orthodontic bracket to the metal dowel could be improved. Currently the orthodontic brackets are mounted on the metal dowels by hand and it is difficult to ensure that the bracket is located at the center of the metal dowel. A repeatable method of securing the orthodontic brackets would simplify the measurement of the load-cell offset since the position of the bracket with respect to the metal dowel would be known. Repeatability bonding the brackets to the dowels would also help to reduce additional forces and moments from being applied to the orthodontic bracket due to misalignments that may occur between the wire and bracket slot caused by the gluing method.

An optimal amount of epoxy should also be found in order to secure the orthodontic brackets to the metallic dowels. By using an exact amount of epoxy it will be possible to ensure that the brackets do not debond during testing and using a measured amount of epoxy will help to prevent the epoxy from interfering with the ARC or bracket slot.

6.3 Future Work

A number of potential experiments can be carried out using the 3D version of the OTS. These experiments will help to further understand the bracket-archwire interaction used to control tooth inclination.

One potential area for study is the effect of repeated loading on the bracket-archwire interaction. Using repeated archwire rotation cycles it would be possible to determine if fatigue affects the deformation of bracket TWs.

The biological response of the periodontal ligament could be taken into account through simulation of the interaction between archwire rotation and the periodontal ligament could be undertaken using the 3D version of the OTS. This study would allow for the

complete interaction between the archwire, bracket, tooth and periodontal ligament to be described.

A more comprehensive study should be undertaken to understand the behaviour of self-ligating brackets and archwires. A larger sample size and greater variety of passive and active ligating brackets should be selected and tested to demonstrate the three dimensional behaviour of all self-ligating brackets. Self-ligating brackets such as: GAC In-Ovation R, GAC In-Ovation C, 3M Unitek Smartclip, 3M Clarify SL, Ormco Damon2, Ormco Damon3, Ormco Damon Q, Strite Industries Speed and other bracket designs could be tested. Conventional ligation brackets should also be evaluated using the 3D measurement system to determine if the three dimensional behaviour of conventional ligation brackets differs from that of self-ligating brackets. Also, brackets of varying material properties should also be evaluated. For this thesis only metallic brackets were evaluated. Ceramic, plastic and polycarbonate brackets should be compared with metallic brackets to demonstrate how material properties may affect bracket deformation. As well, more extensive testing is required on the archwires used for testing orthodontic brackets. The thesis only utilized a stainless steel 0.483x0.635mm (0.019x0.025") archwire that is typically used in later stages of treatment. A more comprehensive study of archwire sizes and materials should be tested to evaluate the effect of wire size and material on bracket deformation.

The results collected using the 3D version of the OTS should be compared with a FEA model of the bracket-archwire interaction. The FEA model will need to include a non-linear contact model to accurately model the bracket-archwire interaction. The FEA study must also be able to simulate permanent deformation that may occur to the bracket TWs due to archwire rotation. Therefore, the standard linear-elastic assumption cannot be used to model bracket TW deformation. Both self-ligating and conventional ligation

bracket FEA models should be compared with the DIC results collected using the OTS. The self-ligating bracket models must account for the bracket slot-archwire interaction as well as the archwire-ARC interaction. As well, the FEA model must accurately take into account the material properties of the brackets and archwires to be used in the bracket-archwire simulation.

The FEA bracket model should be validated by comparing the 3D DIC results collected using the OTS. Once the FEA model has been validated with the 3D DIC results it will be possible to apply loads other than pure archwire rotation. Validation of the bracket-archwire interaction will then allow for the bracket-epoxy-tooth interaction to be examined.

The OTS is a useful orthodontic measurement device that can be used to evaluate the deformation of orthodontic brackets due to archwire rotation. The above suggestions will help to improve the accuracy and repeatability of the OTS. The OTS results can also be used for the validation of a FEA model of the bracket-archwire interaction. Finally, the 3D version of the OTS can be used to evaluate many of the orthodontic appliances commonly used to correct tooth inclination. The OTS provides a standardized and repeatable method that can be used to quantify brackets of varying geometry or material as well as archwires of varying geometry and material.

Appendix A Force-Torque Equation Derivation

A.1 Load Cell Bracket Offset

The transformation from the load cell to the bracket is calculated using the translation and rotation matrices A.1 and A.2 respectively. The coordinate system transformation method is a common approach used for robot manipulators [1]. The translation matrix represents the offset of the bracket from the center of the load cell while the rotation matrix is the rotation of the bracket about the z -axis shown in Figure A. 1.

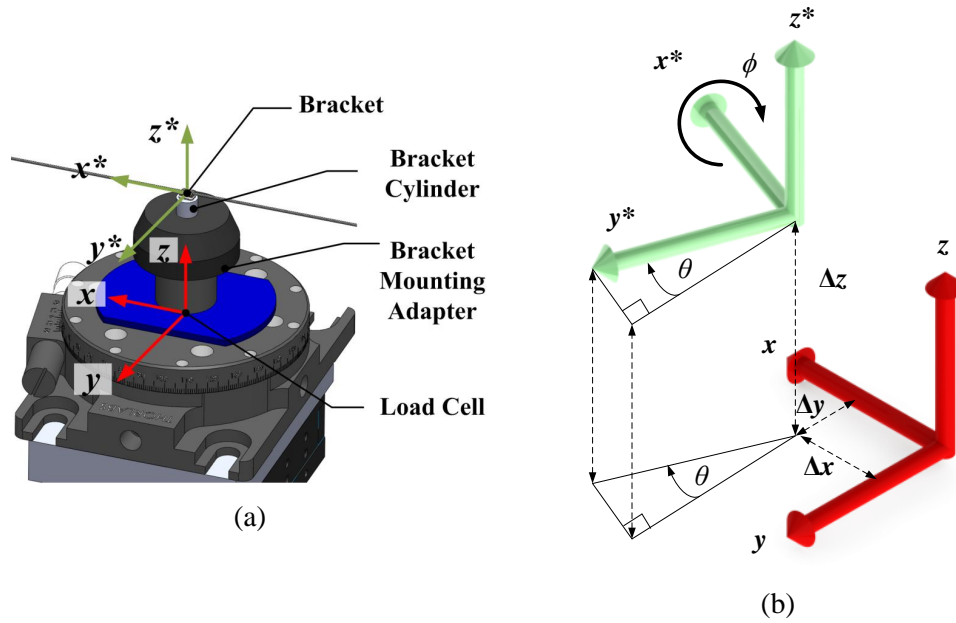


Figure A. 1 Load cell and bracket coordinate systems. (a) Offset of orthodontic bracket from load cell (b) Coordinate system transformation showing displacement, rotation about the z axis and the angle ϕ indicating the direction of archwire rotation.

The transformation matrix, T , is the product of the translation and rotation matrices A.3.

This transformation is known as the differential coordinate transformation.

$$trans(\Delta x, \Delta y, \Delta z) = \begin{bmatrix} 1 & 0 & 0 & \Delta x \\ 0 & 1 & 0 & \Delta y \\ 0 & 0 & 1 & \Delta z \\ 0 & 0 & 0 & 1 \end{bmatrix} \quad (\text{A.1})$$

$$rotation(z, \theta) = \begin{bmatrix} \cos \theta & -\sin \theta & 0 & 0 \\ \sin \theta & \cos \theta & 0 & 0 \\ 0 & 0 & 1 & 0 \\ 0 & 0 & 0 & 1 \end{bmatrix} \quad (\text{A.2})$$

$$T = trans(x, y, z) \bullet rotation(z, \theta)$$

$$T = \begin{bmatrix} 1 & 0 & 0 & \Delta x \\ 0 & 1 & 0 & \Delta y \\ 0 & 0 & 1 & \Delta z \\ 0 & 0 & 0 & 1 \end{bmatrix} \begin{bmatrix} \cos \theta & -\sin \theta & 0 & 0 \\ \sin \theta & \cos \theta & 0 & 0 \\ 0 & 0 & 1 & 0 \\ 0 & 0 & 0 & 1 \end{bmatrix} \begin{bmatrix} n_x & o_x & a_x & p_x \\ n_y & o_y & a_y & p_y \\ n_z & o_z & a_z & p_z \\ 0 & 0 & 0 & 1 \end{bmatrix} \quad (\text{A.3})$$

The forces experienced at the bracket are computed by multiplying the measured load cell forces and moments by the Jacobian. The Jacobian is composed of elements of the transformation matrix A.4. The resultant bracket forces and moments are determined using A.5.

$$F_{bracket} = J^T F_{Loadcell}$$

$$J^T = \begin{bmatrix} n_x & n_y & n_z & (p \times n)_x & (p \times n)_y & (p \times n)_z \\ o_x & o_y & o_z & (p \times o)_x & (p \times o)_y & (p \times o)_z \\ a_x & a_y & a_z & (p \times a)_x & (p \times a)_y & (p \times a)_z \\ 0 & 0 & 0 & n_x & n_y & n_z \\ 0 & 0 & 0 & o_x & o_y & o_z \\ 0 & 0 & 0 & a_x & a_y & a_z \end{bmatrix} \quad (\text{A.4})$$

$$F_{loadcell} = \begin{pmatrix} m_{xloadcell} \\ m_{yloadcell} \\ m_{zloadcell} \\ f_{xloadcell} \\ f_{yloadcell} \\ f_{zloadcell} \end{pmatrix}$$

$$F_{\text{bracket}} = \begin{pmatrix} m_{x\text{bracket}} \\ m_{y\text{bracket}} \\ m_{z\text{bracket}} \\ f_{x\text{bracket}} \\ f_{y\text{bracket}} \\ f_{z\text{bracket}} \end{pmatrix}$$

$$\begin{aligned} m_{x\text{bracket}} &= m_{xLC} \cos \theta - f_{xLC} (\Delta y \cos \theta - \Delta x \sin \theta) + \\ & m_{yLC} \Delta x \sin \theta + \Delta z (f_{yLC} \cos \theta - f_{xLC} \sin \theta) \end{aligned} \quad (\text{A.5})$$

$$\begin{aligned} m_{y\text{bracket}} &= f_{zLC} (\Delta x \cos \theta + \Delta y \sin \theta) + m_{yLC} \cos \theta - \\ & m_{xLC} \sin \theta - \Delta z (f_{xLC} \cos \theta + f_{yLC} \sin \theta) \end{aligned}$$

$$m_{z\text{bracket}} = m_{zLC} - \Delta x f_{yLC} + \Delta y f_{xLC}$$

$$f_{x\text{bracket}} = f_{xLC} \cos \theta + f_{yLC} \sin \theta$$

$$f_{y\text{bracket}} = f_{yLC} \cos \theta - f_{xLC} \sin \theta$$

$$f_{z\text{bracket}} = f_{zLC}$$

A.2 Force/Torque Transformation Error Analysis

An error analysis was performed to determine the effect on the force/ torque transformation used to convert from the load cell to bracket coordinate system [2]. The uncertainty for the bracket forces and moments was determined by performing an error propagation analysis based on the ASME Power Test Codes (PTC) 19.1 Test Uncertainty test standard discussed in [2]. Several sources of uncertainty have been identified which will contribute to the errors associated with the load cell/ bracket transformation, including the load cell force f_{xLC} , f_{yLC} , f_{zLC} ; load cell moment m_{xLC} , m_{yLC} , m_{zLC} ; bracket offset Δx , Δy , Δz and bracket angular offset θ . Equation A.6 illustrates that the forces and moments measured at the bracket are a function of ten parameters Δx , Δy , Δz , θ , f_{xLC} , f_{yLC} ,

f_{zLC} , m_{xLC} , m_{yLC} , and m_{zLC} . There is an associated uncertainty with each of the parameters (Equation A.7). The sensitivity index $\theta_{F_{bracket}}$ was computed for each parameter and the resulting 10 X 6 sensitivity matrix is shown in Equation A.8. The propagation of uncertainty in the variables is determined using Equation A.9. This equation is the square root of the sum of squares of all errors associated with the force/ torque transformation.

$$F_{bracket} = f(\Delta x, \Delta y, \Delta z, \theta, f_{xLC}, f_{yLC}, f_{zLC}, m_{xLC}, m_{yLC}, m_{zLC}) \quad (A.6)$$

$$u_{F_{bracket}} = f(u_{\Delta x}, u_{\Delta y}, u_{\Delta z}, u_{\theta}, u_{f_{xLC}}, u_{f_{yLC}}, u_{f_{zLC}}, u_{m_{xLC}}, u_{m_{yLC}}, u_{m_{zLC}}) \quad (A.7)$$

An example of the bracket/load cell offset measurement as well as the recorded load cell force and moment data is shown in Table A. 1. This table also shows the uncertainty in the offset and load cell measurements.

Table A. 1: Bracket offset from load cell measurements and uncertainty

Measurement		Uncertainty	
Variable	Measured Offset	Uncertainty Variable	Measurement Uncertainty
Δx	-0.4047mm	$u_{\Delta x}$	± 0.018 mm
Δy	0.7673mm	$u_{\Delta y}$	± 0.018 mm
Δz	17.650mm	$u_{\Delta z}$	± 0.018 mm
θ	3°	u_{θ}	$\pm 0.5^\circ$
F_x	-1.80596 N	u_{F_x}	1.00% of full scale load
F_y	1.033064 N	u_{F_y}	1.00% of full scale load
F_z	1.278975 N	u_{F_z}	1.00% of full scale load
T_x	131.1219 Nmm	u_{T_x}	1.75% of full scale load
T_y	37.57799 Nmm	u_{T_y}	1.5% of full scale load
T_z	-2.05822 Nmm	u_{T_z}	1.75% of full scale load

$$\theta_{Fbracket} = \begin{bmatrix} \frac{\partial F_{bracket1}}{\partial x_1} & \dots & \frac{\partial F_{bracket1}}{\partial x_n} \\ \vdots & \ddots & \vdots \\ \frac{\partial F_{bracketm}}{\partial x_m} & \dots & \frac{\partial F_{bracketm}}{\partial x_n} \end{bmatrix} n = 1, 2, \dots, 10; m = 1, 2, \dots, 6 \quad (\text{A.8})$$

$$u_{Fbracketm} = \left[\sum_{i=1}^m \left(\theta_{Fbracketm,i} u_{Fbracketi} \right)^2 \right]^{1/2} n = 1, 2, \dots, 10; m = 1, 2, \dots, 6 \quad (\text{A.9})$$

A.3 References

- [1] R. P. Paul, *Robot Manipulators: Mathematics, Programming, and Control: The Computer Control of Robot Manipulators*. Cambridge, Mass: MIT Press, 1981.
- [2] R. S. Figliola, "Uncertainty analysis," in *Theory and Design for Mechanical Measurements*, 5th ed. Anonymous Hoboken, NJ: John Wiley & Sons, 2011, pp. 161.

Appendix B Digital Image Correlation

B.1 Two-Dimensional Digital Image Correlation

B.1.1 Overview of Digital Image Correlation

The digital image correlation algorithm was first described by [1-3] and is summarized by [4]. Displacement between the reference and deformed image is calculated using the displacement mapping function B.1.

$$\begin{aligned} x'_i &= x_i + \xi(x_i, y_j) \\ y'_j &= y_j + \eta(x_i, y_j) \end{aligned} \quad (i, j = -M : M) \quad (\text{B.1})$$

In this equation (x_i, y_i) is the coordinate of the original image and (x'_i, y'_i) is the coordinate of the deformed image. The terms ξ and η are the shape functions. If only rigid body motion is observed then the zero- order shape function can be utilized. The zero- order shape function can be seen in equation B.2. From this equation it can be seen that the displacement of the deformed image from the reference image only depends on the original position (x_i, y_i) and the x and y displacement components of the reference subset (u, v) . If translation, rotation, shear and normal strains exist then the first- order shape function should be used. The first-order shape function is shown in equation B.3. This equations shows that the displacement of the deformed image depends on x_i, y_i, u, v

$\frac{\partial u}{\partial x}, \frac{\partial u}{\partial y}, \frac{\partial v}{\partial x}, \frac{\partial v}{\partial y}$ to allow for translation, rotation, shear and normal strain. In Equation

B.3 $\frac{\partial u}{\partial x}, \frac{\partial u}{\partial y}, \frac{\partial v}{\partial x}, \frac{\partial v}{\partial y}$ are the first-order displacement gradients for the reference subset.

Additionally, a higher order shape function can be utilized for more complicated deformations shown in Equation B.4

Shape Function	
Zero	$\xi_o(x_i, y_j) = u$
Order	$\eta_o(x_i, y_j) = v$
First	$\xi_1(x_i, y_j) = u + \frac{\partial u}{\partial x} \Delta x + \frac{\partial u}{\partial y} \Delta y$
Order	$\eta_1(x_i, y_j) = v + \frac{\partial v}{\partial x} \Delta x + \frac{\partial v}{\partial y} \Delta y$
Second	$\xi_2(x_i, y_j) = u + \frac{\partial u}{\partial x} \Delta x + \frac{\partial u}{\partial y} \Delta y + \frac{1}{2} \frac{\partial^2 u}{\partial^2 x} \Delta x^2 + \frac{1}{2} \frac{\partial^2 u}{\partial^2 y} \Delta y^2$
Order	$\eta_2(x_i, y_j) = v + \frac{\partial v}{\partial x} \Delta x + \frac{\partial v}{\partial y} \Delta y + \frac{1}{2} \frac{\partial^2 v}{\partial^2 x} \Delta x^2 + \frac{1}{2} \frac{\partial^2 v}{\partial^2 y} \Delta y^2$

The cross-correlation criterion used to determine the correlation between the reference and deformed image are shown in equations B.5 and B.6. These equations show the Cross-Correlation (CC) and Sum of Squared Difference (SSD) correlation methods. Additional cross-correlation equations exist which normalize the cross-correlation coefficient. The details of the more advanced cross-correlation criterion are summarized by [4]. For the cross correlation criterion $f(x_i, y_j)$ represents the gray scale intensity at positions (x_i, y_i) for the reference image and $g(x'_i, y'_j)$ represents the gray scale intensity at positions (x'_i, y'_j) of the deformed image. The cross- correlation C_{cc} determines the peak maximum correlation between the reference and deformed image while the sum of squared differences C_{SSD} determines the peak minimum correlation.

$$\text{Cross-Correlation (CC)} \quad C_{cc} = \sum_{i=-M}^M \sum_{j=-M}^M [f(x_i, y_j)g(x'_i, y'_j)] \quad (\text{B.5})$$

$$\begin{array}{l} \text{Sum of Squared} \\ \text{Differences (SSD)} \end{array} \quad C_{SSD} = \sum_{i=-M}^M \sum_{j=-M}^M [f(x_i, y_j) - g(x'_i, y'_j)]^2 \quad (\text{B.6})$$

B.1.2 Demonstration of the DIC Method

To demonstrate the digital image correlation algorithm a sample image was displaced a known amount. The sample DIC program was written using MATLAB (The MathWorks, Inc., Matlab, Natick, Massachusetts, USA) and is shown in **Figure B. 3 Sample 2D DIC program**

Using this program a 9 x 9 pixel image is generated with a random pattern of grayscale intensities. The reference image generated using this program is shown in Figure B. 1 (a). The image was displaced 1 pixel in the x -direction to generate the deformed image. The deformed image is shown in Figure B. 1 (b).

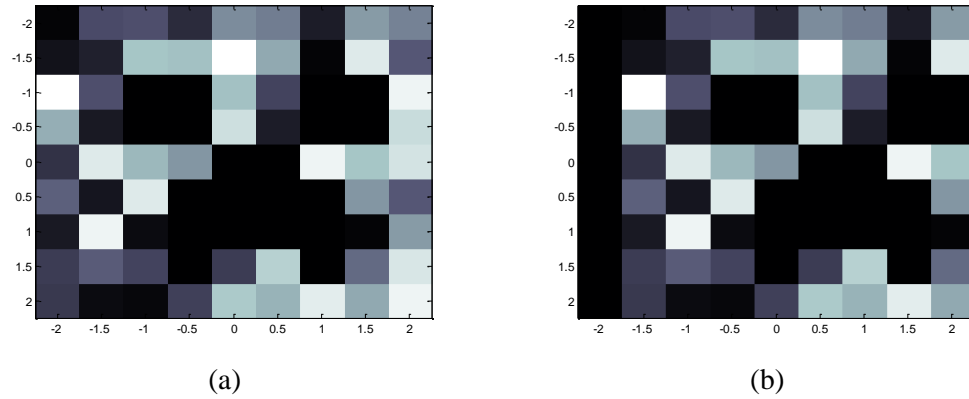


Figure B. 1 Sample 9x9 Image (a) Reference Image (b) Deformed image shifted 1 pixel to the right

The cross-correlation of the reference and deformed image was calculated using both the cross- correlation and sum of squared differences C_{SSD} methods. The cross-correlation coefficient distributions are shown in Figure B. 2 (a) and (b). Figure B. 2 Resultant cross-correlation coefficient distribution (a) SSD method (b) CC method

(a) shows the peak minimum found using the SSD method while Figure B. 2 (b) shows the peak maximum using the CC method. The correlation coefficient *extrema* for both

the SSD and CC method show that maximum correlation occurs at $u=1$, $v=0$ indicating the deformed image has translated 1 pixel in the x direction which corresponds the actual displacement of the reference image shown in Figure B. 1 (b).

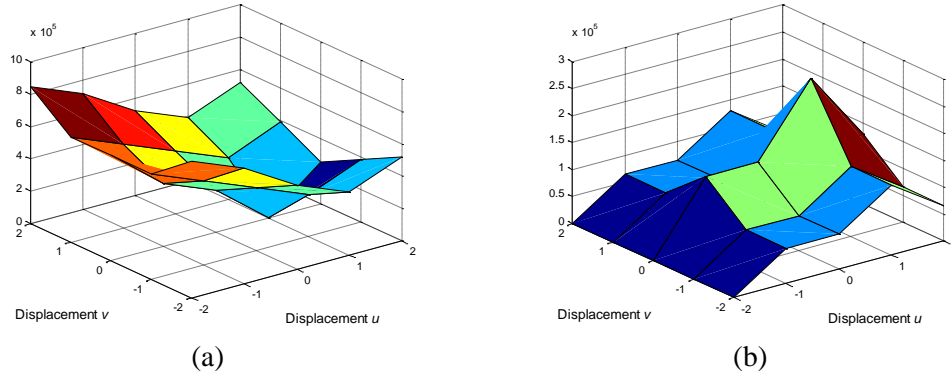


Figure B. 2 Resultant cross-correlation coefficient distribution (a) SSD method (b) CC method

This simple example shows that the deformation of an image can be determined using the digital image correlation method. More advance DIC method exist which allow for sub-pixel displacements to be measured. A summary of sub-pixel displacement algorithms is presented by [4].

```

%% 2D DIC proof
% Author: Garrett Melenka
% email: gmelenka@ualberta.ca
% date: February 22, 2012
%% Sample 9 x 9 grayscale images
%% Create a random image and translate the image a known amount tx and ty
% Image linear transformation source:
% http://www.mathworks.com/support/solutions/en/data/1-18WGT/index.html?pro
% duct=IP&solution=1-18WGT
I = randi([0 255], 9, 9); % create image of random intergers
tx = 1; % Integer translation along the horizontal component
ty = 0; % Integer translation along the vertical component
% Transform image
t = maketform('affine',[1 0 ; 0 1; tx ty]);
bounds = findbounds(t,[1 1; size(I)]);
bounds(1,:) = [1 1];
J = imtransform(I,t,'XData',[1 9],'YData',[1 9]);
%% DIC Algorithm
% This program compares both the Cross-Correlation (CC) and Sum of Square
% differences (SSD) methods for digital image correlation
% Examples of cross correlation algorithms can be found in:
% Pan, B., Qian, K., Xie, H., & Asundi, A. (2009). Two-dimensional digital
% image correlation for in-plane displacement and strain measurement:
% a review. Measurement Science and Technology
% Use 5 x 5 window size
N=5;
M = (N - 1)/2;
% Center of image
x=5;y=5;a=1;b=1;
% u and v are guesses for the displacement from image 1 to 2 in the x and
% y directions respectively
% The CC method will produce a peak maximum while the SSD method will
% produce a peak minimum
for u = -2:2
for v = -2:2
for j=-M:M
for i = -M:M
% Using Sum of Squared Differences Correlation Method (SSD)
CSSD = (I(y-j,x+i) - J(y-v-j,x+u+i))^2;
% Using cross-correlation criterion (CC)
C_crossCorrelation = (I(y-j,x+i) * J(y-v-j,x+u+i));
Cout_SSD(j+3,i+3) = CSSD;
Cout_CC(j+3,i+3) = C_crossCorrelation;
end
end
output(v+3,u+3) = sum(sum(Cout_SSD));
output_CC(v+3,u+3) = sum(sum(Cout_CC));
end
end
figure('Name','Correlation Peak SSD Method'); surf(-2:2,2:-1:-2,output)
figure('Name','Correlation Peak CC Method'); surf(-2:2,2:-1:-2,output_CC)
figure('Name','Original Image'); imagesc([-2 2], [-2 2], I); colormap(gray);
figure('Name','Displaced Image'); imagesc([-2 2], [-2 2], J); colormap(gray);

```

Figure B. 3 Sample 2D DIC program

B.2 3D DIC Method

DIC can be used in 2D or 3D configurations. The 2D configuration (single camera) allows for in-plane motion (x^*, y^*) to be measured whereas the 3D configuration (2 or more cameras) allows for both in-plane and out of plane motion (x^*, y^*, z^*) [5]. The measurement of three dimensional deformation can be achieved using a three dimensional (3D) digital image correlation technique. This method was initially

developed by Luo et al. [6] and applies the principles of stereovision and digital image correlation. The method of 3D deformation measurement has been used for many applications [5, 7-9]. In addition this method has been used in conjunction with a stereo microscope to measure the deformation of small scale objects [10, 11].

B.2.1 Stereo Vision Description

A schematic of a typical stereo vision setup is shown in Figure B. 4. This figure shows a point P which is a point on a physical object that is to be measured. The coordinates of the point P in the world coordinate system are X_w , Y_w , and Z_w . The physical point P is imaged in the image plane of the left (C_1) and right (C_2) camera at points P_1 and P_2 respectively. Each camera has its own coordinate system (X_{Ci} , Y_{Ci} , Z_{Ci}) where $i=1,2$. Using the two cameras shown in Figure B. 4 it is possible to determine the world coordinates of point P . To determine the world coordinates of point P two steps are required [6, 12]. First, a calibration must be performed to orient the cameras in three dimensional space. Second, stereo image matching is carried out to determine the difference between the two cameras. Once these two steps have been performed it is possible to determine the 3D position of point P . The accuracy of the 3D DIC measurement is highly dependent on the parameters that are calculated during the camera calibration [12].

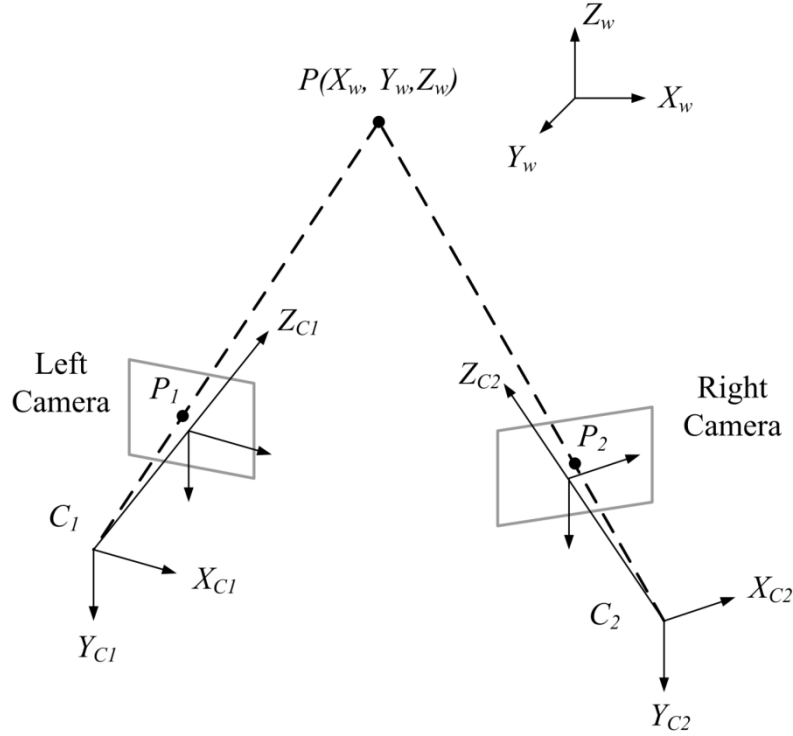


Figure B. 4 Schematic for stereo vision measurement

B.2.2 Stereo Camera Calibration

Calibration of the stereo cameras is performed to orient the cameras in 3D space. The calibration procedure determines the 3D position of each camera relative to the world coordinate system. Calibration for the stereomicroscope setup was carried out using a glass calibration target (Microscope Calibration Plate 0.2 to 1mm dot spacing, LaVision GmbH, Gottingen, Germany) that has a regular grid on the surface. The stereomicroscope calibration plate is shown in Figure B. 5. The target was displaced a known amount in the Z_w coordinate and three image pairs of the calibration targets were acquired. The calibration plate was displaced a known amount using a micrometer driven stage (MT01 Translation Stage, Thor Labs, Newton NJ, USA).

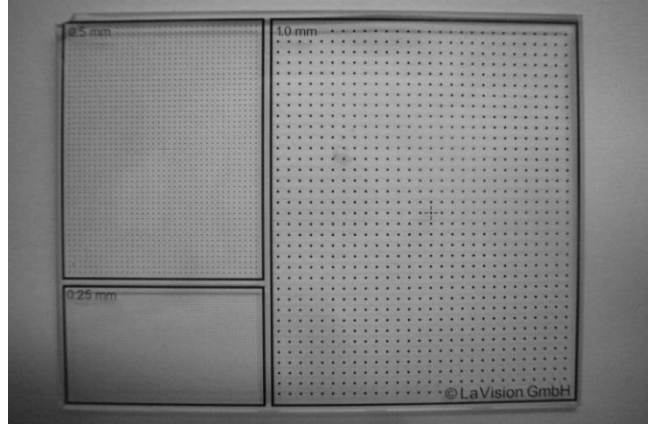


Figure B. 5: Stereo microscope calibration plate

The camera calibration is used to determine the intrinsic and extrinsic camera parameters M_{xi} , M_{yi} , f_i , k_i , $(h_o, v_o)_i$, $\{X_c, Y_c, Z_c\}_i$ and $(\theta_p, \theta_t, \theta_s)_i$ described by Luo et al.[6]. The magnification factors for each camera are described by the terms (M_{xi}, M_{yi}) which convert pixel coordinates to physical dimensions. The term f_i represents the focal length for the two cameras and k_i is the radial distortion for each camera. Terms $(h_o, v_o)_i$ describe the location of the center of the image plane for the two cameras. Terms $(\theta_p, \theta_t, \theta_s)_i$ represent the pan, tilt and swing angles for the two cameras and $\{X_c, Y_c, Z_c\}_i$ represent the global coordinates for each camera's origin. The terms M_{xi} , M_{yi} , f_i , k_i , and $(h_o, v_o)_i$ are the intrinsic camera parameters and depend only on the internal camera configuration. Variables $\{X_c, Y_c, Z_c\}$ and $(\theta_p, \theta_t, \theta_s)_i$ are the extrinsic camera parameters and are not predetermined by the camera configuration.

The 12 parameters for each camera are determined using a non-linear least squares method described by Luo et al.[6]. The error function that is minimized to determine the J^{th} camera parameters is described in B.7. In this equation J represents the camera

$$E(J) = \sum_{m=1}^{m=N} \left[(H_{Jm} - h_m)^2 + (V_{Jm} - v_m)^2 \right] \quad (\text{B.7})$$

number and m is the number of calibration images.

The calibration of a stereo camera setup described above is typically performed using a pin-hole camera model. It has been shown by Schreier et al. [13] that the pin-hole calibration model is not valid for the calibration of a stereomicroscope due to distortions caused by the internal optics of the microscope therefore a 3rd order polynomial calibration was implemented for the stereo microscope calibration [14]. A schematic of a common objective stereo microscope such as the Zeiss Stereo Discovery v8 is shown in Figure B. 6. The schematic shows that several lenses are used in the stereo microscope and that the cumulative distortion caused by the individual lenses results in strong distortion to the final image.

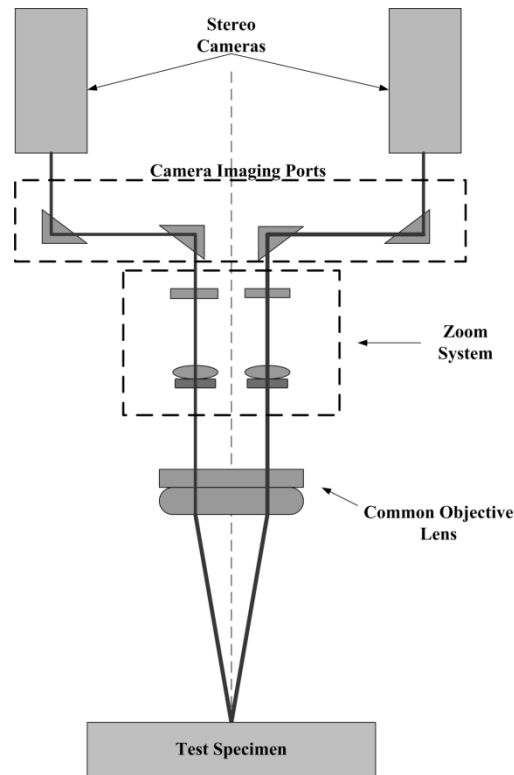


Figure B. 6: Common objective stereo microscope setup

B.2.3 Stereo Image Matching

Once the 12 parameters have been determined for each camera using the stereo calibration procedure described in Section B.2.2 the stereo image matching procedure can be carried out. Stereo image matching uses a similar method as the 2D DIC algorithm described in Section B.1. Instead of correlating between images taken a time t and $t+dt$ the image correlation algorithm is used to correlate between the left and right cameras (C_1 and C_2).

B.3 References

- [1] W. H. Peters and W. F. Ranson, "Digital Imaging Techniques in Experimental Stress Analysis," *Optical Engineering*, vol. 21, pp. 427-431, 1982.
- [2] T. C. Chu, W. F. Ranson and M. A. Sutton, "Applications of digital-image-correlation techniques to experimental mechanics," *Exp. Mech.*, vol. 25, pp. 232-244, 1985.
- [3] M. Sutton, C. Mingqi, W. Peters, Y. Chao and S. McNeill, "Application of an optimized digital correlation method to planar deformation analysis," *Image Vision Comput.*, vol. 4, pp. 143-150, 1986.
- [4] B. Pan, K. Qian, H. Xie and A. Asundi, "Two-dimensional digital image correlation for in-plane displacement and strain measurement: A review," *Meas Sci Technol*, vol. 20, 2009.
- [5] J. -. Orteu, "3-D computer vision in experimental mechanics," *Opt Lasers Eng*, vol. 47, pp. 282-291, 2009.
- [6] P. F. Luo, Y. J. Chao, M. A. Sutton and W. H. Peters III, "Accurate measurement of three-dimensional deformations in deformable and rigid bodies using computer vision," *Exp. Mech.*, vol. 33, pp. 123-132, 1993.
- [7] P. Synnergren, "Measurement of three-dimensional displacement fields and shape using electronic speckle photography," *Optical Engineering*, vol. 36, pp. 2302-2310, 1997.
- [8] P. Synnergren and M. Sjö Dahl, "A stereoscopic digital speckle photography system for 3-D displacement field measurements," *Optics and Lasers in Engineering*, vol. 31, pp. 425-443, 1999.

- [9] D. Garcia, J. J. Orteu and L. Penazzi, "A combined temporal tracking and stereo-correlation technique for accurate measurement of 3D displacements: Application to sheet metal forming," *J. Mater. Process. Technol.*, vol. 125-126, pp. 736-742, 2002.
- [10] N. J. Lawson and J. Wu, "Three-dimensional particle image velocimetry: Experimental error analysis of a digital angular stereoscopic system," *Measurement Science and Technology*, vol. 8, pp. 1455-1464, 1997.
- [11] M. A. Sutton, X. Ke, S. M. Lessner, M. Goldbach, M. Yost, F. Zhao and H. W. Schreier, "Strain field measurements on mouse carotid arteries using microscopic three-dimensional digital image correlation," *Journal of Biomedical Materials Research - Part A*, vol. 84, pp. 178-190, 2008.
- [12] B. Pan, H. Xie, L. Yang and Z. Wang, "Accurate measurement of satellite antenna surface using 3D digital image correlation technique," *Strain*, vol. 45, pp. 194-200, 2009.
- [13] H. Schreier, D. Garcia and M. Sutton, "Advances in light microscope stereo vision," *Experimental Mechanics*, vol. 44, pp. 278-288, 2004.
- [14] S. M. Soloff, R. J. Adrian and Z. -. Liu, "Distortion compensation for generalized stereoscopic particle image velocimetry," *Measurement Science and Technology*, vol. 8, pp. 1441-1454, 1997.

Appendix C Experimental Procedure

C.1 Overview

Testing of orthodontic bracket using the orthodontic torque simulator and stereo microscope requires that orthodontic brackets are prepared and tested in a standardized manner. The testing of the orthodontic brackets entails four major steps: sample preparation; camera calibration; data collection using the orthodontic torque simulator and stereo microscope; and post processing of the collected images. A flowchart describing the orthodontic test procedure is shown in Figure C. 1. The details of each measurement process will be described below.

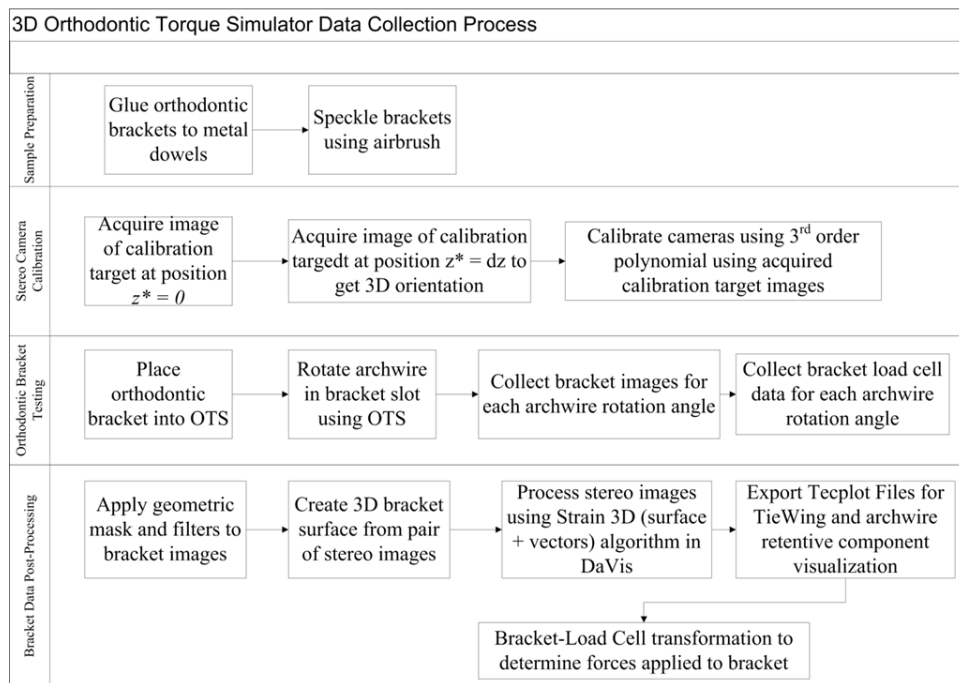


Figure C. 1 Overview of 3D strain imaging process

C.2 Sample Preparation

Sample preparation entails the gluing of the orthodontic brackets to the metallic dowels and then coating the surface of the brackets with a fluorescent paint. A bracket prepared using epoxy is shown in Figure C. 2.

C.2.1 Bracket Gluing Procedure

1. Drag one side of cylinders across P240 sandpaper (can be obtained from engineering machine shop). A single paper should be about 8"x11", and if you drag the cylinder in one direction across the width of the paper, that should be sufficient. This is to etch the surfaces and enhance epoxy adhesion.
2. Clean and prepare the bracket dowels in a fume hood. Obtain a thick paper towel, and wet the towel wet with acetone. Using the wet part of the towel, clean the tops of the cylinders. This will help remove oils and residue from the sandpaper to help adhesion. Acetone can also be used to remove epoxy from old bracket dowels.
3. Use Loctite Hydrosyl E-60HP to bond the brackets to cylinders. Apply a small amount of epoxy into a paper cup and mix the epoxy until the two parts of the epoxy become homogeneous. Apply epoxy to cylinder and place the bracket on top, as near center as possible.
4. Place the brass weight on top of the cylinder. The bar across the brass holder should partially engage the slot. Push down firmly to ensure the bracket is all way against the cylinder.
5. Allow epoxy to set for approximately 24 hours prior to testing



Figure C. 2: Bracket mounted on steel dowel. Brass weight is used to hold bracket in place while epoxy cures.

Note Regarding Bonding Procedure: It will take several attempts to determine how much glue is required. Too little glue and the bracket will debond during testing. Too much glue and the door could be glued shut. This is especially an issue with SPEED brackets.

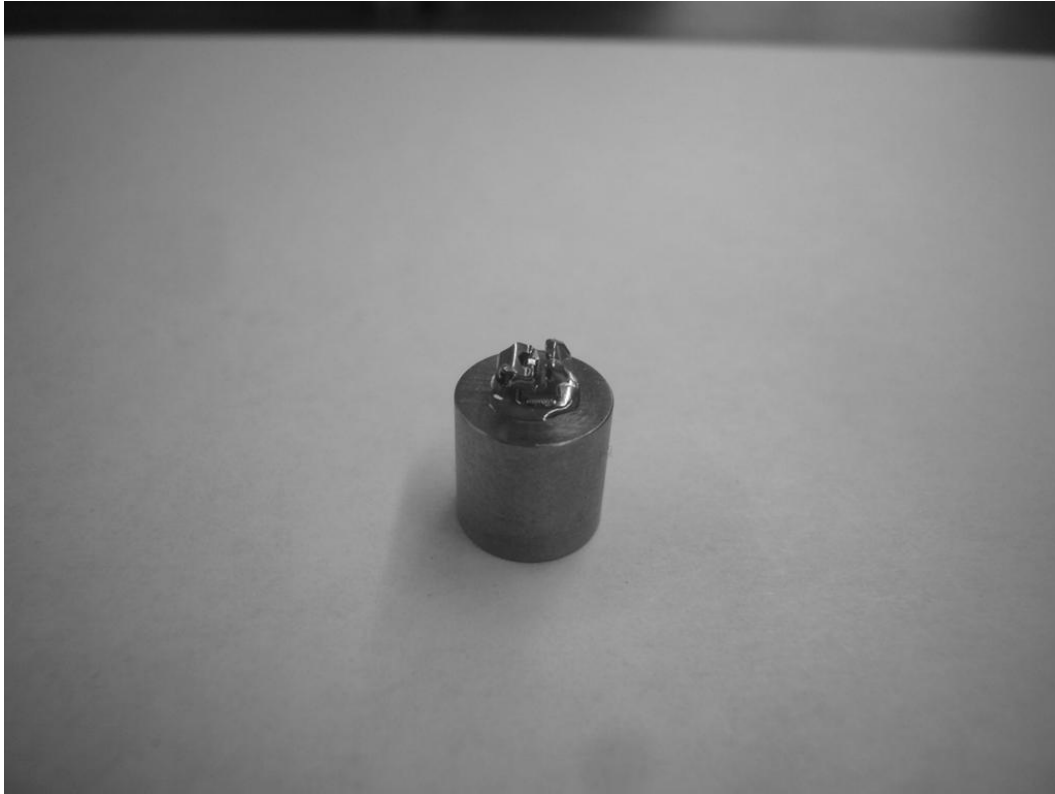


Figure C. 3: Bracket mounted on steel dowel after epoxy has cured.

C.2.2 Bracket Speckle Pattern Application

The orthodontic brackets are sprayed with fluorescent particles to produce a random pattern on the surface of the bracket. Ensure that size of particles is sufficient to track motion of bracket and ensure that fluorescent illumination provides adequate signal to noise ratio.

1. Line up 5-10 brackets on an archwire and close the archwire retentive component for each bracket around the archwire. This provides a convenient way to ensure the bracket dowels do not move when applying paint with the airbrush.
2. Set air regulator to approximately 65 psi
3. Use the Iwata Custom Micron- B airbrush (shown in Figure C. 4) to apply a random speckle pattern to the bracket surface
4. Coat the surface of the bracket with green fluorescent airbrush paint (5404 Fluorescent Green Createx Airbrush Colors, Createx Colors, East Granby CT). Reduce the paint with airbrush reducer at a ratio of approximately

2:1 to improve the flow of the paint through an airbrush (Wicked W100 Reducer Createx Airbrush Colors, Createx Colors, East Granby CT).

5. Spray the brackets until an even coat is on the surface of all the brackets. This may take several passes with the airbrush and the air flow through the brush may need to be adjusted.

An archwire with fluorescent paint is shown in Figure C. 5. This figure shows a close-up (Figure C. 5 (a)) and macro image (Figure C. 5 (b)) of the archwire. This figure shows that the even coating of fluorescent paint results in a random speckle pattern when viewed using the stereo microscope. Figure C. 5 (c) shows two orthodontic brackets that have been coated with the fluorescent paint. This figure shows the approximate amount of fluorescent paint required to produce a random speckle pattern on the bracket surfaces.



Figure C. 4: Iwata Custom Micron-B Airbrush

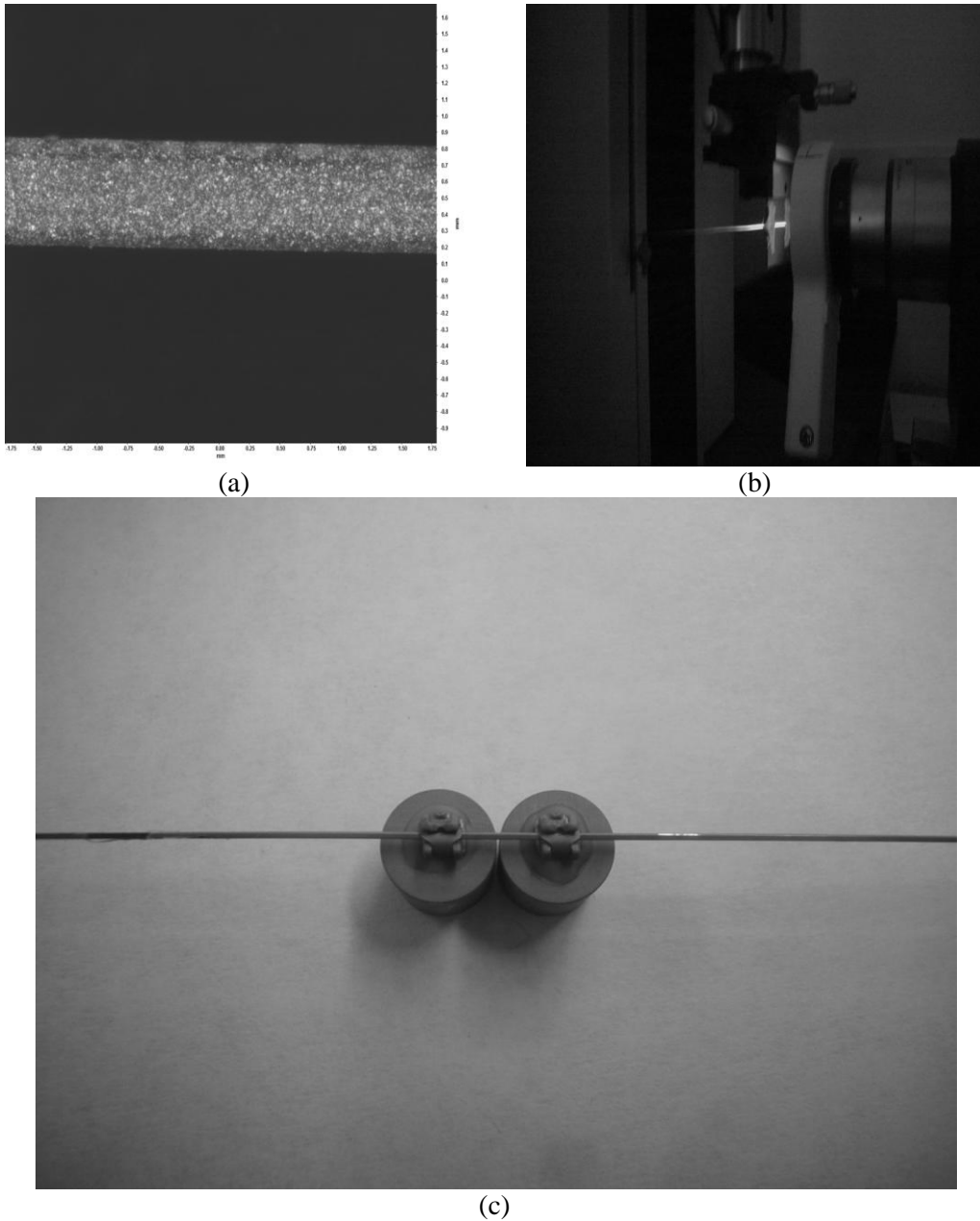


Figure C. 5: Fluorescent speckle pattern (a) Archwire at 2.0x magnification (b) Archwire in front of stereo microscope (c) two brackets sprayed with fluorescent airbrush paint.

C.2.3 Camera Calibration

Calibration of the stereo cameras is performed to orient the cameras in 3D space. The calibration procedure determines the 3D position of each camera relative to the world coordinate system. Calibration for the stereo microscope setup was carried out using a glass calibration target (Microscope Calibration Plate 0.25 to 1mm dot spacing, LaVision GmbH, Gottingen, Germany) that has a regular grid on the surface. The

stereomicroscope calibration plate is shown in Figure C. 6. The target was displaced a known amount in the Z_w coordinate and four image pairs of the calibration targets were acquired. The calibration plate was displaced a known amount using a micrometer driven stage (MT01 Translation Stage, Thor Labs, Newton NJ, USA). The calibration of the stereo microscope for measuring bracket deformation was completed using the 0.5mm calibration target grid. The calibration target was displaced in 25.4 μ m increments using the micrometer driven translation stage.

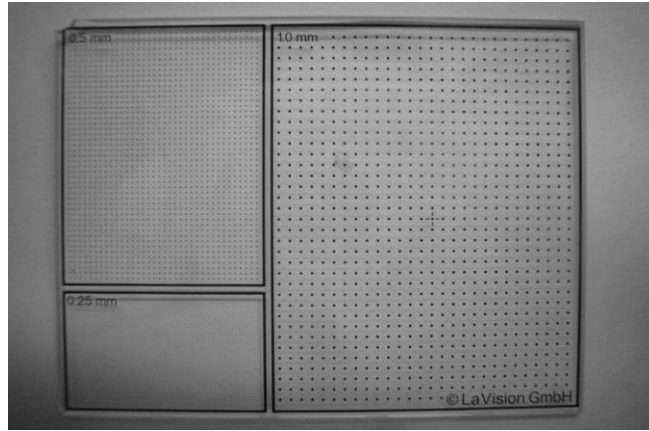


Figure C. 6: Stereo microscope calibration plate

C.3 Data Collection

C.3.1 Bracket/Load Cell Offset Measurement

1. Measure Bracket dowel height (Δz) before bracket is mounted on dowel using calipers
2. Measure dowel diameter (Φ) using calipers
3. Image bracket at 1.0x zoom using stereo microscope to measure Δx and Δy offsets
4. Use measured Δx , Δy and Δz values for load cell to bracket transformation

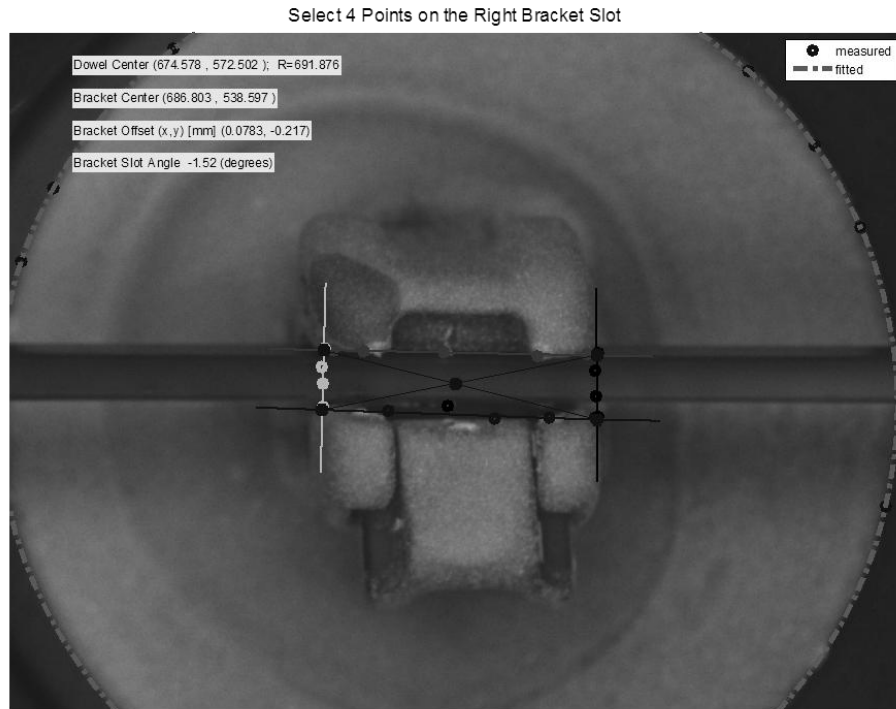


Figure C. 7: Bracket offset measurement

C.3.2 Orthodontic Torque Simulator Operation

1. Open “Auto Torsion Rig” from desktop.
2. Insert wire into dies.
3. Insert the cylinder into holder on the load cell with the door open and facing away
4. Raise the bracket up so that the wire is *nearly* engaging the slot, but still not touching it. Use the tool with a square end to set the distance from the edge of the bracket to the die.
5. Tighten the archwire dies.
6. Press “**Start**” under “Setup” on left hand side. This begins showing the forces and moments real-time, as well as the angle as read off the inclinometer.
 - a. Note, the inclinometer read-out angle is based on a user-set zero point. Selecting “Reset” under the inclinometer dial will set a new zero point.
 - b. Also note that when the “Start” button under the “Setup” section is not selected, the current angle can be read by selecting “Read Angle” under the inclinometer dial.
 - c. **Important:** the angle should only be moved manually when the motor is not running. The angle can be manually adjusted using the knob attached to the worm gear.
7. Select “**Zero Loadcell**”. Keep in mind we have not inserted the wire into the slot yet.
8. Once load cell is zeroed, raise the bracket so that the wire engages the slot.

9. Approximately zero the load cell using the y and z-axis stages, and utilize the rotation from the unfastened cylinder in the holder. (Note: the holder is always fastened)
10. Tighten the cylinder into place.
11. Re-zero as close as possible using x, y, and rotation stages. Usually $F_x < 0.3\text{N}$, F_y and $F_z < 0.08\text{N}$, and $T_z < 0.5\text{Nmm}$. T_x will change with angle and T_y is impossible to alter.
12. Press the button called **“File Header”** under the section labeled “3-Documentation”. Ensure the file has a unique name.
 - a. If you wish to use the “Experiment Information” section, it will title the *.log file with a header. If you use this you *cannot* change the header information after naming the file. If you do, it will produce an error message while trying to start the experiment.
13. Assuming you are still nearly zeroed, deselect the **“Start”** button in “Setup” (it will say “Stop” while selected, and after deselecting will go back to “Start”).
14. Select **“Start”** under the “Motor Control” section.
15. Select **“Go to Origin”** under the “Motor Control” section.
 - a. If an origin has been set, it will go to it. The origin should be the start angle of the experiment.
 - b. If an origin has not been set, then set the desired origin. This can be done either with the motor running or not. Typically, origin and the zero point of the inclinometer are set to the same place.
16. Select **“Start Exp”** to begin data acquisition. The machine will automatically go to all the specified angles in the range. This can take several minutes, depending on your settings.
17. Select the button labeled **“Running”** under the “Motor Control” section to stop the motor.
18. After selecting **“Start”** from the “Setup” section to get a real-time angle, set the angle to somewhere in the torque play region. Open the bracket door and lower the bracket away from the wire. The wire can then be removed or moved to a fresh part of it. Do not reuse the same part of the wire.
19. To repeat more experiments, return to *Step 2* above.
20. Once finished collecting data, close the Auto Torsion Jig window. It will prompt you to save the settings. Select yes or no as desired. It will save the zero angle for the inclinometer and the origin of the motor, assuming nothing is unplugged until the next session.
21. Proceed to post-processing of data.
22. When finished with the machine, turn off the optical light, put the cover back on the camera, and unplug the power from the top of the camera.

C.4 Bracket Post Processing Method

Images of orthodontic brackets collected using the Orthodontic Torque Simulator (OTS) were post processed using DaVIS 8.0.6 (LaVision GmbH DaVis 8.06. Gottingen, Germany; 2009) [1, 2]. The 3D surface was recreated using this software and three dimensional (3D) digital image correlation (DIC) was performed on the collected images to determine the displacement of the orthodontic brackets due to archwire rotation. An

example raw image of a bracket is shown in Figure C. 8 (a). Prior to computing the 3D displacement vectors for the brackets an image mask, sliding average and normalization filter were applied to the bracket. The geometric mask can be seen in Figure C. 8 (b). This image shows that the out of focus regions, such as the bracket base and the dowel shown in Figure C. 8 (a), were eliminated using the geometric mask.

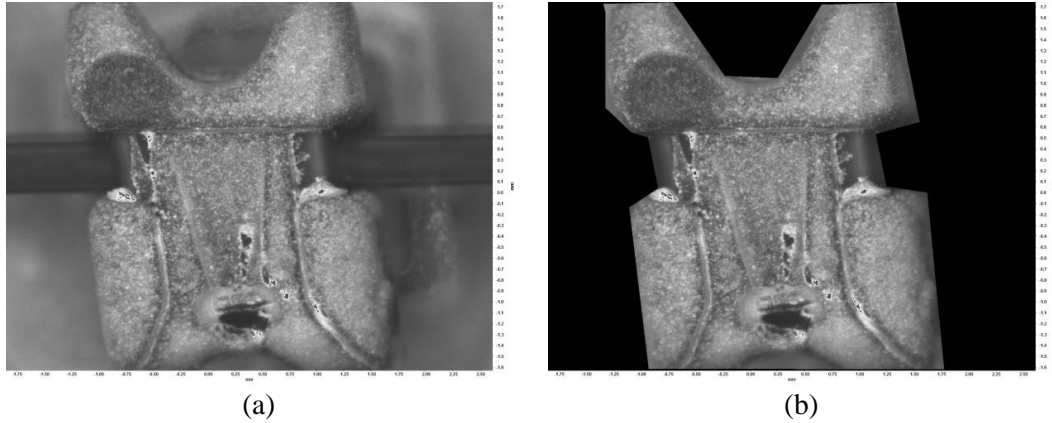


Figure C. 8:Orthodontic bracket (a) raw image (b) geometric mask applied to image

After the geometric mask was applied to the bracket a sliding average filter and normalization filters were applied to the bracket image. The result of the sliding average and normalization filters are shown in Figure C. 9 (a) and (b) respectively. Figure C. 9 (b) shows the consistent speckle pattern that is exists on the bracket surface after the image has been filtered.

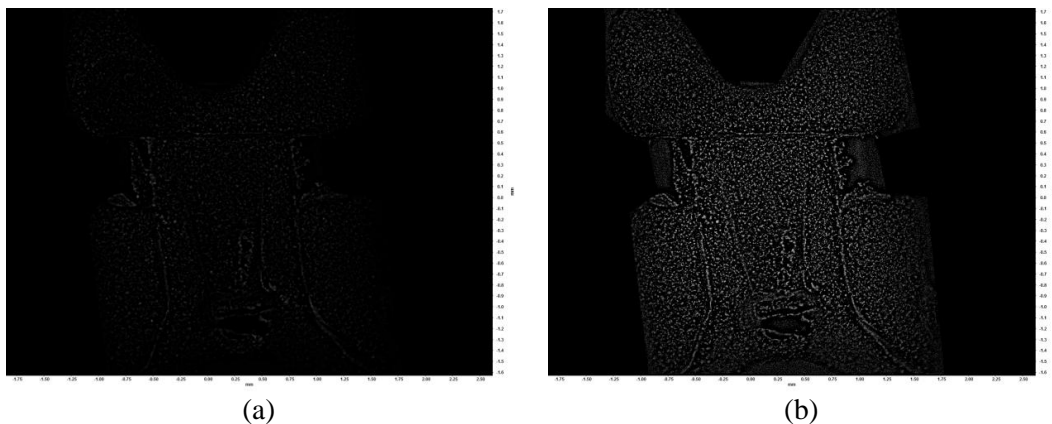


Figure C. 9: Filters applied to bracket (a) subtract sliding average filter (b) max-min normalization

Once the bracket images have been filtered using the sliding average and normalization filter the initial 3D surface is created. The 3D surface is created as a reference for subsequent stereo image pairs. The 3D surface created from a pair of stereo images is shown in Figure C. 10 (a). Finally, once the reference 3D surface has been created the 3D displacement vectors can be calculated. An example of the 3D displacement vectors calculated for an orthodontic bracket can be seen in Figure C. 10 (b).

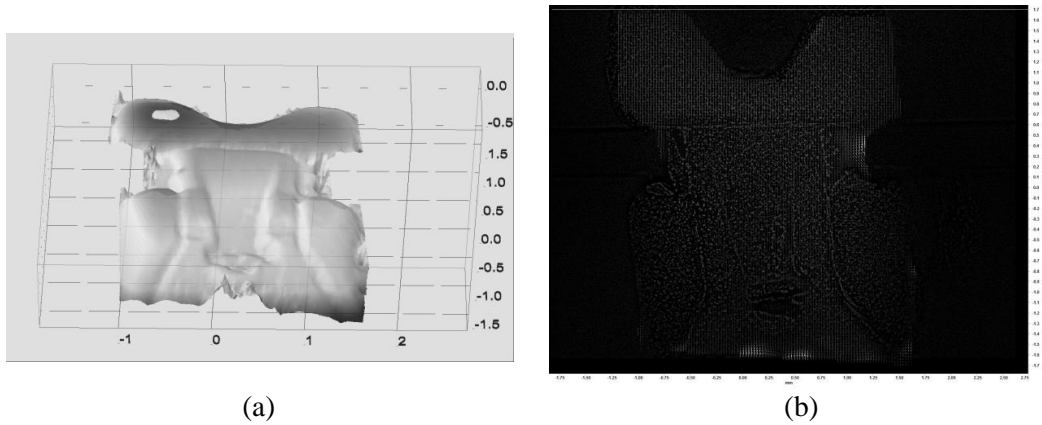


Figure C. 10: Processed bracket data (a) calculated bracket surface height (b) 3D displacement vectors of bracket surface

The processing method and the settings used in the DaVIS 8.0.6 (LaVision GmbH DaVis 8.06. Gottingen, Germany; 2009) software to process 3D orthodontic bracket deformation is summarized in Table C. 1.

Table C. 1 Summary of Image Processing Settings

Processing Method	Description
Measurement Window Size	1376×1040 pixels or 4.25 x 3.3 mm at 2.0x Magnification
Processing Routine	Strain3D(surface + vectors)
Subtract Sliding Average Filter	Filter Length in Pixel: 8 Pixels
Max-Min Filter For Intensity	Filter Length in Pixel: 7 Pixels
Normalization	
Initial Surface Height Calculation	Max Residual Image Shift: 64 pixel Size of Surface Pattern 8 pixel Type of Sample: Steep
Processing Specification	First Pass: 128 x128 pixel 50% overlap 1 pass Second Pass 64 x 64 87 % overlap 3 passes
Post Processing	Median Filter Fill all empty positions by interpolation

C.5 3D Bracket Data Post Processing Program

The 3D bracket data processing program loads the TecPlot vector data from DaVIS as well as the LOG file collected from the Torque Machine. The program automates the measurement of 3D bracket deformation, creation of VTK files for ParaView Visualization and creation of an excel file with bracket deformation and load cell data. The operation of the 3D bracket measurement program is summarized in Figure C. 11. The graphical user interface (GUI) used with this program is shown in Figure C. 12. The code used to generate the GUI used to process the bracket data is shown in Figure C. 20.

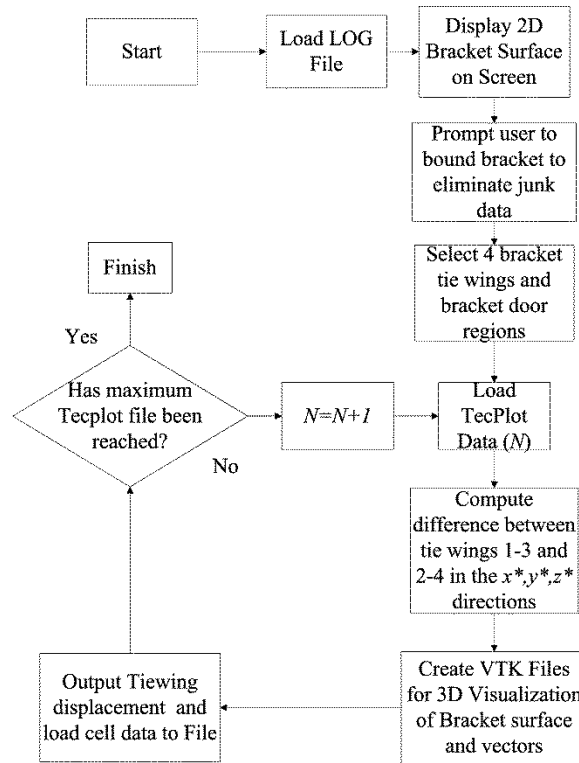


Figure C. 11: Flow chart of 3D bracket data processing program

The graphical user interface calls the function *TrackBracketDef* which is shown in Figure C. 21. This function allows the user to select the four bracket tie-wings and archwire retentive component and determines the motion of the bracket tie-wings. The function *TrackBracketDef* calls the function *choose_tiewing* to determine the average displacement in the x, y, z directions of each tie-wing. The function *choose_tiewing* is shown in Figure C. 23.

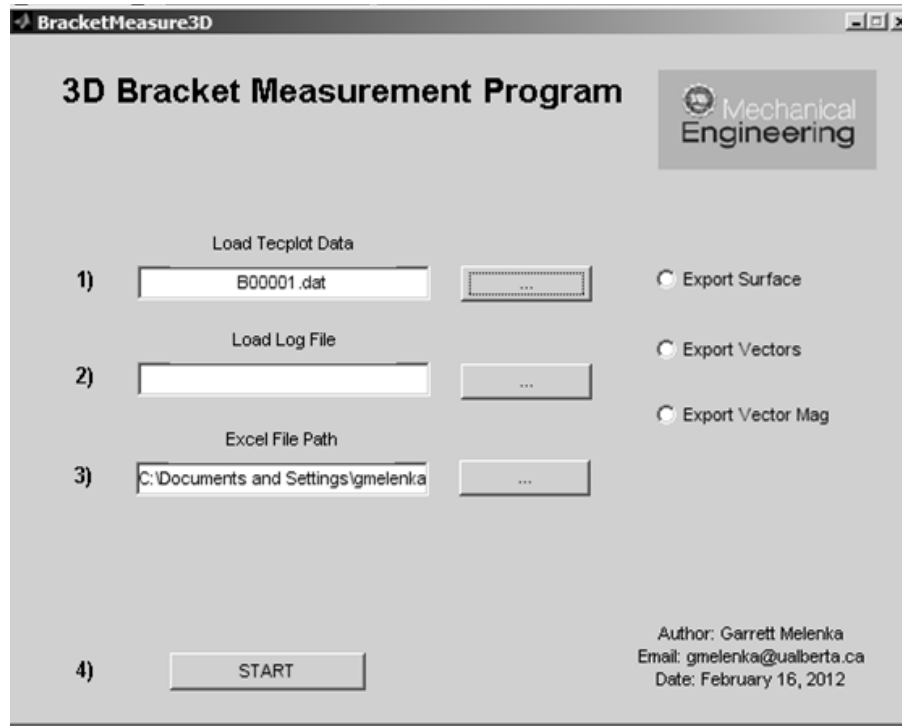


Figure C. 12: 3D Bracket measurement GUI

First, the TecPlot surface is loaded into Matlab. This is shown in Figure C. 13. The color in this image represents the surface height. The user is prompted to create a box which bounds the bracket. This will be used to eliminate the junk data created by DaVIS for ParaView Visualization. The bounded bracket without junk data can be seen in Figure C. 15.

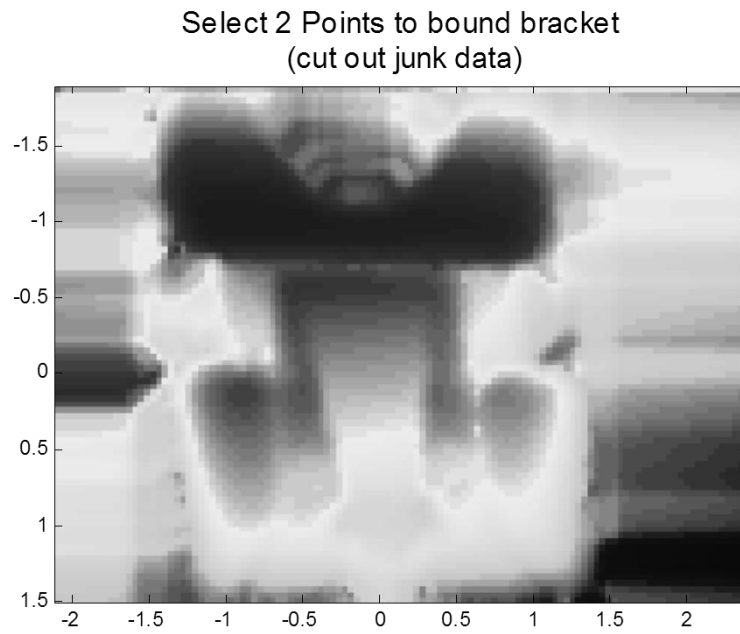


Figure C. 13: Original bracket surface in MATLAB

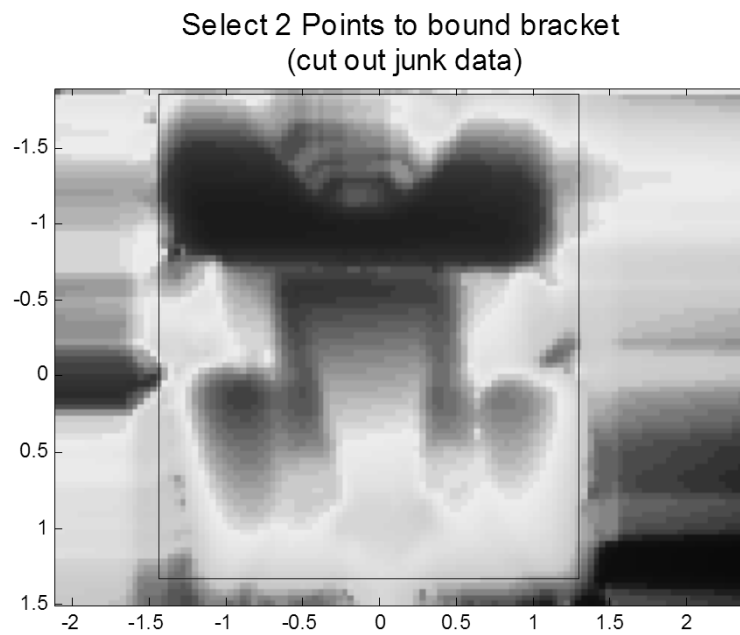


Figure C. 14: Bounding box around bracket to eliminate extra image data

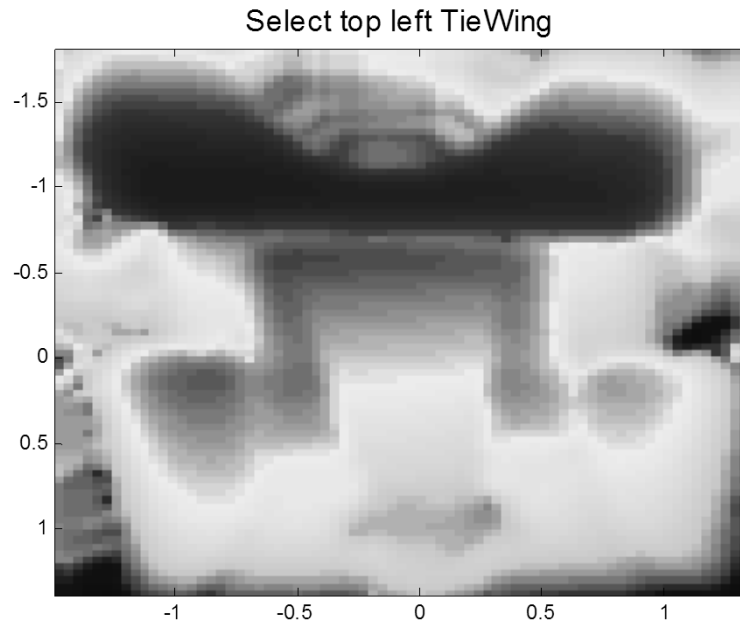


Figure C. 15: Cropped bracket image

The user is then prompted to select the four bracket tie wings. The selected bracket tie wings are shown in Figure C. 16. The resultant displacement of the tie wings in the x^* , y^* and z^* directions are shown in Figure C. 17, Figure C. 18, Figure C. 19 respectively.

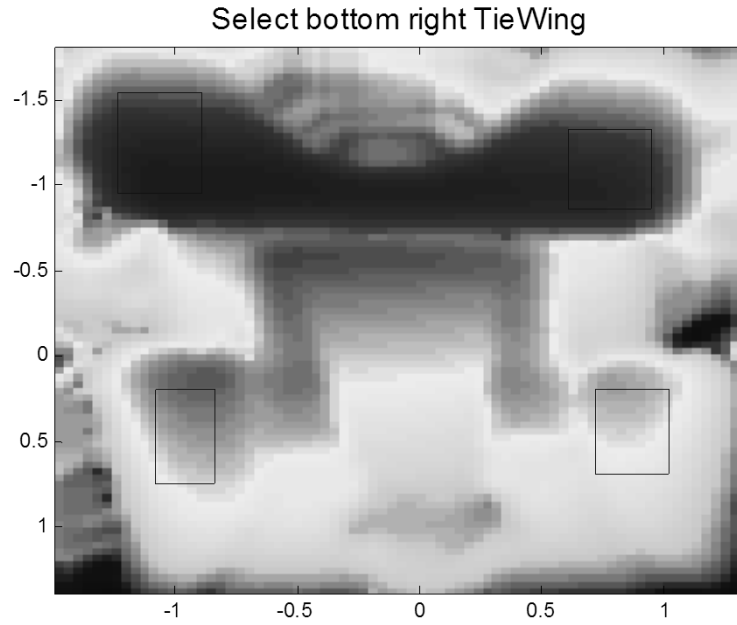


Figure C. 16: Four selected bracket tie-wings

Finally, the resultant displacement data is written to an excel file. The data processed using the functions *TrackBracketDef* and *choose_tiewing* is written to an excel file using the function *dataToExcel* shown in Figure C. 24. The displacement of the bracket tie-wings in the x^* , y^* and z^* directions are shown in Figure C. 17, Figure C. 18, and Figure C. 19 respectively.

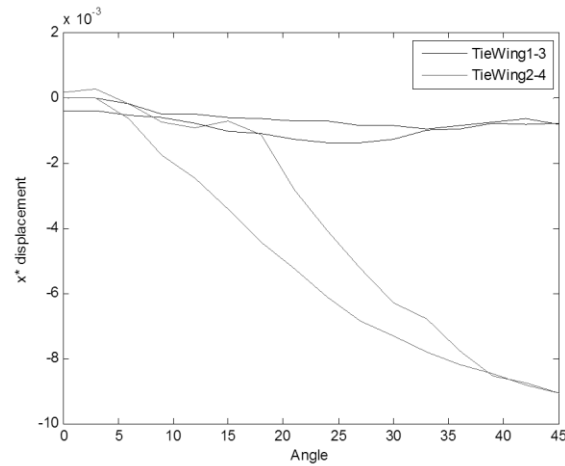


Figure C. 17: x^* Deformation

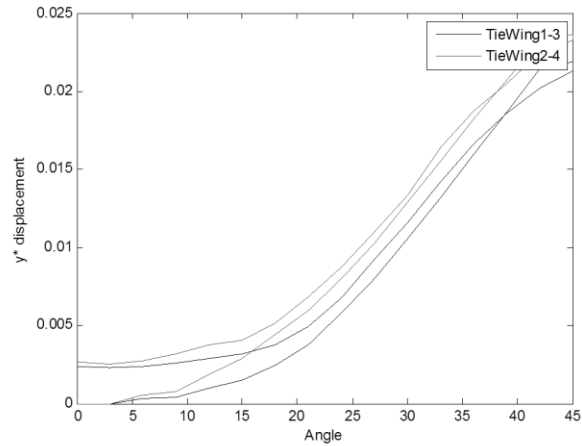


Figure C. 18: y^* Deformation

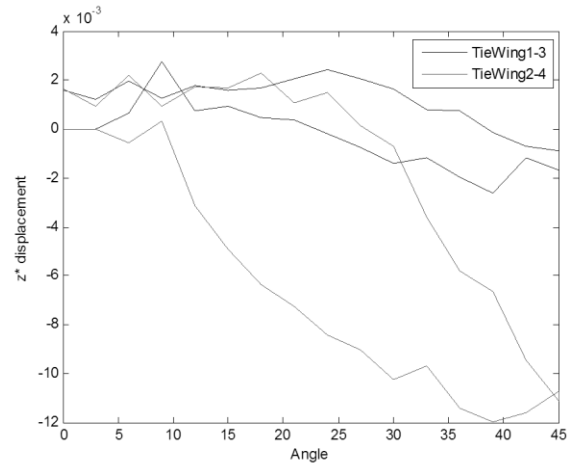


Figure C. 19: z^* Deformation

```
function varargout = BracketMeasure3D(varargin)
% BRACKETMEASURE3D M-file for BracketMeasure3D.fig
%   BRACKETMEASURE3D, by itself, creates a new
BRACKETMEASURE3D or raises the existing
%   singleton*.
%
%   H = BRACKETMEASURE3D returns the handle to a new
BRACKETMEASURE3D or the handle to
%   the existing singleton*.
%
%   BRACKETMEASURE3D('CALLBACK',hObject,eventData,handles,...)
calls the local
%   function named CALLBACK in BRACKETMEASURE3D.M with the
given input arguments.
%
%   BRACKETMEASURE3D('Property','Value',...) creates a new
BRACKETMEASURE3D or raises the
```

```

%     existing singleton*. Starting from the left, property
value pairs are
%     applied to the GUI before BracketMeasure3D_OpeningFcn gets
called. An
%     unrecognized property name or invalid value makes property
application
%     stop. All inputs are passed to
BracketMeasure3D_OpeningFcn via varargin.
%
%     *See GUI Options on GUIDE's Tools menu. Choose "GUI
allows only one
%     instance to run (singleton)".
%
% See also: GUIDE, GUIDATA, GUIHANDLES

% Edit the above text to modify the response to help
BracketMeasure3D

% Last Modified by GUIDE v2.5 27-Mar-2012 10:12:15
% Begin initialization code - DO NOT EDIT

gui_Singleton = 1;
gui_State = struct('gui_Name',       mfilename, ...
                  'gui_Singleton',   gui_Singleton, ...
                  'gui_OpeningFcn',   @BracketMeasure3D_OpeningFcn, ...
                  'gui_OutputFcn',    @BracketMeasure3D_OutputFcn, ...
                  'gui_LayoutFcn',    [] , ...
                  'gui_Callback',     []);
if nargin && ischar(varargin{1})
    gui_State.gui_Callback = str2func(varargin{1});
end

if nargout
    [varargout{1:nargout}] = gui_mainfcn(gui_State, varargin{:});
else
    gui_mainfcn(gui_State, varargin{:});
end
% End initialization code - DO NOT EDIT

% --- Executes just before BracketMeasure3D is made visible.
function BracketMeasure3D_OpeningFcn(hObject, eventdata, handles,
varargin)
% This function has no output args, see OutputFcn.
% hObject     handle to figure
% eventdata   reserved - to be defined in a future version of
MATLAB
% handles     structure with handles and user data (see GUIDATA)
% varargin    command line arguments to BracketMeasure3D (see
VARARGIN)

% Choose default command line output for BracketMeasure3D
handles.output = hObject;

```

```

% Update handles structure
guidata(hObject, handles);
MecEImg=imread('MecE.jpg');
imshow(MecEImg);

% UIWAIT makes BracketMeasure3D wait for user response (see
UIRESUME)
% uiwait(handles.figure1);

% --- Outputs from this function are returned to the command
line.
function varargout = BracketMeasure3D_OutputFcn(hObject,
eventdata, handles)
% varargout    cell array for returning output args (see
VARARGOUT);
% hObject      handle to figure
% eventdata    reserved - to be defined in a future version of
MATLAB
% handles      structure with handles and user data (see GUIDATA)

% Get default command line output from handles structure
varargout{1} = handles.output;

function LoadTecplotDataEdit_Callback(hObject, eventdata, handles)
% hObject      handle to LoadTecplotDataEdit (see GCBO)
% eventdata    reserved - to be defined in a future version of
MATLAB
% handles      structure with handles and user data (see GUIDATA)

% Hints: get(hObject,'String') returns contents of
LoadTecplotDataEdit as text
%           str2double(get(hObject,'String')) returns contents of
LoadTecplotDataEdit as a double

% --- Executes during object creation, after setting all
properties.
function LoadTecplotDataEdit_CreateFcn(hObject, eventdata,
handles)
% hObject      handle to LoadTecplotDataEdit (see GCBO)
% eventdata    reserved - to be defined in a future version of
MATLAB
% handles      empty - handles not created until after all
CreateFcns called

% Hint: edit controls usually have a white background on Windows.
%           See ISPC and COMPUTER.
if ispc && isequal(get(hObject,'BackgroundColor'),
get(0,'defaultUicontrolBackgroundColor'))
    set(hObject,'BackgroundColor','white');
end

```

```

end

function LoadLogfileEdit_Callback(hObject, eventdata, handles)
% hObject      handle to LoadLogfileEdit (see GCBO)
% eventdata    reserved - to be defined in a future version of
MATLAB
% handles      structure with handles and user data (see GUIDATA)

% Hints: get(hObject,'String') returns contents of
LoadLogfileEdit as text
%          str2double(get(hObject,'String')) returns contents of
LoadLogfileEdit as a double

% --- Executes during object creation, after setting all
properties.
function LoadLogfileEdit_CreateFcn(hObject, eventdata, handles)
% hObject      handle to LoadLogfileEdit (see GCBO)
% eventdata    reserved - to be defined in a future version of
MATLAB
% handles      empty - handles not created until after all
CreateFcns called

% Hint: edit controls usually have a white background on Windows.
%          See ISPC and COMPUTER.
if ispc && isequal(get(hObject,'BackgroundColor'),
get(0,'defaultUiControlBackgroundColor'))
    set(hObject,'BackgroundColor','white');
end

function LoadIM7Edit_Callback(hObject, eventdata, handles)
% hObject      handle to LoadIM7Edit (see GCBO)
% eventdata    reserved - to be defined in a future version of
MATLAB
% handles      structure with handles and user data (see GUIDATA)

% Hints: get(hObject,'String') returns contents of LoadIM7Edit as
text
%          str2double(get(hObject,'String')) returns contents of
LoadIM7Edit as a double

% --- Executes during object creation, after setting all
properties.
function LoadIM7Edit_CreateFcn(hObject, eventdata, handles)
% hObject      handle to LoadIM7Edit (see GCBO)
% eventdata    reserved - to be defined in a future version of
MATLAB
% handles      empty - handles not created until after all
CreateFcns called

```

```

% Hint: edit controls usually have a white background on Windows.
%       See ISPC and COMPUTER.
if ispc && isequal(get(hObject,'BackgroundColor'),
get(0,'defaultUicontrolBackgroundColor'))
    set(hObject,'BackgroundColor','white');
end

% --- Executes on button press in LoadTecplotDataButton.
function LoadTecplotDataButton_Callback(hObject, eventdata, handles)
% hObject      handle to LoadTecplotDataButton (see GCBO)
% eventdata    reserved - to be defined in a future version of
MATLAB
% handles      structure with handles and user data (see GUIDATA)
global tecplot_name
global tecplot_path
[tecplot_name, tecplot_path] =
uigetfile({'*.dat'; '*.DAT'}, 'Choose Tecplot File');

if tecplot_name ~= 0
    set(handles.LoadTecplotDataEdit, 'String', tecplot_name);
    set(handles.ExcelFilenameEdit, 'String', tecplot_path);
else
    set(handles.LoadTecplotDataEdit, 'String', '');
end

% --- Executes on button press in LoadLogfileButton.
function LoadLogfileButton_Callback(hObject, eventdata, handles)
% hObject      handle to LoadLogfileButton (see GCBO)
% eventdata    reserved - to be defined in a future version of
MATLAB
% handles      structure with handles and user data (see GUIDATA)
global log_name
global log_path
[log_name, log_path] = uigetfile({'*.log'; '*.LOG'}, 'Choose Log
File');

if log_name ~= 0
    set(handles.LoadLogfileEdit, 'String', log_name);
else
    set(handles.LoadLogfileEdit, 'String', '');
end

% --- Executes on button press in LoadIM7Button.
function LoadIM7Button_Callback(hObject, eventdata, handles)
% hObject      handle to LoadIM7Button (see GCBO)
% eventdata    reserved - to be defined in a future version of
MATLAB
% handles      structure with handles and user data (see GUIDATA)
global im7_path
global im7_name
[im7_name, im7_path] = uigetfile({'*.im7'; '*.IM7'}, 'Choose DaVis

```



```

IM7 File');

if im7_name ~= 0
    set(handles.LoadIM7Edit,'String',im7_name);
else
    set(handles.LoadIM7Edit,'String','');
end

% --- Executes on button press in start.
function start_Callback(hObject, eventdata, handles)
% hObject      handle to start (see GCBO)
% eventdata    reserved - to be defined in a future version of
MATLAB
% handles      structure with handles and user data (see GUIDATA)
global im7_path
global im7_name
global log_name
global log_path
global tecplot_name
global tecplot_path
log_nm = strcat(log_path,log_name);
% Load Torque Machine Log Data
logdata = Load_LogData(log_nm);
SurfaceSelect = 0;
VectorSelect = 0;
VectorMagSelect = 0;
newbox = 0;
if (get(handles.SurfaceRadio,'Value') == 1)
    % Surface Radio Button Selected
    SurfaceSelect = 1;
end
if (get(handles.VectorRadio, 'Value') == 1)
    VectorSelect = 1;
end
if (get(handles.VectorMagRadio, 'Value') == 1)
    VectorMagSelect =1;
end
if (get(handles.ReuseBoxesRadio, 'Value') ==1)
    newbox = 1;
end

TrackBracketDef(im7_path,im7_name,log_name,log_path,tecplot_name,
tecplot_path, SurfaceSelect, VectorSelect,
VectorMagSelect,newbox, logdata);

function ExcelFilenameEdit_Callback(hObject, eventdata, handles)
% hObject      handle to ExcelFilenameEdit (see GCBO)
% eventdata    reserved - to be defined in a future version of
MATLAB
% handles      structure with handles and user data (see GUIDATA)

% Hints: get(hObject,'String') returns contents of
ExcelFilenameEdit as text
%          str2double(get(hObject,'String')) returns contents of

```

ExcelFilenameEdit as a double

```
% --- Executes during object creation, after setting all
properties.
function ExcelFilenameEdit_CreateFcn(hObject, eventdata, handles)
% hObject    handle to ExcelFilenameEdit (see GCBO)
% eventdata  reserved - to be defined in a future version of
MATLAB
% handles    empty - handles not created until after all
CreateFcns called

% Hint: edit controls usually have a white background on Windows.
%         See ISPC and COMPUTER.
if ispc && isequal(get(hObject,'BackgroundColor'),
get(0,'defaultUiControlBackgroundColor'))
    set(hObject,'BackgroundColor','white');
end

% --- Executes on button press in ExcelFilenameButton.
function ExcelFilenameButton_Callback(hObject, eventdata,
handles)
% hObject    handle to ExcelFilenameButton (see GCBO)
% eventdata  reserved - to be defined in a future version of
MATLAB
% handles    structure with handles and user data (see GUIDATA)
global tecplot_path
global excel_path
excel_path = uigetdir(tecplot_path);

if excel_path ~= 0
    set(handles.ExcelFilenameEdit,'String',excel_path);
else
    set(handles.ExcelFilenameEdit,'String',tecplot_path);
end

% --- Executes on button press in SurfaceRadio.
function SurfaceRadio_Callback(hObject, eventdata, handles)
% hObject    handle to SurfaceRadio (see GCBO)
% eventdata  reserved - to be defined in a future version of
MATLAB
% handles    structure with handles and user data (see GUIDATA)

% Hint: get(hObject,'Value') returns toggle state of SurfaceRadio

% --- Executes on button press in VectorRadio.
function VectorRadio_Callback(hObject, eventdata, handles)
% hObject    handle to VectorRadio (see GCBO)
% eventdata  reserved - to be defined in a future version of
MATLAB
% handles    structure with handles and user data (see GUIDATA)
```

```

% Hint: get(hObject,'Value') returns toggle state of VectorRadio

% --- Executes on button press in VectorMagRadio.
function VectorMagRadio_Callback(hObject, eventdata, handles)
% hObject      handle to VectorMagRadio (see GCBO)
% eventdata    reserved - to be defined in a future version of
MATLAB
% handles      structure with handles and user data (see GUIDATA)

% Hint: get(hObject,'Value') returns toggle state of
VectorMagRadio

% --- Executes on button press in ReuseBoxesRadio.
function ReuseBoxesRadio_Callback(hObject, eventdata, handles)
% hObject      handle to ReuseBoxesRadio (see GCBO)
% eventdata    reserved - to be defined in a future version of
MATLAB
% handles      structure with handles and user data (see GUIDATA)

% Hint: get(hObject,'Value') returns toggle state of
ReuseBoxesRadio

```

Figure C. 20: MATLAB graphical user interface to select and process bracket vector data

```

function
TrackBracketDef(im7_path,im7_name,log_name,log_path,tecplot_name,
tecplot_path, SurfaceSelect, VectorSelect,
VectorMagSelect,newbox, logdata)

n = length(logdata);
r = length(2:n);
U = zeros(n,5);
V = zeros(n,5);
W = zeros(n,5);
for im = 2:n
tecplotName = sprintf('%sB000%02d.dat',tecplot_path,im);

%load data from tecplot file
[x, y, z, u, v, w, vector_data] = loadTecPlotFile(tecplotName);
%convert tecplot data from 6 x n array to a m x n grid
[xGrid,yGrid,zGrid,uGrid,vGrid,wGrid] = Tec2Grid(x, y, z, u, v,
w, vector_data);

if im == 2
figure; imagesc(xGrid,yGrid,zGrid);
if newbox == 1 %create new bounding box to cut out junk data
title(sprintf('Select %d Points to bound bracket\n (cut out junk
data)',2),'FontSize',14);
[a, b] = ginput(2);

gcf;

```

```

    line([a(1) a(1)], [b(1) b(2)]);
    line([a(2) a(2)], [b(1) b(2)]);
    line([a(1) a(2)], [b(1) b(1)]);
    line([a(1) a(2)], [b(2) b(2)]);

    %write fields to text file
    fid =
fopen(strcat(tecplot_path, '\', 'bracketbound', '.txt'), 'w');

    fprintf(fid, num2str(a(1))); fprintf(fid, '\n');
    fprintf(fid, num2str(a(2))); fprintf(fid, '\n');
    fprintf(fid, num2str(b(1))); fprintf(fid, '\n');
    fprintf(fid, num2str(b(2))); fprintf(fid, '\n');

    fclose(fid);

end

if newbox == 0 %load bounding box to cut out junk data
    %read fields from text file
    fid =
fopen(strcat(tecplot_path, '\', 'bracketbound', '.txt'), 'r');

    a(1) = str2double(fgetl(fid)); a(2) =
str2double(fgetl(fid));
    b(1) = str2double(fgetl(fid)); b(2) =
str2double(fgetl(fid));

    fclose(fid);

end

end

xIndexMin = 1;
xIndexMax = 1;

yIndexMin = 1;
yIndexMax = 1;
for i=1:length(xGrid)
    if (xGrid(i) < a(1))
        xIndexMin = xIndexMin + 1;
    end

    if (xGrid(i) < a(2))
        xIndexMax = xIndexMax + 1;
    end
end

for i=1:length(yGrid)
    if (yGrid(i) < b(1))
        yIndexMin = yIndexMin + 1;
    end
end

```

```

        if (yGrid(i) < b(2))
            yIndexMax = yIndexMax + 1;
        end
    end

% Reduce the size of the regular grid to eliminate junk data
xGridNew = xGrid(xIndexMin:xIndexMax);
yGridNew = yGrid(yIndexMin:yIndexMax);
zGridNew = zGrid(yIndexMin:yIndexMax,xIndexMin:xIndexMax);

uGridNew = uGrid(yIndexMin:yIndexMax,xIndexMin:xIndexMax);
vGridNew = vGrid(yIndexMin:yIndexMax,xIndexMin:xIndexMax);
wGridNew = wGrid(yIndexMin:yIndexMax,xIndexMin:xIndexMax);

xGridSizeNew = size(xGridNew);
yGridSizeNew = size(yGridNew);

if im == 2 && newbox == 1 %create new tying box regions
    figure; imagesc(xGridNew,yGridNew, zGridNew);
    [U_out1, V_out1, W_out1, xpos1, ypos1, zpos1] =
choose_tiewing(1,'top left',xGridSizeNew, yGridSizeNew, xGridNew,
yGridNew, zGridNew, uGridNew, vGridNew, wGridNew);
    [U_out2, V_out2, W_out2, xpos2, ypos2, zpos2] =
choose_tiewing(1,'top right',xGridSizeNew, yGridSizeNew,
xGridNew, yGridNew, zGridNew, uGridNew, vGridNew, wGridNew);
    [U_out3, V_out3, W_out3, xpos3, ypos3, zpos3] =
choose_tiewing(1,'bottom left',xGridSizeNew, yGridSizeNew,
xGridNew, yGridNew, zGridNew, uGridNew, vGridNew, wGridNew);
    [U_out4, V_out4, W_out4, xpos4, ypos4, zpos4] =
choose_tiewing(1,'bottom right',xGridSizeNew, yGridSizeNew,
xGridNew, yGridNew, zGridNew, uGridNew, vGridNew, wGridNew);
    [U_out5, V_out5, W_out5, xpos5, ypos5, zpos5] =
choose_tiewing(1, 'Bracket Door', xGridSizeNew, yGridSizeNew,
xGridNew, yGridNew, zGridNew, uGridNew, vGridNew, wGridNew);

    xpos1 = xpos1 + U_out1; ypos1 = ypos1 + V_out1; zpos1 =
zpos1 + W_out1;
    xpos2 = xpos2 + U_out2; ypos2 = ypos2 + V_out2; zpos2 =
zpos2 + W_out2;
    xpos3 = xpos3 + U_out3; ypos3 = ypos3 + V_out3; zpos3 =
zpos3 + W_out3;
    xpos4 = xpos4 + U_out4; ypos4 = ypos4 + V_out4; zpos4 =
zpos4 + W_out4;
    xpos5 = xpos5 + U_out5; ypos5 = ypos5 + V_out5; zpos5 =
zpos5 + W_out5;

    U(im,1) = U_out1; U(im,2) = U_out2; U(im,3) = U_out3; U(im,4)
= U_out4; U(im,5) = U_out5;
    V(im,1) = V_out1; V(im,2) = V_out2; V(im,3) = V_out3; V(im,4)
= V_out4; V(im,5) = V_out5;
    W(im,1) = W_out1; W(im,2) = W_out2; W(im,3) = W_out3; W(im,4)
= W_out4; W(im,5) = W_out5;

%write fields to text file

```

```

        fid =
fopen(strcat(tecplot_path, '\\', 'tiewingboxes', '.txt'), 'w');

        fprintf(fid, num2str(xpos1(1))); fprintf(fid, '\\n');
        fprintf(fid, num2str(xpos1(2))); fprintf(fid, '\\n');
        fprintf(fid, num2str(ypos1(1))); fprintf(fid, '\\n');
        fprintf(fid, num2str(ypos1(2))); fprintf(fid, '\\n');
        fprintf(fid, num2str(xpos2(1))); fprintf(fid, '\\n');
        fprintf(fid, num2str(xpos2(2))); fprintf(fid, '\\n');
        fprintf(fid, num2str(ypos2(1))); fprintf(fid, '\\n');
        fprintf(fid, num2str(ypos2(2))); fprintf(fid, '\\n');
        fprintf(fid, num2str(xpos3(1))); fprintf(fid, '\\n');
        fprintf(fid, num2str(xpos3(2))); fprintf(fid, '\\n');
        fprintf(fid, num2str(ypos3(1))); fprintf(fid, '\\n');
        fprintf(fid, num2str(ypos3(2))); fprintf(fid, '\\n');
        fprintf(fid, num2str(xpos4(1))); fprintf(fid, '\\n');
        fprintf(fid, num2str(xpos4(2))); fprintf(fid, '\\n');
        fprintf(fid, num2str(ypos4(1))); fprintf(fid, '\\n');
        fprintf(fid, num2str(ypos4(2))); fprintf(fid, '\\n');
        fprintf(fid, num2str(xpos5(1))); fprintf(fid, '\\n');
        fprintf(fid, num2str(xpos5(2))); fprintf(fid, '\\n');
        fprintf(fid, num2str(ypos5(1))); fprintf(fid, '\\n');
        fprintf(fid, num2str(ypos5(2))); fprintf(fid, '\\n');

        fclose(fid);
elseif im == 2 && newbox == 0 %load tieing box regions
        fid =
fopen(strcat(tecplot_path, '\\', 'tiewingboxes', '.txt'), 'r');

        xpos1(1) = str2double(fgetl(fid)); xpos1(2) =
str2double(fgetl(fid));
        ypos1(1) = str2double(fgetl(fid)); ypos1(2) =
str2double(fgetl(fid));
        zpos1(1) = 0; zpos1(2) = 0;
        xpos2(1) = str2double(fgetl(fid)); xpos2(2) =
str2double(fgetl(fid));
        ypos2(1) = str2double(fgetl(fid)); ypos2(2) =
str2double(fgetl(fid));
        zpos2(1) = 0; zpos2(2) = 0;
        xpos3(1) = str2double(fgetl(fid)); xpos3(2) =
str2double(fgetl(fid));
        ypos3(1) = str2double(fgetl(fid)); ypos3(2) =
str2double(fgetl(fid));
        zpos3(1) = 0; zpos3(2) = 0;
        xpos4(1) = str2double(fgetl(fid)); xpos4(2) =
str2double(fgetl(fid));
        ypos4(1) = str2double(fgetl(fid)); ypos4(2) =
str2double(fgetl(fid));
        zpos4(1) = 0; zpos4(2) = 0;
        xpos5(1) = str2double(fgetl(fid)); xpos5(2) =
str2double(fgetl(fid));
        ypos5(1) = str2double(fgetl(fid)); ypos5(2) =
str2double(fgetl(fid));
        zpos5(1) = 0; zpos5(2) = 0;
        fclose(fid);

```

```

[U_out1, V_out1, W_out1, xpos1, ypos1, zpos1] =
choose_tiewing(0,'top left',xGridSizeNew, yGridSizeNew, xGridNew,
yGridNew, zGridNew, uGridNew, vGridNew, wGridNew,xpos1, ypos1,
zpos1);
[U_out2, V_out2, W_out2, xpos2, ypos2, zpos2] =
choose_tiewing(0,'top right',xGridSizeNew, yGridSizeNew,
xGridNew, yGridNew, zGridNew, uGridNew, vGridNew, wGridNew,xpos2,
ypos2, zpos2);
[U_out3, V_out3, W_out3, xpos3, ypos3, zpos3] =
choose_tiewing(0,'bottom left',xGridSizeNew, yGridSizeNew,
xGridNew, yGridNew, zGridNew, uGridNew, vGridNew, wGridNew,xpos3,
ypos3, zpos3);
[U_out4, V_out4, W_out4, xpos4, ypos4, zpos4] =
choose_tiewing(0,'bottom right',xGridSizeNew, yGridSizeNew,
xGridNew, yGridNew, zGridNew, uGridNew, vGridNew, wGridNew,xpos4,
ypos4, zpos4);
[U_out5, V_out5, W_out5, xpos5, ypos5, zpos5] =
choose_tiewing(0, 'Bracket Door', xGridSizeNew, yGridSizeNew,
xGridNew, yGridNew, zGridNew, uGridNew, vGridNew, wGridNew,xpos5,
ypos5, zpos5);

xpos1 = xpos1 + U_out1; ypos1 = ypos1 + V_out1; zpos1 =
zpos1 + W_out1;
xpos2 = xpos2 + U_out2; ypos2 = ypos2 + V_out2; zpos2 =
zpos2 + W_out2;
xpos3 = xpos3 + U_out3; ypos3 = ypos3 + V_out3; zpos3 =
zpos3 + W_out3;
xpos4 = xpos4 + U_out4; ypos4 = ypos4 + V_out4; zpos4 =
zpos4 + W_out4;
xpos5 = xpos5 + U_out5; ypos5 = ypos5 + V_out5; zpos5 =
zpos5 + W_out5;

U(im,1) = U_out1; U(im,2) = U_out2; U(im,3) = U_out3; U(im,4)
= U_out4; U(im,5) = U_out5;
V(im,1) = V_out1; V(im,2) = V_out2; V(im,3) = V_out3; V(im,4)
= V_out4; V(im,5) = V_out5;
W(im,1) = W_out1; W(im,2) = W_out2; W(im,3) = W_out3; W(im,4)
= W_out4; W(im,5) = W_out5;

Else % Determine the displacement of the bracket tie wings and
bracket door
[U_out1, V_out1, W_out1, xpos1, ypos1, zpos1] =
choose_tiewing(0,'top left',xGridSizeNew, yGridSizeNew, xGridNew,
yGridNew, zGridNew, uGridNew, vGridNew, wGridNew,xpos1, ypos1,
zpos1);
[U_out2, V_out2, W_out2, xpos2, ypos2, zpos2] =
choose_tiewing(0,'top right',xGridSizeNew, yGridSizeNew,
xGridNew, yGridNew, zGridNew, uGridNew, vGridNew, wGridNew,xpos2,
ypos2, zpos2);
[U_out3, V_out3, W_out3, xpos3, ypos3, zpos3] =
choose_tiewing(0,'bottom left',xGridSizeNew, yGridSizeNew,
xGridNew, yGridNew, zGridNew, uGridNew, vGridNew, wGridNew,xpos3,
ypos3, zpos3);
[U_out4, V_out4, W_out4, xpos4, ypos4, zpos4] =
choose_tiewing(0,'bottom right',xGridSizeNew, yGridSizeNew,

```

```

xGridNew, yGridNew, zGridNew, uGridNew, vGridNew, wGridNew, xpos4,
ypos4, zpos4);
[U_out5, V_out5, W_out5, xpos5, ypos5, zpos5] = choose_tiewing(0,
'Bracket Door', xGridSizeNew, yGridSizeNew, xGridNew, yGridNew,
zGridNew, uGridNew, vGridNew, wGridNew, xpos5, ypos5, zpos5);

    xpos1 = xpos1 + U_out1; ypos1 = ypos1 + V_out1; zpos1 =
zpos1 + W_out1;
    xpos2 = xpos2 + U_out2; ypos2 = ypos2 + V_out2; zpos2 =
zpos2 + W_out2;
    xpos3 = xpos3 + U_out3; ypos3 = ypos3 + V_out3; zpos3 =
zpos3 + W_out3;
    xpos4 = xpos4 + U_out4; ypos4 = ypos4 + V_out4; zpos4 =
zpos4 + W_out4;
    xpos5 = xpos5 + U_out5; ypos5 = ypos5 + V_out5; zpos5 =
zpos5 + W_out5;

U(im,1) = U_out1; U(im,2) = U_out2; U(im,3) = U_out3; U(im,4) =
U_out4; U(im,5) = U_out5;
V(im,1) = V_out1; V(im,2) = V_out2; V(im,3) = V_out3; V(im,4) =
V_out4; V(im,5) = V_out5;
W(im,1) = W_out1; W(im,2) = W_out2; W(im,3) = W_out3; W(im,4) =
W_out4; W(im,5) = W_out5;
end

%create files for Paraview display
    if SurfaceSelect == 1
        VTKsurface(xGridSizeNew, yGridSizeNew, xGridNew, yGridNew,
zGridNew, uGridNew, vGridNew, wGridNew, im, tecplot_path);
    end
    if VectorSelect == 1
        VTKvector(xGridSizeNew, yGridSizeNew, xGridNew, yGridNew,
zGridNew, uGridNew, vGridNew, wGridNew, im, tecplot_path);
    end
    if VectorMagSelect == 1
        VTKvectorMag(xGridSizeNew, yGridSizeNew, xGridNew, yGridNew,
zGridNew, uGridNew, vGridNew, wGridNew, im, tecplot_path);
    end
end
%write data to excel file
dataToExcel(log_path, log_name, logdata, U,V,W);

```

Figure C. 21 Determine the bracket tie-wing displacement

```

%% Determine the grid spacing of the Tecplot Data
% makes a regular grid for the x,y,z data
% Author: Garrett Melenka
% email: gmelenka@ualberta.ca
% date: February 17, 2012
function [xGrid,yGrid,zGrid,uGrid,vGrid,wGrid] =Tec2Grid(x, y, z,
u, v, w, vector_data)

```



```

xSize = length(x);
ySize = length(y);
zSize = length(z);
%% Determine the grid spacing of the Tecplot Data
% makes a regular grid for the x,y,z data
a = zeros(xSize,3);

a(:,1) = x;
a(:,2) = y;
a(:,3) = z;

b = sortrows(a, [1 2]);
xmin = min(x);
xmax = max(x);

ymin = min(y);
ymax = max(y);

k = 1;
for i=1:length(y)

    if y(i) == ymin

        k=k+1;
    end
end

ySpacing = ymax - y(k);

%yGrid = ymin:ySpacing:(ymax+ySpacing);
yGrid = ymin:ySpacing:(ymax);

xSort = sortrows(x);

c = 1;

for j=1:length(x)
    if xSort(j) == xmin
        c = c + 1;
    end
end

xSpacing = xSort(c) - xmin;

xGrid = xmin:xSpacing:(xmax+xSpacing);
%xGrid = xmin:xSpacing:(xmax);
xGridSize = size(xGrid);
yGridSize = size(yGrid);

zGrid = zeros(yGridSize(2),xGridSize(2));
uGrid = zeros(yGridSize(2),xGridSize(2));
vGrid = zeros(yGridSize(2),xGridSize(2));
wGrid = zeros(yGridSize(2),xGridSize(2));

```

```

for i=1:yGridSize(2)
    l = z((i*xGridSize(2))-(xGridSize(2)-1):(i)*xGridSize(2));
    m = u((i*xGridSize(2))-(xGridSize(2)-1):(i)*xGridSize(2));
    n = v((i*xGridSize(2))-(xGridSize(2)-1):(i)*xGridSize(2));
    o = w((i*xGridSize(2))-(xGridSize(2)-1):(i)*xGridSize(2));
    zGrid(i,:) = l;
    uGrid(i,:) = m;
    vGrid(i,:) = n;
    wGrid(i,:) = o;
end

```

Figure C. 22: Convert tecplot data to grid

```

%% Extract the U,V,W displacement of the bracket tiewings
% function finds the average U,V,W motion of the four selected
% tiewings
% Author: Garrett Melenka
% email: gmelenka@ualberta.ca
% date: February 17, 2012
function [U_out, V_out, W_out, xpos, ypos, zpos] =
choose_tiewing(input,peg_name,xGridSizeNew,...
    yGridSizeNew, xGridNew, yGridNew, zGridNew, uGridNew,
vGridNew, wGridNew, xpos, ypos, zpos)

if input == 1
   (gcf;
    title(sprintf('Select %s TieWing',peg_name),'FontSize',14);
    [xpos,ypos] = ginput(2);
    zpos=0;
    %U_out = []; V_out = []; W_out = [];

   (gcf;
    line([xpos(1) xpos(1)],[ypos(1) ypos(2)]);
    line([xpos(2) xpos(2)],[ypos(1) ypos(2)]);
    line([xpos(1) xpos(2)],[ypos(1) ypos(1)]);
    line([xpos(1) xpos(2)],[ypos(2) ypos(2)]);

end
%else
xIndexMin = 1;
xIndexMax = 1;

yIndexMin = 1;
yIndexMax = 1;
for i=1:length(xGridNew)
    if (xGridNew(i) < xpos(1))
        xIndexMin = xIndexMin + 1;
    end

    if (xGridNew(i) < xpos(2))
        xIndexMax = xIndexMax + 1;
    end
end
end

for i=1:length(yGridNew)

```

```

    if (yGridNew(i) < ypos(1))
        yIndexMin = yIndexMin + 1;
    end

    if (yGridNew(i) < ypos(2))
        yIndexMax = yIndexMax + 1;
    end
end
U_out =
mean(mean(uGridNew(yIndexMin:yIndexMax,xIndexMin:xIndexMax)));
V_out =
mean(mean(vGridNew(yIndexMin:yIndexMax,xIndexMin:xIndexMax)));
W_out =
mean(mean(wGridNew(yIndexMin:yIndexMax,xIndexMin:xIndexMax)));
%end

```

Figure C. 23: Determine the average tie-wing displacement

```

%% Write Bracket Deformation Data to Excel
% Author: Garrett Melenka
% email: gmelenka@ualberta.ca
% date: February 17, 2012
function dataToExcel(log_path,log_name, logdata, U,V,W)

excel_name = sprintf('%s%s.xls',log_path,log_name);

n = length(logdata);
angle = cell(n+1,1); F = cell(n+1,3); T = cell(n+1,3);
angle(1) = {'Angle [degrees]'};
for i = 1:n
    angle(i+1,1) = {logdata(i).Angle};
    %F(i+1,:) = {log_data(i).Fx log_data(i).Fy log_data(i).Fz};
    %T(i+1,:) = {log_data(i).Tx log_data(i).Ty log_data(i).Tz};
end
%create heading for excel data
UVW = cell(n+1,21);
str = {'TieWing1X [mm]', 'TieWing2X [mm]', 'TieWing3X [mm]',...
      'TieWing4X [mm]', 'TieWing1Y [mm]', 'TieWing2Y [mm]',...
      'TieWing3Y [mm]', 'TieWing4Y [mm]', 'TieWing1Z [mm]',...
      'TieWing2Z [mm]', 'TieWing3Z [mm]', 'TieWing4Z [mm]',...
      'BracketDoorX [mm]', 'BracketDoorY [mm]', 'BracketDoorZ
[mm]',...
      'TieWing1-3X [mm]', 'TieWing2-4X [mm]', 'TieWing1-3Y [mm]',...
      'TieWing2-4Y [mm]', 'TieWing1-3Z [mm]', 'TieWing2-4Z [mm]'};
UVW(1,:) = str;
%organize bracket data to match excel headings
for i = 1:n
    UVW(i+1,1:4) = {U(i,1) U(i,2) U(i,3), U(i,4)};

    UVW(i+1,5:8) = {V(i,1) V(i,2) V(i,3), V(i,4)};

    UVW(i+1,9:12) = {W(i,1) W(i,2) W(i,3), W(i,4)};

    UVW(i+1,13:15) = {U(i,5) V(i,5) W(i,5)};

```

```

        UVW(i+1,16:18) = {(U(i,1)- U(i,3)) (U(i,2)- U(i,4)) (V(i,1)-
V(i,3))});

        UVW(i+1,19:21) = {(V(i,2)- V(i,4)) (W(i,1)- W(i,3)) (W(i,2)-
W(i,4))});
end
% wrt = {'TieWing1_U', 'TieWing1_V', 'TieWing1_W', 'TieWing2_U',
'TieWing2_V', 'TieWing2_W',...
%      'TieWing3_U', 'TieWing3_V', 'TieWing3_W', 'TieWing4_U',
'TieWing4_V', 'TieWing4_W';...
%      U(:,1), V(:,1), W(:,1), U(:,2), V(:,2), W(:,2), U(:,3),
V(:,3), W(:,3), U(:,4), V(:,4), W(:,4)};
wrt = [angle UVW];

%write excel data to file
xlswrite(excel_name,wrt,'Sheet1');

```

Figure C. 24: Write bracket data to Excel

C.6 References

- [1] LaVision GmbH, "Product-Manual for DaVis 7.2 StrainMaster 2D Item-Number(s): 1105021," .
- [2] LaVision GmbH, "Product-Manual for DaVis 7.2 StrainMaster Software Item-Number(s): 1105022," 2006.

Appendix D ParaView Scientific Visualization

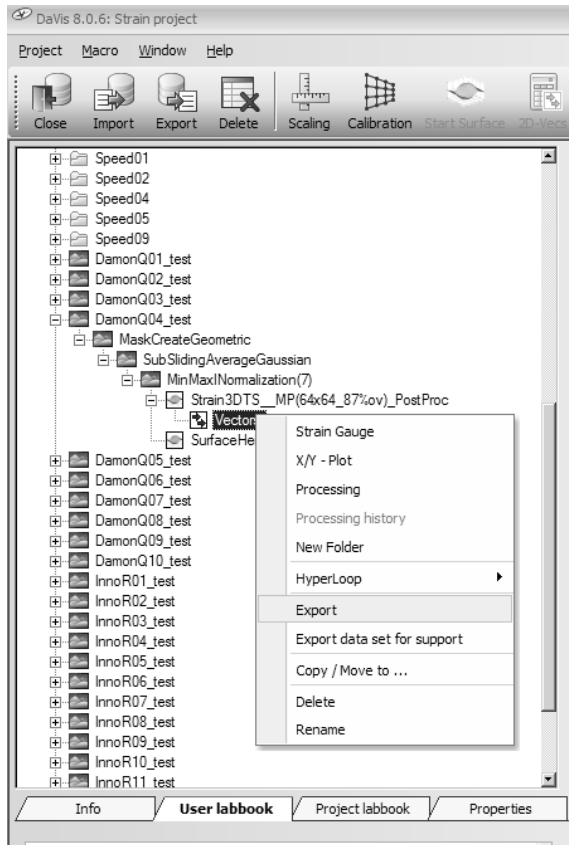
The 3D vector files generated using commercial digital image correlation software (LaVision GmbH DaVis 8.06, Gottingen, Germany, 2009) were exported so that the bracket-archwire interaction could be visualized. A scientific visualization software package (ParaView, Kitware, Inc. Clifton Park, New York) [1, 2] was used to display the 3D displacement vectors and surfaces of the orthodontic brackets. The image files from DaVis were loaded and processed using MATLAB so that the 3D data could be visualized using ParaView.

D.1 Load Data into MATLAB from DaVIS

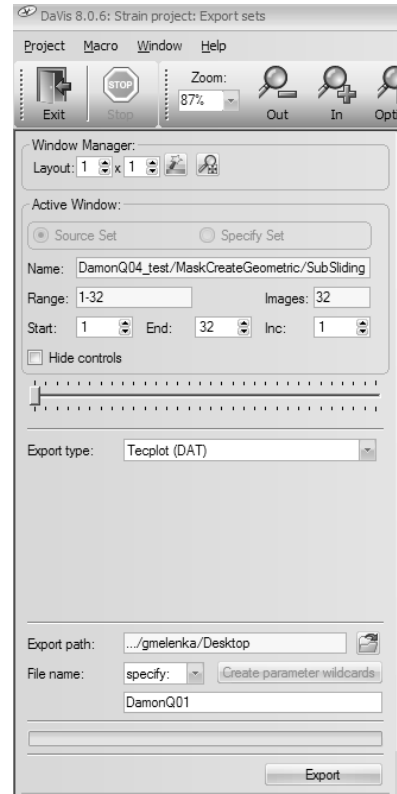
ReadIMX and ShowIMX functions provided by LaVision [3, 4] to load data into MATLAB can be used to load 2D data as well as load the determined displacement magnitude or strain found in DAVIS. The surface height and displacement data will be in the IM7 file format. The ReadIMX/ ShowIMX functions cannot be used to load the resultant 3D vectors generated in DaVIS. These 3D vectors must be exported as a Tecplot DAT file. MATLAB will be used to load the Tecplot data files and then generate the ParaView VTK files.

D.2 TECPLOT Data

Currently, the ReadIMX function provided by LaVision does not support 3D Strain data or any vector data with six components. The ReadIMX function can be used for StereoPIV where there are 5 components (x,y,u,v,w) but does not support information in the z direction. The process for creating the Tecplot DAT files is shown in Figure D. 1.



(a)



(b)

Figure D. 1 Select Export to create Tecplot File

To load the Tecplot DAT files into MATLAB the function *loadTecPlotFile* was created.

This file opens the Tecplot DAT file and discards the header information in the file (top three lines). After this the x,y,z,u,v, and w data is loaded into MATLAB. The *loadTecPlotFile* function can be seen in Figure D. 2.

```
function [x, y, z, u, v, w, vector_data] =
loadTecPlotFile(tecplotName)
% SYNOPSIS: This function reads a tomographic PIV 3D vectorfield
saved in
% TecPlot's .DAT format containing
% IxJxK arrays for X, Y, Z, U, V, and W, which represent the
three
% positional coordinates and the three velocity components.
%
%
% SYNTAX: [x,y,z,u,v,w,vector_data] = tecplot_loader(filename),
%   where:
%   x, y, z, u, v, w are the output arrays read from the tecplot
file
%   vector_data is all all six components written to one n x 6
array
```

```

%   containing x, y, z and u, v, w data
%   Author: Garrett Melenka gmelenka@ualberta.ca
%   Date: December 8, 2011

fid = fopen(tecplotName,'r'); % Open file
for n = 1:3, fgetl(fid); end % Read in first three lines and
ignore them
file_content = fread(fid); fclose(fid); % Read in the rest of
data

%disp('Creating temporary file...')
fid = fopen('tmp.txt','w'); % Open up a temporary file
fwrite(fid, file_content); % Write all data to this file
fclose(fid); % Close file

%disp('Loading data to memory...')
B = load('tmp.txt'); delete tmp.txt % Load data into table and
del tmp file

% Determine I-size of data
I = length(unique(B(:,1)));
J = length(unique(B(:,2)));
K = length(B(:,3));

% Read out the components
x = B(:,1);
y = B(:,2);
z = B(:,3);

u = B(:,4);
v = B(:,5);
w = B(:,6);

%Create N x 6 array to contain all data
vector_data = zeros(length(x),6);
%Write 6 components to N x 6 array
vector_data(:,1) = x;
vector_data(:,2) = y;
vector_data(:,3) = z;

vector_data(:,4) = u;
vector_data(:,5) = v;
vector_data(:,6) = w;
end

```

Figure D. 2: Load Tecplot Data into MATLAB

D.3 Create VTK File in MATLAB

Data is loaded into Paraview using the VTK (Visualization Toolkit) format. There are five classic formats: Structured Points, Structured Grid, Rectilinear Grid, Unstructured

Grid or Poly Data [2]. Depending on the dataset that is being used one of the above listed VTK formats should be used.

In general the VTK files follow the format described in Figure D. 3. The file format will change depending on the structure of the data set that is to be loaded. The dataset example in Figure D. 3: VTK data format

is for data which is organized in a regularly spaced array.

```
# vtk DataFile Version 1.0 header file information
Structured Points 3D Dataset comment that describes the dataset
ASCII
DATASET STRUCTURED_POINTS VTK format used for dataset
DIMENSIONS 7 4 3 coordinates of the dataset
ORIGIN 0 0 0
SPACING 1 1 1
POINT_DATA 84 number of data points 7x4x3 = 84
SCALARS scalars int dataset scalar values
LOOKUP_TABLE default
```

Figure D. 3: VTK data format

D.3.1 Create 3D Surface with Scalar Data

To create a 3D surface with a scalar data color map the Structured Grid data set format was used. The function *VTKsurface* used to produce the VTK file for the 3D surface and color map is shown in Figure D. 4.


```

%% Creates a 3D Surface for ParaView VTK from Tecplot data
% Author: Garrett Melenka
% email: gmelenka@ualberta.ca
% date: February 17, 2012
function VTKsurface(xGridSizeNew, yGridSizeNew, xGridNew,
yGridNew, zGridNew, uGridNew, vGridNew, wGridNew, im,
tecplot_path)

    output_filename =
sprintf('%sVectorSurface%02d.vtk',tecplot_path,im-1);
    output_unit = fopen ( output_filename, 'wt' );
    fprintf ( output_unit, '# vtk DataFile Version 2.0\n' );
    fprintf ( output_unit, '# %s Surface Data x y z\n',
output_filename );
    fprintf ( output_unit, 'ASCII\n' );
    fprintf ( output_unit, '\n' );
    fprintf ( output_unit, 'DATASET STRUCTURED_GRID\n' );
    fprintf ( output_unit, 'DIMENSIONS %d %d %d\n',
yGridSizeNew(2), xGridSizeNew(2), 1);
    fprintf ( output_unit, 'POINTS %d float\n',
yGridSizeNew(2)*xGridSizeNew(2));

    fprintf ( output_unit, '\n' );

    for i =1:length(xGridNew)
        for j = 1:length(yGridNew)
            fprintf ( output_unit, '%g %g %g\n', xGridNew(i), -
yGridNew(j), 0.000);
        end
    end

    fprintf ( output_unit, '\n');
    fprintf ( output_unit, 'POINT_DATA %d\n',
xGridSizeNew(2)*yGridSizeNew(2));
    fprintf ( output_unit, '\n');
    fprintf ( output_unit, 'SCALARS scalars float\n');
    fprintf ( output_unit, 'LOOKUP_TABLE default\n');

    fprintf ( output_unit, '\n' );

    for i =1:length(xGridNew)
        for j = 1:length(yGridNew)

            fprintf( output_unit, '%g\n', zGridNew(j,i));

        end
    end

    fclose(output_unit);

```

Figure D. 4: Create VTK surfaces from tecplot data

D.3.2 Create 3D Vectors

To create a 3D vectors PolyData data set format was used [2]. The function *VTKvector* used to create the vector field of the bracket displacement data is shown in Figure D. 5.

```
%% Creates a 3D vectors for ParaView VTK from Tecplot data
% Author: Garrett Melenka
% email: gmelenka@ualberta.ca
% date: February 17, 2012
function VTKvector(xGridSizeNew, yGridSizeNew, xGridNew,
yGridNew, zGridNew, uGridNew, vGridNew, wGridNew, im,
tecplot_path)

%% Write vector data

    output_filename =
sprintf('%sVTKvector%02d.vtk',tecplot_path,im-1);
    output_unit = fopen ( output_filename, 'wt' );
    fprintf ( output_unit, '# vtk DataFile Version 2.0\n' );
    fprintf ( output_unit, '# %s Vector Data x y z u v w\n',
output_filename );
    fprintf ( output_unit, 'ASCII\n' );
    fprintf ( output_unit, '\n' );
    fprintf ( output_unit, 'DATASET POLYDATA\n' );
    fprintf ( output_unit, 'POINTS %d float\n',
xGridSizeNew(2)*yGridSizeNew(2));

    for i =1:length(xGridNew)
        for j = 1:length(yGridNew)
            fprintf ( output_unit, '%g %g %g\n', xGridNew(i), -
yGridNew(j), zGridNew(j,i));
        end
    end

%% Write Vector Data to file
    fprintf ( output_unit, '\n' );
    fprintf ( output_unit, 'POINT_DATA %d\n',
xGridSizeNew(2)*yGridSizeNew(2));
    fprintf ( output_unit, '\n' );
    fprintf ( output_unit, 'VECTORS vectors float\n');

    fprintf ( output_unit, '\n' );
    for i =1:length(xGridNew)
        for j = 1:length(yGridNew)
            fprintf ( output_unit, '%g %g %g\n', uGridNew(j,i),
vGridNew(j,i), wGridNew(j,i));
        end
    end

    fclose(output_unit);
```

Figure D. 5: Create VTK file in MATLAB for 3D Vectors

D.3.3 Create 3D Surface with Displacement Magnitude

The magnitude of displacement can be visualized as a contour plot on the 3D object surface. The 3D surface and vector magnitude was created using the PolyData data set format. The function *VTKvectorMag* used to create the vector field of the bracket displacement data is shown in Figure D. 6

```
%% Creates a 3D Surface with Vector Magnitude as contour plot
%for ParaView VTK from Tecplot data
% Author: Garrett Melenka
% email: gmelenka@ualberta.ca
% date: February 17, 2012
function VTKvectorMag(xGridSizeNew, yGridSizeNew, xGridNew,
yGridNew, zGridNew, uGridNew, vGridNew, wGridNew, im,
tecplot_path)

    %% Write vectorMag data

    output_filename =
sprintf('%sVTKvectorMag%02d.vtk',tecplot_path,im-1);
    output_unit = fopen ( output_filename, 'wt' );
    fprintf ( output_unit, '# vtk DataFile Version 2.0\n' );
    fprintf ( output_unit, '# %s Vector Data x y z u v w\n',
output_filename );
    fprintf ( output_unit, 'ASCII\n' );
    fprintf ( output_unit, '\n' );
    fprintf ( output_unit, 'DATASET UNSTRUCTURED_GRID\n' );
    fprintf ( output_unit, 'POINTS %d float\n',
xGridSizeNew(2)*yGridSizeNew(2));

    for i =1:length(xGridNew)
        for j = 1:length(yGridNew)
            fprintf ( output_unit, '%g %g %g\n', xGridNew(i), -
yGridNew(j), zGridNew(j,i));
        end
    end

    %% Creates single points
    numCells = xGridSizeNew(2)*yGridSizeNew(2);
    numCellPoints = numCells * 2;

    fprintf ( output_unit, '\n');

    fprintf( output_unit, 'CELLS %d %d\n', numCells,
numCellPoints);

    fprintf ( output_unit, '\n');

    for i=1:numCells
```

```

%         fprintf ( output_unit, '%d %d\n', 1,i);
%
%     end
%
%%     Creates quadrilaterals
numCells = (xGridSizeNew(2)-1)*(yGridSizeNew(2)-1);
numCellPoints = numCells * 5;

fprintf ( output_unit, '\n');

fprintf( output_unit, 'CELLS %d %d\n', numCells,
numCellPoints);

% create a grid of quadralaterals for displaying 3D Data

for i=1:length(xGridNew)-1
for j=1:(length(yGridNew))-1
    if i == 1 && j ==1
        a=0;
        b=1;
        c=length(yGridNew);
        d=c+1;
    else
        a = a + 1;
        b = b + 1;
        c = c + 1;
        d = d + 1;
    end
    fprintf( output_unit, '%d %d %d %d %d\n', 4, a, b, c, d);

end
    a = a + 1;
    b = b + 1;
    c = c + 1;
    d = d + 1;
end

%% Write Cell Type info to file
fprintf ( output_unit, '\n');

fprintf ( output_unit, 'CELL_TYPES %d\n', numCells);

for i=1:numCells
    %fprintf ( output_unit, '%d\n', 1);
    fprintf ( output_unit, '%d\n', 10);
end
%% Write Scalar data to file
fprintf ( output_unit, '\n');
fprintf ( output_unit, 'POINT_DATA %d\n',
xGridSizeNew(2)*yGridSizeNew(2));
%fprintf ( output_unit, 'POINT_DATA %d\n', 100*100);
fprintf ( output_unit, '\n' );
fprintf ( output_unit, 'SCALARS vectorMag float\n');
fprintf ( output_unit, 'LOOKUP_TABLE default\n');

```

```

for i=1:length(xGridNew)
    for j = 1:length(yGridNew)
        fprintf ( output_unit, '%g\n', vGridNew(j,i));
    end
end

fclose(output_unit);

```

Figure D. 6: Create VTK file in MATLAB for 3D surface with displacement magnitude

D.3.4 Load VTK Data into ParaView

Data is loaded into Paraview by selecting File> Open. When opening files in Paraview select a single file or multiple files. If files are numbered sequentially, Paraview will open all files as a time series.

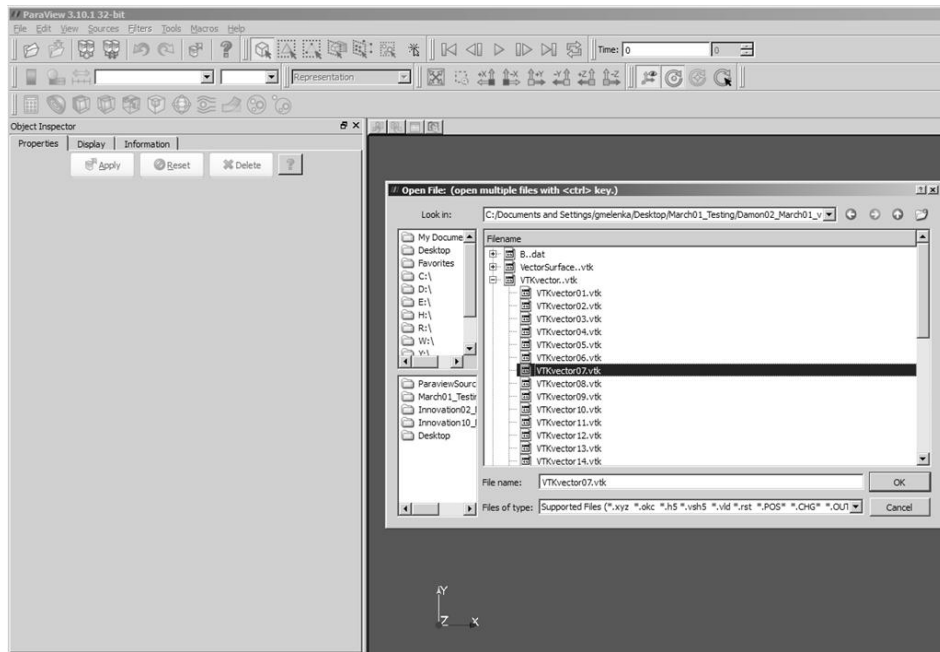


Figure D. 7: Load Paraview Data. Shown is a time series of vector.vtk. The user can select an individual file i.e. vector07.vtk or select the time series vector..vtk to display 3D vector data

D.3.5 Load 3D Surface with Scalar Data

Once the 3D surface data created using the *vtkSurface* function is loaded into Paraview select Display in the Object Inspector (Figure D. 8). The WarpByScalar function is used to show the 3D surface.

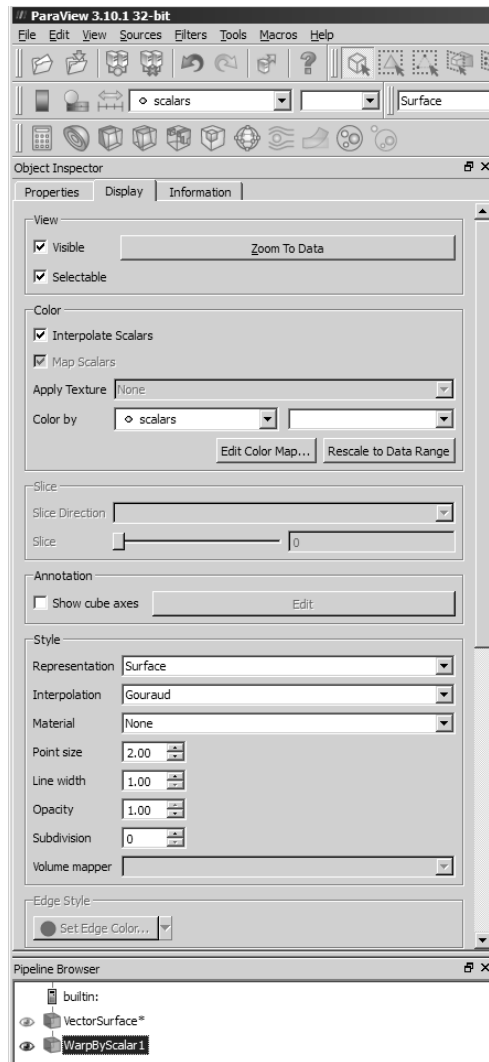


Figure D. 8: 3D Surface data display

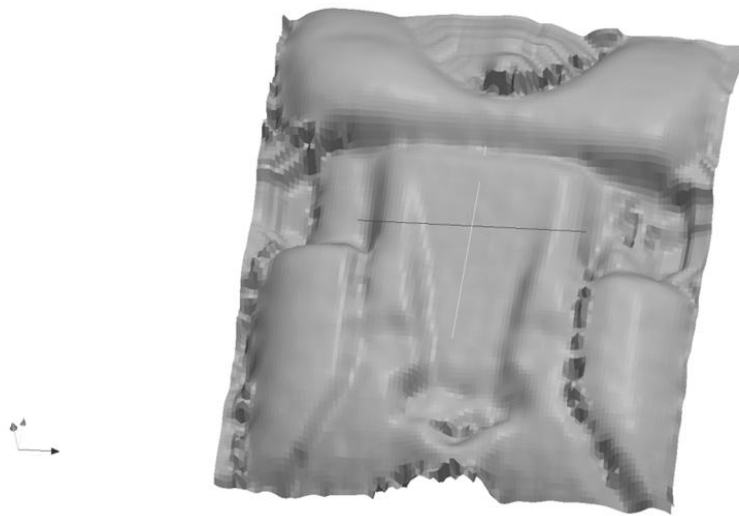


Figure D. 9: Final 3D surface

D.3.6 Load 3D Vectors

The 3D vector data is loaded in a similar method to the 3D surface data. The 3D vector data is created using the *vtkVector* function described above. Once the vector data is loaded in Paraview a few filters are required. The first filter that must be used is the Calculator. Loading 3D Vectors is equivalent to the `quiver3` command in MATLAB.



Figure D. 10: Calculator Filter

In the calculator filter dialog box enter the following formula:

$$vector_x * iHat + vector_y * jHat + vector_z * kHat \quad (D.1)$$

This formula multiplies the scalar components by unit vectors x, y, z to create a vector field.

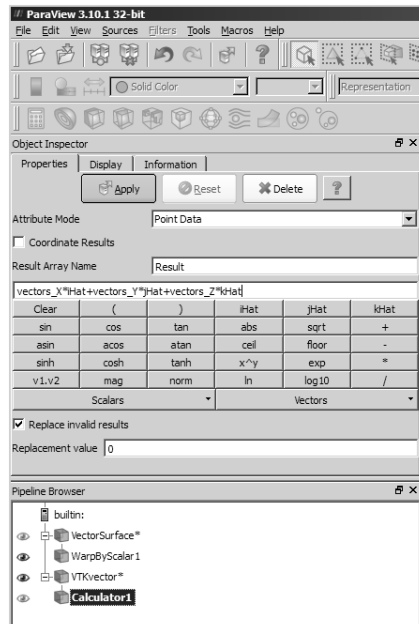


Figure D. 11: Vector Calculator

Once the vector field has been created select the Glyph filter (Figure D. 12). This will display the 3D Vector field and allow the user to edit the vector arrows.

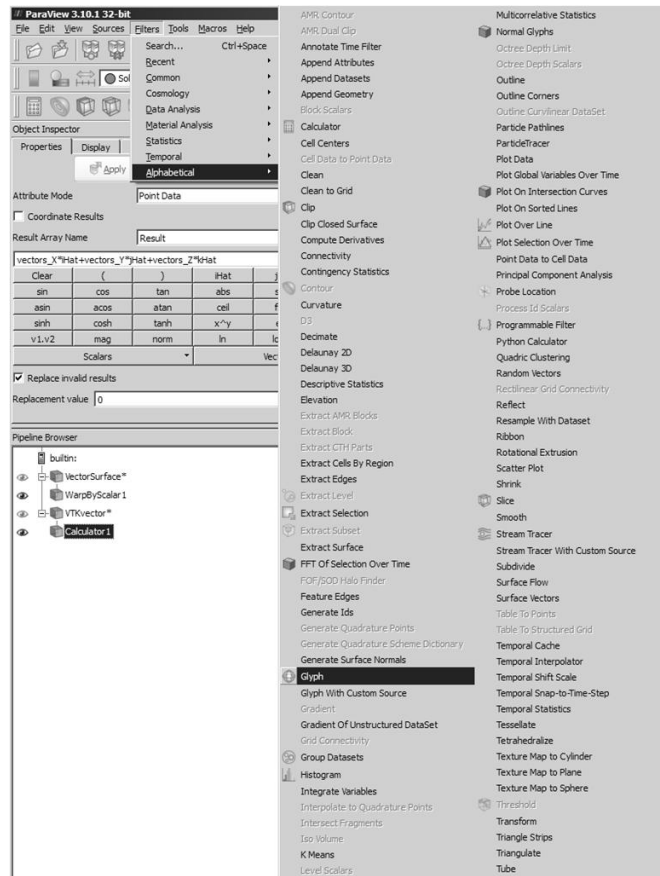


Figure D. 12: Select Glyph Filter

An example of the resulting 3D Vectors is shown in Figure D. 13.

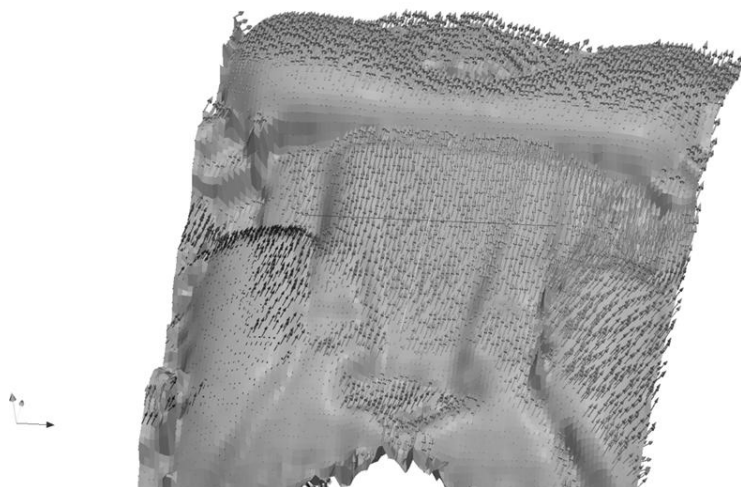


Figure D. 13: 3D Vectors and 3D bracket surface in ParaView

The 3D surface and contour plot generated using the *VTKvectorMag* function is shown in Figure D. 14. This figure shows the magnitude of displacement as a contour on the surface of the bracket.

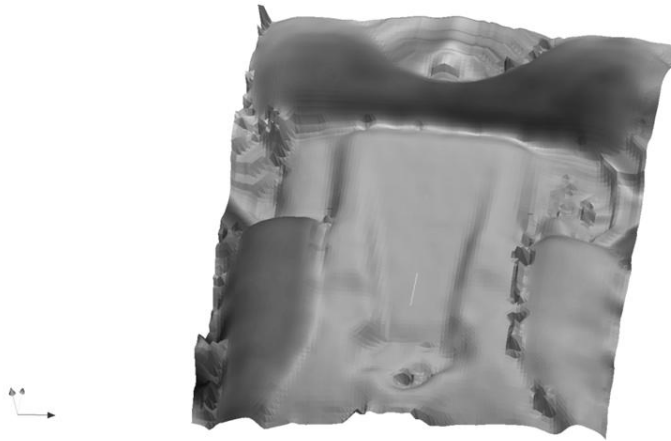


Figure D. 14: 3D bracket surface with color indicating the magnitude of displacement

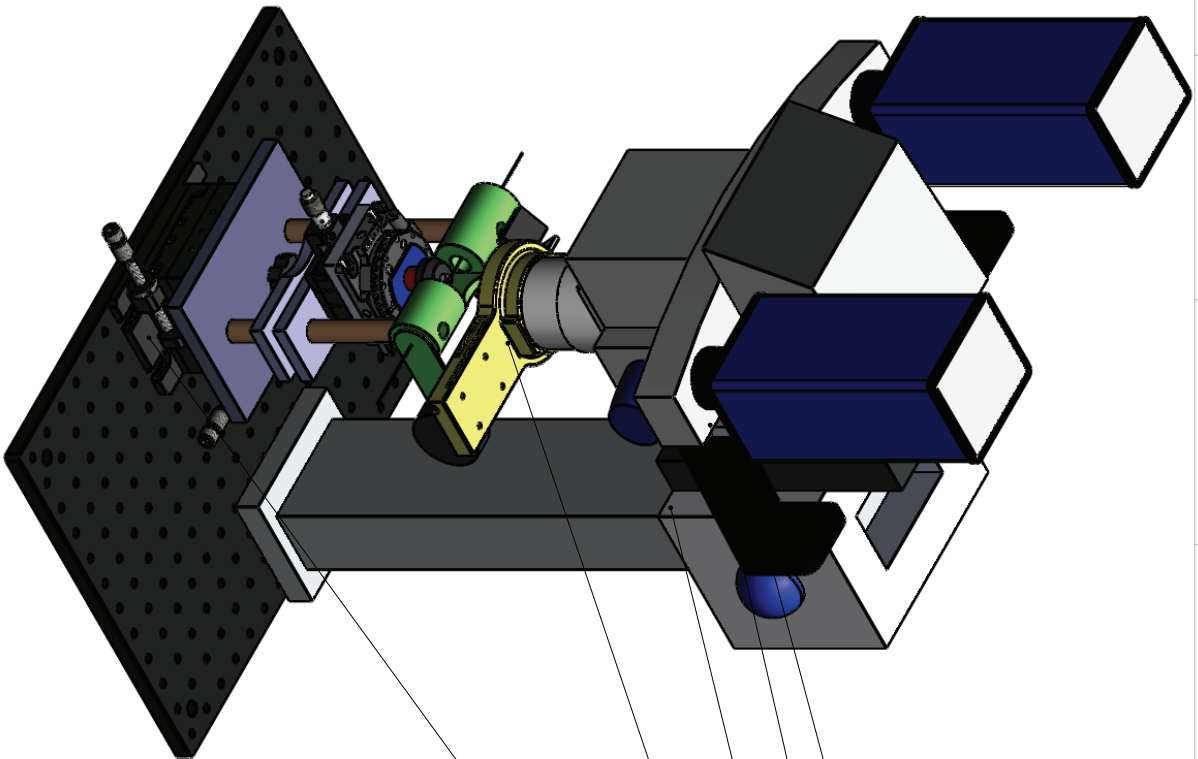
D.4 References

- [1] L. S. Avila, *The VTK User's Guide: Updated for VTK Version 5*. Kitware Inc., 2006.
- [2] W. Schroeder, *The Visualization Toolkit: An Object-Oriented Approach to 3D Graphics*. Kitware Inc., 2006.
- [3] LaVision GmbH, "Product-Manual for DaVis 7.2 StrainMaster 2D Item-Number(s): 1105021," .
- [4] LaVision GmbH, "Product-Manual for DaVis 7.2 StrainMaster Software Item-Number(s): 1105022," 2006.

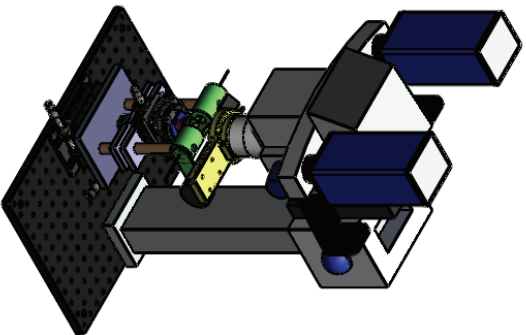
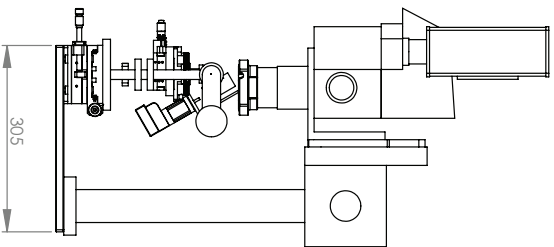
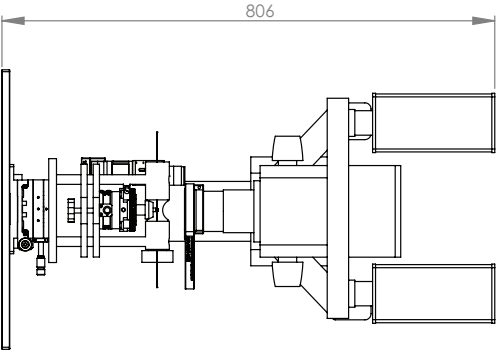
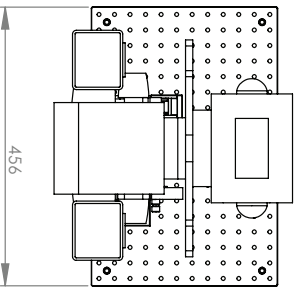
Appendix E 3D Orthodontic Torque Simulator Solid Model


Drawings

ITEM NO.	PART NUMBER	manual explode/QTY.
1	Strain_Imaging_Assem	1
2	ZeissProfilosColumn	1
3	MicroscopeAdapter	1
4	Camera&Microscope	1
5	RP_Ringlight	1



Nobes Lab		UNLESS OTHERWISE SPECIFIED:		NAME	
CARTAGE:		DIMENSIONS ARE IN MM		DRAWN	GW1
FINISH:		TOLERANCES:		CHECKED	
PICKUP:		ANGULAR: ± 0.5°		ENG APPR.	
COMMENTS:		X = ± 0.25		SPEED CODE	
		XX = ± 0.10			
		XXX = ± 0.05			
		SURFACE FINISH		Meet Job #	
		µm			
		0.6			
		MATERIAL:		File Name:	Strain_Imaging_Assembly.dwg
		Lab Location:		gmelenka	
		DO NOT SCALE DRAWING		6/13/2012 8:55:50 AM	
				Wednesday, June 13, 2012	
				SCALE: 1:10	MASS:
				SHEET 1 OF 9	REV



Nobes Lab		UNLESS OTHERWISE SPECIFIED:		NAME	 The Department of Mechanical Engineering UNIVERSITY OF ALBERTA	
Centre:	DIMENSIONS ARE IN MM	DRAWN BY		GWMA		
Enote:	ANGULAR: $\pm 0.5^\circ$	SMB		GWMA		
Priorite:	X = ± 0.25	CHECKED BY				
Comments:	XX = ± 0.05	Speed Code				
SURFACE FINISH		0.6			Project: REV	
MATERIAL:						
Lab Location:		Mecc Job #				
		File Name				
		gmelinka				
DO NOT SCALE DRAWING		Wednesday, June 13, 2012 8:44:56 AM			SHEET 2 OF 9	
		Friday, July 25, 2008 2:06:42 AM				



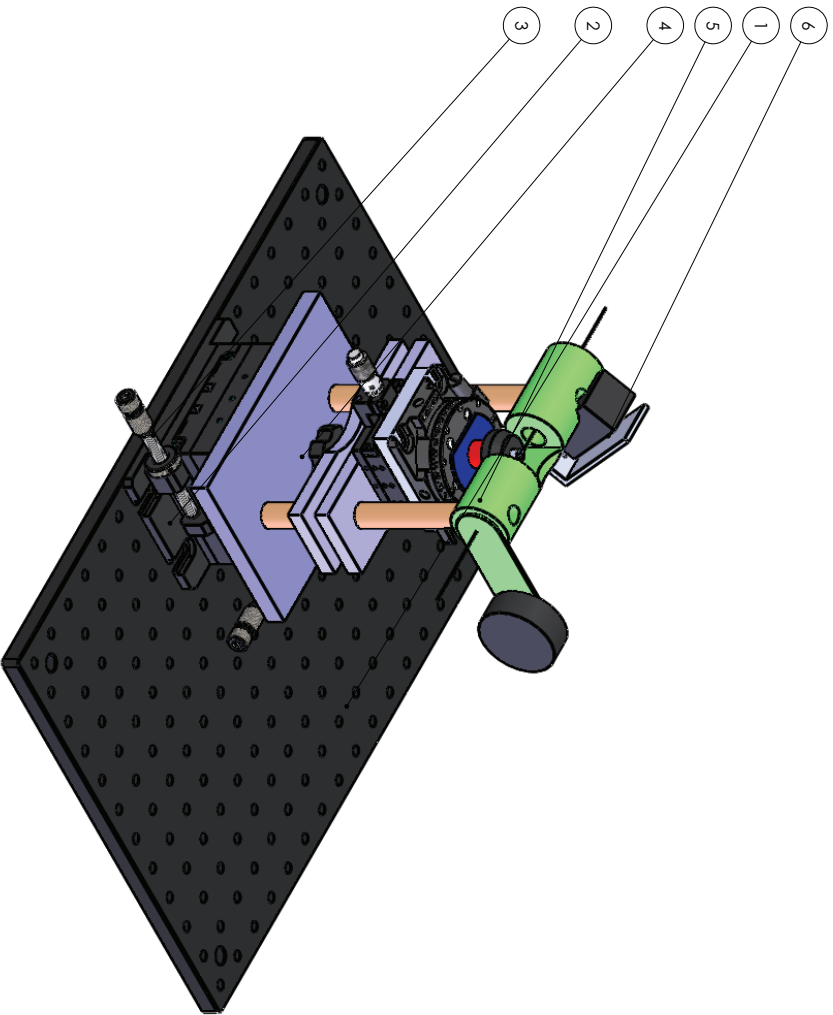
DO NOT SCALE DRAWING

SCALE: 1:8

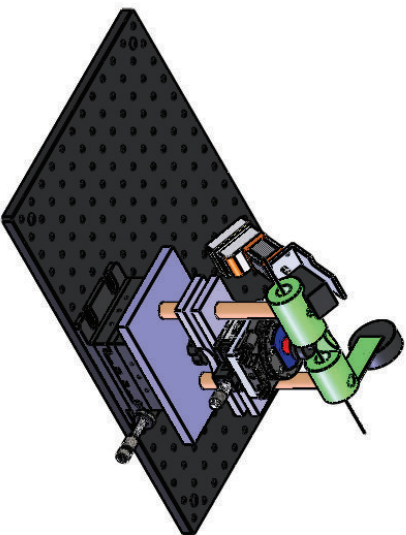
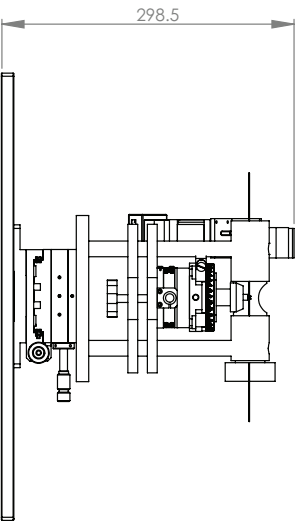
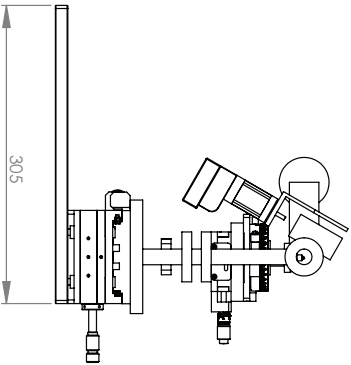
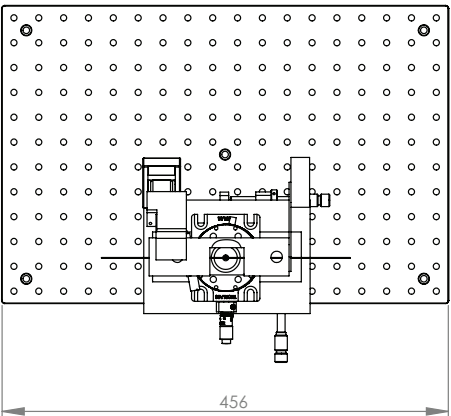
MASS:

SHEET 2 OF 9

ITEM NO.	PART NUMBER	manual explode/Qty.
1	MB1218	1
2	LT101	1
3	LT1	2
4	Torsion_Jig_Assem_May2_GM	1
5	TJ_Top	1
6	CurrentMotorAdppler	1
7	Motor	1



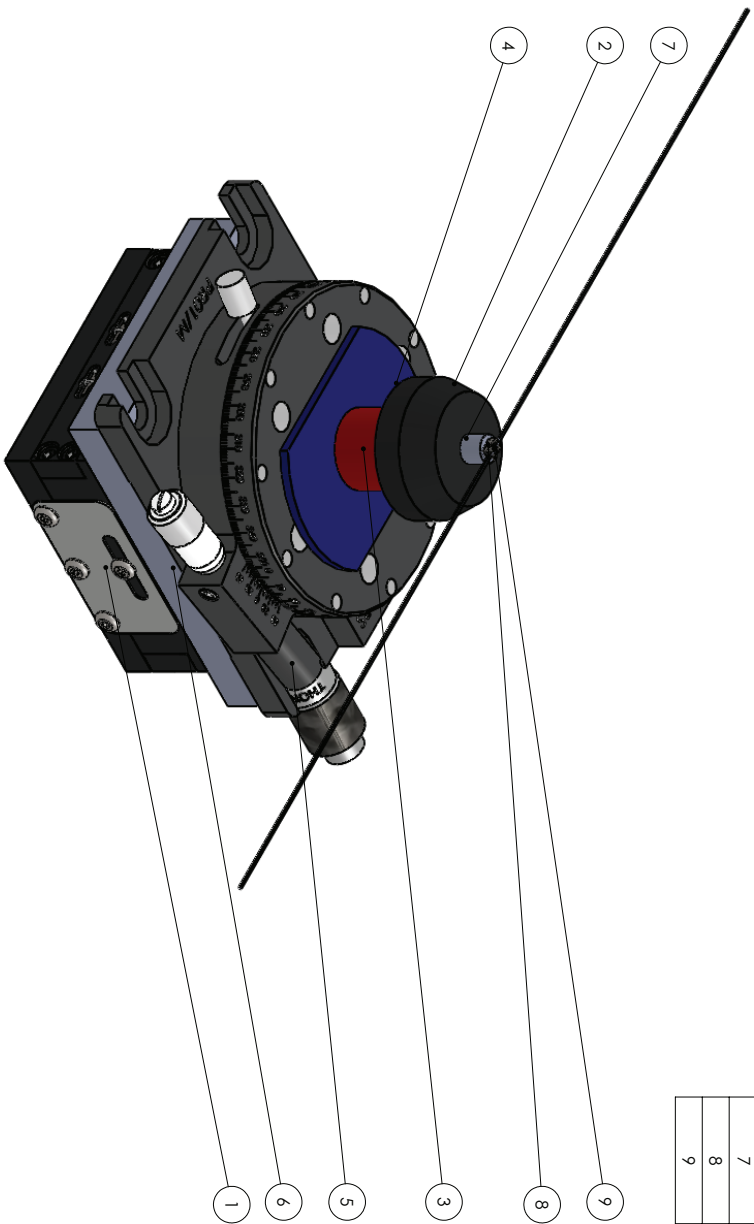
Nobes Lab		UNLESS OTHERWISE SPECIFIED:	
CARTAGE:		DIMENSIONS ARE IN MM	
FINISH:		TOLERANCES:	
PRIORITY:		ANGULAR: ± 0.5°	
COMMENTS:		X = ± 0.25	
		XX = ± 0.125	
		XXX = ± 0.005	
SURFACE FINISH		SPEED CODE	
μm			
MATERIAL:		Meat Job #	
Lab Location:		File Name:	
DO NOT SCALE DRAWING		gmelenka	
		6/13/2012 8:55:50 AM	
		Wednesday, June 13, 2012	
		SCALE: 1:8	
		MASS:	
		SHEET 3 OF 9	
		REV	
		PROJECT:	
		TITLE:	
		OTS Torque Assembly	
		The Department of Mechanical Engineering	
		UNIVERSITY OF ALBERTA	



Nobes Lab		UNLESS OTHERWISE SPECIFIED:		NAME	The Department of Mechanical Engineering UNIVERSITY OF ALBERTA	
Centre:		DIMENSIONS ARE IN MM	DRAWN	GW1	TITLE:	
Print:		TOLERANCES:	CHECKED		OTS Torque Assembly	
Phone:		ANGULAR: $\pm 0.5^\circ$	ENG APPR.		Project:	
Comments:		X = ± 0.25	Speed Code		REV	
		XXX = ± 0.005			File Name: Strain Imaging Assembly	
		SURFACE FINISH	Meet Job #		6/13/2012 8:55:50 AM	
		μm			Wednesday, June 13, 2012	
		0.6			SCALE: 1:8	
		Lab Location:	gmelenka		Mass:	
					SHEET 4 OF 9	
		DONOT SCALE DRAWING				



ITEM NO.	PART NUMBER	manual explode/Qty.
1	ThorlabsTranslationStage	1
2	Dowel_LoadCell_Adapter_April2012	1
3	loadCell_April2012	1
4	Load_Cell_Adapter_2012	1
5	ThorlabsRotationStage	1
6	StageOffset_2012	1
7	BracketDowel_April2012	1
8	OmcoOrthoSSBracket	1
9	Omco19x25Archwire	1

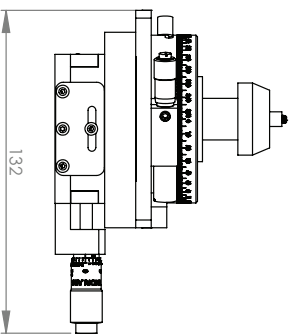
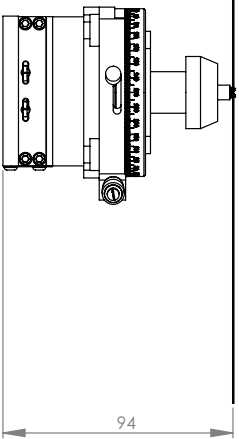
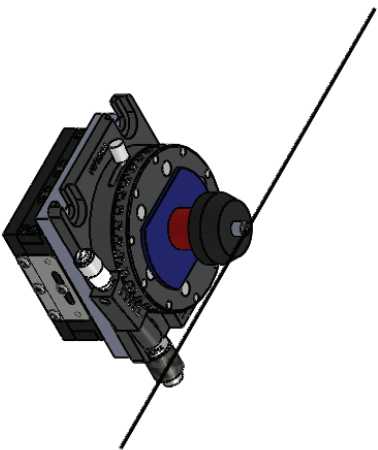
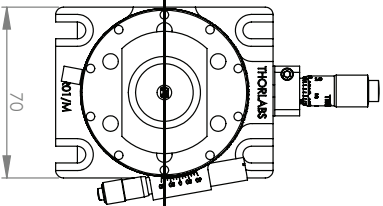


Nobes Lab		UNLESS OTHERWISE SPECIFIED:	
Contact: gmelenka@ualberta.ca		DRAWN: GWM	
Phone: 780-492-7476		CHECKED: ENG APPL	
Fax: 780-492-7476		Speed Code	
Comments:		MATERIAL: 0.6 /	
SURFACE FINISH: 0.6 /		File Name: LoadCellAlignmentASIZE	
Lab Location: MECE 6-23		gmelenka	
DONOT SCALE DRAWING		6/13/2012 8:55:50 AM	
		Wednesday, June 13, 2012	
		SCALE: 1:8	
		MASS:	
		SHEET 5 OF 9	

The Department of Mechanical Engineering
UNIVERSITY OF ALBERTA

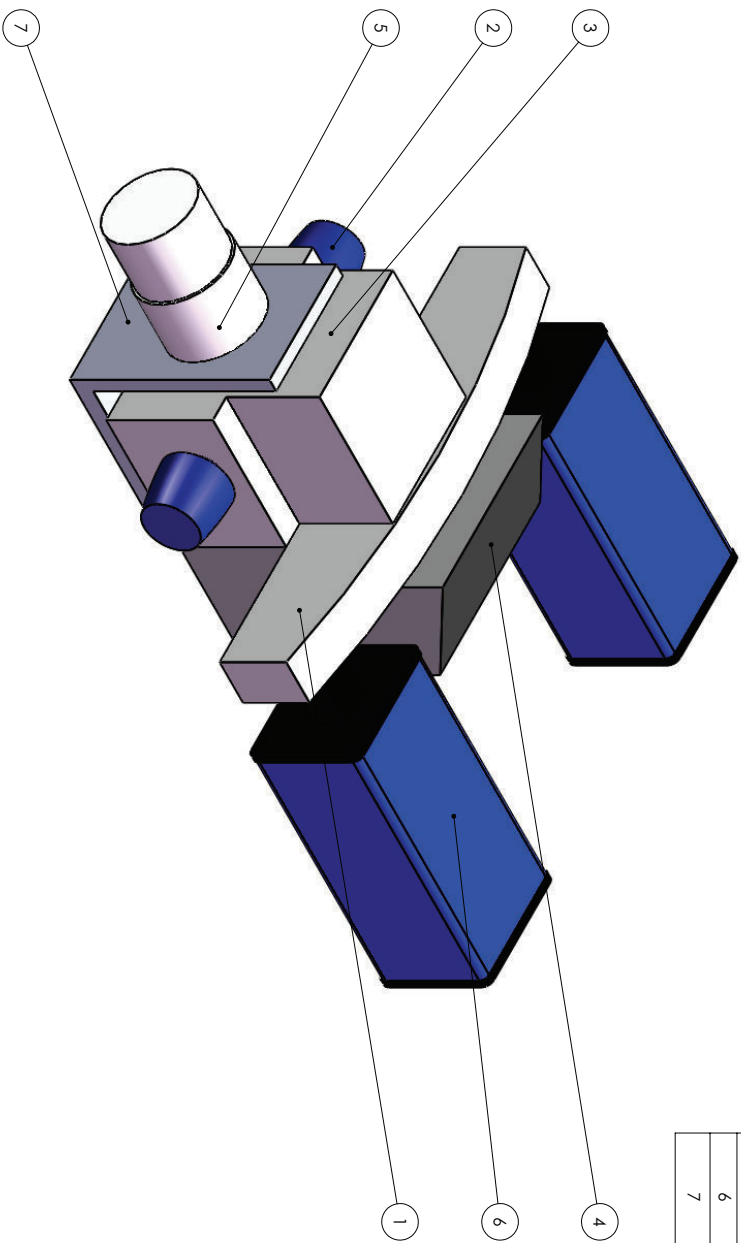
TITLE:
**Load Cell Alignment
Assembly**

Project: REV



Nobes Lab		UNLESS OTHERWISE SPECIFIED:		NAME	The Department of Mechanical Engineering UNIVERSITY OF ALBERTA	
CARTAGE:		DIMENSIONS ARE IN MM		DRAWN	GWM	
FROM: gmelinka@ualberta.ca		TOLERANCES:		CHECKED	TITLE:	
FROM: 780-492-7476		X = ± 0.25		ENG APPR.	Load Cell Alignment	
COMMENTS:		XXX = ± 0.005		SPEED CODE	Assembly	
		SURFACE FINISH		MEET JOB #	Project:	
		µm		File Name:	REV	
		0.6 /		Lab Location:		
				MECE 6-23		
				DONOT SCALE DRAWING		
				6/13/2012 8:55:50 AM		
				Wednesday, June 13, 2012		
				SCALE: 1:8		
				MASS:		
				SHEET 6 OF 9		

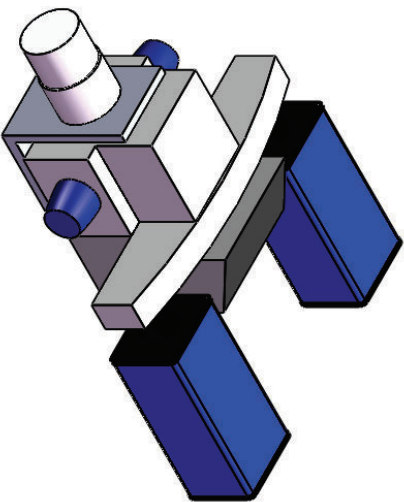
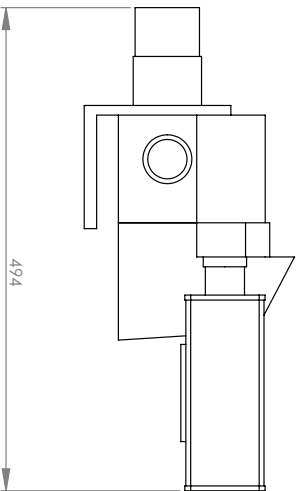
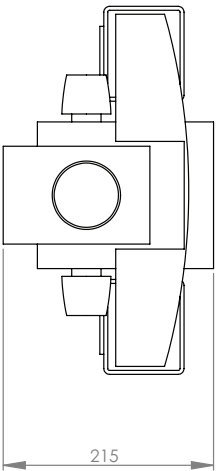
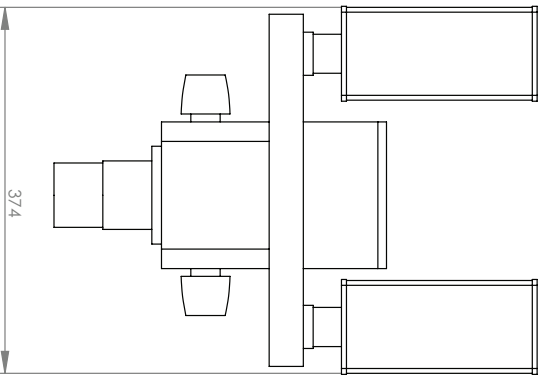
ITEM NO.	PART NUMBER	manual explode/Qty.
1	Zeiss_50-50phototube	1
2	ZeissMagaAdjust	2
3	ZeissStereodiscovery	1
4	ZeissViewport	1
5	Zeiss60mmLens	1
6	ImagerIntense	2
7	MicroscopeAngleBracket_April 2012	1



Nobes Lab		UNLESS OTHERWISE SPECIFIED:	
Customer:		DRAWN	NAME
Project:		CHECKED	GWMI
Part:		ENG APPR.	
Comments:		Speed Code	
SURFACE FINISH		Meat Job #	
µm			
MATERIAL:		File Name:	Camera&Microscope&Size
Lab Location:		gmelenka	Project:
DO NOT SCALE DRAWING		6/13/2012 8:55:50 AM	REV
		Wednesday, June 13, 2012	
		SCALE: 1:8	MASS:
		SHEET 7 OF 9	

The Department of Mechanical Engineering
UNIVERSITY OF ALBERTA

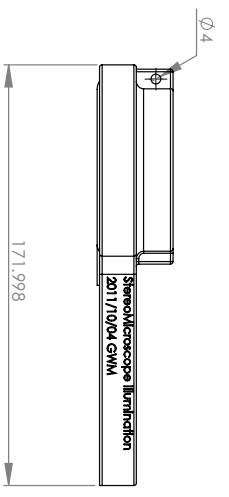
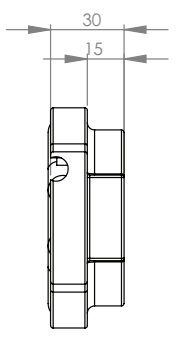
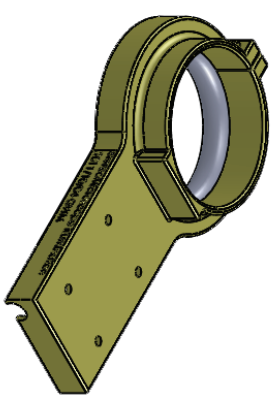
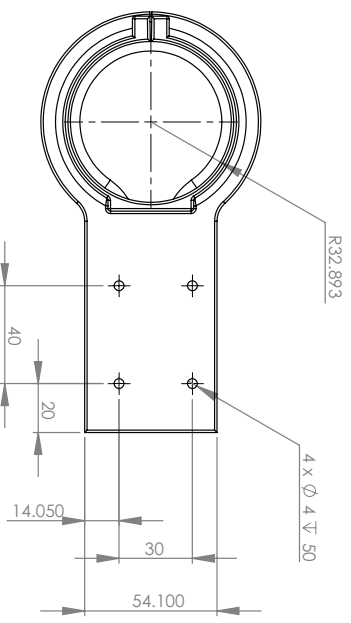
TITLE:
Stereo Microscope and
Camera Assembly



Nobes Lab		UNLESS OTHERWISE SPECIFIED:		NAME	The Department of Mechanical Engineering UNIVERSITY OF ALBERTA	
Centre:		DIMENSIONS ARE IN MM	DRAWN	GW1	TITLE:	Stereo Microscope and Camera Assembly
Print:		TOLERANCES:	CHECKED		DATE:	6/13/2012 8:55:50 AM
Phone:		ANGULAR: ± 0.5°	ENG APPR.		FILED:	Wednesday, June 13, 2012
Comments:		X = ± 0.25 Y = ± 0.25 ZXX = ± 0.005	Speed Code		Project:	
		SURFACE FINISH	Meet Job #		REV	
		µm	0.6			
		MATERIAL:	Camera & Microscope			
		Lab Location:	gmelenka			
		DONOT SCALE DRAWING	6/13/2012 8:55:50 AM Wednesday, June 13, 2012			



SCALE: 1:5
MASS:
SHEET 8 OF 9



Nobes Lab		UNLESS OTHERWISE SPECIFIED:		NAME	
Customer:		DIMENSIONS ARE IN MM		DRAWN	GWM
Part:		TOLERANCES:		CHECKED	
Project:		ANGULAR: ± 0.5°		ENG APPR.	
Comments:		X = ± 0.25		Speed Code	
		Y = ± 0.25			
		XXX = ± 0.005			
		SURFACE FINISH	0.6 /	Meet Job #	
		µm			
		MATERIAL:		File Name:	RP_Ringlight
		Lab Location:			gmelenka
		DONOT SCALE DRAWING			6/13/2012 8:55:50 AM
					Wednesday, June 13, 2012
		SIZE	Project:	REV	
		B			
		SCALE: 1:8	Mass:		
					SHEET 9 OF 9

The Department of Mechanical Engineering
UNIVERSITY OF ALBERTA
TITLE:
RP Ring Light Assembly